BEILSTEIN JOURNAL OF ORGANIC CHEMISTRY

Artificial photosynthesis

Edited by Andrea Pannwitz and Kalina Peneva

Imprint

Beilstein Journal of Organic Chemistry
www.bjoc.org
ISSN 1860-5397
Email: journals-support@beilstein-institut.de

The *Beilstein Journal of Organic Chemistry* is published by the Beilstein-Institut zur Förderung der Chemischen Wissenschaften.

Beilstein-Institut zur Förderung der Chemischen Wissenschaften
Trakehner Straße 7–9
60487 Frankfurt am Main
Germany
www.beilstein-institut.de

BEILSTEIN JOURNAL OF ORGANIC CHEMISTRY

Photoredox catalysis harvesting multiple photon or electrochemical energies

Mattia Lepori‡, Simon Schmid‡ and Joshua P. Barham*

Review

Open Access

Address:
Fakultät für Chemie und Pharmazie, Universität Regensburg, Universitatsstraße 31, 93040 Regensburg, Germany

Email:
Joshua P. Barham* - Joshua-Philip.Barham@chemie.uni-regensburg.de

* Corresponding author ‡ Equal contributors

Keywords:
consecutive photoinduced electron transfer; electro-activated photoredox catalysis; photoelectrochemistry; photoredox catalysis; radical ions

Beilstein J. Org. Chem. **2023,** *19,* 1055–1145.
https://doi.org/10.3762/bjoc.19.81

Received: 06 April 2023
Accepted: 07 July 2023
Published: 28 July 2023

This article is part of the thematic issue "Artificial photosynthesis".

Guest Editor: A. Pannwitz

Abstract

Photoredox catalysis (PRC) is a cutting-edge frontier for single electron-transfer (SET) reactions, enabling the generation of reactive intermediates for both oxidative and reductive processes via photon activation of a catalyst. Although this represents a significant step towards chemoselective and, more generally, sustainable chemistry, its efficacy is limited by the energy of visible light photons. Nowadays, excellent alternative conditions are available to overcome these limitations, harvesting two different but correlated concepts: the use of multi-photon processes such as consecutive photoinduced electron transfer (conPET) and the combination of photo- and electrochemistry in synthetic photoelectrochemistry (PEC). Herein, we review the most recent contributions to these fields in both oxidative and reductive activations of organic functional groups. New opportunities for organic chemists are captured, such as selective reactions employing super-oxidants and super-reductants to engage unactivated chemical feedstocks, and scalability up to gram scales in continuous flow. This review provides comparisons between the two techniques (multi-photon photoredox catalysis and PEC) to help the reader to fully understand their similarities, differences and potential applications and to therefore choose which method is the most appropriate for a given reaction, scale and purpose of a project.

Review

1 Introduction

Owing to the unique reactivity patterns of free radicals that often provide access to new dimensions of synthetic chemical space, the field of single electron transfer (SET) in organic synthesis has expanded considerably in the past two decades. Among this area, photoredox catalysis (PRC) is highly attractive due to its abilities i) to generate reactive intermediates under mild conditions for both oxidative and reductive reactions and ii) to use photons as traceless reagents to drive reactions in a “greener” manner [1-6]. As depicted in Figure 1, for an oxidative PRC cycle, the excited photocatalyst (***PC**) firstly

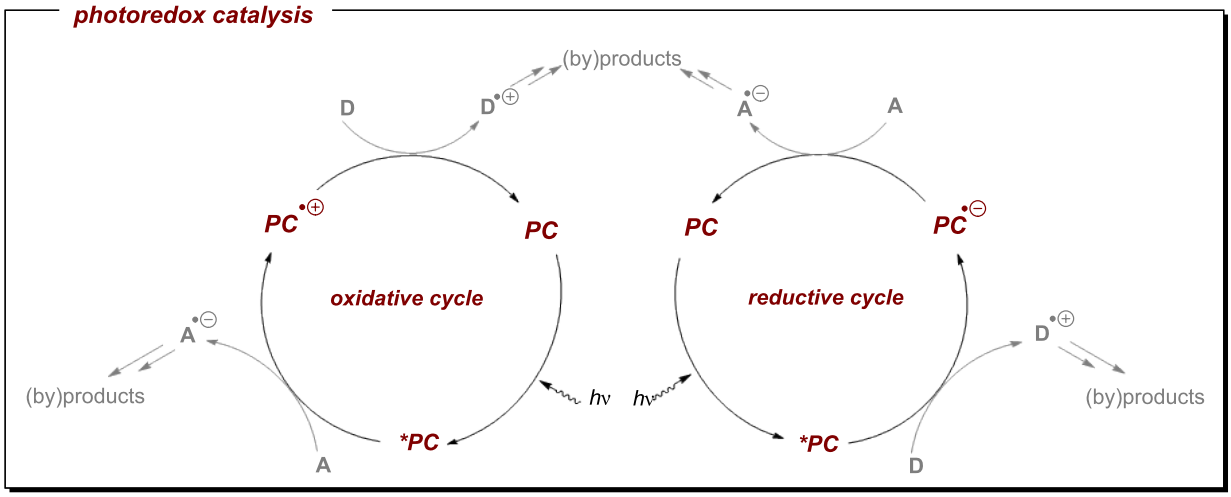

Figure 1: Oxidative and reductive activations of organic compounds harvesting photoredox catalysis.

undergoes oxidative quenching by SET with an electron acceptor (**A**), leading to $\mathbf{PC}^{\bullet+}$ and $\mathbf{A}^{\bullet-}$. The ground state photocatalyst is then regenerated by an SET reaction with an electron donor (**D**), affording also $\mathbf{D}^{\bullet+}$. Both species described can be further involved in various organic transformations to form the target products (or byproducts). In a complementary manner, ***PC** generates $\mathbf{A}^{\bullet-}$ and $\mathbf{D}^{\bullet+}$ within a reductive quenching cycle via SET reactions. The milder conditions that PRC enjoys to access potent redox agents guarantees sustainable and safer processes when compared to classical methods of equivalent redox power. For example, in the context of deeply reductive reactions, dissolving alkali metal conditions have remained the most commonly employed both in academia and industry for over a century and even to date continue to be used despite their hazards, poor selectivity and chemical waste [7-10]. Nowadays, excellent alternative conditions are available via PRC (vide infra).

However, even if PRC provides elegant methods to circumvent these issues, it comes with its own set of limitations. In particular, the accessible energy for photocatalytically-driven transformations is generally limited by the energy of a single visible light photon (400–700 nm; 1.8–3.1 eV). In addition, this energy is also diminished by as much as ≈25% through vibrational relaxation, internal conversion and intersystem crossing [11] and hence, many highly stabilized molecules including important feedstock molecules such as arenes, haloarenes or olefins remain inert to direct photoredox activation powered by visible light [12]. Irradiation with UV photons that intrinsically possess higher energy, however, is generally unfavorable due to the high expense and thermal footprint of the reactors. Although most organic molecules directly absorb photons in the UV region, side reactions and selectivity issues arise upon direct excitation of organic molecules. In recent years, two conceptually distinct but mechanistically related strategies have emerged that enable access to excited state catalysts wielding i) higher redox power than standard monophotonic photoredox catalysts and ii) energy that parallels the energy of UV-driven transformations, but under cheaper, safer conditions and in a more selective manner by indirect substrate activation via a catalyst. These are: a) multi-photon processes that accumulate visible light photon energies for electron transfer processes and b) photoelectrochemistry (PEC) in which electronic and photonic energies are either compiled or productively utilized. This Review summarizes key examples of both strategies, presents their respective advantages and drawbacks and aims to draw comparisons that can help readers decide which strategy is a more suitable fit for a given purpose. In order to do so, the scope of our Review is thus restricted to *electron transfer* redox processes and does not include energy transfer or atom/group transfer processes. Particularly interesting are instances where the *same active catalytic intermediate is proposed* in conPET and PEC reactions (e.g., a photoexcited radical anion), yet *different reactivity outcomes arise*; the underlying reasons for such are discussed. Finally, we provide our perspective on current challenges and target areas for future exploration.

1.1 Multi-photon processes

As mentioned, the energy accessible for a PRC reaction relying on a single visible photon is limited and does not suffice for many desirable target organic substrates. Direct cumulative absorption of visible light photons by a given molecule is extremely challenging, since the short lifetimes of excited states generally do not allow their accumulation in appreciable con-

centrations to absorb a subsequent photon and be further photoexcited. In biological photosynthesis – nature's omnipresent example of light-driven reactions – this limitation is overcome by transferring the energy of an initial photoexcitation process at photosystem II (**PSII**) via an electron transfer chain to photosystem I (**PSI**) where a second photoexcitation occurs [13,14]. Mimicry of this "Z-scheme" led to a seminal disclosure the concept of consecutive photoinduced electron transfer (conPET) by König and co-workers in 2014 for the generation of super-reductants [15] and by Wagenknecht in 2018 for the generation of super-oxidants [16]. Herein, initial excitation of the photocatalyst by a single photon is followed by reduction or oxidation by a sacrificial SET donor (e.g., Et_3N [15]) or acceptor (e.g., SF_6 [16]) to yield the catalyst radical anion or radical cation. As a semi-stable, higher energy ground-state entity, this can accumulate in sufficient concentration under the reaction conditions to absorb another photon and thereby generate a super-reducing or super-oxidizing excited state (Figure 2 left). In addition to 'radical ion' conPET, this Review will also cover deviating variants such as neutral (acridine) radical conPET as well as polysulfide or 'tandem' photoredox catalysis that similarly rely on the absorption of two photons to access activated catalyst states that engage redox-inert substrates.

Other two-photon processes where the photoredox-active species is generated by an initial energy transfer process – such as triplet-triplet annihilation (TTA) upconversion – are excluded from this Review as i) they are comprehensively and elegantly reviewed elsewhere [17], and ii) comparisons are not straightforward to make with PEC, a main theme of this Review. Protocols for sensitization-initiated electron transfer (SenI-ET) relying on a dual catalytic system of transition-metal based photocatalysts and pyrenes to generate highly reductive species are also excluded as such reported transformations are now equally achievable by a single catalyst entity [18-21].

1.2 Photoelectrochemistry (PEC)

Another important vehicle for SET is synthetic organic electrochemistry (SOE) [22,23]. While undoubtedly powerful, electrochemistry can suffer limitations in reaction selectivity because the constant application of high magnitude potentials can lead to uncontrolled reactions due to the accumulation of reactive intermediates within proximity of the electrode surface. Compared to homogeneous photocatalytic processes that lend themselves to high selectivity for taming radical intermediates by taking place in bulk solution, direct electrolytic reactions taking place at the heterogeneous interface presents an additional layer of complexity to mechanistic understanding and conferring selectivity. Nonetheless, SOE has enjoyed a dramatic rise in popularity in the last decade [24-27], partly driven by reactor standardization but also thanks to developments in technology (flow, alternating polarity) and understanding that fundamentally improve selectivity. Among these is its innovative merger with PRC (synthetic PEC) in a fashion that tackles the issues of both parent techniques and has risen to the forefront of methods for SET chemistry.

In the context of synthetic molecular photoelectrochemistry, there are various sub-fields classified depending on how the

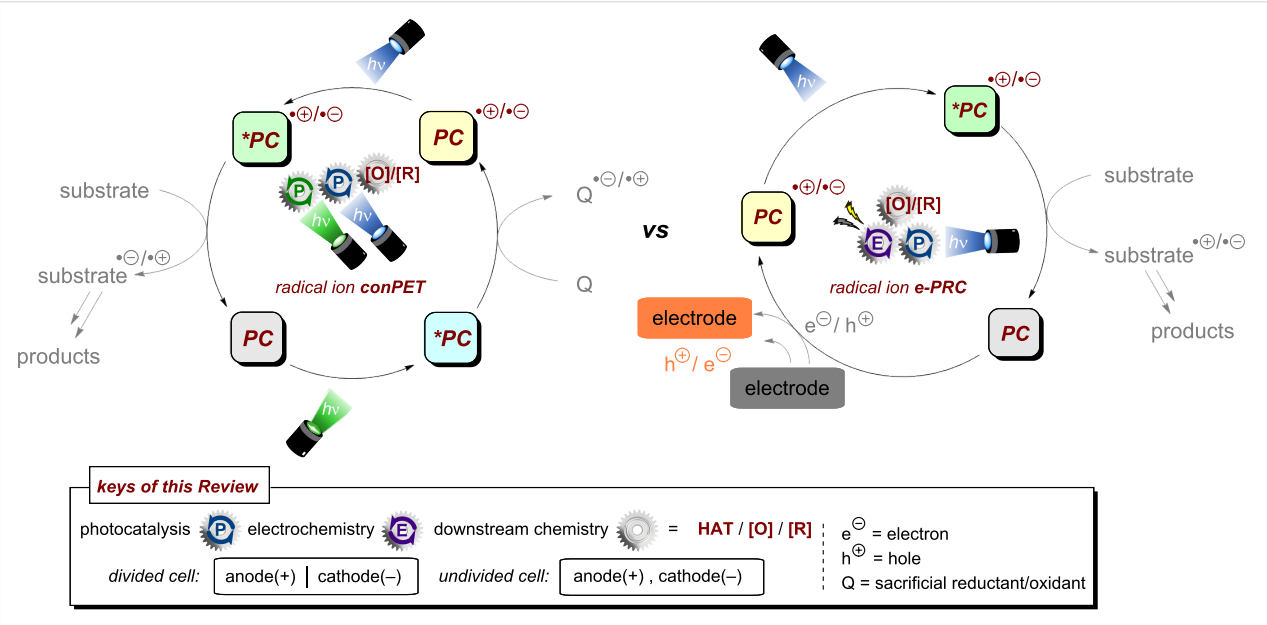

Figure 2: General catalytic cycles of radical ion conPET (left) and radical ion e-PRC (right).

electrochemical and photochemical steps interplay in the mechanism. This Review's main focus is on electrochemically mediated photoredox catalysis (e-PRC), where the electrochemical and photochemical steps are intimately involved within the same catalytic cycle, as subsequent steps. This broadly separates into two subcategories, "radical ion e-PRC" (Figure 2, right) and "recycling e-PRC". Radical ion e-PRC typically implicates electrogenerated radical ion doublet states which are photoexcited to yield super-oxidants or super-reductants while recycling e-PRC involves the turnover of a 'standard' (typically closed-shell) photoredox catalyst (**PC**) by means of anodic oxidation or cathodic reduction [28,29]. Furthermore, a series of new protocols using decoupled photoelectrochemistry (*d*PEC), where electrochemical and photochemical components have separate, discrete roles will be presented. This review excludes interfacial photoelectrochemistry (*i*PEC) processes, where reactions occur at photoelectrode surfaces. These are reviewed exhaustively elsewhere [28].

In recent years, both multi-photon processes and PEC developed from conceptually interesting techniques into widely applicable and well-developed methods capable of efficiently mediating and enabling difficult chemical transformations. Following a temporal order of discoveries, the reader will find the first section dedicated to reductive substrate activations via conPET and other multi-photon processes followed by more recently developed protocols for oxidative conPET. Hereafter, to provide continuity and highlight differences and comparisons between the two techniques, the Review will then focus attention on oxidative substrate activations in PEC before reductive activation examples of this field. Before plunging into the details of the two techniques, Figure 3 offers some advice for newcomers, a "Beginner's guide" flowchart, to understand which of the two techniques might be more appropriate in certain contexts of application. Broadly speaking, it can be concluded that carrying out reactions with conPET, both in academia and industry, has a lower barrier of accessibility due to more intuitive/standardized reactor setups. Essentially, the reactor setup can be identical to standard photoredox catalysis reaction setups, although it should be noted that since there are two photoactive species with often different absorption bands or different extinction coefficients at any given wavelength, it is necessary to use i) polychromatic wavelength which is less well-defined or ii) dual(/multi) wavelength LEDs that complicate the setup. The simpler reaction setups and lack of a heterogeneous surface (electrodes) can make the mechanistic investigation more accessible. While quantum parameters (quantum yield, quadratic relationships with light intensity, etc) have been touched upon for a monochromatic light source, the impact of relative intensities of different wavelengths ($\lambda_{max,ex}$ of **PC** and $\mathbf{PC}^{\bullet-/+}$) has never been investigated.

Notwithstanding the above, for longer-term industrial purposes, PEC is ultimately more suitable because only one species need be photoactive, and in purely economic terms generating one photon is cheaper than two (or more). Electrons (/holes, in the form of applied potential) are cheaper than photons as well. Regarding the additives necessary for the processes, even if electrolytes needed to reduce the Ohmic drop in PEC reactions are more expensive or more abundant than sacrificial reductants/oxidants employed in conPET (e.g., tetraalkylammonium salts vs trialkylamines), it is worth emphasizing that electrolytes, generally, are chemically innocent to undesired reactions, whereas the byproducts of sacrificed amines may be involved in processes that lower the efficiency and selectivity of the reactions (vide infra, conPET section).

Electrolytes have the potential to be i) aqueous-separated and recovered in batch, or ii) decreased, even ultimately eliminated by flow reactors as an engineering control.

Regarding purely the chemical reactivity and scope of applications, the most marked difference between the two types of processes, however, is that conPET is more appropriate for redox-neutral reactions, whereas PEC is more appropriate for net oxidations or reductions due to the radical polar crossover nature of its reactivity [30,31]. In the former, the neutral photoexcited catalyst must be able to engage substrates/intermediates in PET to achieve a redox neutral process. In the latter, following the first photoinduced electron transfer (PET) step a subsequent electrochemical SET occurs in the same redox direction and this subsequent SET is user-tunable by the applied cell potential. These divergent reactivity features make the two techniques totally complementary, allowing the exploration of a large portion of SET-driven organic transformations using at least one of them at a time. Since 'radical ion' conPET/e-PRC are proposed to involve the same radical ion catalyst intermediate, the same catalyst can in principle be repurposed for either technique, and mechanistic learnings will thus be highly transferrable between the fields.

Although asymmetric transformations are yet to be achieved using conPET, the PEC section of this Review will also describe pioneering first efforts in this direction [32,33]. Finally, both techniques are amenable to large-scale synthesis and ideally integrated with state-of-the-art reactor technology platforms, such as continuous flow reactors and high throughput screening plates. Various examples of scalability will be highlighted in this Review, with a particular emphasis on the challenges and areas for improvement, such as the standardization of reactors capable to conjugate applied potential and light irradiation either in different modules or within the same flow path.

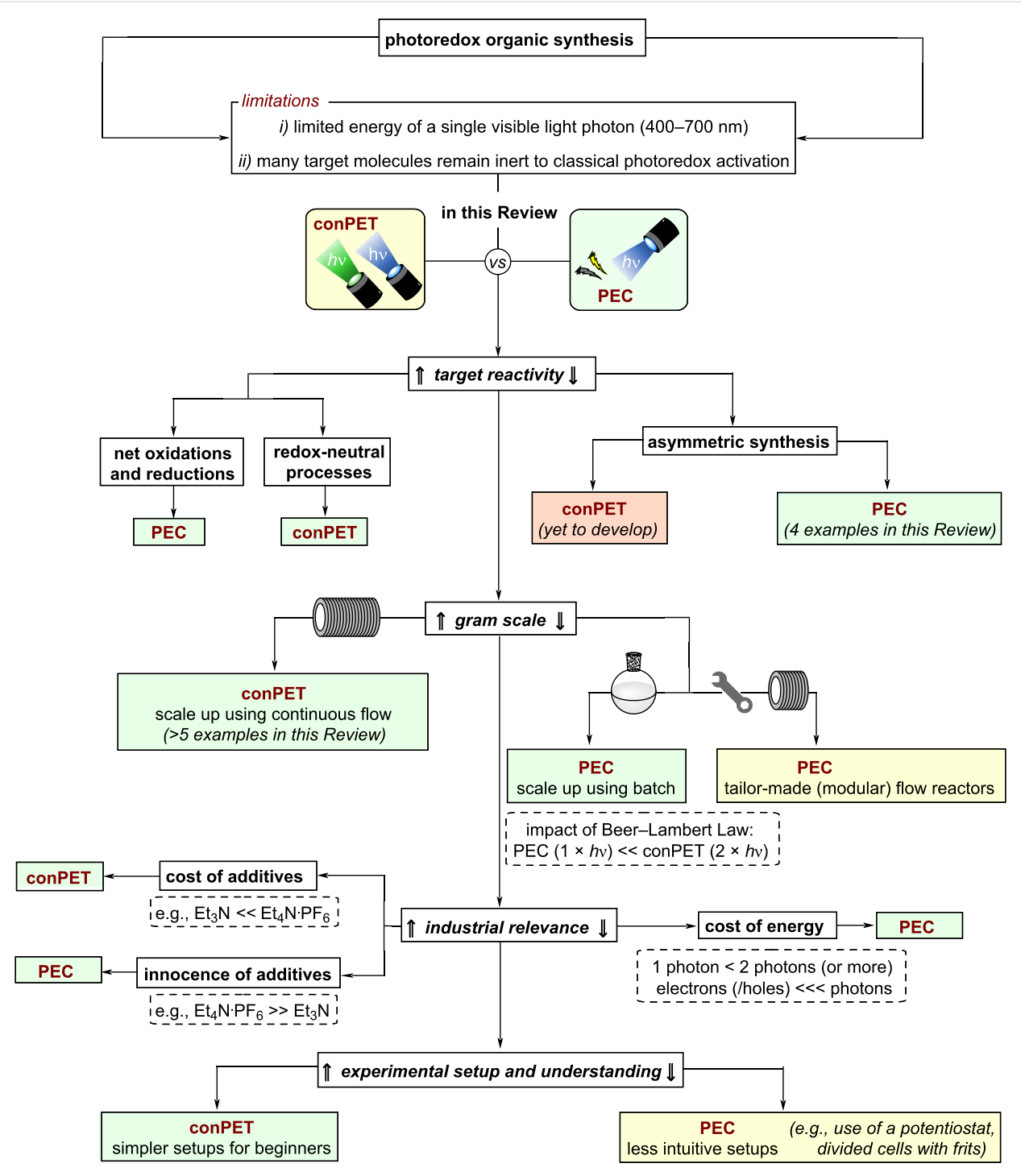

Figure 3: "Beginner's guide": comparison between advantages, capacities, and prospectives of conPET and PEC.

2 conPET in organic synthesis

2.1 Reductive activation

2.1.1 C(sp^2)–X activation: In the rise of visible light-mediated PRC, the generation of aryl radicals for C(sp^2)–C($sp^{2/3}$) couplings under mild conditions (room temperature, visible light activation of a catalyst) was heavily investigated [34-36]. However, initially the procedures were generally limited to electron-poor arenes like diazonium/iodonium salts or aryl iodides with electron-withdrawing substituents as aryl radical precursors, due to the limited accessible reducing power of photocatalysts that relied on a monophotonic excitation event. However, the vast majority of inexpensive, commercially avail-

able aryl halides are chlorides [37,38], with potentials for reduction that almost exclusively lie beyond the threshold of monophotonically-excited photoredox catalysts (i.e., more deeply negative than $E_{1/2}$ = −2.0 V vs SCE). Considering this, state-of-the-art developments have focused on the generation of super-reductants ($^*E_{1/2}$ > −2.0 V vs SCE) that accumulate the energy of multiple photons. Case studies will now be presented.

Hereafter, while we quote the excited state redox potentials from the report in question, it should be noted that these are estimates associated with uncertainties especially in the case of excited radical ions which oftentimes exhibit unusual wavelength dependencies on catalytic efficiency. Light source wavelengths/input powers (radiant flux is rarely reported) are quoted if available, readers are directed to the report in question for details. When not available, the qualitative description is used as per the report in question (e.g., 'blue LEDs').

The König group first reported a photocatalytic approach to C(sp^2)–X activation harnessing multiple photon energies in their seminal work on perylene diimide (**PDI**) catalysts [15]. In their proposed consecutive photoinduced electron transfer (conPET) mechanism (Figure 4C), **PDI** is photoexcited and reductively quenched by Et_3N to form its stable, colored radical

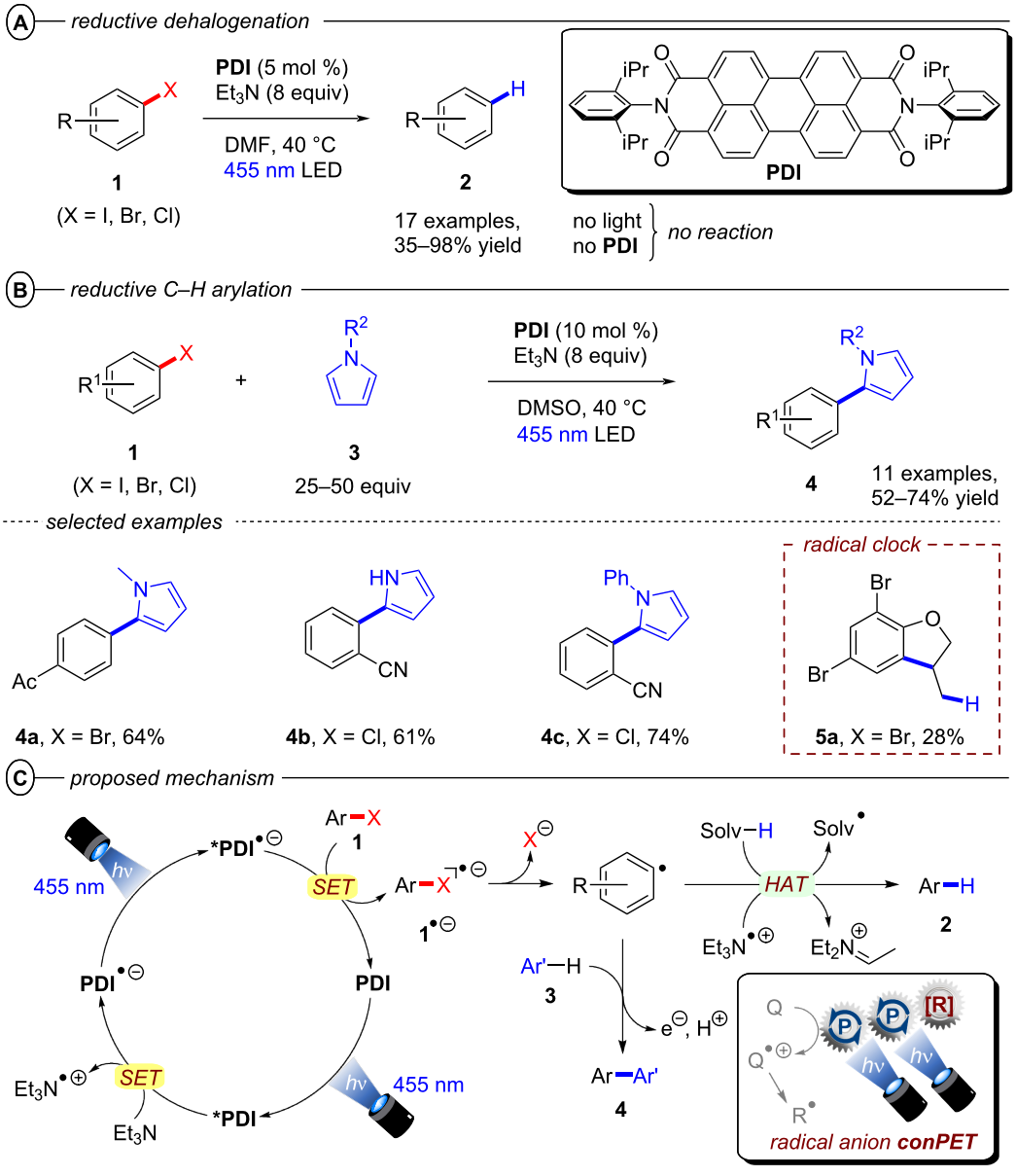

Figure 4: A) conPET reductive dehalogenation of aryl halides with **PDI**. B) Reductive C–H arylation with pyrroles (top) and selected examples from the substrate scope (bottom). C) Proposed mechanism.

anion **PDI**$^{\bullet-}$ that can be photoexcited again to generate an even stronger reductant; ***PDI**$^{\bullet-}$ (*$E_{1/2}$ = −1.87 V vs SCE) [34]. A SET process to the aryl halide regenerates neutral **PDI** and forms the aryl halide's radical anion, which then undergoes C(sp^2)–X bond fission to afford the aryl radical as a reactive intermediate. The aryl radical then either reacts via hydrogen atom transfer (HAT) with solvent molecules or $Et_3N^{\bullet+}$ in an overall dehalogenation to furnish product **2**, or it is trapped with pyrrole derivatives **3** in a C–C bond formation to afford arylated products **4**. Based on the ultrashort lifetime of ***PDI**$^{\bullet-}$ (τ = 145 ps), the notion of its photochemistry has attracted skepticism and it has been suggested decomposition products of ***PDI**$^{\bullet-}$ may instead serve as reductants as a theme of ongoing debate [39]. Nonetheless, this protocol enabled the reduction of various electron-poor aryl iodides and aryl bromides and, for the first time, the reduction of aryl chlorides (albeit electron-poor ones) via visible light PRC in good to excellent yields (35–98%) (Figure 4A). Notably, the protocol was also applicable to 4-iodotoluene as a moderately deactivated aryl iodide and the C(sp^2)–I bond cleavage occurred chemoselectively in the presence of a C(sp^2)–Br bond. *N*-Methylpyrrole and various other substituted pyrroles could be applied as trapping agents for electron-poor aryl halides and the coupling products were obtained in good yields (52–74%) (Figure 4B). To suppress the rapid HAT with solvent DMF that yields the dehalogenated product, DMSO was chosen as solvent for the C–H arylation. When applying the catalytic protocol to 2-allyloxy-1,3,5-tribromobenzene, the 5-*exo-trig* cyclized product **5a** was obtained – albeit only in 28% yield – corroborating a radical mechanism. **PDI** catalysts have since found applications in other chemical transformations, their photophysical properties have been investigated further [40], and new variants [41] including heterogeneous versions have been introduced [42-44].

Since radical ion conPET chemistry gives access to different reducing species of the same catalyst and both are photoactive, König and co-workers developed a synthetic protocol that allows the chromoselective (wavelength-dependent) regulation of catalytic behavior and thus enabling controlled bond activations [45]. Regarding the reductive C–C arylation, the application of the xanthene dye rhodamine 6G (**Rh-6G**) as a catalyst for the reduction of heteroarenes bearing two or three bromine atoms (e.g., **6**) under irradiation with green light (λ = 530 nm) gave monosubstituted products (e.g., **7**) whereas irradiation with blue light (λ = 455 nm) provided disubstituted products **8** (Figure 5A). Additionally, adding a different trapping reagent before switching from green to blue light allows for a sequential and controlled substitution in a one-pot reaction (Figure 5B). 2,4,6-Tribromopyrimidine (**6a**), whose core pyrimidine structure can be found in many biologically active compounds, could be sequentially substituted with 1,3,5-trimethoxybenzene and *N*-methylpyrrole to give **8a**. The protocol also enabled the selective reductive dehalogenation at the benzylic position of **9a** with green light while the C(sp^2)–Br bond remained untouched. Subsequent irradiation with blue light gave the sequentially substituted products **9c** and **9d**. As with **PDI**, the xanthene dye rhodamine 6G (**Rh-6G**) can undergo reductive quenching upon excitation with green or blue light (Figure 5C). Considering that **Rh-6G** describes a chloride salt, the photocatalyst itself is a monocationic species (**Rh-6G**$^+$) that forms a neutral radical (**Rh-6G**$^\bullet$) upon reductive quenching. The radical **Rh-6G**$^\bullet$ itself ($E_{1/2}$ = −1.0 V vs SCE) can directly reduce certain aryl bromides or other substrates with sufficiently accessible reduction potentials whereas a second excitation with blue light yields the excited state ***Rh-6G**$^\bullet$ that can reduce substrates with much more negative reduction potentials (E^p_{red} < −2.4 V vs SCE). The authors also demonstrated the applicability of **Rh-6G** for reductive arylation reactions (Figure 5D). While the use of **PDI** was mostly limited to electron-poor aryl halides, ***Rh-6G**$^\bullet$ could reach a step further and reductively activate electron-rich aryl bromides such as 4-bromotoluene and 4-bromoanisole, albeit providing low (27% and 25%) yields of the coupled products **4d** and **4e**, respectively.

Building on this work, König and co-workers also demonstrated the synthesis of pyrrolo[1,2-*a*]quinolines (**12**) and ullazines (**13**) from *N*-arylpyrroles (**10**) with arylalkynes (**11**) using **Rh-6G** (Figure 6) [46]. Additionally, the König group also used **Rh-6G** as a catalyst for a photo-Arbuzov reaction to generate arylphosphonates (**15**) from aryl halides and trialkylphosphites (**14**) via a similar conPET mechanism (Figure 7) [47]. Notably, even 4-bromoanisole could be reductively activated and phosphorylated in 58% yield (**15b**).

Reports from Eggins [48], Lund and Eriksen [49] have shown that upon excitation, the radical anions of anthraquinones – a class of organic dyes widely applied as catalysts in organic PRC [50] – are capable of reducing aryl halides with deeply negative reduction potentials. Starting from these premises, the König group in 2017 demonstrated the use of 1,8-dihydroxyanthraquinone (**AQN**) as a suitable conPET catalyst for reductive dehalogenations (Figure 8A), C–H arylations and olefinations of aryl halides (Figure 8B) [51]. In addition to the classical conPET mechanism involving the formation of ***AQN**$^{\bullet-}$, the authors also confirmed formation of the semiquinone anion **AQN-H**$^-$ via formal addition of a hydrogen atom (e.g., through protonation and successive reduction or HAT) that upon excitation also acts as a super-reductant (Figure 8C).

Simultaneously, Jacobi von Wangelin, Pérez-Ruiz and co-workers introduced the structurally related 9,10-dicyano-

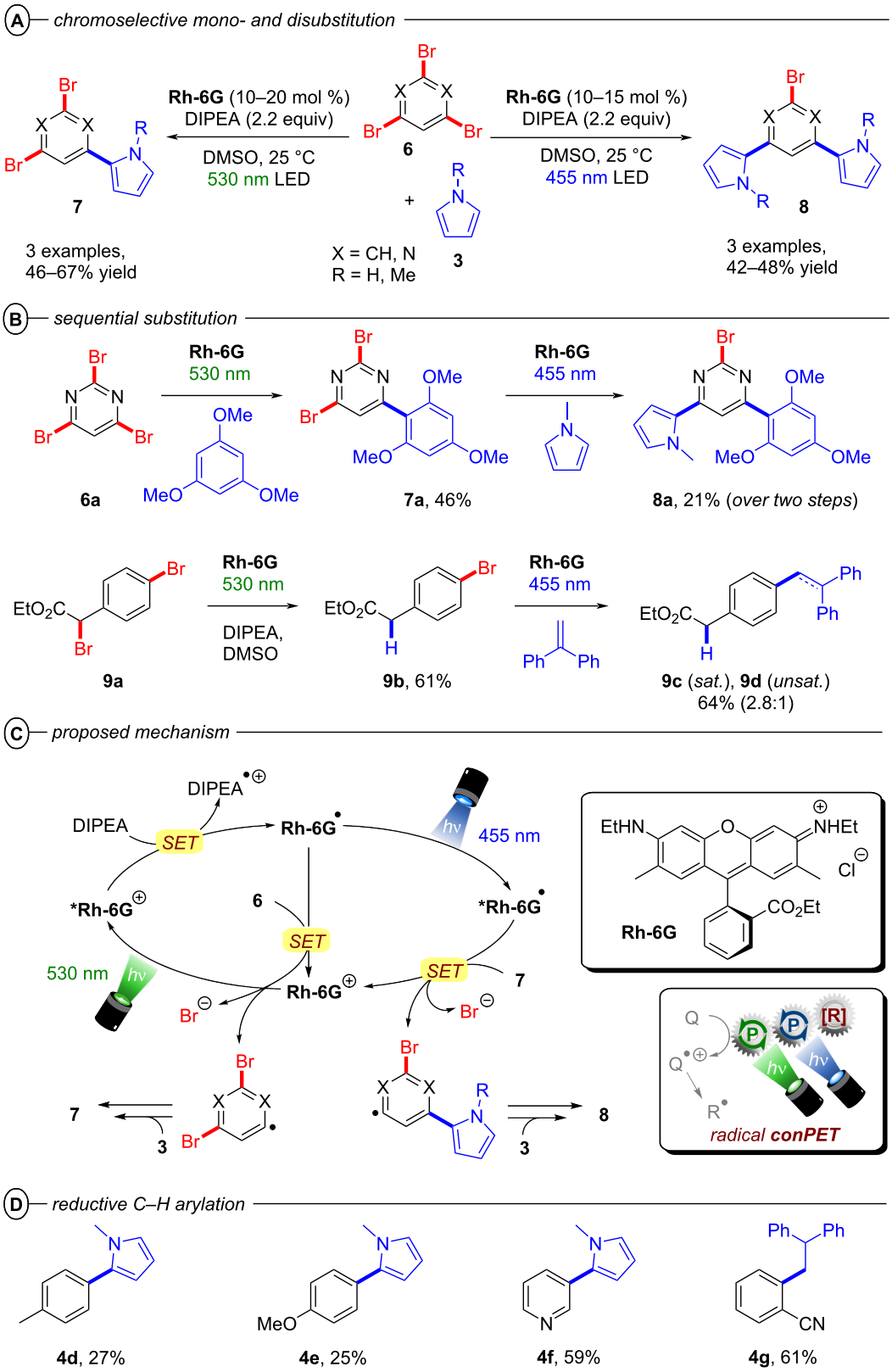

Figure 5: A) Chromoselective mono- and disubstitution or polybrominated pyrimidines with pyrroles. B) Sequential substitution with distinct trapping reagents. C) Proposed mechanism. D) Selected examples from the substrate scope of the C–H arylation via monosubstitution of aryl halides.

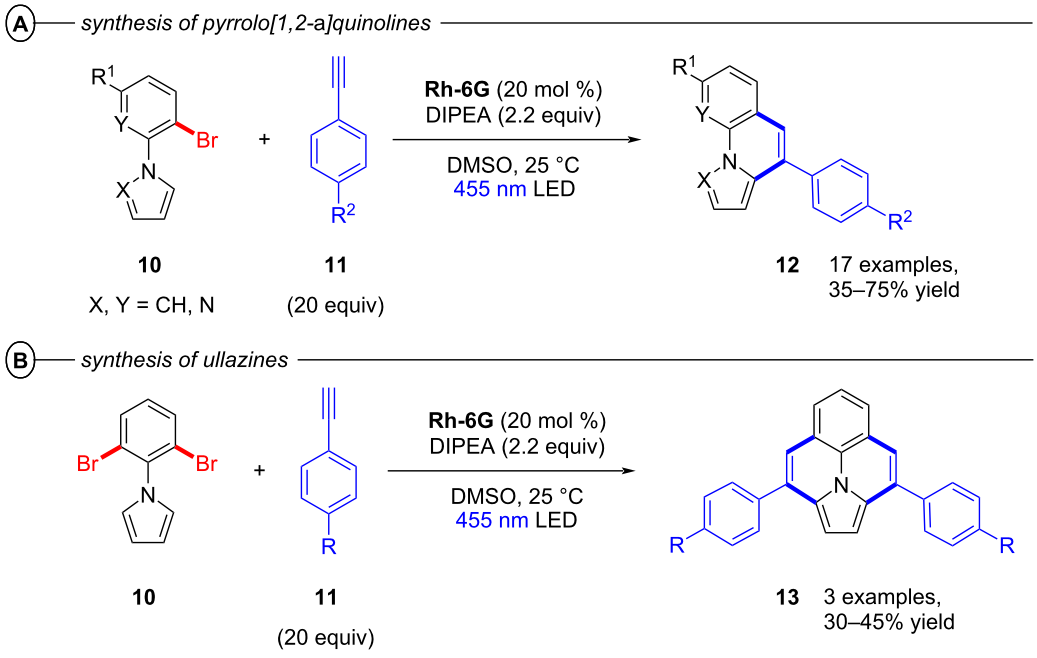

Figure 6: A) Synthesis of pyrrolo[1,2-*a*]quinolines. B) Synthesis of ullazines.

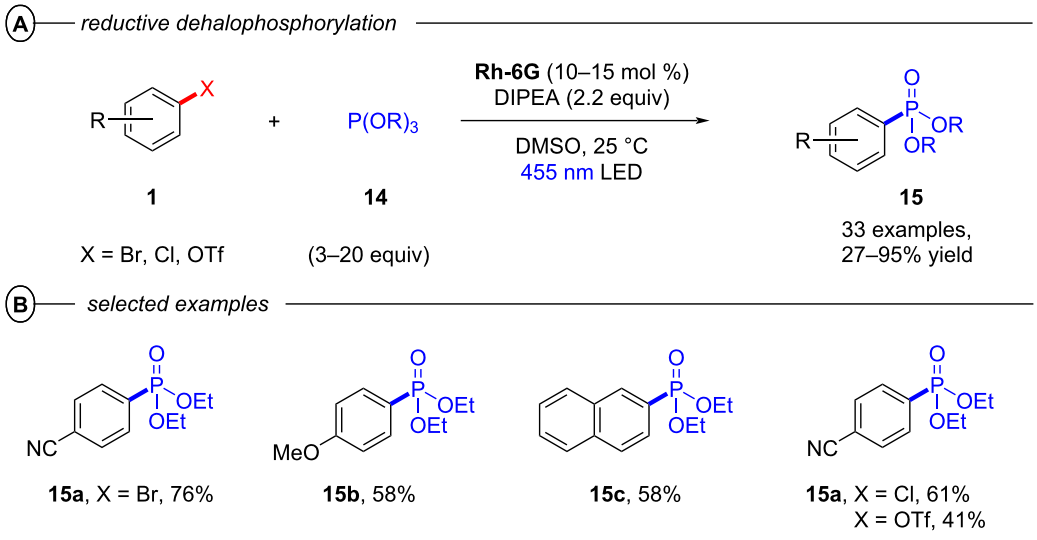

Figure 7: A) Reductive phosphorylation of aryl halides via conPET. B) Selected examples from the substrate scope.

anthracene (**DCA**) as a conPET catalyst. Excitation of PET-generated radical anion **DCA**$^{\bullet-}$ generates *$\mathbf{DCA}^{\bullet-}$ as a super-reductant capable of reducing aryl bromides and chlorides [52]. Due to minimal overlap in the absorption spectral bands of **DCA** and **DCA**$^{\bullet-}$, a cold-white LED (λ = 410–700 nm) was used for polychromatic irradiation. The protocol for reductive C–H arylations with pyrroles was applicable to electron-poor aryl halides including various heterocyclic halides, affording their products in poor to excellent yields (4–92%) (Figure 9A). Regarding the unsatisfactory results, the coupled products of the strongly deactivated 4-bromoanisole (E^{p}_{red} = −2.75 V vs SCE) and 4-chloroanisole (E^{p}_{red} = −2.88 V vs SCE) were only obtained in yields of 6% and 4%, respectively, which the authors attributed to insufficient redox power of *$\mathbf{DCA}^{\bullet-}$ in its D_1 state ($^*E_{1/2}$ = −2.60 V vs SCE) [53]. These results strongly contrast to the work of Lambert and Lin on e-PRC reductions with **DCA** (vide infra) where these exact electron-rich aryl halides could be engaged successfully.

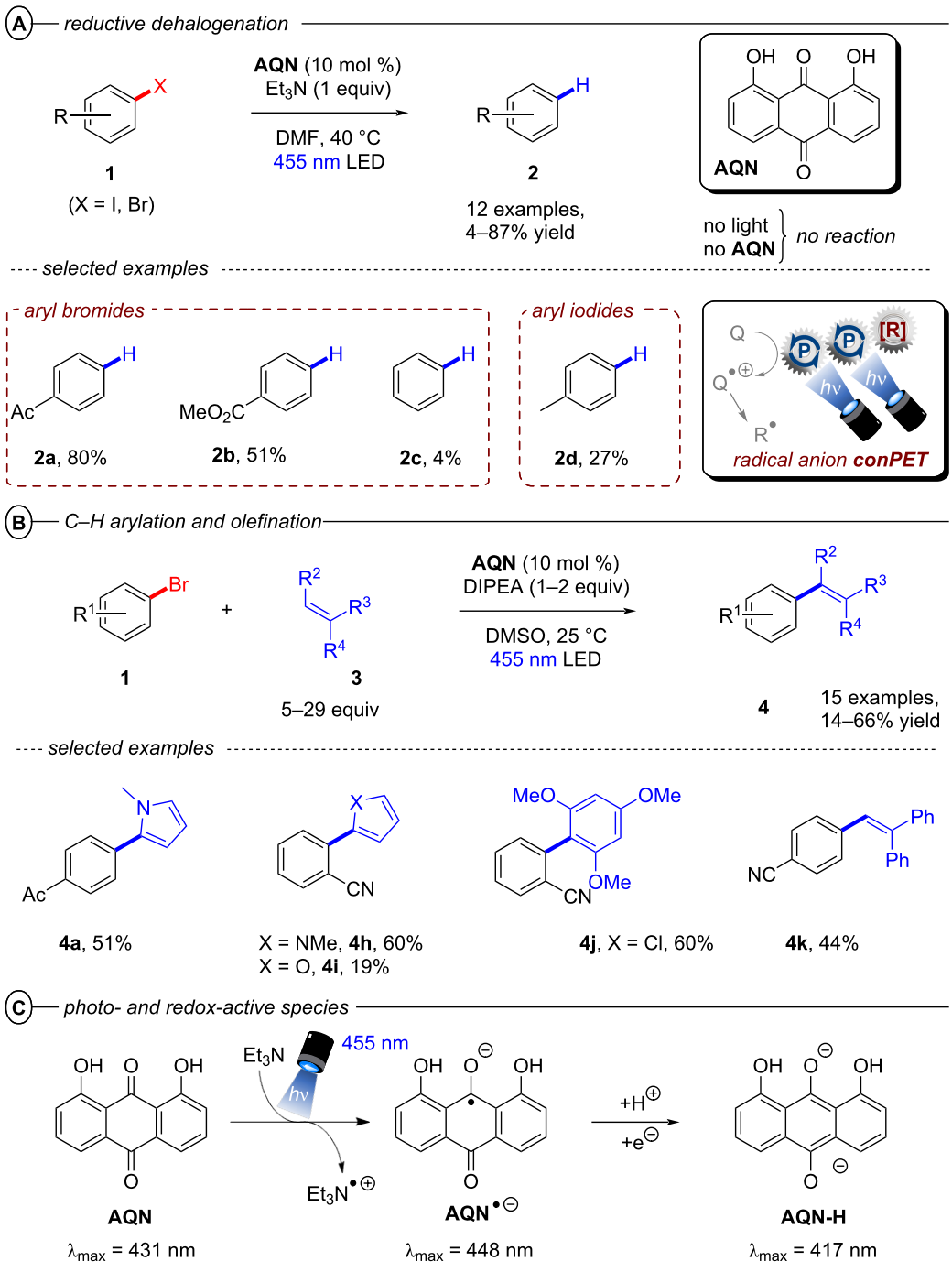

Figure 8: A) Reductive dehalogenation of aryl halides via conPET and selected examples from the substrate scope. B) Reductive C–H arylation and olefination (top) and selected examples from the substrate scope (bottom). C) Photo- and redox-active species of **AQN**.

This contrast suggests either i) a different active species was involved in the latter report (vide infra: Figure 60 in PEC reductive activations) or ii) that the higher steady-state concentrations of $\mathbf{DCA}^{\bullet-}$ available by electrogeneration favor a preassembly with Ar–X that i) upon photoexcitation accesses excited states higher than the first (D_1) to bolster reactivity and/or ii) following PET assists in the Ar–$X^{\bullet-}$ fragmentation step.

The scope was expanded using triethylphosphite ($P(OEt)_3$), dimethyl disulfide (MeSSMe) and bis(pinacolato)diboron (B_2pin_2) as trapping agents for C(sp^2)–Het(Arene) couplings (Figure 9B).

The successful activation of electron-neutral and electron-rich aryl halides via conPET mostly remained an unsolved chal-

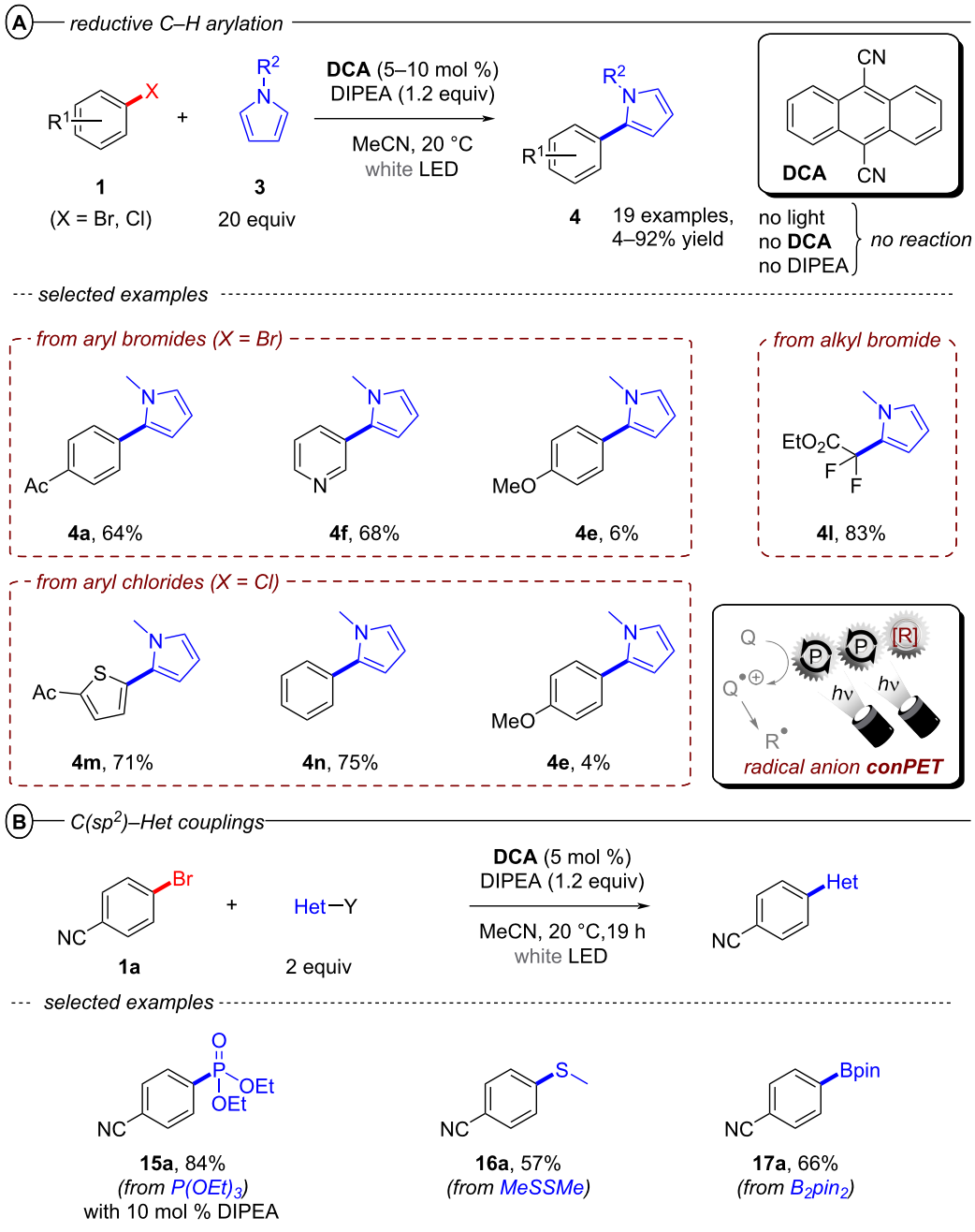

Figure 9: A) Reductive C–H arylation of aryl halides via conPET (top) and selected examples from the substrate scope (bottom). B) Methodology extension to C(sp^2)–Het(Arene) couplings (top) and selected examples from the substrate scope (bottom).

lenge until the Nicewicz group in 2020 disclosed a modified acridinium (Fukuzumi) salt **Mes-Acr-BF$_4$** as a suitable conPET catalyst. Following the conPET catalytic cycle, the **Mes-Acr$^+$** cation is excited and reductively quenched by DIPEA to yield the acridine radical **Mes-Acr$^•$** (Figure 10C) [54]. Upon excitation to its twisted intramolecular charge-transfer (TICT) state, **Mes-Acr$^•$** has an excited-state half potential ($^*E_{1/2}$ = −3.36 V vs SCE) even more negative than alkali metals including lithium, making it one of the most potent chemical reductants ever reported.

Owing to this exceptional reductive redox power, hydrodehalogenation of various electron-poor and electron-rich aryl bromides and chlorides including 4-bromoanisole and 4-chloro-

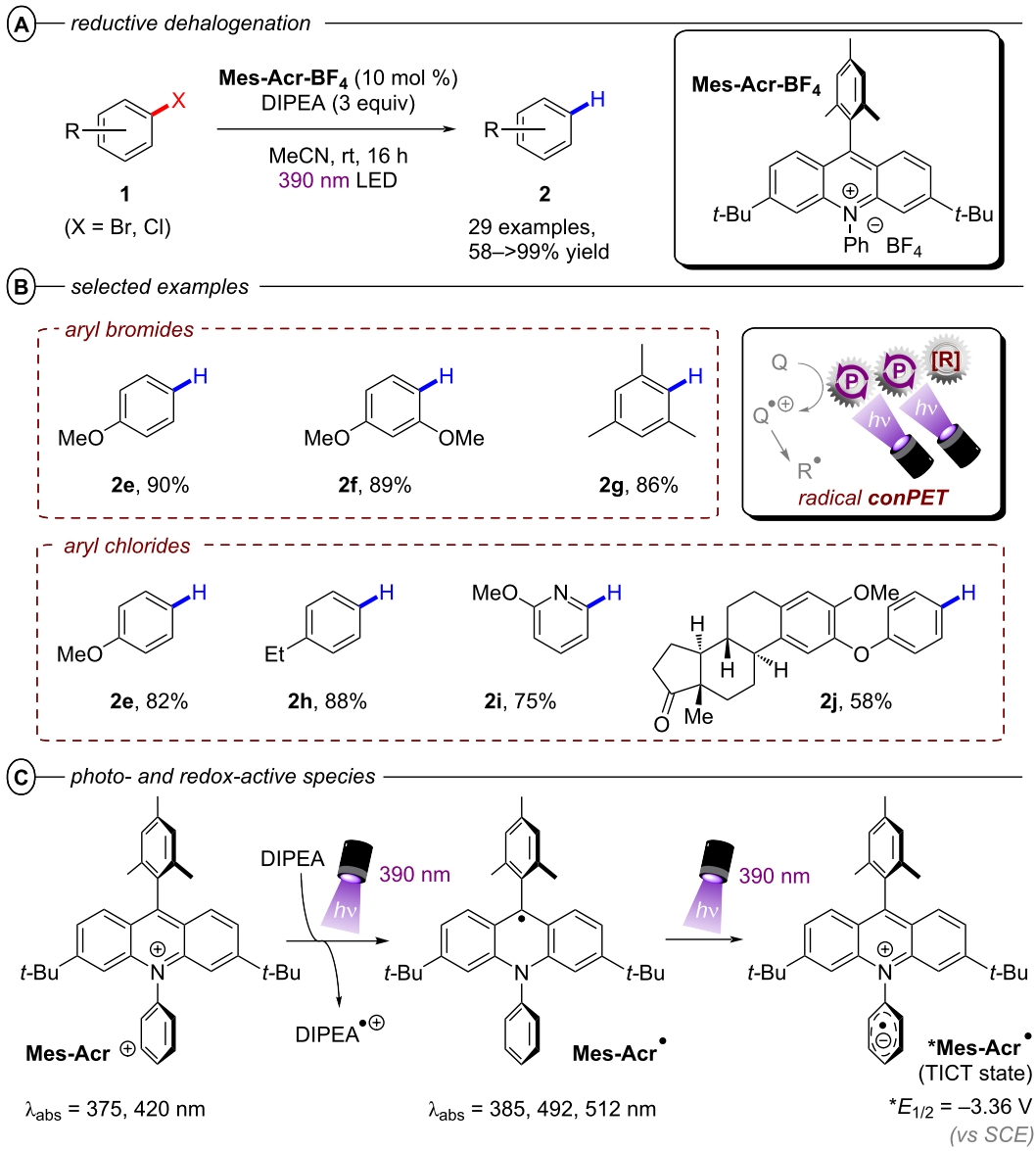

Figure 10: A) Reductive hydrodehalogenation of aryl halides with **Mes-Acr-BF$_4$**. B) Selected examples from the substrate scope. C) Photo- and redox-active species of **Mes-Acr-BF$_4$**.

anisole (**2e**), 1-bromo-2,4- dimethoxybenzene (**2f**) and 4-ethylchlorobenzene (**2h**) occurred in good to excellent yields (58–99%) (Figure 10B).

Based on their exciting success with isophthalonitrile derived compounds as electron-primed photocatalysts in e-PRC (vide infra, Figure 69), the Wickens group developed a conPET protocol using 2,4,5,6-tetrakis(diphenylamino)isophthalonitrile (**4-DPAIPN**) for the reduction of electron-rich aryl chlorides [55]. With **4-DPAIPN** as an electron-primed photocatalyst, substrates with reduction potentials as deep as E^{p}_{red} = −3.4 V vs SCE (**1c**) were readily reduced and dehalogenated products obtained in excellent yields (70–92%) (Figure 11A). Sodium formate was found to be a more efficient terminal reductant than trialkylamines which the authors attributed to the formation of a carbon dioxide radical anion ($CO_2^{\bullet-}$) upon oxidation of the formate via SET to **4-DPAIPN** and successive deprotonation by a second formate anion (Figure 11B). Due to its reducing nature, $CO_2^{\bullet-}$ (E^0 = −2.2 V vs SCE) may promote the photoreductant activity either by reducing another equivalent of photocatalyst or the direct reduction of sufficiently electron-poor aryl halide substrates (Figure 11C). While trialkylamines like Et_3N or DIPEA have been proven to be suitable terminal reductants in conPET chemistry [15,45,46,51,54], they may still

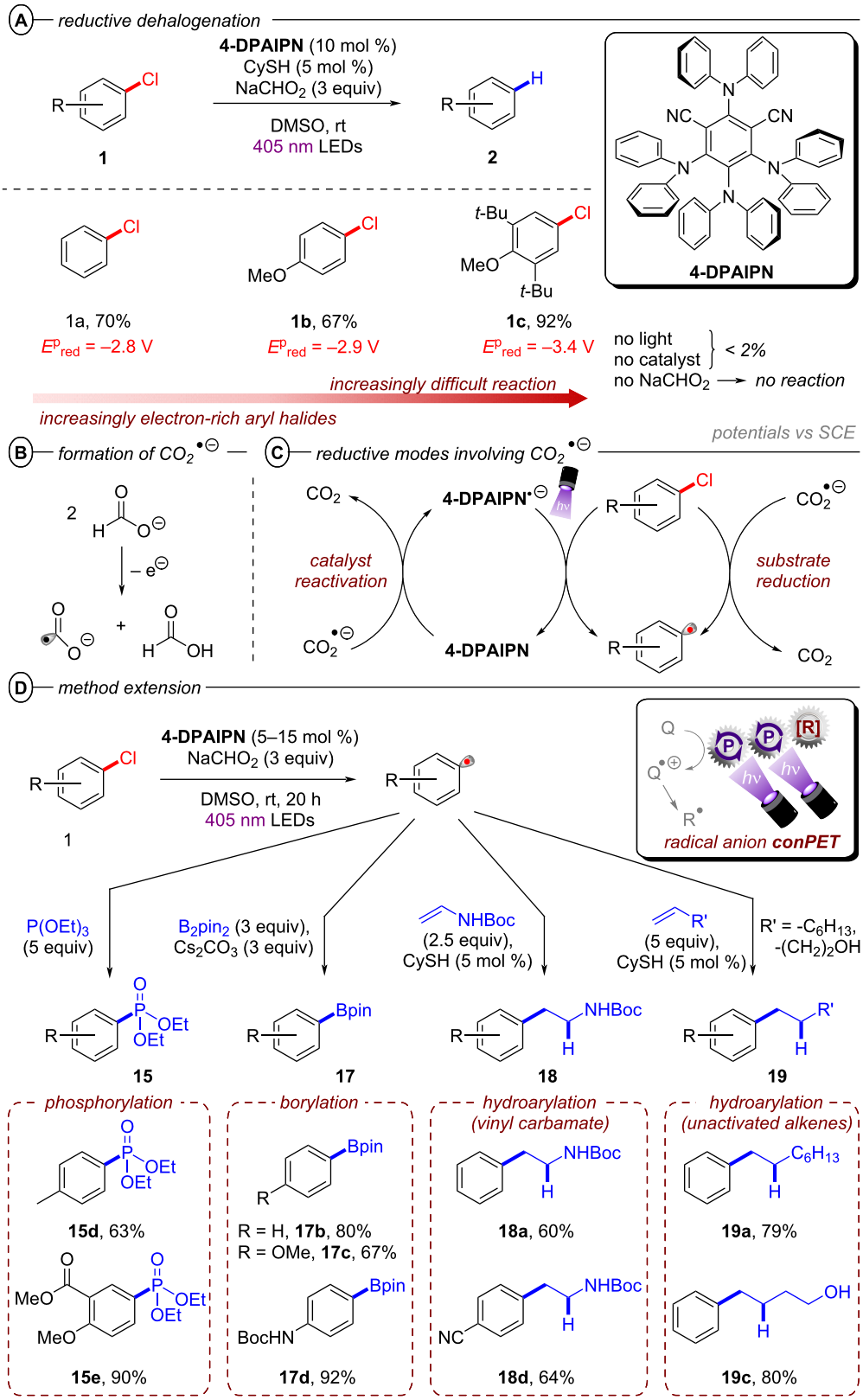

Figure 11: A) Reductive hydrodechlorination of aryl chlorides with **4-DPAIPN**. B) Proposed formation of $CO_2^{\bullet-}$. C) Potential reductive modes involving $CO_2^{\bullet-}$. D) Extension to phosphorylation, borylation and hydroarylation of olefins.

decrease photoreductant activity via back electron transfer [56], in contrast to $CO_2^{\bullet-}$ which has an entropic driving force (evolution of CO_2). Triethylphosphite $P(OEt)_3$ and bis(pinacolato)diboron B_2pin_2 were successfully applied as trapping reagents for redox-neutral photo-Arbuzov and borylation reactions with good to excellent yields (Figure 11D). Additionally, the authors were able to perform the net-reductive hydroarylation of *tert*-butyl vinylcarbamate and unactivated alkenes like 1-octene and 3-buten-1-ol although the vinyl carbamate substrate (E^p_{red} = −2.2 V vs SCE) is significantly easier to reduce than most aryl chlorides. This selectivity, especially considering the need for an excess of the vinyl carbamate, might indicate a preassembly between **4-DPAIPN**$^{\bullet-}$ and the aryl chloride.

Simultaneously, Zhou, Wu and co-workers demonstrated 2,4,5-tri(9*H*-carbazol-9-yl)-6-(ethyl(phenyl)amino)isophthalonitrile (**3CzEPAIPN**) as yet another isophthalonitrile derived photocatalyst suitable for conPET chemistry [57]. Similar to **4-DPAIPN**, both electron-poor and electron-rich aryl chlorides with reduction potentials up to E^p_{red} = −2.94 V vs SCE were readily reduced by ***3CzEPAIPN**$^{\bullet-}$. The authors demonstrated an impressive scope of borylation reactions with B_2pin_2 as well as other boronate esters (**17h**) and several examples of late-stage functionalization (**17i** and **17j**) (Figure 12A). Interestingly, sodium oxalate could be used as the electron donor provided a catalytic loading of 4-cyanopyridine was added. Although the role of the latter species was not proposed by authors, it is more facile to reduce than an aryl chloride so could act as an electron shuttle (potentially via a π-stacking assembly).

The synthetic scope was extended to C(sp^2)–P bond formations by trapping with phosphines or phosphites (Figure 12B), and in all these cases DIPEA was used as the electron donor (0.5–5 equiv). Arylphosphonium chlorides **20** that are widely used as reagents, organocatalysts, or phase transfer reagents [58-61] were synthesized from aryl chlorides in various yields (20–87%) under mild photocatalytic conditions whereas previously reported protocols typically relied on transition metal catalysis or high temperature processes [62-64]. Arylphosphonates **15** were obtained in a photo-Arbuzov reaction by trapping with trimethylphosphite in good to excellent yields (62–88%) (Figure 12B). Additionally, intramolecular trapping via dearomative hydroarylation gave access to spirocyclic cyclohexadienes bearing dihydrobenzofuran and indoline scaffolds (**22a**,**b**) via a radical-polar crossover mechanism (Figure 12C) [65], showcasing the power of conPET in dearomatization reactions. Finally, the synthesis of tetraphenylphosphonium chloride (**20a**) could be scaled up efficiently in an operationally very simple continuous-flow setup with only 2.5 mol % of photocatalyst and a productivity of 13.1 g/day (Figure 13). Of note, only 0.5 equiv of DIPEA was required for all reactions of aryl chlorides with triarylphosphines, suggesting the intermediate tetraarylphosphine radical reduces DIPEA$^{\bullet+}$ to regenerating DIPEA.

Even though various organic compounds have been successfully implemented as radical (anion) photocatalysts for Ar–X bond activation in the reports of König, Jacobi von Wangelin and Pérez-Ruiz, Nicewicz, Wickens, Zhou and Wu above [15,45,46,51,54-57,66], the underlying mechanism has largely remained elusive. While Kasha's rule is classically applied only for photophysical phenomena stating that emission events generally occur only from the lowest excited state of a certain multiplicity due to very fast relaxation via internal conversion (IC) and vibronic relaxation [67-69], it can also be adapted to photochemical reactions stating that outer sphere ET events generally occur only from the lowest excited state due to the same relaxation pathways [69]. It has been largely proven that this limitation is circumvented by the involvement of excited radical anions and two excitation processes; to access molecular orbitals beyond the frontier orbitals of the neutral photocatalyst and thus, higher redox potentials. However, the identity of the key intermediate has remained a matter of debate [40,70,71]. Full elucidations of the mechanism toward confirming the key(/main) active catalyst species and possible deactivation pathways are incredibly important for the development of new radical ion catalysts with improved photon economies and novel applications. Lee, Cho, You, and co-workers recently disclosed a fully elucidated mechanism of the reductive borylation of aryl halides using three newly developed photocatalysts bearing indolocarbazole electron donor and benzothienopyrimidine electron acceptor moieties (Figure 14A and B) [72].

In general, three possible pathways can lead to catalyst deactivation and thus, kinetically limit the overall photon economy (Figure 14C, red arrows). Firstly, both photoinduced electron transfer steps are competing with the intrinsic relaxation of the excited states ***PC** and ***PC**$^{\bullet-}$. In particular, the latter is commonly a very short-lived species (e.g., τ_{obs}(***PC1**$^{\bullet-}$) = 64 ps vs τ_{obs}(***PC1**) = 2.2 μs). Secondly, even if the initial PET generation of **PC**$^{\bullet-}$ succeeds, it can be quickly reversed by charge recombination via unproductive back electron transfer (**PC**$^{\bullet-}$ + D$^{\bullet+}$ → **PC** + D), preventing the second excitation. The prevalence of this charge recombination process in conPET effectively regulates a lower steady-state concentration of active photocatalyst compared to PEC where the electrochemical reduction to **PC**$^{\bullet-}$ ensures higher concentrations that are directly user-influenced. Upon activation, **PC1** could successfully reduce various aryl halides generating borylated products in

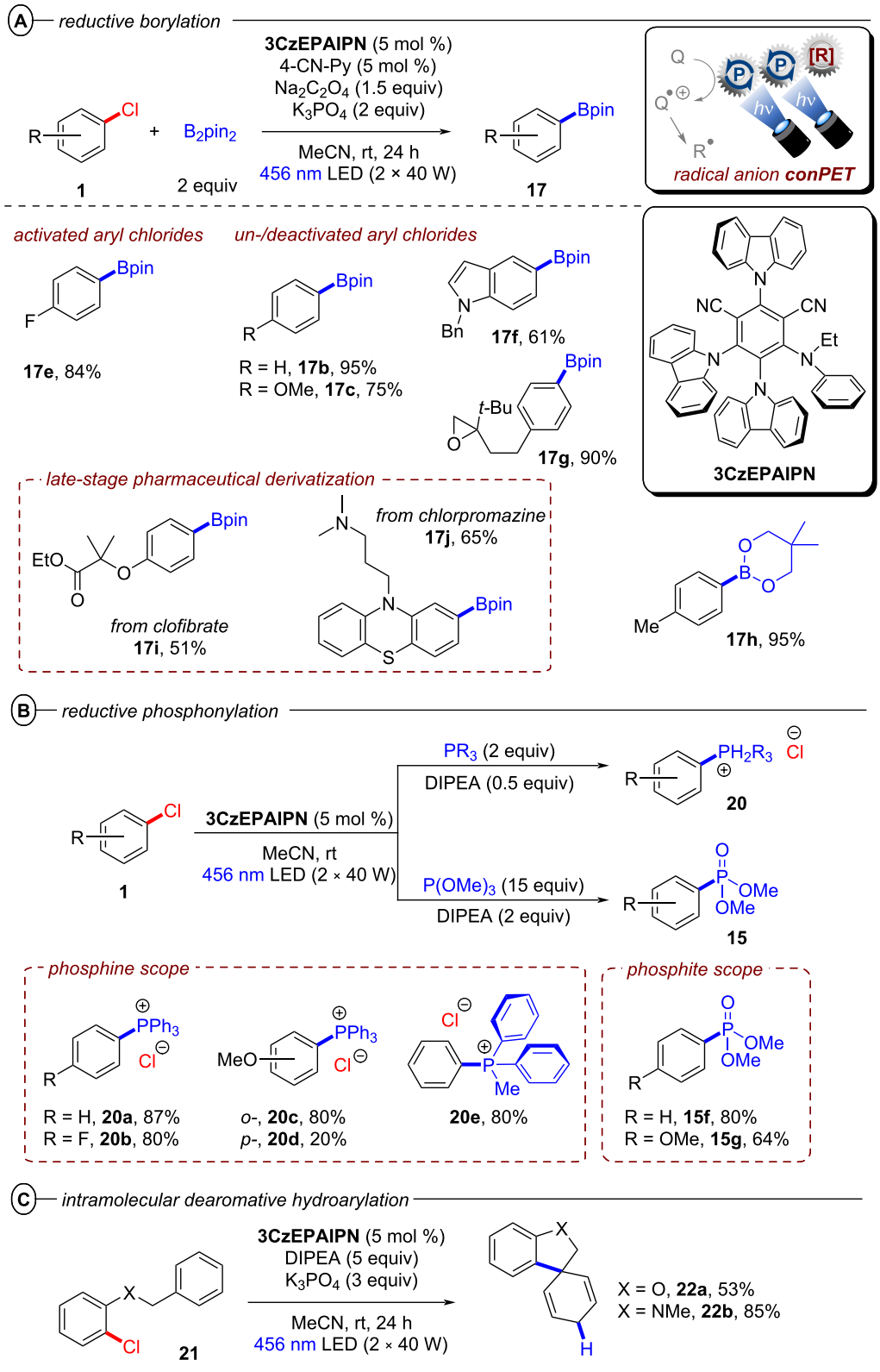

Figure 12: A) Reductive conPET borylation with **3CzEPAIPN** (top) and selected examples from the substrate scope (bottom). B) Phosphonylation scope. C) Intramolecular dearomative hydroarylation scope.

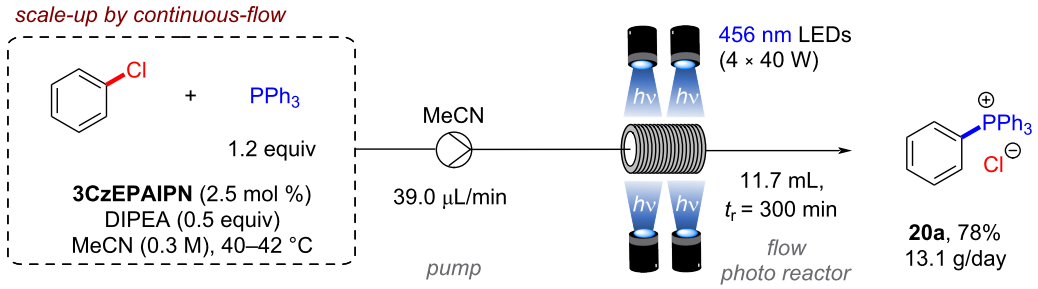

Figure 13: Scale-up of conPET phosphorylation with **3CzEPAIPN**.

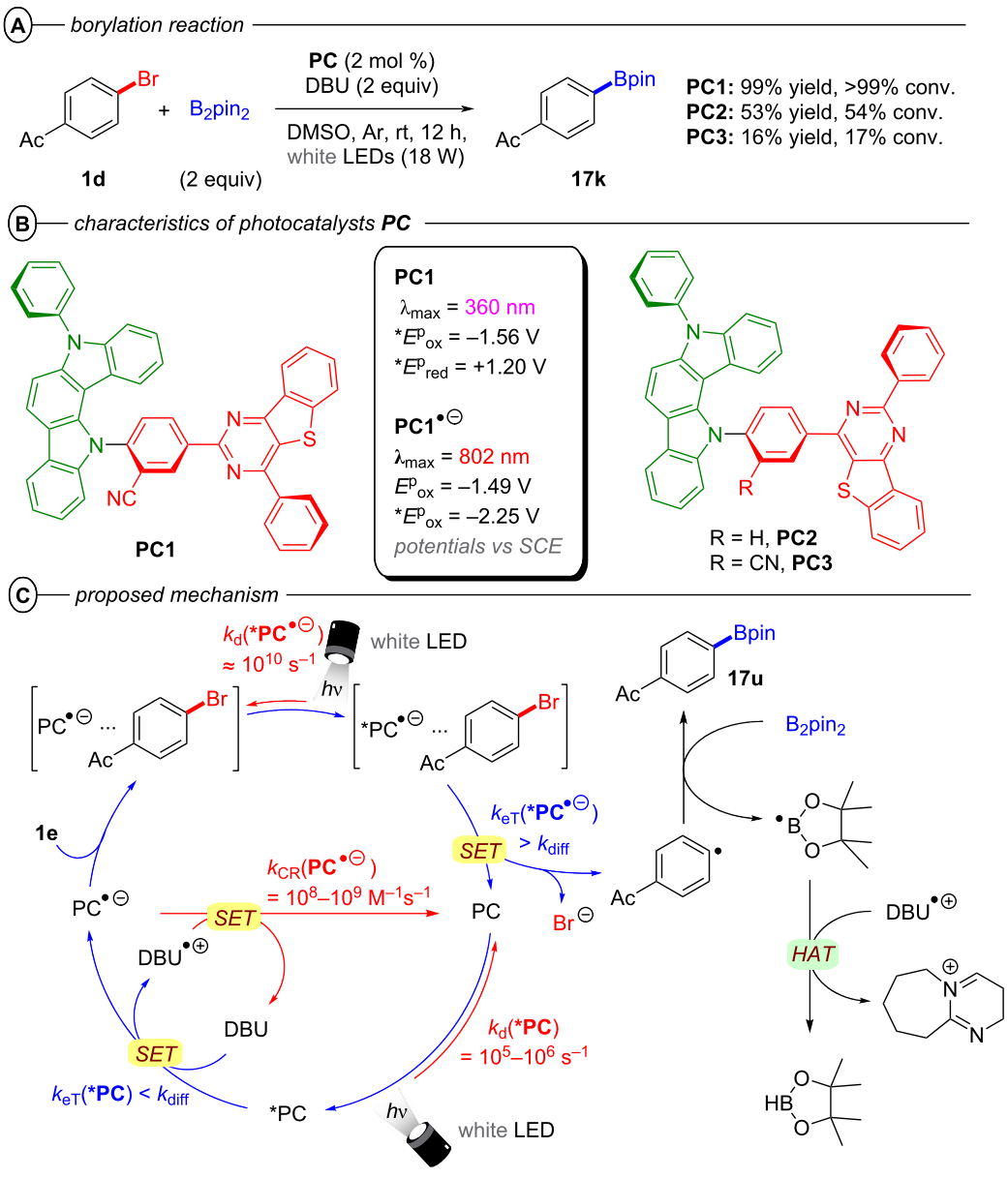

Figure 14: A) Borylation of **1d**. B) Characteristics and structure of **PC1** with green and red parts showing the localization of HOMO and LUMO, respectively. C) Full mechanism for the conPET borylation of **1d** with blue and red arrows indicating activating and deactivating pathways, respectively.

modest to excellent (30–99%) yields. Control experiments confirmed that light, catalyst and DBU as a sacrificial electron donor were all essential for product formation. A diminished yield of 19% under aerobic conditions indicates the involvement of a triplet excited state. Addition of i) 2,2,6,6-tetramethylpiperidine-*N*-oxide (TEMPO) as a free-radical quencher or ii) 1,4-dinitrobenzene as an electron trap inhibited product formation which corroborates the involvement of free radicals. The authors argued against radical chain propagation on the basis of lack of reactivity in the dark during the light ON-OFF cycle experiments (we note that this does not rule out chain propagation with an efficient chain death). Investigations of the photon stoichiometry by elucidation of the relation between product yield and light intensity, as well as the insufficient reductive power of both ***PC1** (*$E_{1/2}$ = −1.56 V vs SCE) and **PC1**$^{\bullet-}$ ($E_{1/2}$ = −1.49 V vs SCE) for the reduction of **1d** (E^{p}_{red} = −1.66 V vs SCE) confirmed the borylation is indeed a two-photon process. DBU was found to quench the steady-state fluorescence of ***PC1** with a quenching rate constant two orders of magnitude smaller than the diffusion rate constant in DMSO at 298 K and one order of magnitude greater under the borylation reaction conditions (i.e., 0.20 M DBU) than the intrinsic decay rate of ***PC1**. Since no quenching by **1d** or B_2pin_2 could be observed, the formation of **PC1**$^{\bullet-}$ can be attributed exclusively to the thermodynamically favored reductive quenching of ***PC1** by DBU. Nanosecond laser flash photolysis techniques were employed to directly monitor the back electron transfer. Second-order kinetics analyses revealed that rapid charge recombination (e.g., k_{CR} (**PC1**$^{\bullet-}$) = 2.6×10^8 M^{-1} s^{-1}) is a significant deactivation pathway in the generation of the key intermediate. This deactivation by back electron transfer taking place in the Marcus-inverted region of electron transfer can be significantly suppressed by using photocatalysts with a more negative reduction half potential $E_{1/2}$ (**PC**/**PC**$^{\bullet-}$) [73,74].

The involvement of an excited state radical anion ***PC1**$^{\bullet-}$ was further supported by analysis of the product quantum yield (QY). The QY exceeded the theoretical limit of a single-photon process when only taking the absorption of **PC1** into account but gave a reasonable value (Φ_{prod} = 8.2%) for the two-photon process involving excitation of both **PC1** and **PC1**$^{\bullet-}$. Electron transfer from ***PC1**$^{\bullet-}$ (*$E_{1/2}$ = −2.25 V vs SCE) to **1d** is thermodynamically favored. While **1d** does not quench the distinctive absorption band (λ_{max} = 802 nm) of **PC1**$^{\bullet-}$ (electrochemically generated) in the absence of light, this absorption band rapidly vanished upon irradiation with red light (λ_{max} = 630 nm), corroborating ***PC1**$^{\bullet-}$ as the key catalytic species. The rate constants for SET from ***PC**$^{\bullet-}$ to **1d** were obtained by transient absorption spectroscopy with femtosecond pulsed laser excitation and were 2–3 orders of magnitude greater (e.g., k_{eT} (***PC1**$^{\bullet-}$) = 6.8×10^{10} s^{-1}) than the diffusion rate in DMSO (k_{diff} = 4.0×10^8 s^{-1} of 0.12 M **1d**) confirming a preassociation of **PC1**$^{\bullet-}$ and the substrate prior to PET. This is further supported by the inability of ***PC3** ($E_{1/2}$ = −1.76 V vs SCE) to reduce **1d** in the absence of DBU although this is thermodynamically favored. Additionally, the UV–vis–NIR absorption spectrum of a mixture of **PC1**$^{\bullet-}$ and **1d** does not fit the mathematical sum of absorption spectra of both individual compounds but does in fact show additional charge-transfer bands from the preassembly. After electron transfer from ***PC1**$^{\bullet-}$ to **1d**, the C(sp^2)–Br bond is cleaved and the aryl radical readily reacts with B_2pin_2 in a radical substitution reaction yielding the borylated product **17k** and a Bpin radical that is subsequently quenched to HBpin by HAT from DBU$^{\bullet+}$.

As an alternative to organic radical anion conPET, the Chiba group reported the use of homoatomic polysulfide anions as cheap, readily available and potent photocatalysts [75]. Based on the ground state redox potentials and the visible light absorptions of $\mathbf{S_4^{2-}}$ and $\mathbf{S_3^{\bullet-}}$, the authors developed a catalytic system that employs these species as photoexcited reductants and oxidants in an elegant redox interplay of the $\mathbf{S_4^{\bullet-}/S_4^{2-}}$ and $\mathbf{S_3^{\bullet-}/S_3^{2-}}$ redox couples (Figure 15D). Irradiation of $\mathbf{S_4^{2-}}$ with blue light generates the potent reductant $\mathbf{*[S_4^{2-}]}$ enabling the single electron reduction of aryl halides while simultaneously generating $\mathbf{S_4^{\bullet-}}$. Upon C(sp^2)–X bond cleavage, an aryl radical is formed and trapped by a trapping reagent such as *N*-methylpyrrole, yielding the open-shell species **4**$^{\bullet}$. Upon irradiation of $\mathbf{S_3^{\bullet-}}$, the excited species $\mathbf{*[S_3^{\bullet-}]}$ oxidizes **4**$^{\bullet}$ to the corresponding carbocation **4**$^{+}$ while simultaneously generating $\mathbf{S_3^{2-}}$. Subsequent deprotonation of **4**$^{+}$ yields the C–H arylated product **4** while SET between $\mathbf{S_4^{\bullet-}}$ and $\mathbf{S_3^{2-}}$ regenerates the catalytically active polysulfide species $\mathbf{S_4^{2-}}$ and $\mathbf{S_3^{\bullet-}}$ and closes both catalytic cycles. Showing high versatility, the direct application of commercially available potassium (poly)sulfide (K_2S_x) with H_2O, the top-down generation from elemental sulfur (S_8) with sodium *tert*-butoxide (NaO*t*-Bu), and the bottom-up generation from lithium sulfide (Li_2S) or triisopropylsilanethiol (iPr_3SiSH) were all suitable methods of catalyst generation for the reduction of aryl halides. Compared to conPET chemistry with organic photocatalysts, no terminal reductants like trialkylamines or formates were required for redox-neutral transformations like the C–H arylation, borylation or phosphorylation owing to the interplay between the two polysulfide redox couples. However, K_2CO_3 was needed to quench liberated protons.

A large variety of electron-poor aryl bromides bearing different functional groups readily underwent SET reductions to give biaryl cross-coupled products **4** in poor to excellent yields (20–93%) (Figure 15A). The protocol was also applicable to both electron-rich and electron-poor heteroaryl halides. Due to

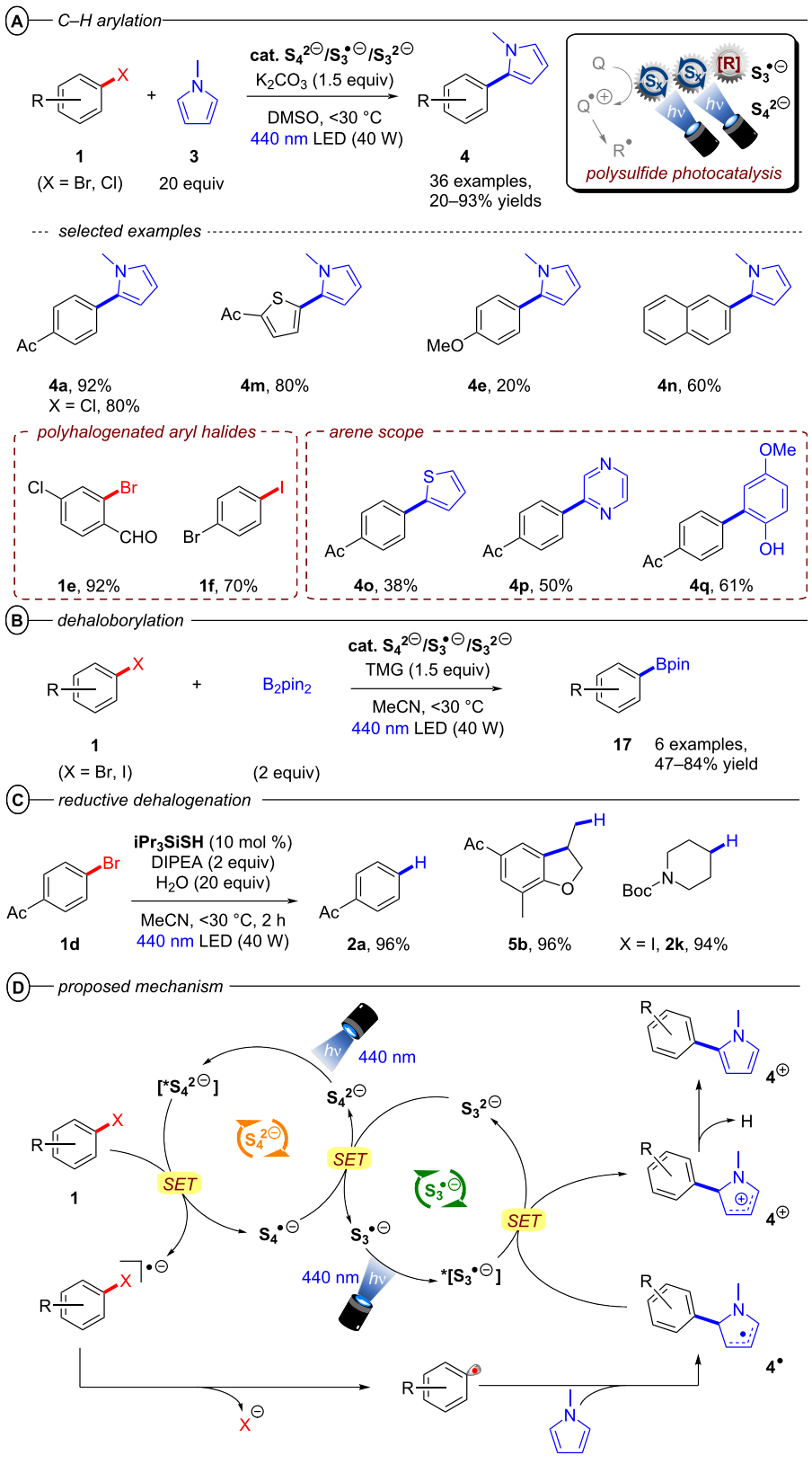

Figure 15: A) Reductive C–H arylation scope with polysulfide conPET (top) and selected examples from the substrate scope (bottom). B) Reductive dehaloborylation. C) Reductive hydrodehalogenation. B) Polysulfide conPET mechanism.

the inherently higher C(sp^2)–Cl bond dissociation energies of reductively more inert aryl bromides or aryl chlorides [76], the bottom-up generation of polysulfides from Li_2S or iPr_3SiSH was found to provide better results than the use of K_2S_x. Unactivated aryl bromides such as 4-bromobiphenyl, 2-bromonaphthalene and 4-bromoanisole could also be reduced, but the sluggish reaction of 4-bromoanisole to **4e** (20% yield) indicates the limit of the reductive power of the polysulfide catalyst system. Notably, several polyhalogenated aromatics could be chemoselectively engaged at one C–X bond, even for 1-bromo-4-iodobenzene (**1f**). Apart from *N*-methylpyrrole, other substituted pyrroles, thiazine (**4o**), pyrazine (**4p**) and electron-rich benzenes (**4q**) were found to be suitable trapping reagents with varying efficiency. The polysulfide catalyst system was also efficiently applied for a dehaloborylation with B_2pin_2 (Figure 15B) and a net-reductive hydrodehalogenation (Figure 15C).

Both the C–H arylation (Figure 16A) and the dehaloborylation (Figure 16B) of aryl chlorides were smoothly transferred to continuous-flow providing products **4a** and **17k** in very good yields and gram-scale per hour productivities demonstrating the ease of scaling up conPET reactions in continuous flow. In general, standardized flow photoreactors which are already widely available enable immediate integration of conPET reactions. On the other hand, PEC reactions require tailor-made reactors that present technical challenges, although in principle these challenges are surmountable by adapting engineering from the already well-established fields of PEC water splitting/fuel cells/photovoltaic fields. So far, the examples of large-scale processes with PEC are limited to the use of recirculated flow or batch (vide infra).

As another alternative to organic photocatalysts, the Polyzos group presented a tandem photocatalytic sequence applying **[Ir^{III}(ppy)$_2$(dtbbpy)]PF_6** (**[Ir1]$^+$**) in combination with Et_3N to accumulate the energy of two visible-light photons [77]. In their previous work, the Polyzos group discovered the capability of **[Ir1]$^+$** to reduce diarylimines via SET in presence of Et_3N albeit the large difference in the oxidation potential of **[Ir1]^0** ($E_{1/2}$ = −1.47 V vs SCE) and the reduction potentials of imines (e.g., E^p_{red} = −2.18 V vs SCE for *N*-(diphenylmethylene)-1-phenylmethanamine) [78]. Spectroscopic investigations later revealed that the change in absorption and luminescence of deaerated solutions of **[Ir1]$^+$** and Et_3N were neither related to i) the formation of **[Ir1]^0** via a single-excitation reductive quenching photocatalytic cycle nor ii) ***[Ir1]^0** via a conPET mechanism. Rather, changes related to a chemical transformation of the dtbbpy ligand of the catalyst under the reaction conditions. Charge neutrality and diamagnetism of the new catalyst species, as well as loss of the C_{2v} symmetry of **[Ir1]$^+$**, indicated the nonsymmetric transformation of the dtbbpy ligand to a monoanionic ligand. Extensive NMR analysis confirmed that upon the formation of **[Ir1]^0** via SET from Et_3N to ***[Ir1]$^+$**, partial saturation of the dtbbpy ligand generates **[Ir2]^0** and initi-

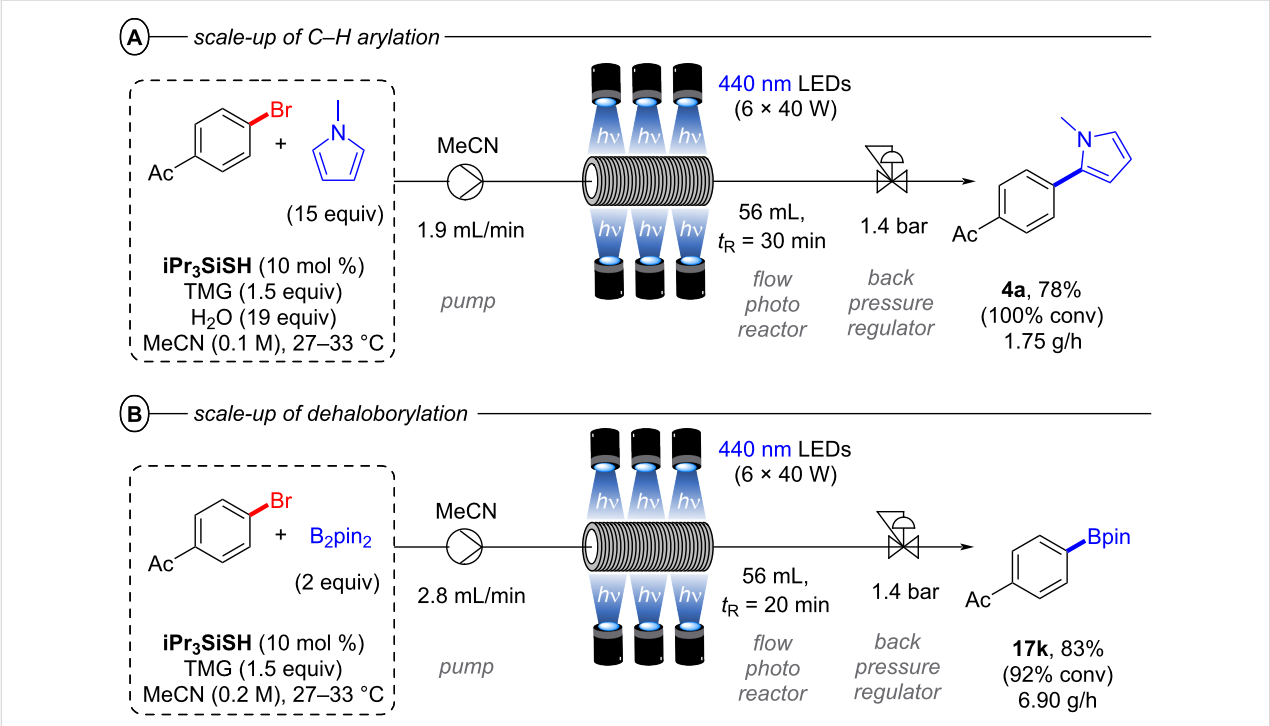

Figure 16: Scale-up of A) C–H arylation and B) dehaloborylation with polysulfide photocatalysis in continuous-flow.

ates the second catalytic cycle (Figure 17A). Upon excitation with blue light, ***[Ir2]^0** reduces aryl halides via SET and is simultaneously oxidized to the Ir^{IV} species **[Ir2]$^+$** (Figure 17B). **[Ir2]$^+$** then undergoes SET with **[Ir1]^0** to regenerate both **[Ir2]^0** and **[Ir1]$^+$**, thereby closing both catalytic cycles.

An alternative pathway for the regeneration of **[Ir1]$^+$** via proton-coupled electron transfer (PCET) from **[Ir2]$^+$** could not be ruled out. With no trapping reagents or further reactants present, the aryl radicals generated by C(sp^2)–X bond cleavage yield hydrodehalogenated products **2** via HAT. Under irradiation with blue light, **[Ir2]^0** was found to reduce a variety of aryl halides to their hydrodehalogenated products **2** in excellent yields (93–99%) including the electron-rich 4-iodoanisole and 4-bromoanisole that were quantitatively reduced to anisole (**2e**) (Figure 18). Notably, the C(sp^2)–I bond of 1-bromo-4-iodobenzene was chemoselectively defunctionalized to **2l** in 93% yield under the reaction conditions.

In 2020, the Polyzos group also demonstrated the carbonylative amidation of aryl halides in continuous flow with the in situ-generated **[Ir2]^0** (Figure 19A) [79]. This multi-photon tandem photocatalysis protocol provides an elegant alternative to established classical procedures for condensing carboxylic acids with amines that typically generate stochiometric amounts of harmful byproducts released [80,81], while simultaneously operating under milder reaction conditions than those applied in transition metal-catalyzed carbonylative amidation protocols [82,83]. Following the same distinct, yet interconnected photocatalytic cycles as the hydrodehalogenation, an aryl radical **2$^\bullet$** is formed via successive PET and C(sp^2)–X bond cleavage (Figure 17B). Carbon monoxide, introduced to the reaction mixture by a tube-in-tube reactor, traps the aryl radical to generate the acyl radical **23** (Figure 17B). Nucleophilic addition of the amine to the acyl radical and amine-assisted intermolecular proton transfer [84] generates the α-hydroxy radical **24** from which formation of the amide **25** proceeds either via i) oxida-

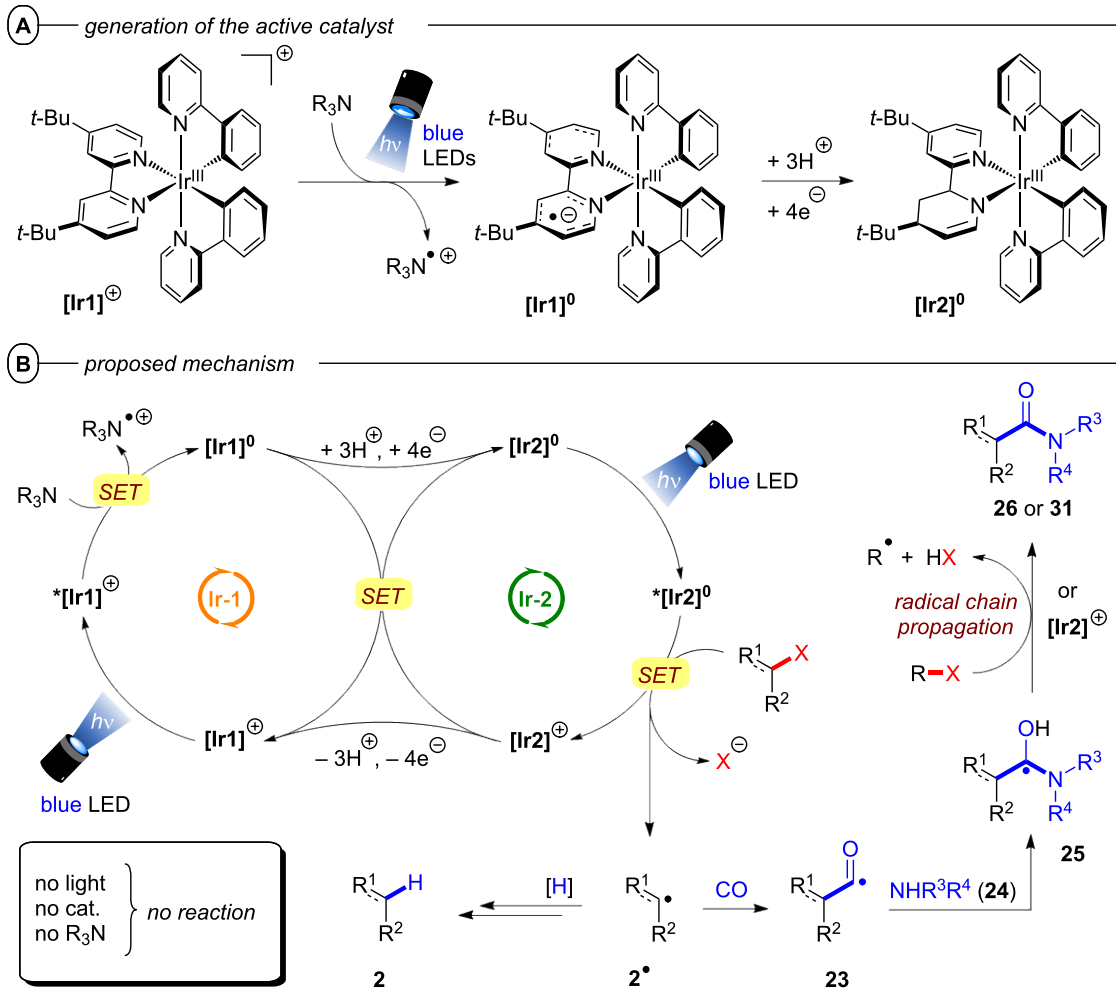

Figure 17: A) Formation of **[Ir1]^0** and **[Ir2]^0** upon PET between **[Ir1]$^+$** and Et_3N. B) Mechanism of multi-photon tandem photocatalysis for the hydrodehalogenation and the carbonylative amidation of aryl halides.

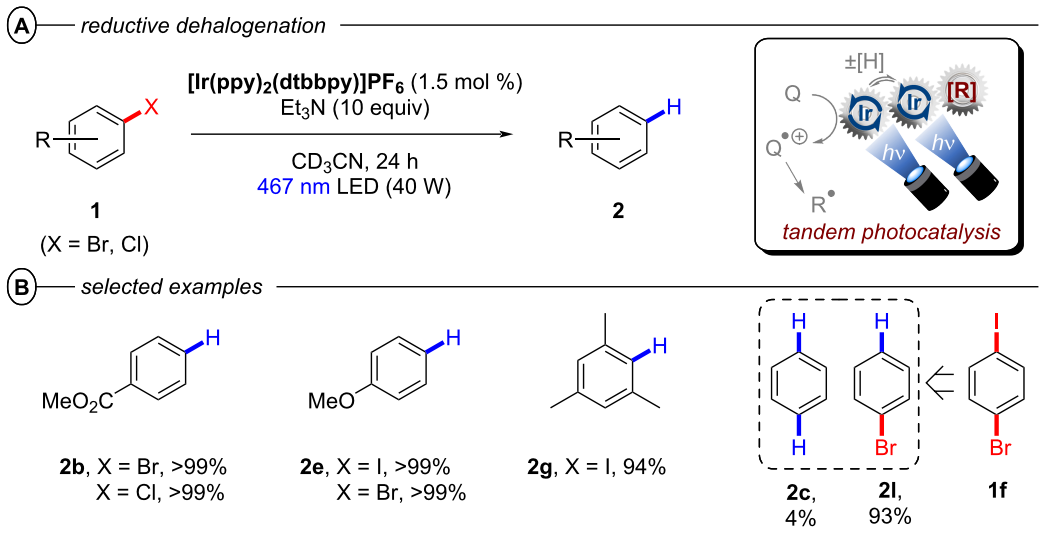

Figure 18: A) Reductive hydrodehalogenation of aryl halides via multi-photon tandem photocatalysis. B) Selected examples from the substrate scope.

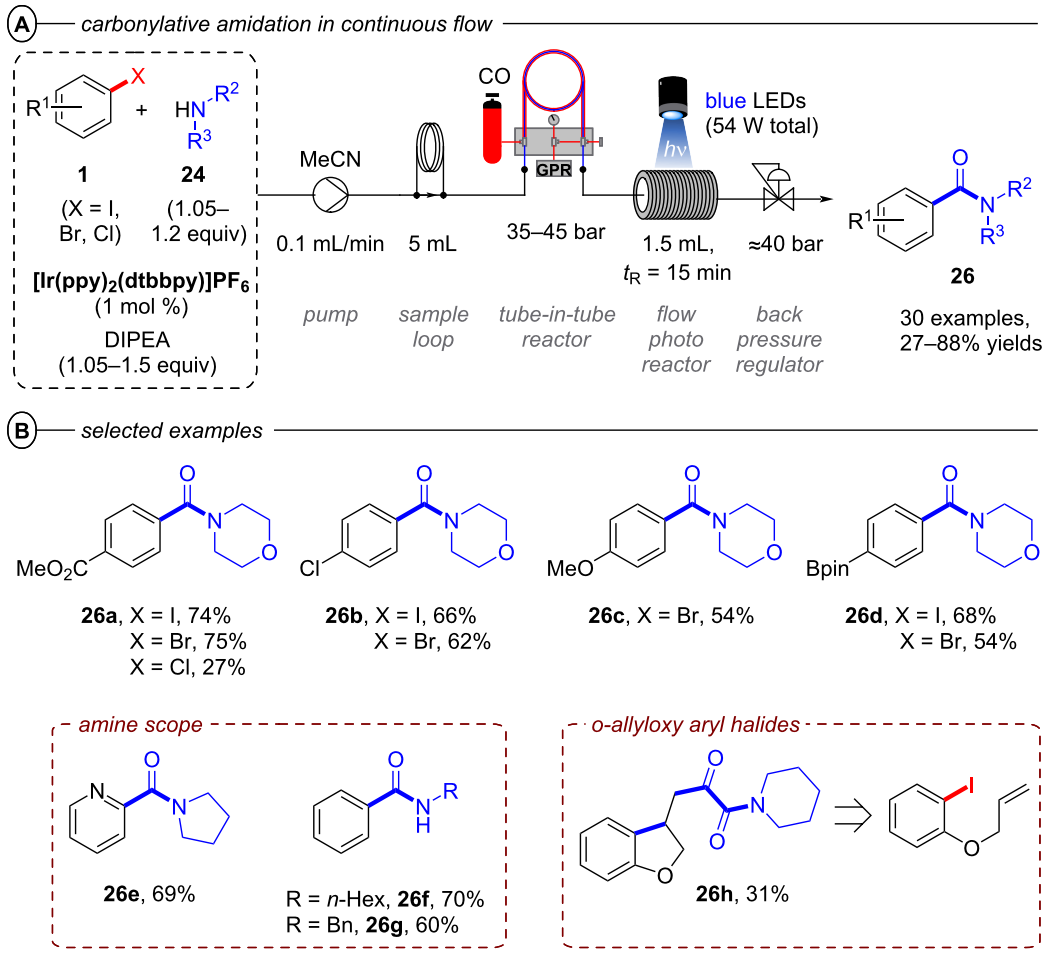

Figure 19: A) Carbonylative amidation of aryl halides in continuous flow. B) Selected examples from the substrate scope.

tion by **[Ir2]**$^+$ and deprotonation or ii) radical chain propagation [85]. Electron-deficient, electron-neutral, and electron-rich aryl halides bearing different functional groups were all well-tolerated and their products obtained in poor to excellent yields (27–88%). 1-Bromo-4-chlorobenzene and 1-chloro-4-iodobenzene were chemoselectively transformed to **26b** without activation of the C(sp^2)–Cl bond.

Notably, carbonylative amidation of a borylated aryl bromide to **26d** proceeded well, where a Pd-catalyzed carbonylative amidation reaction would be plagued by undesired Suzuki coupling. Several secondary cyclic and acyclic amines, as well as primary amines were successfully employed as amine coupling partners. The scope of the protocol was further expanded to a radical cyclization/aminocarbonylation cascade reaction yielding the bis-carbonylated α-keto amide **26h** in 31% yield.

2.1.2 C(sp^3)–X activation: The generation of alkyl radicals using alkyl halides as precursors proves very challenging due their deep reduction potentials and bond dissociation energies comparable to aryl halides [86,87]. Classical activation modes for the homolytic C(sp^3)–X bond cleavage consist of thermolytic or photolytic methods using high temperatures (>220 °C) or irradiation with UV light (λ < 300 nm). These harsh conditions were later replaced by the use of unstable or toxic radical initiators/chain carriers such as peroxides, azonitriles, or very prominently Bu_3SnH [88,89]. Only recently have PRC methods emerged, that mostly relied on the use of metal-based photocatalysts and high energy UV/near-UV light [90,91].

In 2019, the Prato group demonstrated how the **PDI** catalyst first disclosed by the König group (vide supra) could be leveraged for conPET reductions of perfluoroalkyl iodides, providing a photocatalytic alternative for the generation of perfluoroalkyl radicals used in atom transfer radical addition (ATRA) reactions with alkenes [92]. Since the ATRA mechanism involves radical chain propagation, minimal loadings of the **PDI** (0.05 mol %) could be employed as an initiator together with a sub-stoichiometric amount of sodium ascorbate for reductive quenching of **PDI** to generate **PDI**$^{\bullet-}$. While terminal olefin partners were generally well-tolerated, the protocol was limited to perfluoroalkyl iodides. The reductive power of ***PDI**$^{\bullet-}$ ($^*E_{1/2}$ = −1.87 V vs SCE) was well-matched to the redox potentials of perfluoroalkyl iodides, but was insufficient for perfluorobromides (e.g., E^p_{red} = −1.52 V vs SCE for CF_3I and E^p_{red} = −2.10 V vs SCE for CF_3Br) [93].

As a further application of conPET to atom transfer processes, the Wärnmark group recently disclosed an alternative protocol for the ATRA reaction of perfluoroalkyl iodides using the iron-based NHC complex **[Fe^{III}(btz)$_3$](PF$_6$)$_3$** (btz = (3,3'-dimethyl-1,1'-bis(*p*-tolyl)-4,4'-bis(1,2,3-triazol-5-ylidene))) as the first example of an earth-abundant transition metal complex capable of accumulating two photon energies via consecutive ^{2}LMCT and ^{3}MLCT excitations in an overall conPET mechanism [94]. Since iron-based photocatalysts generally suffer notoriously short excited state lifetimes [95,96], most reactions employing such photocatalysts require special reaction design (e.g., coordination of substrates as ligands to enable intramolecular metal to ligand charge transfer (MLCT)). Only recently have a few examples been reported that observed bimolecular quenching of iron CT states (in the nanosecond domain) enabled by the relatively longer lifetimes of e.g. Fe–NHC complexes [97-100]. In particular, the Wärnmark group reported two sets of conditions with and without Et_3N as a sacrificial electron donor, to achieve reductive and oxidative quenching pathways, respectively (Figure 20A). Both protocols were able to successfully engage perfluoroalkyl iodides and bromotrichloromethane in combination with a diverse scope of alkenes and alkynes (Figure 20B). Products of terminal alkenes and alkynes were generally obtained in good to excellent yields while also tolerating several functional groups. Substrates bearing internal double bonds were engaged with varying efficiencies (**30c**), but the reaction showed a clear preference for terminal alkenes (**30d**). The reaction of perfluorohexyl iodide with 3-(allyloxy)-1-propyne gave **30e** and **30f** as the only products, demonstrating a clear preference for addition to alkenes even in the presence of alkyne functionalities.

Due to basic conditions of the reductive quenching (RQ) route, the formation of lactone side product **30h** could be observed with a carboxylic acid functionality. In the absence of Et_3N, the mechanism follows a 'monophotonic' oxidative quenching (OQ) route in which **[Fe^{III}(btz)$_3$]$^{3+}$** is oxidatively quenched to **[Fe^{IV}(btz)$_3$]$^{4+}$** by the alkyl halide substrate after excitation with green light. After addition of the alkyl radical to the alkene or alkyne substrate, the catalyst is regenerated by oxidizing this radical to the corresponding cation. In the presence of Et_3N, **[Fe^{III}(btz)$_3$]$^{3+}$** is reductively quenched after excitation to its ^{2}LMCT excited state to generate **[Fe^{II}(btz)$_3$]$^{2+}$** (equivalent to **PC**$^{\bullet-}$ in the classical conPET mechanism) (Figure 20C). **[Fe^{II}(btz)$_3$]$^{2+}$** is excited again to the more strongly reducing ^{3}MLCT excited state ($^*E_{1/2}$ = −1.6 V to −1.8 V vs Fc), which then induces SET to the alkyl halide generating an alkyl radical via cleavage of the C(sp^3)–X bond. The authors propose that this radical then engages in a radical chain propagation pathway leading to product **30** and a new alkyl radical. This is strongly supported by a single turnover experiment, where exclusive excitation of **[Fe^{II}(btz)$_3$]$^{2+}$** with 700 nm LEDs after in situ generation and substrate addition in the dark generated 5% of product even with only 0.5 mol % of catalyst present. In its

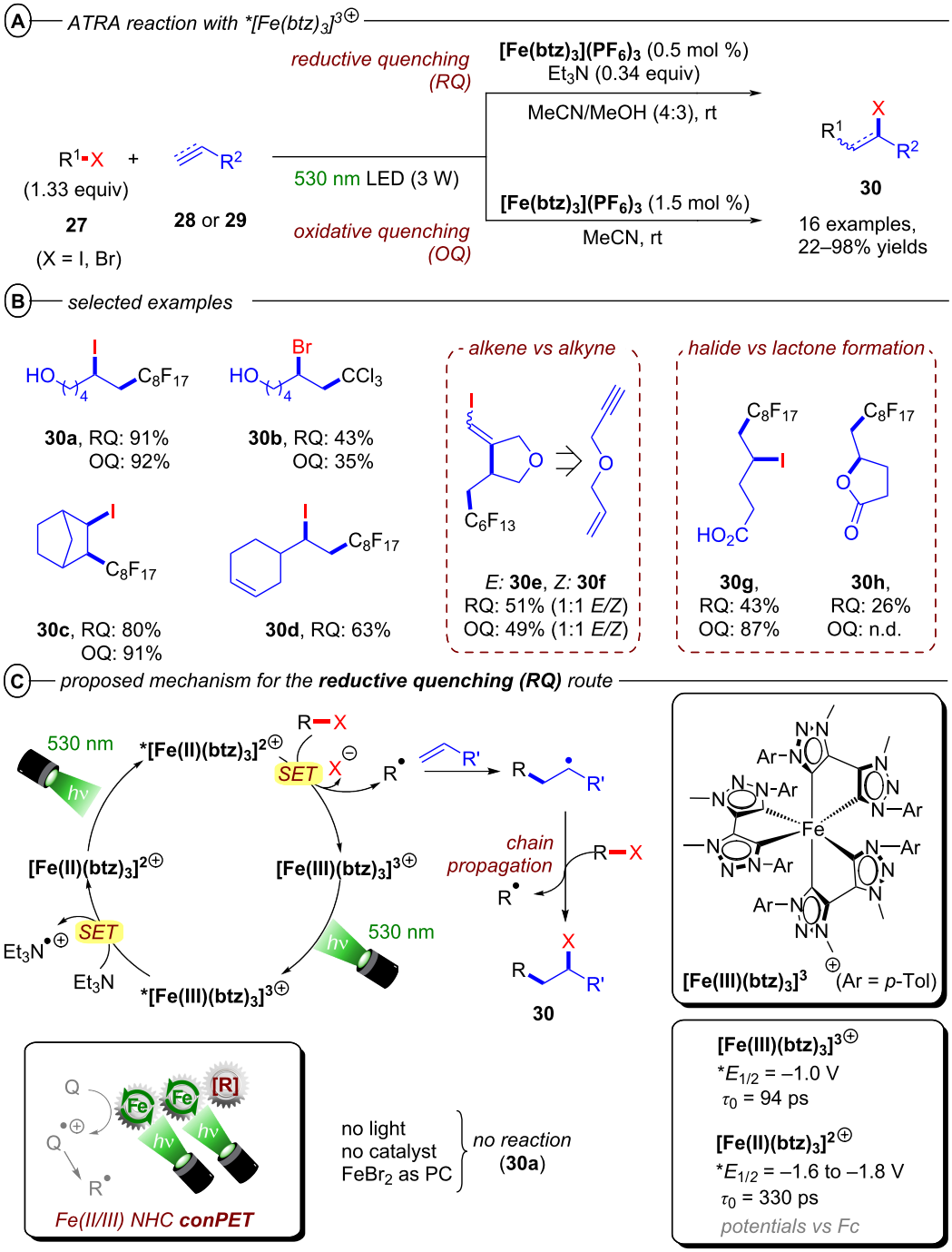

Figure 20: A) General scheme for reductive (RQ) and oxidative quenching (OQ) protocols using $[Fe^{III}(btz)_3](PF_6)_3$ for the ATRA reaction of alkyl halides with alkenes and alkynes. B) Selected examples from the substrate scope. C) conPET mechanism of the RQ pathway.

ground state, $[Fe^{II}(btz)_3]^{2+}$ is not reducing enough to engage the model substrate perfluorooctyl iodide and instead $*[Fe^{II}(btz)_3]^{2+}$ was verified as the key catalytic species by transient absorption spectroscopy; even though the strongly reducing α-amino alkyl radical intermediate might also engage in the reduction of alkyl halides or act as a halogen atom transfer (XAT) agent [101].

While yields of the monophotonic oxidative quenching route and the (biphotonic) conPET reductive quenching route were generally well comparable, the RQ route clearly benefits from a longer lifetime of the key catalytic species, shorter reaction times and lower catalyst loading. The requirement for sub-stoichiometric amounts of the sacrificial electron donor can be justified. While the work of Wärnmark is remarkable on a

conceptual level, the protocol is still limited by the reductive power of the excited state and thus restricted to rather activated alkyl halides like perfluoroalkyl iodides.

Following their work on carbonylative amidation with **[Ir^{III}(ppy)$_2$(dtbbpy)]PF$_6$** (vide supra), the Polyzos group also disclosed a slightly modified procedure for the carbonylative amidation of alkyl iodides in continuous flow with an impressive substrate scope engaging substrates with notably deep reduction potentials (e.g., E^{p}_{red} = −2.33 V vs SCE for *n*-butyl iodide) (Figure 21A) [79]. The reaction follows the same tandem photocatalysis mechanism as the carbonylative amidation of aryl halides (Figure 17B).

Tertiary, secondary, and primary alkyl iodides all readily underwent carbonylative amination with morpholine derivatives to afford morpholinoamides in acceptable to excellent yields (46–99%) (Figure 21B). The high yields obtained with primary alkyl iodides are particularly noteworthy due to the competing

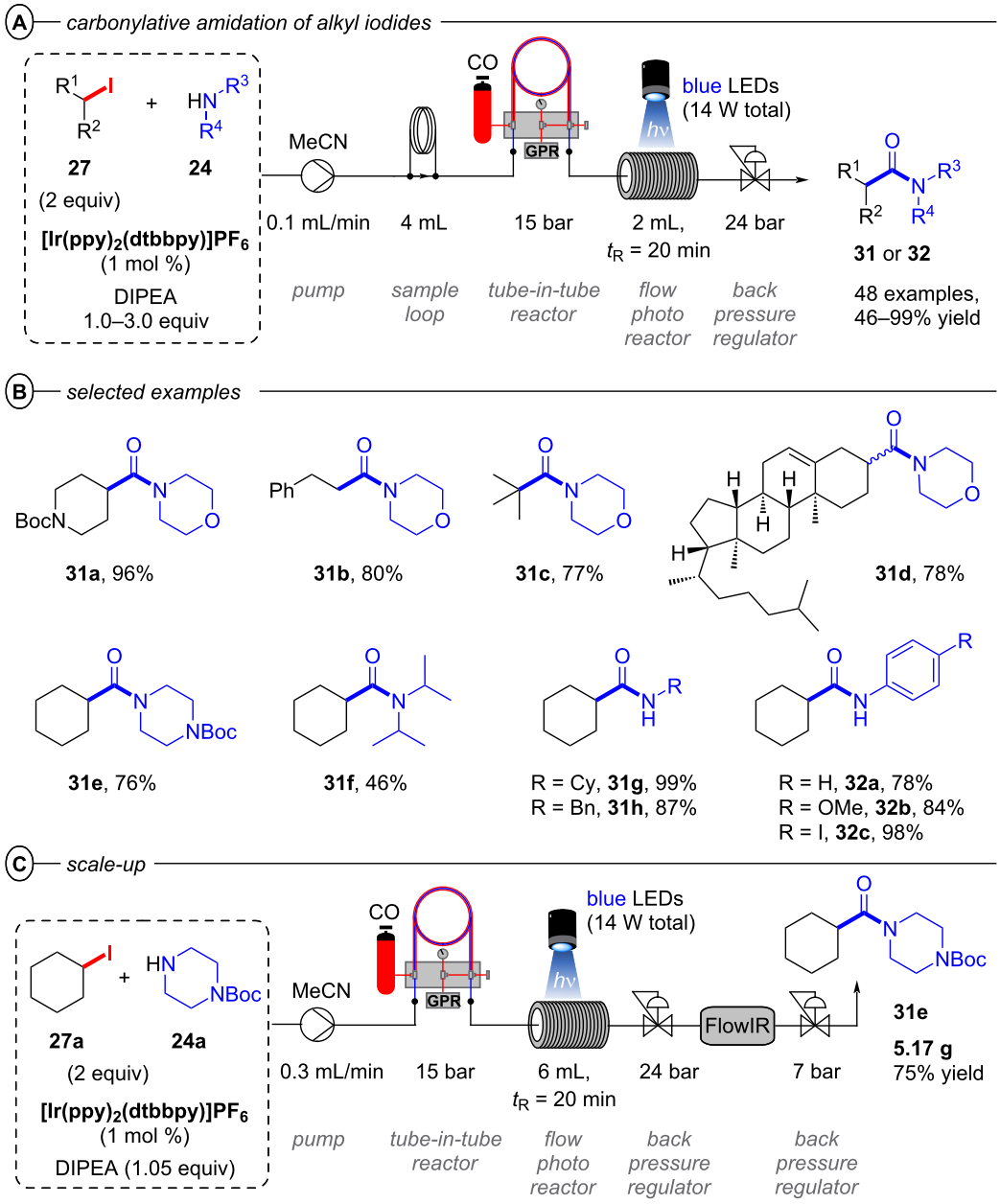

Figure 21: A) Carbonylative amidation of alkyl iodides with **[Ir^{III}(ppy)$_2$(dtbbpy)]PF$_6$**. B) Selected examples from the substrate scope. C) Flow scale up of the **31e**'s synthesis.

S_N2 reaction with amines. Several cholesterol amides were efficiently prepared using this protocol in 1:1 dr (**31d**).

Several primary and secondary amines were successfully employed as coupling partners whereas diisopropylamine led to diminished yield (**31f**), likely due to steric hindrance in reacting with the carbonylated intermediate. Besides, primary anilines bearing a large variety of functional groups proved suitable coupling partners with no obvious influence of the aromatic ring's electron density on the efficiency (**32a–c**). The amenability of *p*-haloanilines **32c** demonstrates orthogonality of this photocatalytic manifold to Pd-catalyzed carbonylative amidation protocols, while competing hydrodehalogenation was not observed as a notable advantage of the former. Scale-up of the reaction employing cyclohexyl iodide (**27a**) and 1-Boc-piperazine (**24a**) gave 5.17 g of **31e** after a collection time of ≈13 h (Figure 21C).

Apart from C(sp^3)–halogen bond activations and cleavages, conPET also enables other C(sp^3)–X bond cleavages. Ye, Yu and co-workers very recently disclosed a protocol for the reductive C–N bond cleavage and carboxylation of cyclic amines **33** for the generation of β-, γ-, δ- and ε-amino acids (generally referred to as **34**) using the isophthalonitrile-derived catalysts **4DPAIPN** and **3DPAFIPN** (Figure 22A) [102]. The authors demonstrated the applicability of the synthetic protocol with a broad substrate scope consisting of 2-arylazetidines and 2-carbonylazetidines for formation of γ-amino acids (42–95%), 2-arylaziridines for formation of β-amino acids (53–94%), pyrrolidines for formation of δ-amino acids (38–66%) and piperidines for formation of ε-amino acids (42–54%) (Figure 22B).

Notably, the reaction of model substrate *N*-Boc-2-phenylazetidine to **34a** could be performed efficiently on a gram scale in 71% yield. Considering that cyclic amines have highly negative reduction potentials (e.g., E^p_{red} = −3.0 V vs SCE for *N*-Boc-2-phenylazetidine), the authors propose that **4-DPAIPN** and **3-DPAFIPN** undergo a conPET cycle for generation of their excited radical anions as the active catalyst (Figure 22C). These highly reducing compounds then engage the amine substrate **33** in a SET reduction. Upon generation of the amine radical anion **33**$^{\bullet-}$, the C–N bond is then cleaved which leads to ring-opening and formation of the benzylic radical **34**$^{\bullet-}$. This was observed in HRMS via TEMPO radical trapping experiments by the authors. The authors propose that protonation (X = H) or carboxylation (X = CO_2) of this amide anion and a second SET happen either consecutively or in a concerted fashion, leading to formation of a benzylic anion (**34**$^-$) which then undergoes carboxylation and protonation to generate the *N*-protected amino acid **34**. An alternative pathway via protonation of **34**$^-$ and subsequent photocatalytic carboxylation of the benzylic C–H bond with CO_2 was ruled out.

Interestingly, while conPET technology forges ahead in *reductive* processes for ring opening and functionalization of cyclic amines that has just been summarized, PEC has recently found applications in *oxidative* ring-opening/functionalization of cyclic alcohols, again demonstrating a complementarity between the two methods (vide infra, Figure 64 and Figure 65).

2.1.3 C(sp^2)–C(sp^2) Bond activation: ***Alkene activation:*** Since olefins present a fundamental and ubiquitous group of commodity chemicals directly accessible from readily available petroleum feedstocks, their activation via hydrofunctionalization for the construction of saturated hydrocarbon scaffolds is an extensively studied chemical transformation. Classical approaches employ Brønsted acids or transition metal catalysts for electrophilic activation of the target π bond to a cationic or bridged intermediate for subsequent reaction with a nucleophile that generally results in formation of Markovnikov products [103]. Modern orthogonal approaches for the generation of nucleophilic radical anion intermediates relying on PRC, however, are strongly limited in their scope by the highly negative reduction potentials of unactivated olefins (E^p_{red} < −2 V vs SCE) [104,105].

The Polyzos group was able to overcome this limitation by employing their tandem iridium photocatalytic system (vide supra, Figure 17A) for generation of a super-reductants that readily engaged in the reduction of various styrene derivatives via transfer hydrogenation (Figure 23A/B) or by nucleophilic addition to unactivated ketones (Figure 23C) [106]. After its generation via excitation and reductive quenching of **[Ir1]**$^+$ with DIPEA, **[Ir2]**^{0} can be further excited effecting SET reduction of styrenes to their radical anions **28**$^{\bullet-}$ (Figure 23D). In the case of transfer hydrogenation, **28**$^{\bullet-}$ is then protonated to afford benzylic radical **35**$^\bullet$. The alkane product **35** is obtained in the major pathway via a second SET reduction and subsequent protonation, while a major contribution by a concerted HAT from DIPEA$^{\bullet+}$ could be ruled out. Addition of formic acid was required to transform DIPEA to its formate salt and thus suppress unproductive reaction of **28**$^{\bullet-}$ and DIPEA$^{\bullet+}$ to form the α-amino adduct. The hydrofunctionalization of ketones to tertiary alcohols **37** likely also involves **28**$^{\bullet-}$ as a key intermediate, but the mechanism has yet to be elucidated.

The transfer hydrogenation protocol tolerated both electron-poor and electron-rich 1,1-diarylethylenes. Competing reduction of aryl halide functionalities (**35c**) was not observed. Cyclic and acyclic α-alkyl styrenes, α,β-unsubstituted styrenes and β-substituted styrenes were all suitable substrates. For the

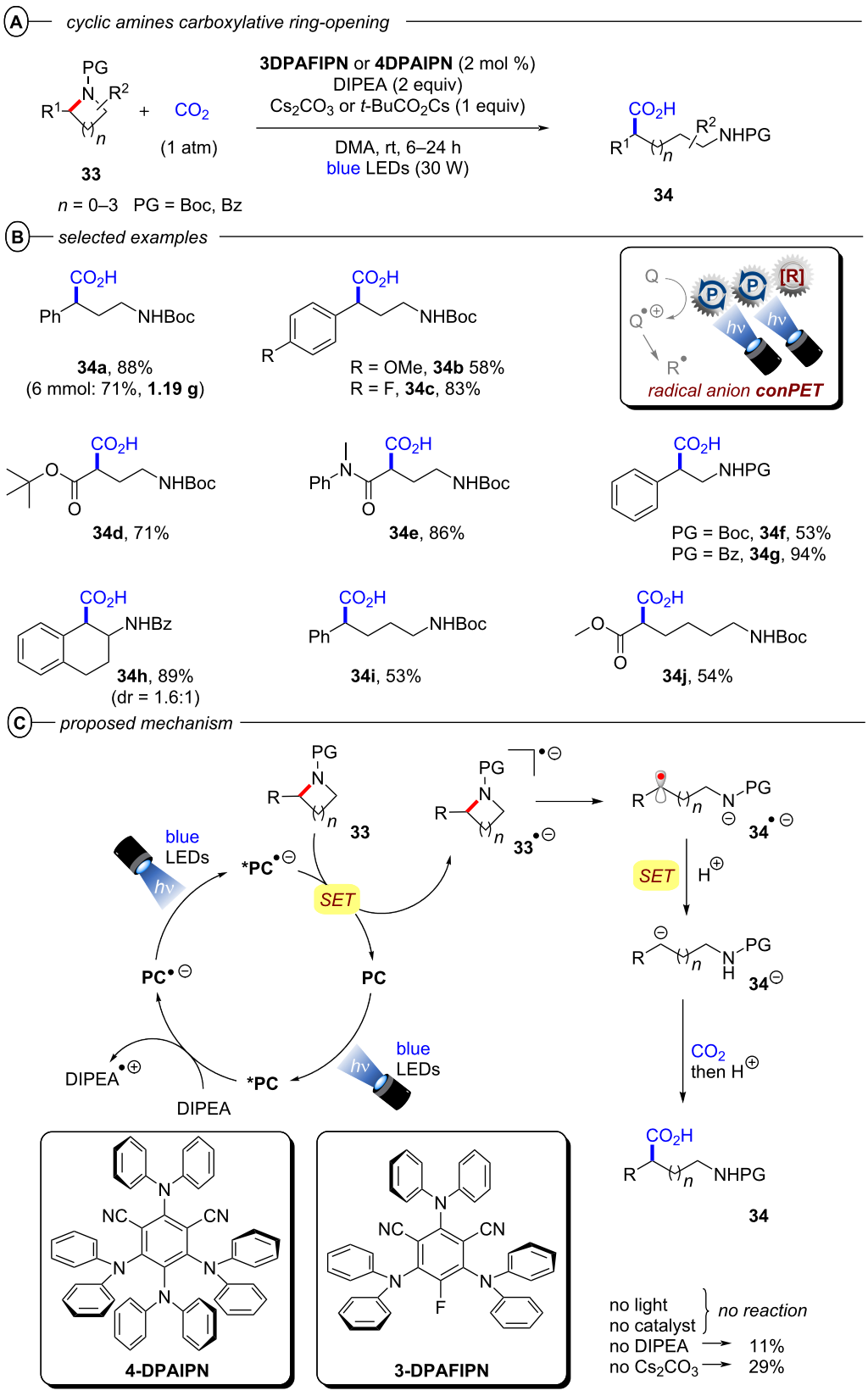

Figure 22: A) Carboxylative C–N bond cleavage in cyclic amines. B) Selected examples from the substrate scope. C) Proposed mechanism.

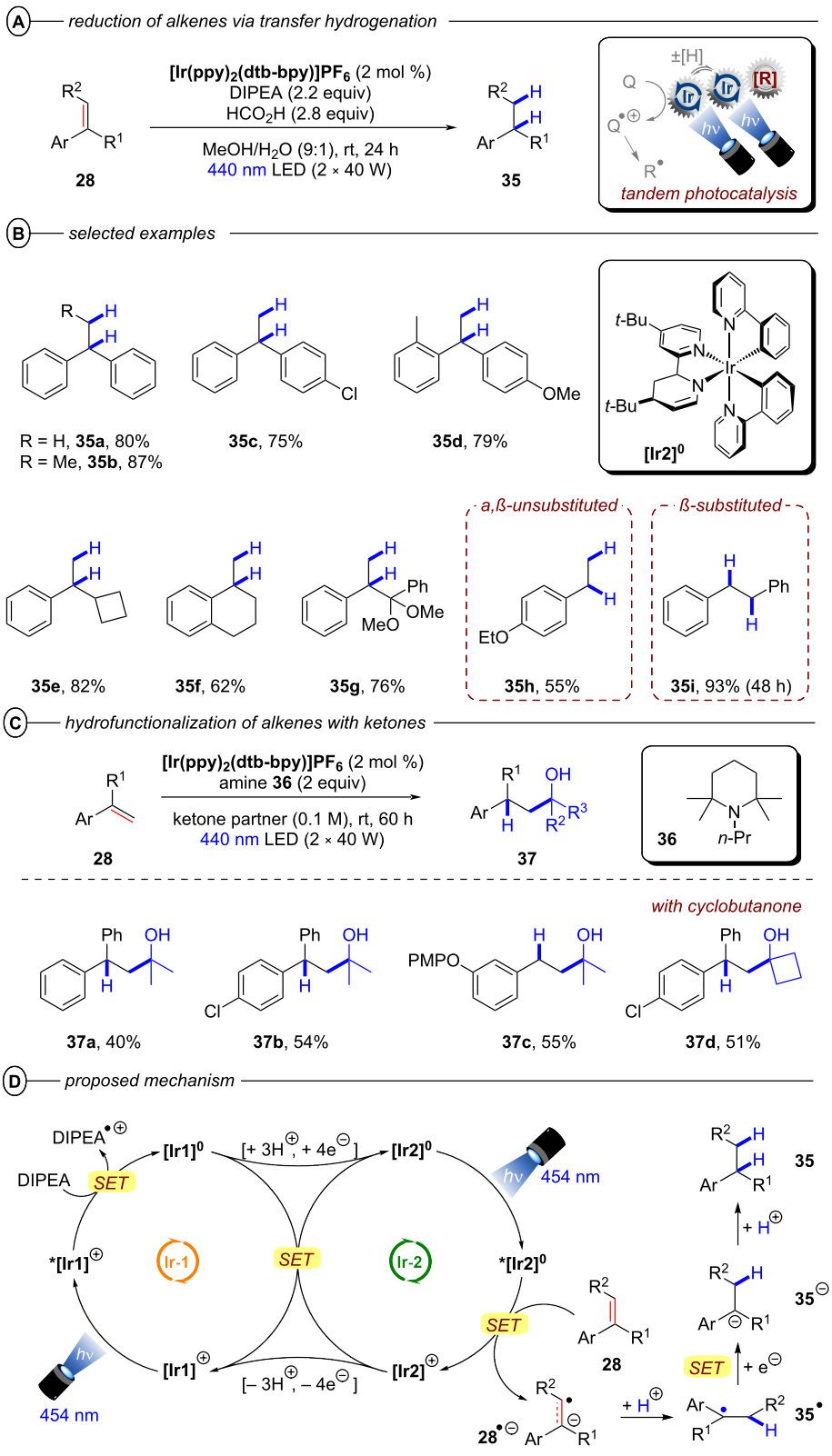

Figure 23: A) Formal reduction of alkenes to alkanes via transfer hydrogenation. B) Selected examples from the substrate scope. C) Hydrofunctionalization of alkenes with ketones and selected examples. D) Proposed mechanism for the reduction of alkenes via tandem Ir photocatalysis with $[Ir^{III}(ppy)_2(dtbbpy)]PF_6$.

hydrofunctionalization of olefins with ketones, the reduction was performed with tetramethylpiperidine derivative **36** as reductive quencher using the ketone coupling partner as solvent.

The reaction proceeded slowly with limited conversion even after 60 h, but the tertiary alcohol products could be obtained in 40–55% yield in a controlled *anti*-Markovnikov manner with both acetone (**37a**–**c**) and cyclobutanone (**37d**).

2.1.4 Arene activation: Similar to olefins, arenes and heteroarenes are important, readily available and versatile commodity chemicals produced in large quantities from petroleum feedstocks. While functionalization of arenes (e.g., by substitution reactions) is generally well-investigated, procedures for the dearomatization via reduction to semi-saturated cyclic products remain scarce. The most established and still widely used method for such transformations is the classical Birch reduction, that employs solvated electrons generated by dissolving alkali metals such as lithium and sodium in cryogenic liquid ammonia [107,108]. For the sake of safety and practicability, variations of the Birch reduction under ammonia-free [109-111], transition metal-catalyzed [112], electrochemical [113], or photochemical conditions [114-117] were developed, however, each of these methods require harsh conditions themselves or suffer other strict limitations. Reported photochemical approaches rely on UV irradiation and large stoichiometric loadings of strong reducing agents to overcome the deeply negative reduction potentials of arenes (e.g., E^{p}_{red} = −3.42 V vs SCE for benzene) [118], rendering such methods unfavorable. While efforts to accumulate visible light photons via conPET provided super-reducing catalysts that should be capable of reducing arenes on thermodynamic grounds, no dearomatized products were observed in the studies on hydrodehalogenation of aryl halides. In 2019, the König group for the first time disclosed a protocol for a Birch-type reduction by visible light iridium photocatalysis employing **[Ir{dF(CF$_3$)ppy}$_2$(dtbbpy)]PF$_6$** (**[Ir^{III}]**) in a combined energy-transfer (EnT) and SET process (not shown) [119]. Key to success was leveraging a triplet-triplet EnT from the excited photocatalyst ***[Ir^{III}]** (E_T = 61.8 kcal mol^{-1}) to the substrate, successfully lowering its reduction potential (e.g., $E_{1/2}$ = −1.98 V vs SCE vs $^*E_{1/2}$ = −0.13 V vs SCE for anthracene). Due to requirement of this EnT step, only substrates with sufficiently low triplet energies accessible to ***[Ir^{III}]** (naphthalenes, etc) could successfully be reduced by this protocol, which excludes arenes with small conjugated system such as benzene (E_T = 84.4 kcal mol^{-1}).

Miyake and co-workers overcame this issue by a modified conPET mechanism [120]. They demonstrated how benzo[*ghi*]perylene monoimides (**BPIs**) could be successfully reduced to their radical anions via an addition of OH^- to the imide, followed by homolysis, whereas commonly applied trialkylamines failed to achieve this. Optimal results were obtained with Me_4NOH as the electron source for reductive quenching in a solvent mixture of MeOH and *t*-amyl alcohol (*t*-AmOH) under irradiation with blue LEDs (λ = 405 nm). Of the investigated photocatalysts, *p*-OMePh-substituted **BPI** (**PMP-BPI**, see Figure 25 for structure) performed best, even in very low catalyst loadings, but due to presumed catalyst degradation the catalyst had to be added sequentially in three portions (0.25 mol % each) over the long course of the reaction (96 h for most substrates) to achieve sufficient conversion. With optimized conditions, the authors were able to reduce various benzene derivatives (**38**) to the corresponding 1,4-dihydrobenzenes (**39**) in poor to high (24–91%) yields (Figure 24B).

Apart from the model substrate 2-phenylethanol (**39a**) and structurally related compounds, benzene (**39e**) and toluene (not shown) were also readily reduced under the reaction conditions. Several functionalities were well-tolerated, including carbamates, amides and acids, albeit with diminished product yields (e.g., **39f**, **39g** and **39h**). Scale-up to a 10 mmol scale was performed successfully for products **39a** and **39i** (albeit requiring even longer reaction times and 4 × LEDs). The reaction protocol was not applicable to electron-rich arenes, substrates bearing alkene, alkyne, alkyl halide or unprotected amine functionalities and N-containing heterocycles.

The successful reduction of benzene and toluene via this protocol is the first and so far only example of a visible-light photocatalytic Birch-type reduction that could engage these simple aromatic feedstock compounds. Modification of the reaction conditions, in particular amounts of catalyst and NMe_4OH and reaction time allowed for selective reductions (Figure 24C). Benzophenone underwent tandem reductive deoxygenation and Birch-type reduction to **39k**. Cinnamyl alcohol could either be reduced on the alkene functionality to **39l** or further reduced to **39m** while reductive ring-opening of *trans*-2-phenylcyclopropane-1-carboxylic acid could be modified to yield either **39n** or the Birch-type reduction product **39o**.

Mechanistic investigations revealed that generation of the key catalytic species proceeds via addition of OH^- to **PMP-BPI**, generating **PMP-BPI-OH$^-$** (Figure 25). After irradiation, a hydroxyl radical is eliminated and **PMP-BPI$^{\bullet-}$** can be excited again to ***[PMP-BPI$^{\bullet-}$]**. While the fate of the hydroxyl radical is unknown, DFT calculations found this PET occurring from the lowest singlet excited state of **PMP-BPI-OH$^-$** to be exergonic by 11.5 kcal mol^{-1} (under irradiation with 405 nm LEDs). **PMP-BPI$^{\bullet-}$** that was generated via mediation with hydroxide or fluoride or even by bulk electrolysis

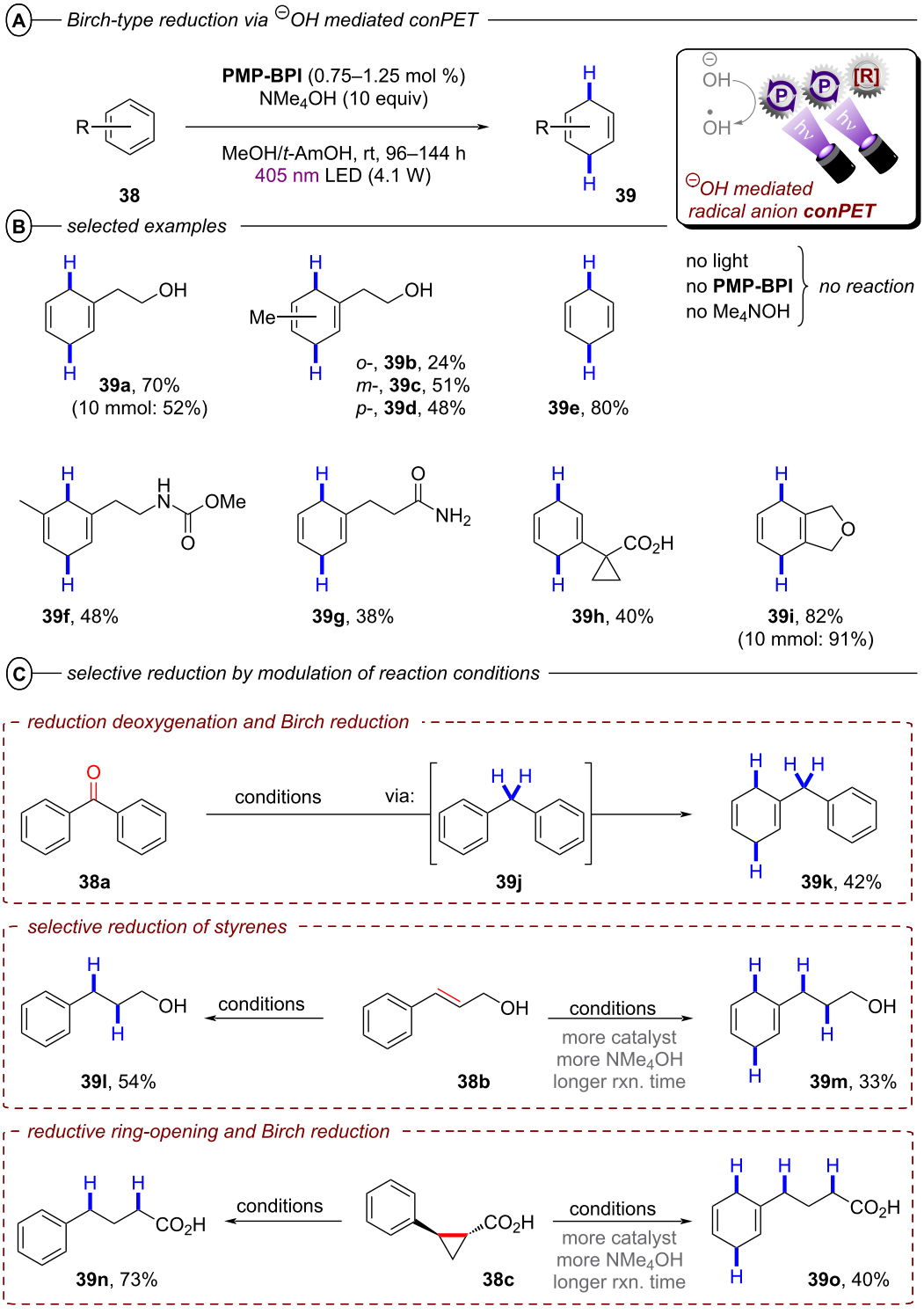

Figure 24: A) Birch-type reduction of benzenes with **PMP-BPI**. B) Selected examples from the substrate scope (scale up reactions under slightly modified conditions). C) Selective reduction by modulation of reaction conditions (reactions conducted under slightly modulated reaction conditions, see original publication for details).

(E_{cell} = −2.26 V vs SCE) all showed the same absorption. A second photoexcitation is required due to the insufficient reducing power of ground state **PMP-BPI**$^{\bullet-}$ ($E_{1/2}$ = −1.24 V vs SCE). Based on DFT calculations and nanosecond transient absorption spectroscopy, the authors favored a plausible mechanism via the generation of a solvated electron, rather than direct

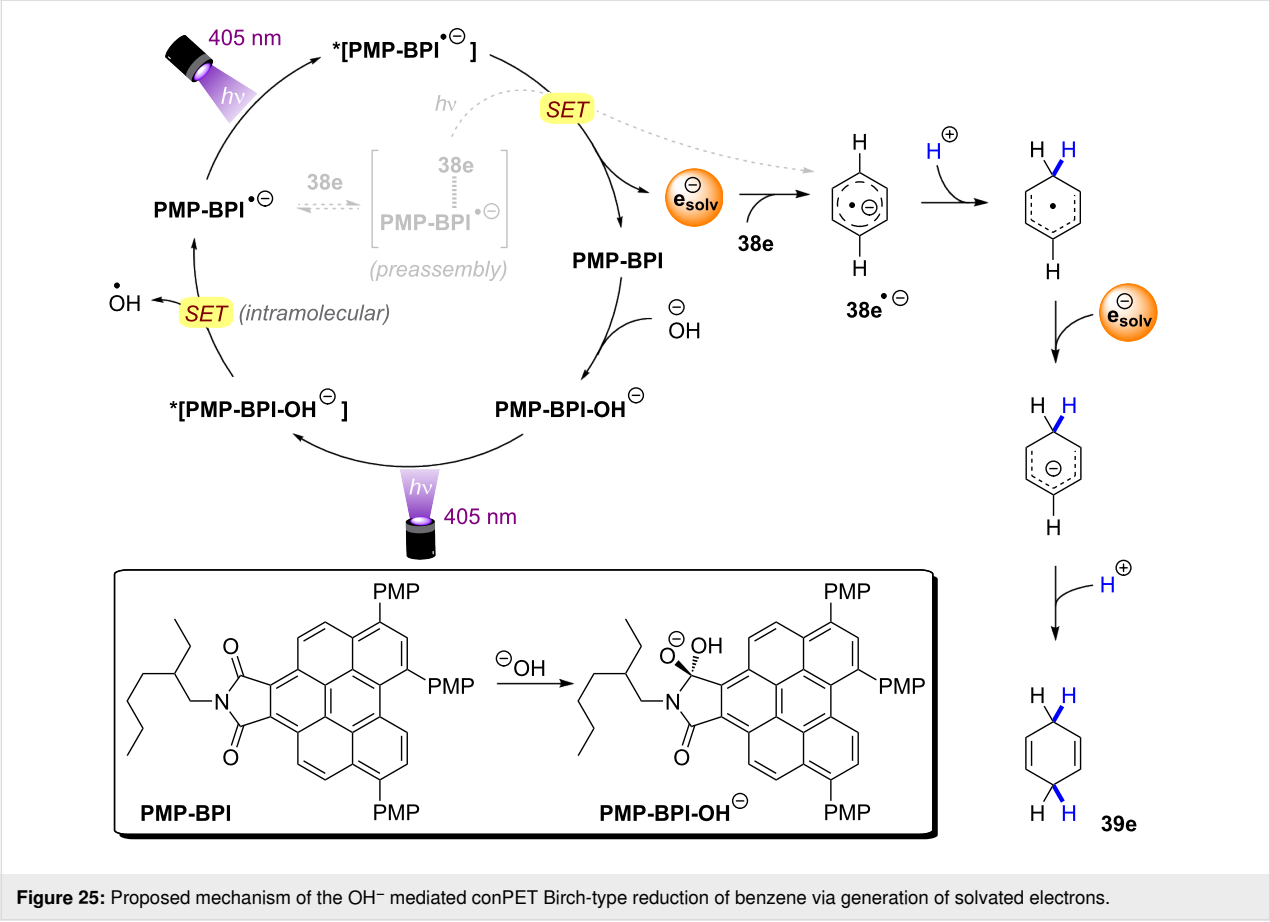

Figure 25: Proposed mechanism of the OH^- mediated conPET Birch-type reduction of benzene via generation of solvated electrons.

SET from the photocatalyst. The prolonged lifetime of ***PMP-BPI$^{\bullet-}$** observed in nanosecond transient absorption spectroscopy with excitation at 532 nm is assumed to stem from an unreactive quartet excited state ***^{4}PMP-BPI$^{\bullet-}$**, arising from ISC from the doublet state ***^{2}PMP-BPI$^{\bullet-}$**. Owing to the absence of significant quenching of this long-lived quarted state by arene substrates, the authors proposed instead that photoexcitation to the first doublet state (or higher order doublet states) ***^{2}PMP-BPI$^{\bullet-}$** liberates a solvated electron. The solvated electron reduces the arene substrate to its radical anion **38$^{\bullet-}$** and the 1,4-dihydrobenzene product **39** is obtained by sequential protonation, reduction by another solvated electron and a second protonation.

Alternatively, the authors could not rule out reduction of arene substrates occurring via direct SET from a higher excited state of ***PMP-BPI$^{\bullet-}$** (D_n) in an anti-Kasha fashion, which would require a catalyst-substrate preassembly. Given the selectivity observed for arene over amide/carbamate reductions and the extended π-system of **PMP-BPI$^{\bullet-}$**, a π–π stacking interaction assembly seems plausible. However, unlike the conPET study of Lee, Chou, You and co-workers [72] and like the e-PRC study of Barham, König and co-workers (vide infra, Figure 72), the authors did not find any evidence for such an assembly of **PC$^{\bullet-}$** by UV–vis spectroscopy. Barham, and co-workers as well as Hauer and co-workers (vide infra, Figure 37 and following discussion) showed in their studies of organic radical cations that a lack of change in steady-state UV–vis spectroscopy cannot speak against a preassembly – especially with non-polarized/electronically symmetrical substrates – and *only transient absorption spectroscopy kinetics is qualified to reveal the necessary operation of a preassembly for radical ion photocatalysis*.

2.1.5 Het–Het bond activation: *N–S and O–S bond activation:* In their work on reductive hydrodehalogenation of aryl halides, the Nicewicz group also disclosed a protocol for reductive detosylation of *N*-tosyl amides with **Mes-Acr-BF$_4$** via a conPET mechanism [54]. Single-electron reduction of a tosylated amine **40** by the twisted intramolecular charge transfer (TICT) state of the **Mes-Acr$^{\bullet}$** radical (Figure 10C) yielded its radical anion, which supposably eliminated a tosylate anion to generate a primary or secondary aromatic or aliphatic amines **41** (Figure 26A). Primary and secondary tosylated anilines were efficiently transformed to the corresponding anilines in moderate to excellent yields (42–99%). Detosylation occurred selec-

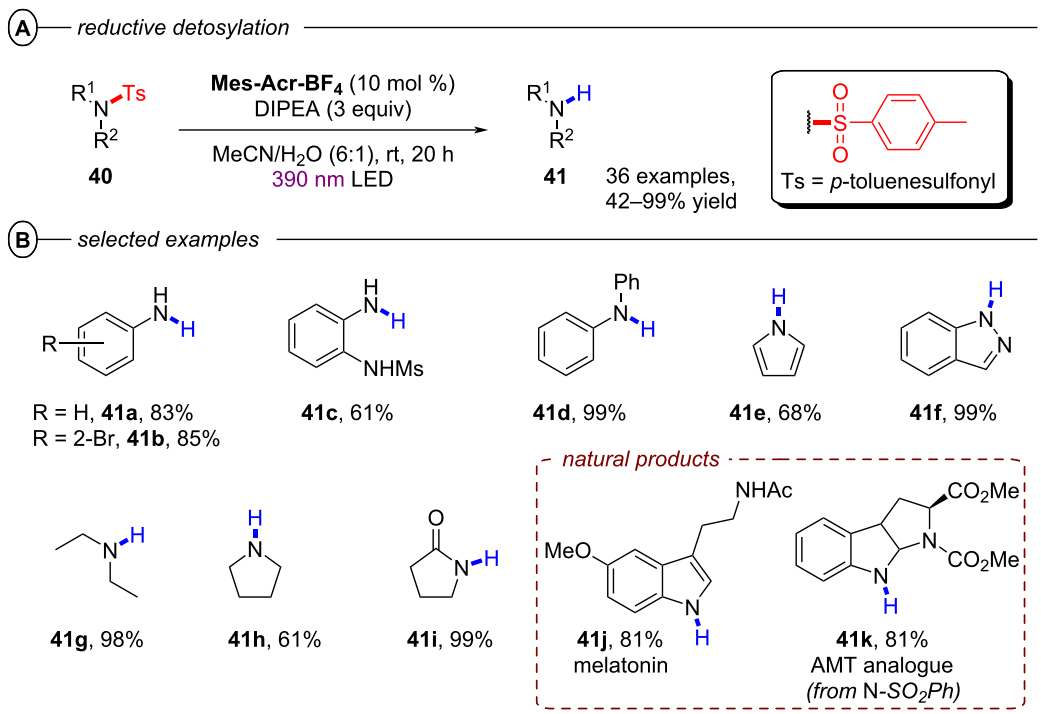

Figure 26: Reductive detosylation of *N*-tosylated amides with **Mes-Acr-BF$_4$**. B) Selected examples from the substrate scope.

tively in presence of a mesylated amine functionality (**41c**). Alkylamines were readily generated from their tosylated counterparts (Figure 26B). Pyrrolidine was obtained in 61% yield (**41h**) whereas the introduction of an adjacent carbonyl group increased the yield to 99% (**41i**). Several heterocyclic amines including pyrrole (**41e**) and 1*H*-indazole (**41f**) as well as natural products like melatonin (**41j**) or the AMT analogue **41k** were also successfully engaged in reductive detosylation.

The Wenger group recently disclosed a dual photoredox catalytic approach for the reductive detosylation of *N*-tosyl amides **40** to secondary amines **41** [121]. Herein, photoexcited **[Cu(dap)$_2$]Cl** assists in the generation of **DCA**$^{\bullet-}$ (from **DCA**) which can be photoexcited to act as a super-reductant. The generation of **DCA**$^{\bullet-}$ by the Cu catalytic cycle without direct excitation of **DCA** allows for irradiation with red light whereas the classical conPET mechanism (vide supra, Figure 9) requires near-UV/blue light irradiation to excite **DCA** [52]. Red photons (for λ = 620 nm, E = 2.0 eV) intrinsically possess substantially lower energy than blue (for λ = 410 nm, E = 3.0 eV) or green photons, which gives the impression they may be unfavorable for photocatalytic reactions. To the contrary, however, the use of red light provides other advantages including less photodamage and greater penetration depth into colored reaction solutions [122]. Furthermore, a dual catalytic system with two fully independent photocatalysts provides increased possibilities for method optimization and development but at the same time requires more careful reaction design. The authors initially developed their dual PRC protocol for the benchmark hydrodehalogenation of various aryl halides and efficiently transformed several moderately difficult-to-reduce substrates to their dehalogenated products.

N-Tosyl amides were also suitable substrates, affording detosylated products in mostly good to even quantitative yields with a few exceptions (Figure 27A, B). Several carbazoles (**41l**) and diarylamines (**41m**) were readily generated, however, aryl ethers such as di(*p*-anisyl)amine (**41n**) and phenoxazine (**41o**) were only obtained in modest yields (35–45%). The efficiency seems to be influenced by electronic effects; an electron-poor benzylic (trifluoromethyl)aniline (**41p**) resulted in >95% yield whereas a more electron-rich benzylic toluidine (**41q**) gave <10% yield. A ditosylated aniline was selectively detosylated once to afford **41r** in >95% yield which is in good accordance with the low conversion observed for the detosylation of **41r** to **41s**. Several heteroaromatic amines including pyrrole (**41e**) were also generated in good to excellent yields (67–98%). Electron-withdrawing carbonyl functionalities enabled the efficient detosylation of cyclic aliphatic amines (e.g., **41t**) whereas detosylation of unsubstituted pyrrolidine gave no product. Several tosylated phenols including a doubly tosylated substrate were efficiently detosylated under the reaction conditions

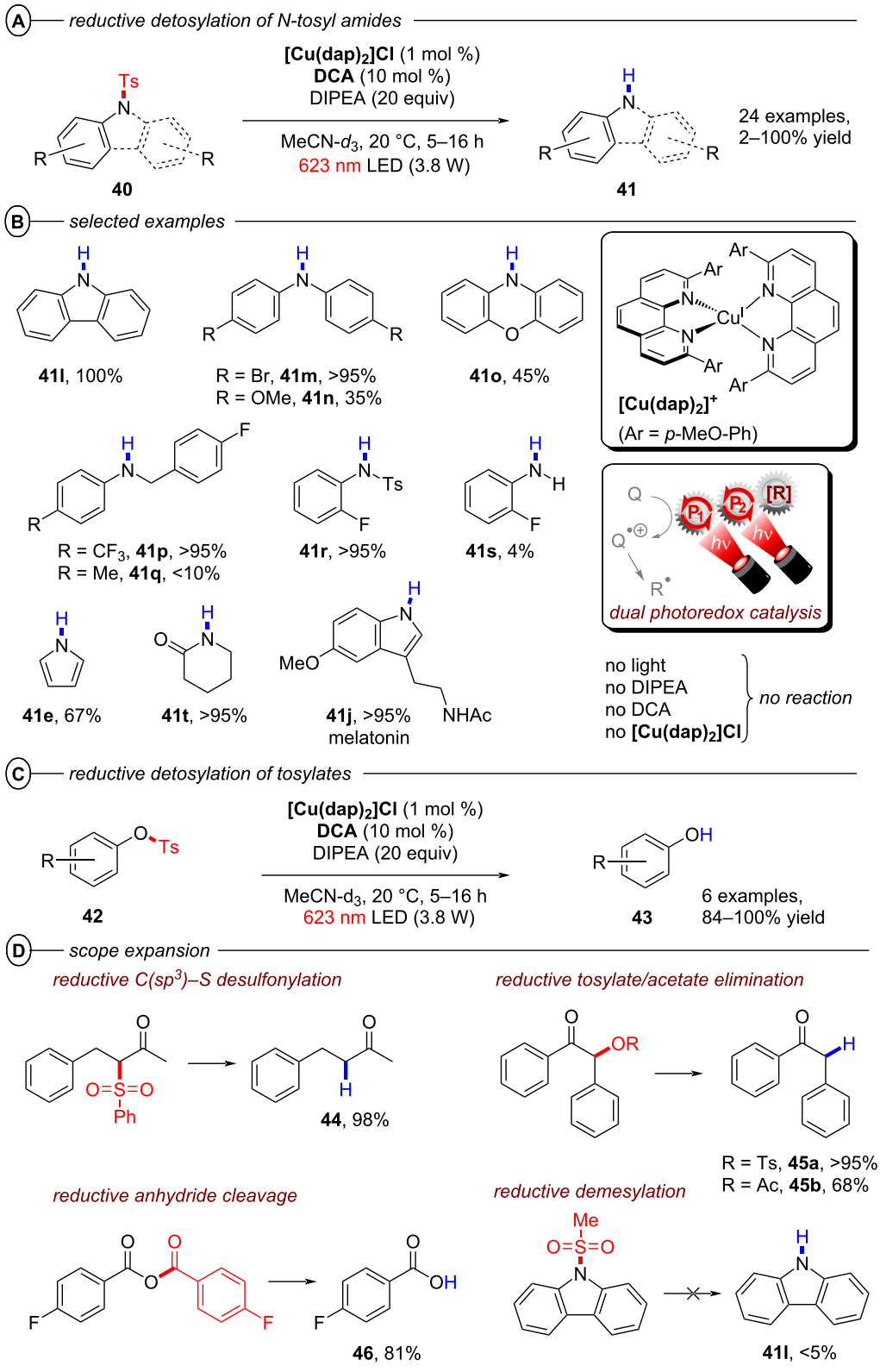

Figure 27: A) Reductive detosylation of *N*-tosyl amides by dual PRC. B) Selected examples from the substrate scope for the detosylation of *N*-tosyl amides. C) Reductive detosylation of tosylates. D) Scope expansion to other reductive transformations achieved by dual PRC.

(Figure 27C). Additionally, selected examples demonstrate the large scope of the dual catalytic system including reductive C(sp^2)–S desulfonylations (**44**), eliminations of tosylates (**45a**) and acetates (**45b**) and reductive anhydride cleavages (**46**) (Figure 27D). Reduction of a mesylated carbazole was not viable and resulted in minimal formation of product **41l**.

The authors proposed two possible mechanisms for the dual PRC with **[Cu(dap)$_2$]Cl** and **DCA**; one relying on PET (Figure 28A) and another relying on triple-triplet energy transfer (TTEnT) (Figure 28B) as the interconnection between both catalytic cycles. For the PET mechanism (Figure 28A), **[Cu^{I}(dap)$_2$]$^+$** (**[Cu^{I}]$^+$**) is initially photoexcited to ^{3}***[Cu^{I}]$^+$** which then undergoes SET to **DCA** to directly access **DCA$^{\bullet-}$**. **[Cu^{I}]$^+$** is subsequently regenerated via reductive quenching of **[Cu^{II}]$^{2+}$** by DIPEA to close the Cu catalytic cycle whereas **DCA$^{\bullet-}$** is excited to ^{2}***DCA$^{\bullet-}$** by the absorption of a red photon. A second SET between ^{2}***DCA$^{\bullet-}$** and the substrate regenerates **DCA** and generates the substrate radical anion. In the TTEnT mechanism (Figure 28B), **DCA$^{\bullet-}$** is formed in a SenI-ET via the generation of ^{3}***DCA** through energy transfer of ^{3}***[Cu^{I}]$^+$** to **DCA** and subsequent reductive quenching by DIPEA. As before, **DCA$^{\bullet-}$** is then excited to ^{2}***DCA$^{\bullet-}$** to enable substrate reduction via SET.

Based on cyclic voltammetry, spectroscopic and spectroelectrochemical data, it was concluded that both pathways are thermodynamically feasible and could simultaneously operate in MeCN as the reaction solvent due to spectroscopic evidence for **[Cu^{II}]$^{2+}$** and ^{3}***DCA**. Based on relative intensity and molar extinction coefficients of the absorption by **DCA$^{\bullet-}$** and ^{3}***DCA** upon excitation of **[Cu^{I}]$^+$**, the authors provided estimations for the concentrations of both species and thus, estimated the relative prevalences of the PET and TTEnT mechanism in MeCN and acetone. Lower concentrations of ^{3}***DCA** than of **DCA$^{\bullet-}$** in MeCN suggest that the PET mechanism herein accounts for roughly 70% of product formation while higher relative concentrations of ^{3}***DCA** in acetone indicate that TTEnT dominates here. Although this proposal has to be judged with caution due to severe simplifications, the study nonetheless emphasizes the critical influence of solvation on photocatalytic mechanisms and their elucidation.

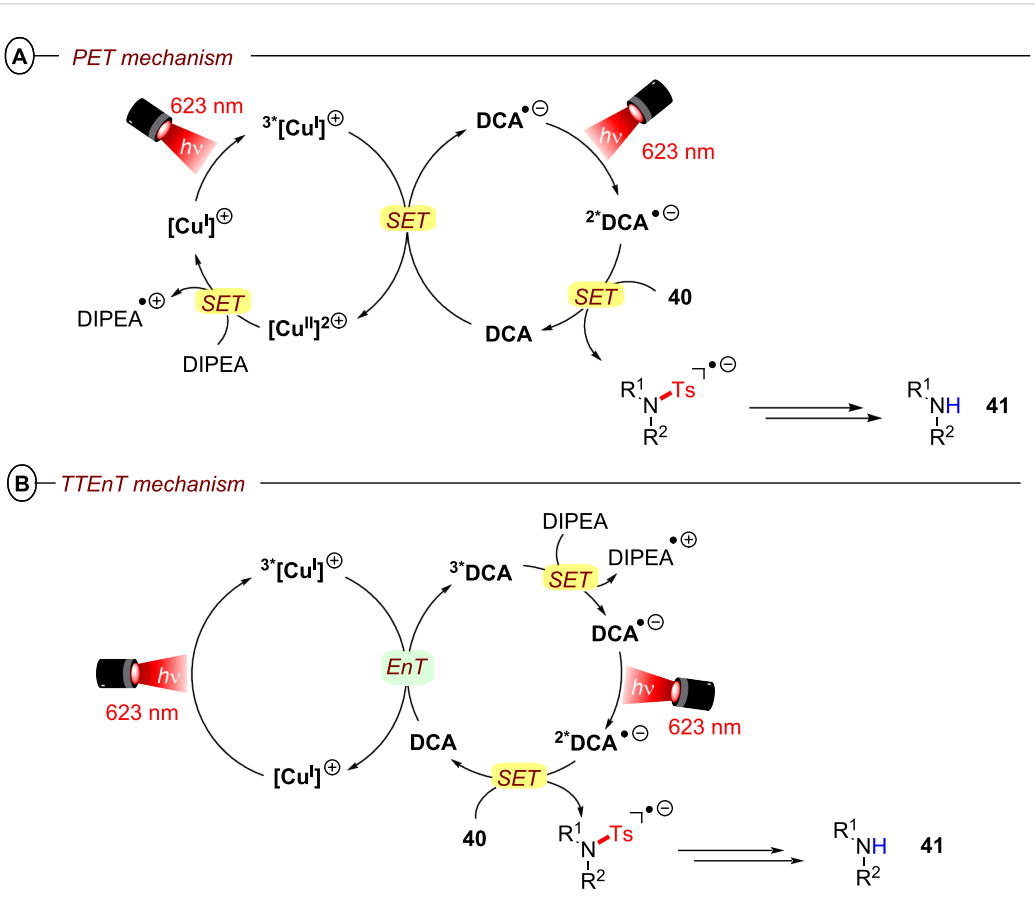

Figure 28: A) Mechanism of the dual PRC based on PET between **[Cu(dap)$_2$]$^+$** and **DCA**. B) Mechanism of the dual PRC based on TTEnT between **[Cu(dap)$_2$]$^+$** and **DCA**.

N–O Bond activation: The Gilmour group recently disclosed a synthetically simple photocatalytic protocol for the reductive cleavage of N–O bonds in Weinreb amides **47** for generation of *N*-methyl amides **48** [123]. Initially, the authors employed anthracene as the photocatalyst and DIPEA as its reductive quencher in a reductive quenching PET cycle, to afford the anthracene radical anion as a potent reductant ($E_{1/2}$ = −1.95 V vs SCE) (Figure 29A). This monophotonic protocol – relying on

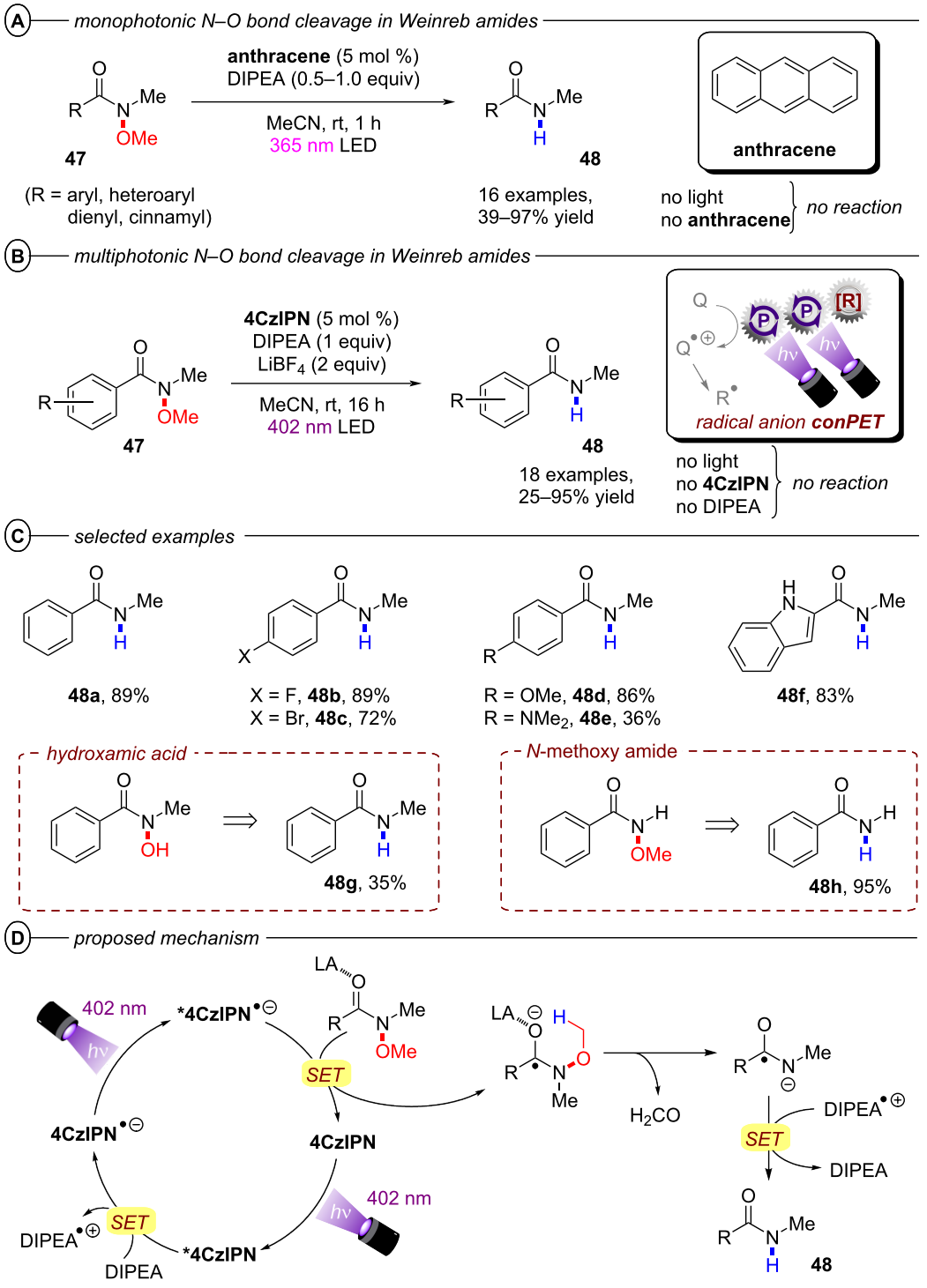

Figure 29: A) N–O bond cleavage in Weinreb amides with anthracene. B) N–O bond cleavage in Weinreb amides relying on conPET. C) Selected examples from the substrate scope. D) Proposed conPET mechanism of the N–O bond cleavage in Weinreb amides with **4CzIPN** and $LiBF_4$ as a Lewis acid (LA).

the energy of a single UV light photon – was found to be sufficiently powerful to reductively cleave several cinnamyl and dienyl Weinreb amides, as well as electron-deficient aryl and heteroaryl Weinreb amides, in moderate to excellent (39–97%) yields. However, electron-neutral or electron-rich aryl Weinreb amides could not be engaged as a redox limitation. This issue was addressed from two distinct strategies to expand the scope of the transformation. On the one hand, Lewis acid activation of amides with $LiBF_4$ significantly facilitated their SET reduction. On the other hand, the reductive power of the photocatalyst was increased by replacing anthracene with **4CzIPN** as a photocatalyst capable of accessing a highly potent reductant (proposed to be *$\mathbf{4CzIPN^{\bullet-}}$) via a conPET mechanism.

Under the modified procedure, electron-rich aryl Weinreb amides **47** were efficiently transformed to the corresponding *N*-methyl aryl amides **48** in poor to excellent (25–95%) yields (Figure 29B/C). Unsubstituted, halogenated, methylated, and arylated *N*-methyl benzamides were generally readily engaged, however, substituents in *ortho*- and *meta*-position decreased the yield compared to *para*-substitution. The more electron-rich *p*-methoxy-*N*-methoxy-*N*-methylbenzamide (E^p_{red} = −2.27 V vs SCE) readily engaged in the reaction and gave 86% yield (**48d**) while *p*-amino-*N*-methylbenzamide was only obtained in 36% yield (**48e**). Additionally, the hydroxamic acid *N*-hydroxy-*N*-methylbenzamide and *N*-methoxybenzamide were exposed to the reaction conditions and successfully transformed to products **48g** and **48h**. A mechanistic proposal for the Lewis acid-assisted reductive N–O bond cleavage following SET from *$\mathbf{4CzIPN^{\bullet-}}$ via conPET is shown in Figure 29D, and was supported by a near quadratic relationship between light intensity and yield. The conPET strategy also allowed for longer wavelength light to be employed, however, the energy efficiency benefit of generating one single UV photon vs two near-UV/purple photons is debatable.

2.2 Oxidative activation

While reductive bond activations via conPET – in particular the reduction of aryl (pseudo)halides – saw considerable development following König's seminal report on **PDI** (vide supra) [15], oxidative activations of substrates via conPET have only recently been demonstrated and remain largely underexplored to date. Since the oxidation potentials of unactivated or deactivated olefins or arenes lie at (or beyond) the energy threshold of single-photon PRC, the development of highly oxidizing photocatalysts is highly desirable to provide access to facile functionalization of these important and abundant feedstock chemicals. While it has been demonstrated that classical chemical oxidant 2,3-dichloro-5,6-dicyano-1,4-benzoquinone (**DDQ**) can function as a closed-shell photocatalyst with an excited-state reduction potential ≈+3 V vs SCE and can oxidatively engage electron-deficient arenes [124,125], the application of **DDQ** is rather undesirable due to the requirement for larger catalyst loadings (10–20 mol %) [126], the use of *tert*-butyl nitrite co-oxidant that forms explosive mixtures in air, evolution of HCN gas upon contact with moisture [127] and catalyst degradation via side reactions with certain amines under the reaction conditions [124]. These limitations are easily overcome by i) oxidative conPET or ii) the merging of photo- and electrochemistry through the use of anodic oxidation (vide infra, especially for **DDQ**) and the former will now be presented.

2.2.1 Alkene activation: In 2018, the Wasielewski group demonstrated the super oxidative power of the excited doublet states of the radical cation of *N*-phenylphenothiazine (***N*-Ph PTZ**$^{\bullet+}$), which set the scene for ***N*-Ph PTZ** as a photocatalyst for oxidative conPET [128]. Simultaneously, Wagenknecht disclosed a protocol for ***N*-Ph PTZ** as a photocatalyst for the pentafluorosulfanylation of diphenylethylene (**49a**) and α-methylstyrene (**49b**) with SF_6 as both terminal oxidant and coupling partner (Figure 30A) [16]. In the mechanism, the radical cation ***N*-Ph PTZ**$^{\bullet+}$ is generated upon oxidative quenching of ****N*-Ph PTZ** by SF_6 (Figure 30B). Thereafter, $SF_6^{\bullet-}$ breaks down into a fluoride ion and a pentafluorosulfanyl radical ($SF_5^{\bullet}$) while ***N*-Ph PTZ**$^{\bullet+}$ is photoexcited to ****N*-Ph PTZ**$^{\bullet+}$ which then oxidizes the styrene substrate to its radical cation **49**$^{\bullet+}$. With no other suitable trapping agents present, **49**$^{\bullet+}$ is trapped by $SF_5^{\bullet}$ and reaction of the resulting cation **50**$^{+}$ with a fluoride ion then generates product **50** (Figure 30B). Subsequent elimination of a fluoride ion mediated by $BF_3{\cdot}OEt_2$ forms pentafluorosulfanylated styrenes **51a** and **51b** (Figure 30A).

While photocatalytic SET reduction of SF_6 had been achieved previously with $\mathbf{Ir(ppy)_2(dtb\text{-}ppy)PF_6}$ by Jamison's group [129], the fragmentation pattern of $SF_6^{\bullet-}$ was proposed to be highly dependent on the excess energy provided by SET. The less potent reducing iridium species in Jamison's work favors the lower energy fragmentation pathway to $F^{\bullet}$ and SF_5^{-} whereas highly potent reductant ****N*-Ph PTZ** provides enough energy for access to $SF_5^{\bullet}$ and thus, pentafluorosulfanylation [16,130]. Addition of catalytic amounts of $Cu(acac)_2$ was found to favor product formation by suppressing undesired side reactions.

Following their initial publication, the Wagenknecht group expanded their scope to the α-alkoxypentafluorosulfanylation of styrenes by addition of alcohols [131]. Herein, addition of the Lewis acid BEt_3 successfully suppressed the competing fluoride addition by complexing fluoride ions generated by oxidative quenching of ****N*-Ph PTZ** and enabled trapping of cation **50**$^{+}$ instead by the alcohol. Acyclic and cyclic aliphatic alcohols as well as alcohols bearing alkene, alkyne and nitrile func-

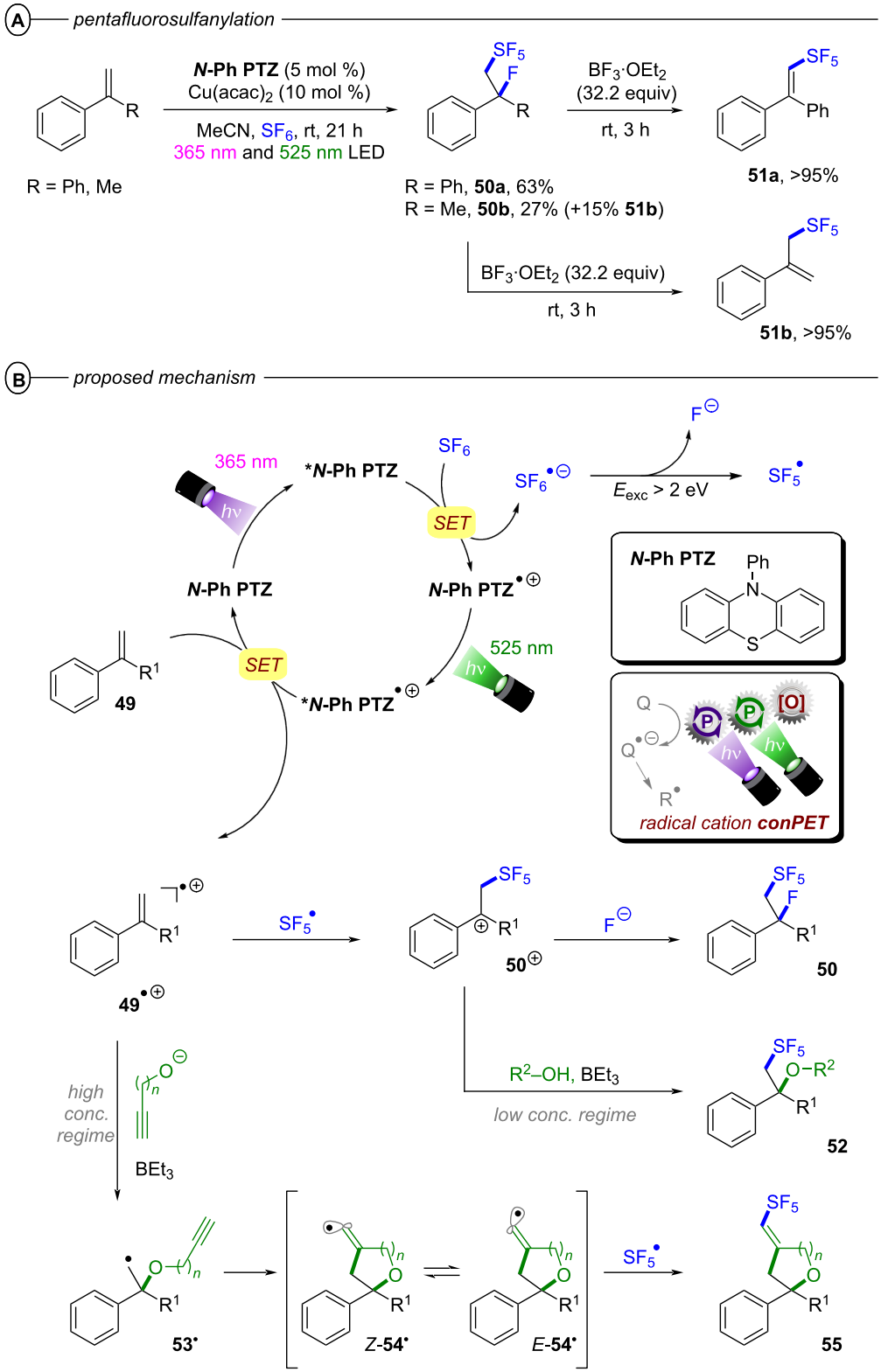

Figure 30: A) Pentafluorosulfanylation and fluoride elimination. B) Mechanism of the pentafluorosulfanylation and α-alkoxypentafluorosulfanylation of α-substituted styrenes with SF_6.

tionalities were successfully applied and gave α-alkoxypentafluorosulfanylated products **52** in poor to moderate yields (13–53%) (Figure 31A). Intramolecular addition of an alcoholic chain allowed for the generation of spiroethers (**52d**). Phenols and water were not tolerated, however, reaction of tertiary alcohols (such as 1-ethynyl-1-cyclopentanol) led to the formation of free alcohols (e.g., **52e** in 13% yield). When investigating the effect of different concentrations of the alcohol nucleophiles, the authors observed that higher concentrations of terminal alkynols suppressed formation of the open-chain product **52** and instead promoted formation of oxaheterocyclic compounds **55** [133]. Depending on the chain length of the alkynol, oxepans, tetrahydropyrans and furans were obtained in <10–32% yields (Figure 31B).

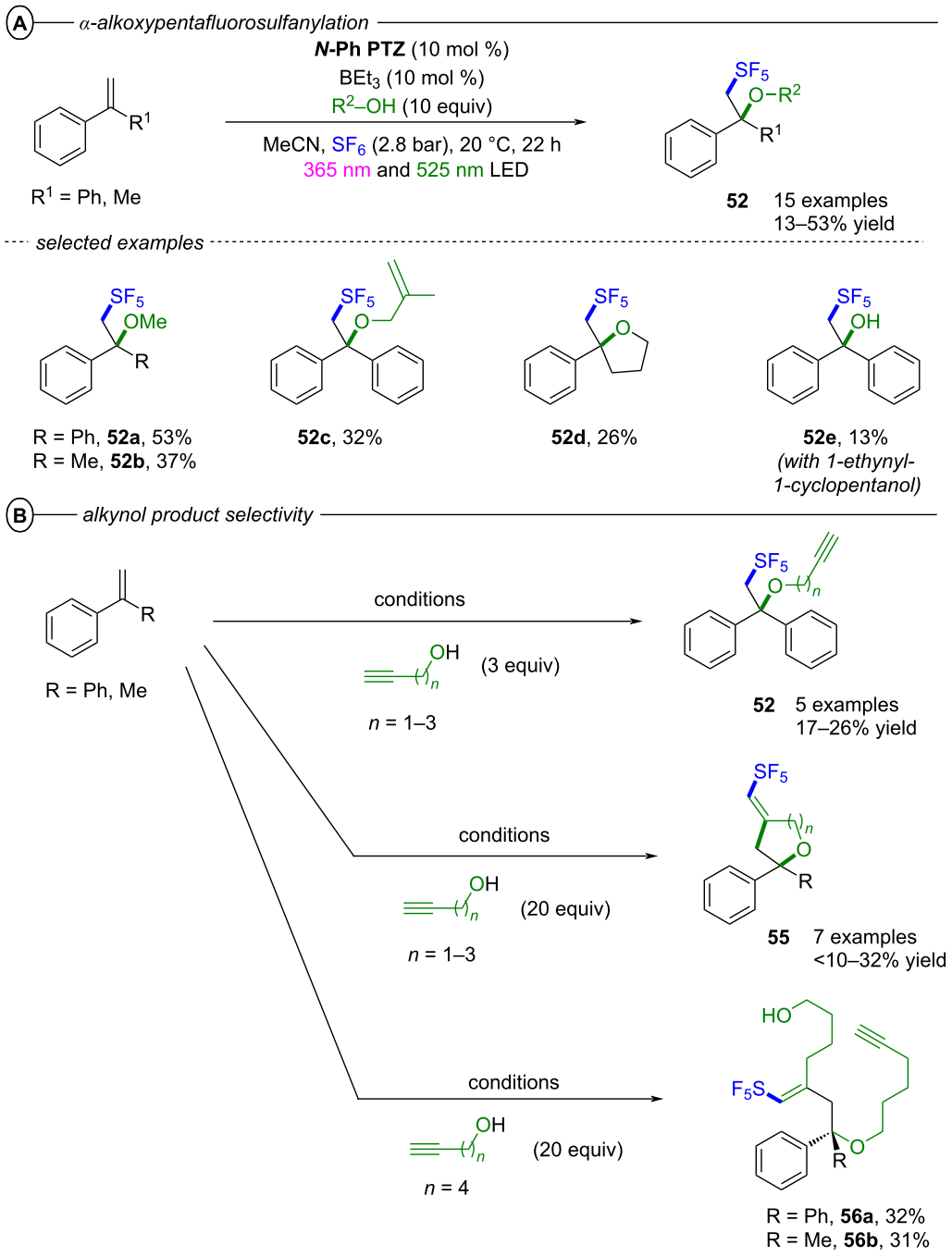

Figure 31: A) α-Alkoxypentafluorosulfanylation (top) and selected examples from the substrate scope (bottom). B) Effect of chain length on alkynol product selectivity.

Mechanistic investigations suggested that the alkynol is deprotonated by fluoride ions in the higher concentration regime and **49**$^{\bullet+}$ is trapped by the alkoxide before it can react with $^{\bullet}SF_5$ (Figure 30B). The oxaheterocyclic compounds **55** were obtained exclusively in their *E*-configurations which the authors tentatively attributed to kinetic differences in product formation as DFT calculations show only a minimal free energy difference of 0.1 kcal mol^{-1} between ***Z*-54**$^{\bullet}$ and ***E*-54**$^{\bullet}$ (Figure 30B). Longer chain lengths of the alkynol, as in 5-hexyn-1-ol, did not afford oxaheterocyclic products but instead doubly substituted open-chain products **56a** and **56b** (Figure 31B).

Although overall the yields of fluoropentafluorosulfonylation and alkoxypentafluorosulfanylation reactions were lacking, these must be viewed in the context of the extraordinary inertness of SF_6 towards chemical reactions [132] and thus represent a remarkable synthetic achievement.

2.2.2 Arenea activation: In 2021, Wickens and co-workers disclosed a conPET protocol for the oxidative azolation of moderately electron-rich and electron-neutral arenes by N-heterocyclic nucleophiles [134], representing a synthetic advancement from the engagement of electron-rich arenes seminally achieved by Nicewicz and co-workers via single-photon PRC [135]. ***N*-Ph PTZ** was employed as a photocatalyst, O_2 as the terminal oxidant and fluorinated alcohols as co-solvents due to their stabilizing effects on radical cations (Figure 32A) [136,137]. The authors postulated that photoexcitation and subsequent SET oxidation of ***N*-Ph PTZ** by O_2 generates ***N*-Ph PTZ**$^{\bullet+}$. A second excitation process furnishes ***N*-Ph PTZ**$^{\bullet+}$ which oxidizes the arene to its radical cation via SET (Figure 32B). The azole **57** then nucleophilically adds to the aryl radical cation, yielding (with the loss of a proton) the aryl radical **58**. Though the authors do not propose a detailed mechanism for the subsequent reaction it can be postulated that deprotonation of the addition product followed by a subsequent oxidation and deprotonation generate product **59**. Oxygen uptake experiments revealed a consumption of roughly 2.3 equiv of O_2 based on the amount of product which indicates that this second oxidation step is either performed by another molecule of ***N*-Ph PTZ**$^{\bullet+}$ or directly by O_2. Addition of substoichiometric amounts of $LiClO_4$ (or other Lewis acids) promoted product formation which the authors attributed to a suppression of back electron transfer between superoxide ($O_2^{\bullet-}$) and ***N*-Ph PTZ**$^{\bullet+}$ by facilitating the disproportionation of superoxide to peroxide and O_2. Under these optimized conditions, benzene was successfully coupled to several pyrazoles bearing electron-withdrawing and electron-donating functionalities as well as triazoles (**59c**) in poor to high (22–88%) yields (Figure 32C). Methyl-substituted arenes (toluene, *m*-xylene and mesitylene) proceeded efficiently under the reaction conditions (**59d–f**). Electron-poor chlorobenzene was oxidized in low (22%) yield (**59g**), representing an upper redox limitation of the system.

An aspect overlooked in all three aforementioned reports proposing ***N*-Ph PTZ**$^{\bullet+}$ as a super photooxidant is its ultrashort excited state lifetime – ≥36 ps as reported by Wasielewski [128] – that renders diffusion-controlled photochemistry implausible. Wickens and co-workers did not detect indications of preassembly in the steady-state UV–vis [134], but it cannot be ruled out (discussion vide supra, section 2.1.4). Since Wickens and co-workers employed a vast excess of arenes in most reactions (up to ≈8 mL as solvent, i.e., 5.6 M PhH w.r.t. ≈ 1.3 mM of ***N*-Ph PTZ**), the statistical probability of an arene molecule in close proximity to the excited state upon its formation is high enough for static quenching [40,53] such that there may be no need to invoke an 'organized' [40,53]. However, lower excesses (5–10 equiv) of more electron-rich alkylarenes were successful, and in Wagenknecht and co-workers' report styrenes were employed as the limiting agent (0.1 M styrene w.r.t. 5.0 mM ***N*-Ph PTZ**). Therefore, an organized preassembly is likely at these lower substrate concentration regimes, which we propose involved π–π stacking interactions based on Barham's results and Hauer's transient absorption spectroscopic investigations of analogous triarylamine radical cations (vide infra, Figure 37 and following discussion).

2.2.3 C(sp^3)–H activation: Apart from previously mentioned applications of conPET for the generation of super-reductants or super-oxidants for SET reduction or oxidation of substrates, it can also provide access to other transformations. Recently, the generation of chlorine radicals as powerful HAT agents has been a topic of increased interest and the challenging generation of Cl$^{\bullet}$ has been achieved by monophotonic PRC oxidation of Cl^- to Cl$^{\bullet}$ by highly oxidizing noble metal photocatalysts or **Mes-Acr**$^+$ [138-140]. Another noteworthy method for accessing this highly reactive HAT agent is the photoelectrochemical generation of Cl$^{\bullet}$ reported by Xu and co-workers (vide infra, Figure 56 in section 3.1.2 focused on Minisci-type processes) [141].

Meyer, Hu and co-workers recently reported how ***N*-Ph PTZ** could function as a conPET catalyst for the generation of Cl$^{\bullet}$, the latter serving as a HAT agent for the activation of unreactive C(sp^3)–H bonds in hydrocarbons (Figure 33A) [142]. In their protocol, ***N*-Ph PTZ** is excited to ***N*-Ph PTZ** by near-UV LED irradiation (390 nm or 405 nm) and this excited state undergoes oxidative quenching by O_2 or CCl_4 to afford ***N*-Ph PTZ**$^{\bullet+}$ (Figure 33B). This radical cation can either disproportionate into ***N*-Ph PTZ** and ***N*-Ph PTZ**$^{2+}$ or be photoexcited to ***N*-Ph PTZ**$^{\bullet+}$ by green LED irradiation (532 nm). While oxidation of Cl^- to Cl$^{\bullet}$ (E^p_{ox} = +1.46 V vs NHE in MeCN) by ***N*-Ph**

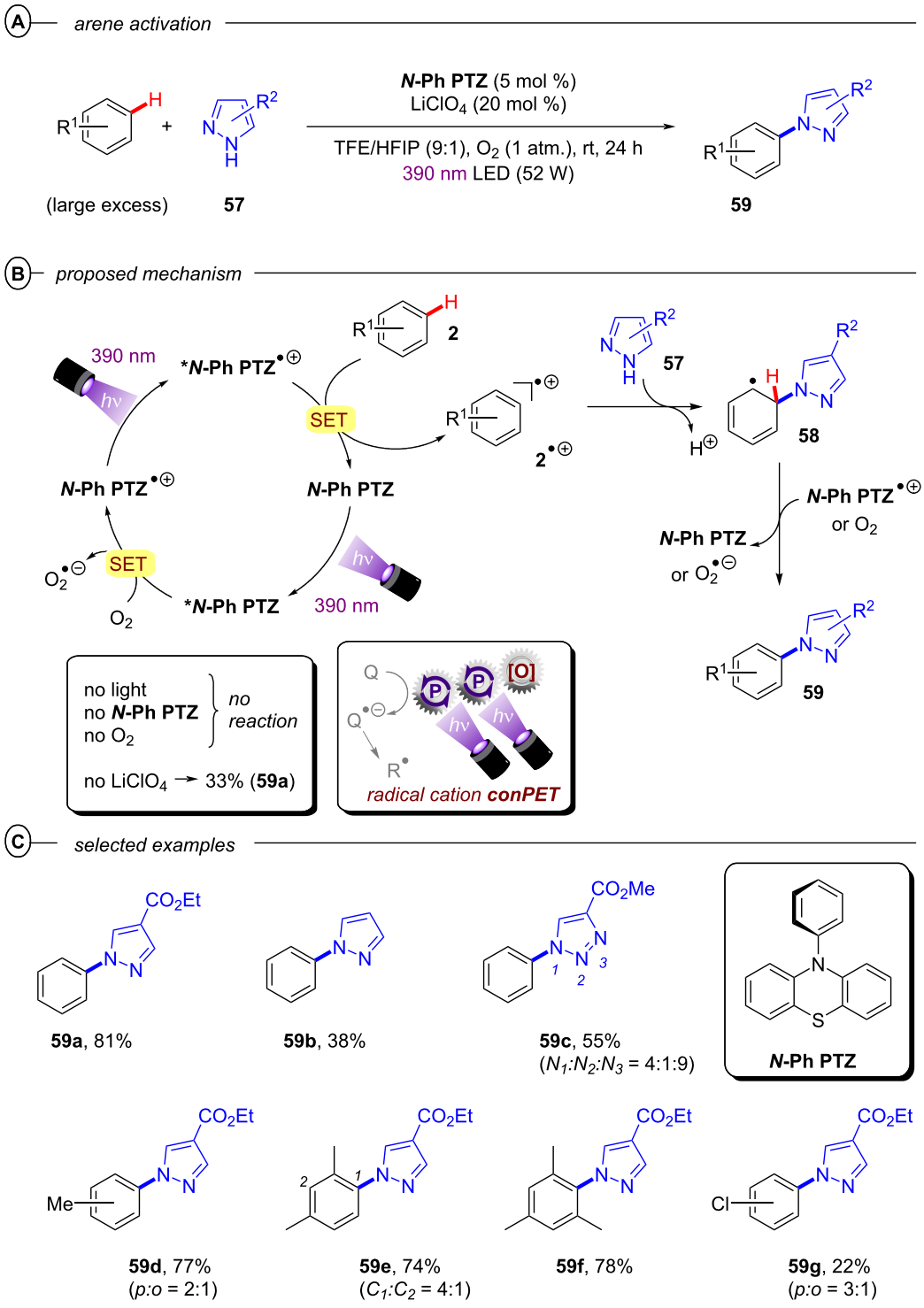

Figure 32: A) Oxidative amination of arenes with azoles catalyzed by ***N*-Ph PTZ**. B) Selected examples from the substrate scope. B) Proposed mechanism.

PTZ or ***N*-Ph PTZ**$^{•+}$ ($E_{1/2}$ = +0.92 V vs NHE) is thermodynamically out of reach, both ***N*-Ph PTZ**$^{2+}$ ($E_{1/2}$ = +1.59 V vs NHE) and ***N*-Ph PTZ**$^{•+}$ ($^*E_{1/2}$ = +2.31 V vs NHE) possess sufficient oxidative redox power to generate Cl$^•$. Experiments were conducted under single wavelength (405 nm) and dual wavelength (405 nm and 532 nm) irradiation with 1,1-

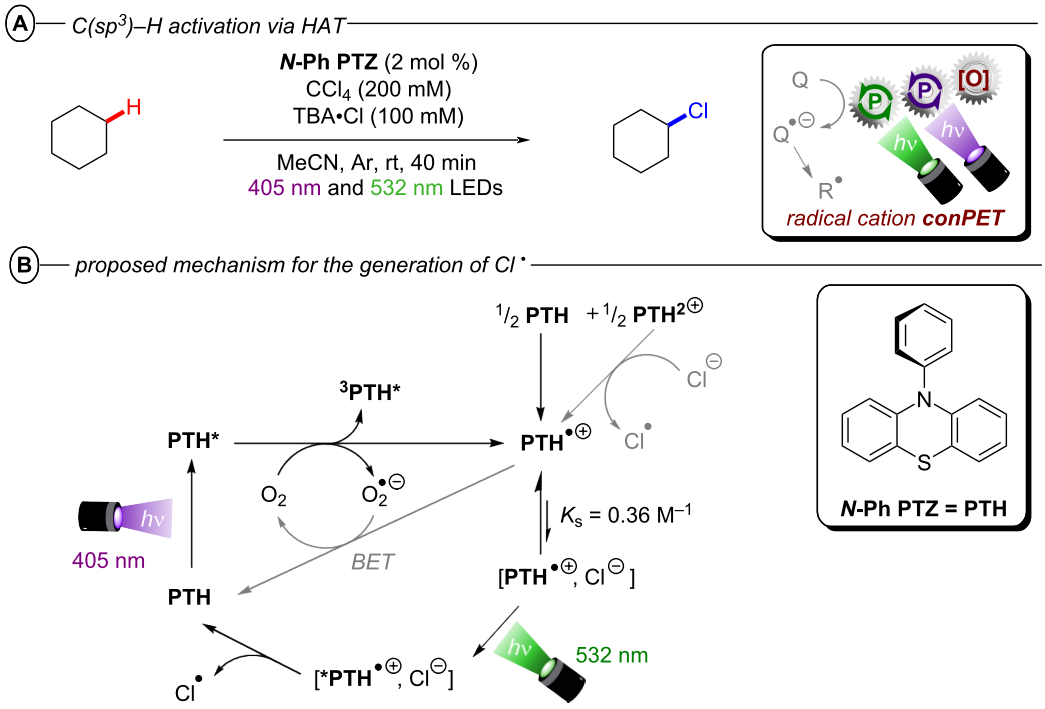

Figure 33: A) C(sp^3)–H bond activation by HAT via chloride oxidation by ***N*-Ph PTZ**$^{\bullet+}$. B) Proposed mechanism for the formation of Cl$^\bullet$ under single and multiple wavelength irradiation.

diphenylethylene, cyclohexane, toluene, 1,4-dioxane and cycloheptane. Chlorinated products were generated under both conditions, however, yields were generally higher when dual wavelength irradiation was employed (increases of 85% for 1,1-diphenylethylene and 38% for cyclohexane). Since ***N*-Ph PTZ**$^{\bullet+}$ barely absorbs near-UV light, the authors attributed the formation of chlorinated products under single wavelength irradiation to oxidation of Cl^- by the disproportionated species ***N*-Ph PTZ**$^{2+}$. However, direct oxidation of Cl^- by ***N*-Ph PTZ**$^{\bullet+}$ formed via less efficient excitation of ***N*-Ph PTZ**$^{\bullet+}$ under exclusive irradiation at 405 nm cannot be ruled out. In this case, the increased yield under two wavelength irradiation could simply be attributed to a more efficient formation of highly oxidizing ***N*-Ph PTZ**$^{\bullet+}$. Due to the aforementioned ultrashort excited state lifetime of ***N*-Ph PTZ**$^{\bullet+}$, a preassembly of ***N*-Ph PTZ**$^{\bullet+}$ with Cl^- is required for efficient oxidation and a Coulombic ion pair is the logical proposal for this.

While the work of Meyer and Hu elegantly demonstrates additional fields of application for highly oxidizing conPET catalysts, their work so far only outlines the conceptual idea. Xu and co-workers' success with photoelectrochemical oxidation of HCl for activation of unreactive C(sp^3)–H bonds demonstrates clear advantages including the absence of any photocatalyst and requirement of only one photon per product molecule (vide infra).

3 Photoelectrochemistry in organic synthesis

3.1 Oxidative activation

3.1.1 Arene activation: *C(sp^2)–H activation:* In the oxidative direction, e-PRC has demonstrated impressive synthetic advancements in C(sp^2)–N and C(sp^2)–O bond formations from arene or alkene substrates. Since such photoredox reactions typically rely on SET oxidation of the unsaturated system, they tend to be carried out with relatively electron-rich substrates due to their lower oxidation potentials that are accessible under (unassisted) monophotonic PRC by closed-shell excited states. In this regard, Xu and Hou disclosed a 'recycling e-PRC' azolation of electron-rich arenes (generally referred to as **60** in this section) with pyrazoles **62** employing 9-mesityl-10-methylacridinium perchlorate **Mes-Acr-ClO$_4$** as photocatalyst (Figure 34A) [143]. In the mechanism for the reaction of oxydibenzene **61a** and pyrazole **62a** (Figure 34B), **Mes-Acr**$^+$ ($E_{1/2}$ = −0.57 V vs SCE) is photoexcited, generating the highly oxidizing state ***Mes-Acr**$^+$ (*$E_{1/2}$ = 2.06 V vs SCE). The latter oxidizes **61a** to arene radical cation **61a**$^{\bullet+}$, generating **Mes-Acr**$^\bullet$ at the same time, which is then oxidized at the anode to regenerate the active catalyst. The radical cation intermediate is trapped with pyrazole to yield the radical **64a**, which reacts with 2,2,6,6-tetramethylpiperidinyloxy (**TEMPO**) in a HAT reaction to generate the target coupling product **63a** in 72% yield and **TEMPO**-H, a species that can also be oxidized at the anode.

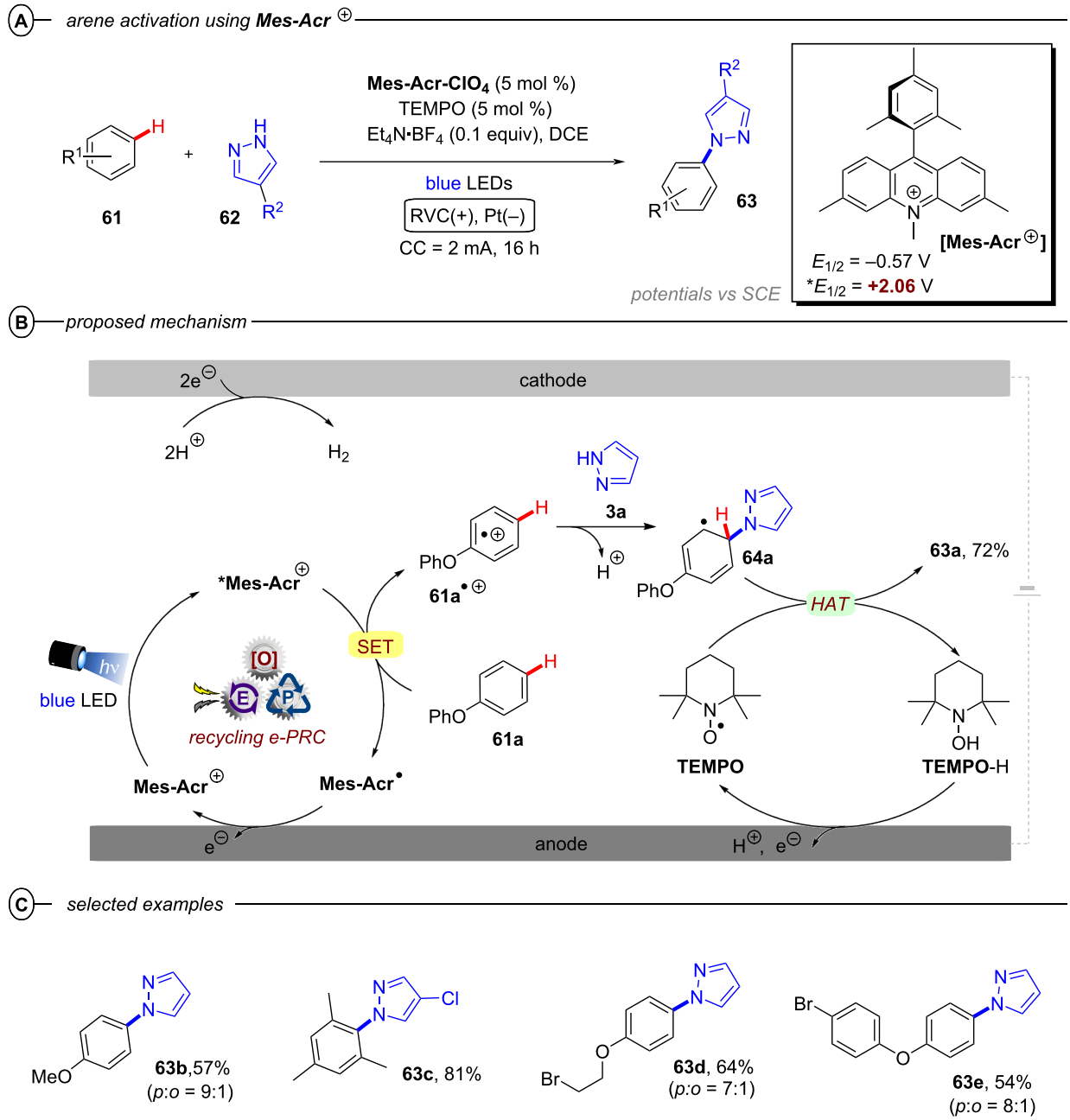

Figure 34: A) Recycling e-PRC C–H azolation of electron-rich arenes with pyrazoles using **Mes-Acr**$^+$ as a photocatalyst. B) Proposed mechanism. C) Selected examples from the substrate scope.

With the optimized conditions in hand, the authors investigated a variety of arenes, obtaining products like **63b–e** in good to high yields (57–81%, Figure 34C). Interestingly, 1-bromo-4-phenoxybenzene reacted selectively only at the phenyl ring, affording **63e** with the *para*-product as the major regioisomer. Compared to the seminal work of Nicewicz [135] under monophotonic PRC that relies on molecular O_2 for catalyst turnover, Xu and co-workers' electrochemical catalyst turnover furnishes a PEC protocol with better prospects for scale up. Moreover, compared to the preceding 'radical ion' photocatalytic protocols of Lambert and co-workers (e-PRC, vide infra), Barham and co-workers (e-PRC, vide infra) and Wickens (conPET, vide supra), Xu and co-workers showed a key advantage of the recycling e-PRC approach that allows arene to be used as the limiting reactant rather than a (vast) stoichiometric excess.

However, as per the groundbreaking report of Nicewicz [135], the limitation of oxidative power remains that allowed only electron-rich arenes to be engaged. In recent years it became desirable to target oxidation of electron-neutral and electron-deficient arenes (e.g., those containing halogen atoms or benzene itself, E^{p}_{ox} = +2.48 → >+3.0 V vs SCE), since these are cheaper chemical feedstocks. In this respect, in 2019 the Lambert group reported a trisaminocyclopropenium cation **TAC**$^{+}$ [144-147] as an e-PRC catalyst for the oxidation of unactivated arenes and their coupling with nitrogen heteroaromatics (Figure 35A) [148]. Mechanistically, the electrochemical oxidation of the colorless **TAC**$^{+}$ cation ($E_{1/2}$ = +1.26 V vs SCE) generates the colored dication radical **TAC**$^{\bullet 2+}$ (Figure 35B) [145-147,149]. Subsequent photoexcitation affords ***TAC**$^{\bullet 2+}$ ($^{*}E_{1/2}$ = +3.33 V vs SCE) as a super oxidant [150], which can oxidize target arene **1** via SET to its aryl radical cation **61**$^{\bullet +}$ with concomitant regeneration of **TAC**$^{+}$. At this point, the mechanism for **61**$^{\bullet +}$ follows a similar pathway described in the conPET oxidative arene activations (vide supra, section 2.2.2, Figure 32C). Proton reduction (HER) was proposed as the corresponding cathodic half-reaction, since gas bubbles were observed and since an excess of AcOH was necessary for reaction efficiency. The reaction tolerated benzene (**63f**) and even aryl chlorides to give products **63g** and **63h**, albeit in modest yields (Figure 35C). This method is also 'backwards compatible' with easily oxidized substrates such as mesitylene and other alkylated benzenes (e.g., forming **63i**).

In the context of e-PRC C(sp^2)–N bond formations, the Barham group unveiled tri(*p*-substituted)arylamine (**TPA**) radical

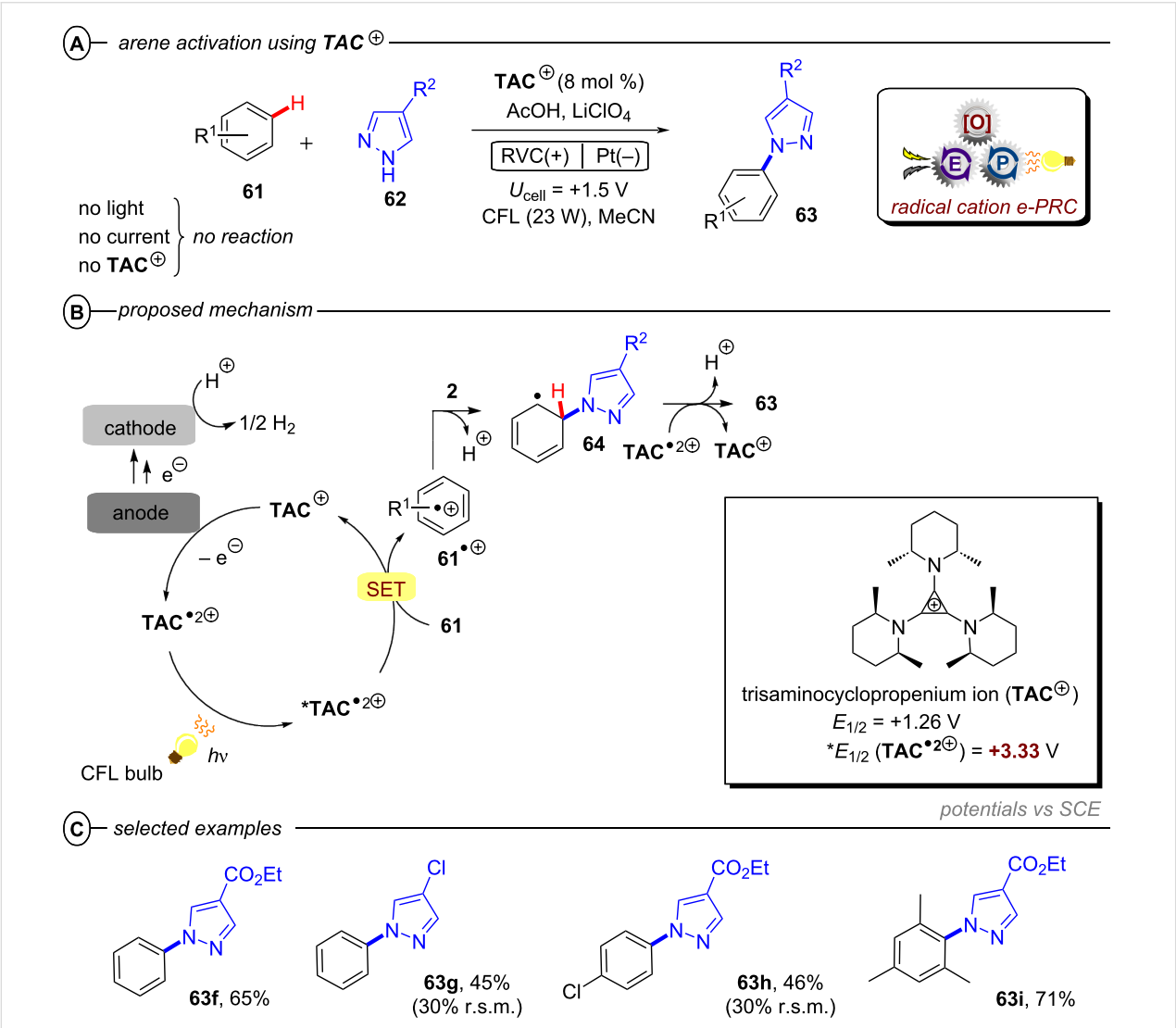

Figure 35: A) Radical ion e-PRC direct oxidation of unactivated arenes using **TAC**$^{+}$ as an electro-activated photocatalyst. B) Proposed mechanism. C) Selected examples from the substrate scope.

cations [151-154] as a tunable class of radical ion e-PRCat (Figure 36A) [155]. The most interesting feature of **TPAs** is that modifying their substituents in *para*-position to the triphenylamine core allows facile tuning of the oxidative power of their radical cationic photocatalyst forms [54,156].

In fact, while the use of a moderately-powerful **TPA** (**T*p*BPA**) enabled the C(sp^2)–H azolations of alkylbenzenes in high yields and chemoselectivity (**63l–o** in Figure 36B), the substitution of its *para*-phenyl group with a *para*-(4-)benzonitrile group resulted in a much more powerful **TCPBA**, that allowed C–H amination of benzene and chlorobenzene in good yields (**63p–q**). Finally, the most potent **TPA** (**TdCBPA**, with a record breaking $*E_{1/2}$ = +4.41 V vs SCE) allowed SET oxidations even of dichlorobenzenes and fluorobenzene (**63r–s**). In the mechanism, electrochemical oxidation of **TPA** generates the radical cation **TPA**$^{\bullet+}$ as the active photocatalyst. The authors demonstrated for the first time the crucial importance of a radical ion photocatalyst-substrate preassembly, necessary to achieve the reactivity of the picosecond-lived photoexcited radical ions like ***TPA**$^{\bullet+}$ (4.6 ps for **T*p*BPA**$^{\bullet+}$ and 8.6 ps for **TCBPA**$^{\bullet+}$, respectively) in competition with their photophysical deactivation (Figure 37). Subsequent photoexcitation of **[TPA**$^{\bullet+}$**--- Sub]** then leads to the reactive assembly ***[TPA**$^{\bullet+}$**--- Sub]**, which, upon inner-sphere SET, generates the arene radical cation **Sub**$^{\bullet+}$ and regenerates **TPA**. Finally, **Sub**$^{\bullet+}$ is intercepted by the N-heterocyclic nucleophile **62** followed by loss of protons and further SET (to the anode or to **TPA**$^{\bullet+}$) to obtain the azolated arene product **63**.

The detailed mechanistic study on preassembly was easily accessible owing to the excellent stability of **TPA**$^{\bullet+}$s, which can be easily chemically generated, isolated and stored in their solid state without special precautions [153,154]. Assemblies **[TPA**$^{\bullet+}$**--- Sub]** were identified spectroscopically via changes in the UV–vis spectra and EPR spectra of isolated **TPA**$^{\bullet+}$s when

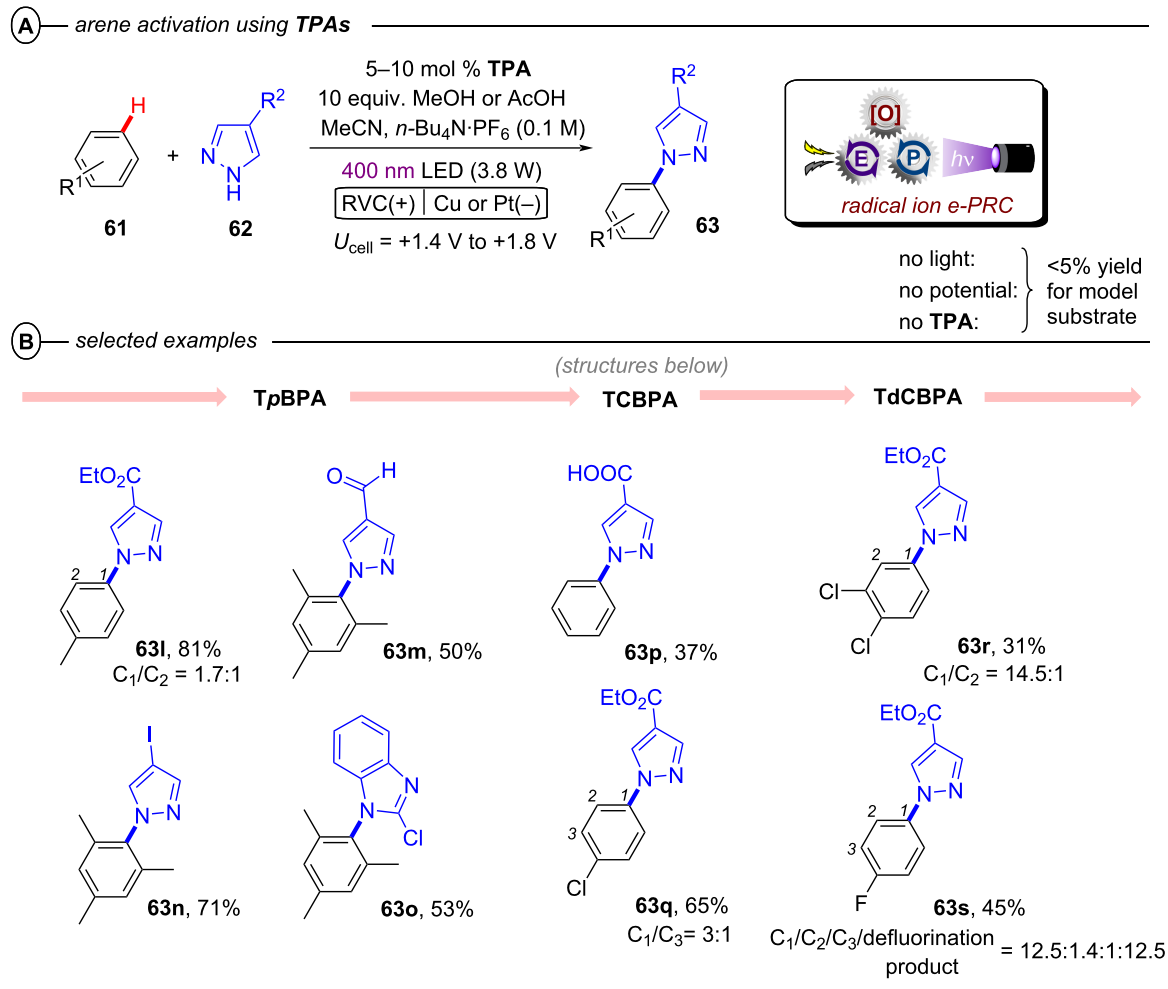

Figure 36: A) Radical ion e-PRC direct oxidation of unactivated arenes using **TPA** as an electro-activated photocatalyst. B) Selected examples from the substrate scope.

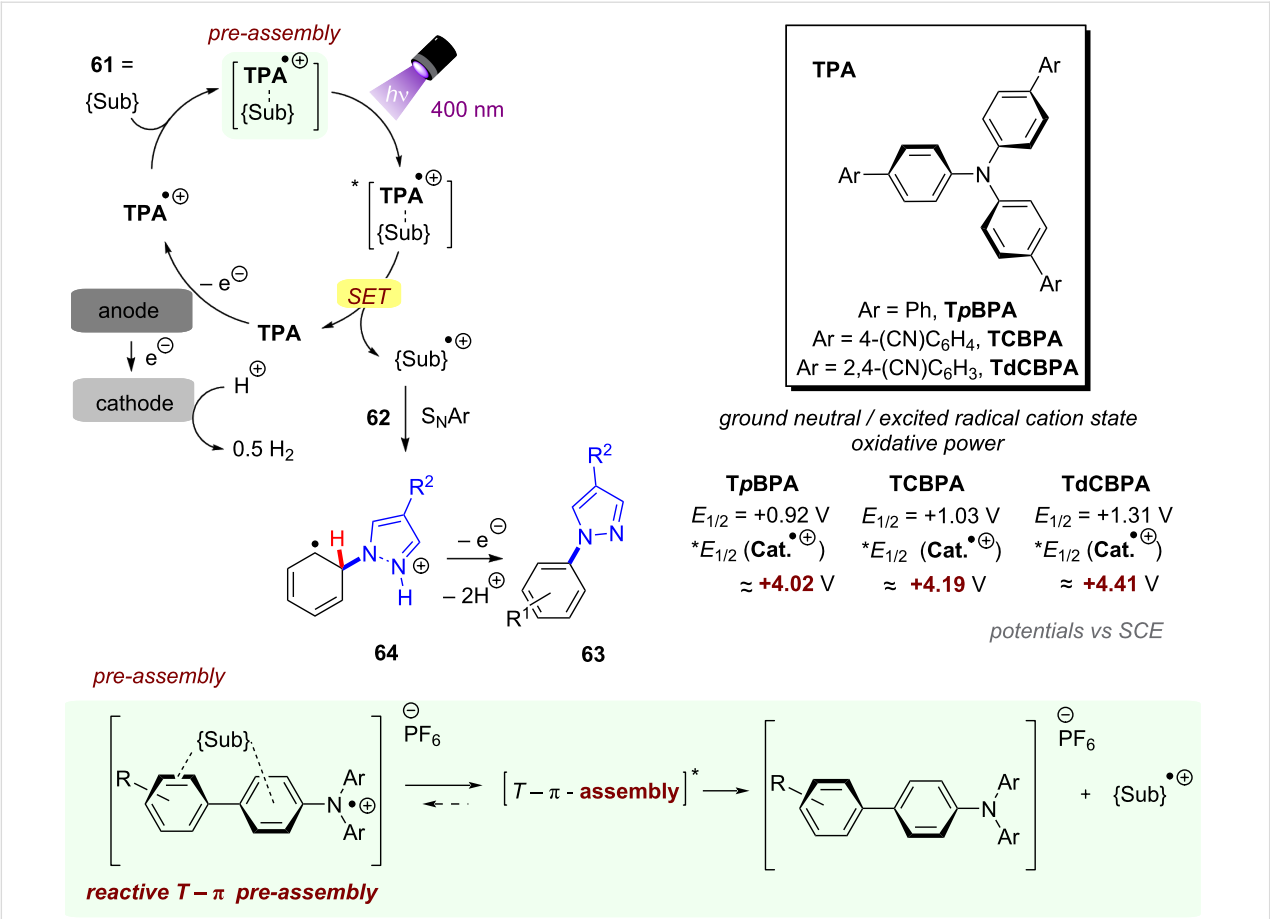

Figure 37: Proposed mechanism (top) and mode of preassembly (bottom).

mixed with arene substrates in excesses representative of the synthetic reaction.

The most noticeable comparison was observed when **TCBPA**$^{\bullet+}$ was exposed to either 1,2- or 1,4 dichlorobenzene. The addition of the former "reactive" substrate caused a disruption in the electron paramagnetic resonance spectroscopy (EPR) signal, enhancing a distinctive triplet pattern. This evidence confirmed the need to localize spin density on the nitrogen atom within the initial preassembly in order to achieve reactivity. On the other hand, when the latter "unreactive" substrate was introduced, the signal was altered to a broad singlet, corroborating a different orientation of preassembly where the spin density was spread out from the N atom. The latter configuration stabilized the radical cation and decreased its oxidative power in the excited state for SET. DFT calculations (ωB97X-D or uB3LYP functionals) were also performed, and optimized structures were found involving T–π or π–π interactions (Figure 38A). It was also possible to evidence a preferred preassembly geometry for unsymmetrical compounds (PhX). In particular, for PhCl, the calculated spin density changed when the Cl atom faced "*in*" but did not change when facing "*out*" (Figure 38B), and thus the former orientation – accorded with spectral changes in the steady-state EPR and UV–vis – was proposed as favored.

The Barham group then concluded how, despite the strong absorption of **TPA**$^{\bullet+}$s in the near-IR visible region (approx. 600–900 nm, a $D_0 \rightarrow D_1$ transition), only shorter wavelength excitations (400 nm) gave reactivity. This was later confirmed by the Hauer group using transient absorption experiments which revealed quenching only of the higher excited state (D_n) of **TpBPA**$^{\bullet+}$ by mesitylene [157]. This is particularly important because for that catalyst/substrate combination no changes in the steady-state UV–vis spectrum were observed by Barham and co-workers [155]. These observations confirm how preassembly can serve as a general platform for anti-Kasha photochemistry, that temporally enables the participation of higher-order excited states participating in SET [69,120,157-160].

Other oxidative coupling protocols involving C–H heterofunctionalization of arenes can be found in the literature that involve

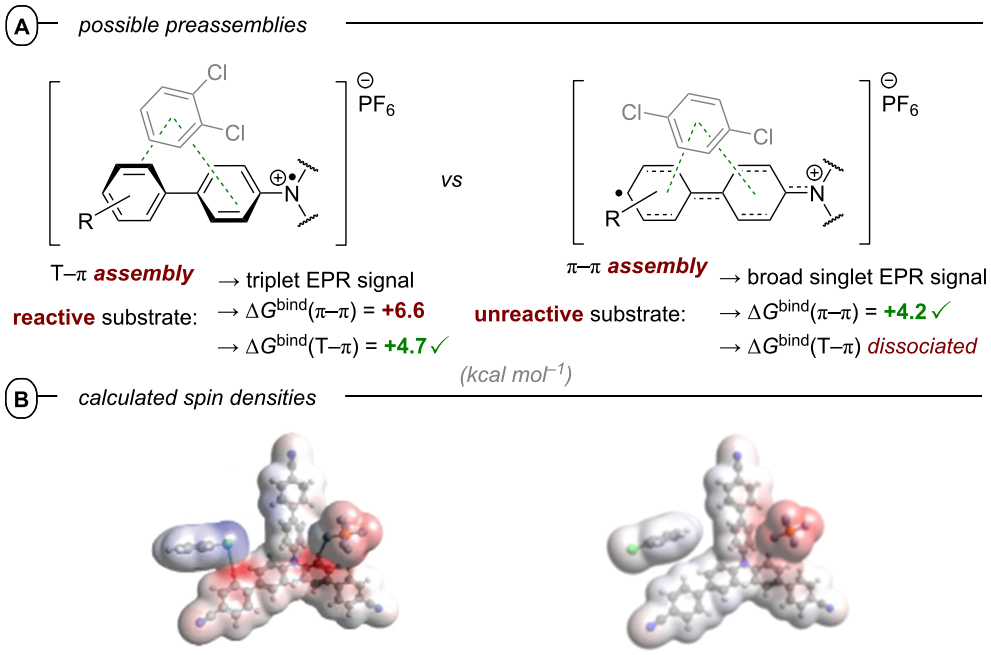

Figure 38: A) Possible preassemblies of reactive (left) vs unreactive (right) arenes. B) Calculated spin densities of T–π preassemblies of **TCBPA**$^{\bullet+}$ with chlorobenzene where the halogen faces "in" (left) or "out" (right). Adapted from [29] (© 2021 S. Wu et al. and *Angewandte Chemie International Edition*, published by Wiley-VCH GmbH, distributed under the terms of the Creative Commons Attribution 4.0 International License, https://creativecommons.org/licenses/by/4.0).

the electrochemical turnover of a photocatalyst [28,29], forging C(sp^2)–O and C(sp^2)–N bonds under recycling e-PRC conditions. In this regard, Lambert and co-workers disclosed arene hydroxylation or acetoxylation using **DDQ** as photocatalyst and water/alcohols (**65**) as reactants (Figure 39A) [161]. The main difference from previous works using this catalyst is that **DDQ** is regenerated by anodic oxidation of the reduced **$DDQH_2$** – with concomitant cathodic reduction of protons to form hydrogen gas – completing the electrochemical reaction (Figure 39B). Thus, this e-PRC approach addresses and obviates one of the key aforementionated drawbacks of DDQ as used in photoredox-only transformations – the presence of a stoichiometric chemical oxidant such as *tert*-butyl nitrile as co-oxidant (vide supra, section 2.2). A plausible mechanism involves the photoexcitation of **DDQ**, which results in the generation of a highly oxidizing excited state ***DDQ** ($^*E_{1/2}$ = +3.18 V vs SCE). The excited state is subsequently engaged in a SET process with the arene species **61**, leading to the formation of two distinct species: the radical anion **DDQ**$^{\bullet-}$ and the reactive radical cation **61**$^{\bullet+}$. At this stage, the alcohol molecule **65** acts as a trapping agent for the latter, leading to **67** after proton loss, that is, in turn, captured by **DDQ**$^{\bullet-}$ to yield **DDQH**$^{\bullet}$. The latter undergoes HAT from **67**, resulting in the formation of hydroquinone **$DDQH_2$** and the desired functionalized product **66**.

The Lambert group also reported large-scale reactions. In particular, they successfully achieved the benzene-to-phenol (**66g**) hydroxylation reaction in a recirculated continuous flow setup, obtaining a 15 mmol scale reaction with 56% yield in 60 h with the use of three flow channels (Figure 40).

***Benzylic C(sp^3)–H activation*:** The Lambert group reported a C–H amination of alkylarenes **69** under radical ion e-PRC with **TAC**$^+$ to yield either dihydroimidazoles **70** or 2-oxazolines **71** and **71'**, depending on the electrolyte employed (Figure 41A) [162]. The authors proposed that the reaction starts with Ritter-type amination [163,164] of the substrate's benzylic C–H bond. The photoexcited radical dication ***TAC**$^{\bullet2+}$ effects SET oxidation (vide supra, Figure 35B) of the substrate **69a** to its radical cation **69a**$^{\bullet+}$ [165]. Deprotonation and subsequent oxidation of the latter leads to the cation **69**$^+$, the solvolysis of which yields Ritter product **72**. At this point, according to the authors, acetamide **72** likely undergoes a reversible, acid-catalyzed elimination to yield α-methylstyrene **73** (Figure 41B) [166]. The subsequent solvent trapping and oxidation lead to the dihydroimidazole or oxazoline product. With these conditions in hand, dihydroimidazoles **70a–c** were obtained in useful yields using $Et_4N{\cdot}PF_6$ as electrolyte. Interestingly, a simple change of electrolyte ($Et_4N{\cdot}BF_4$ → $LiClO_4$) diverted reactivity toward oxazoline products **71a–c** and **71'd** was observed (Figure 41C). Ac-

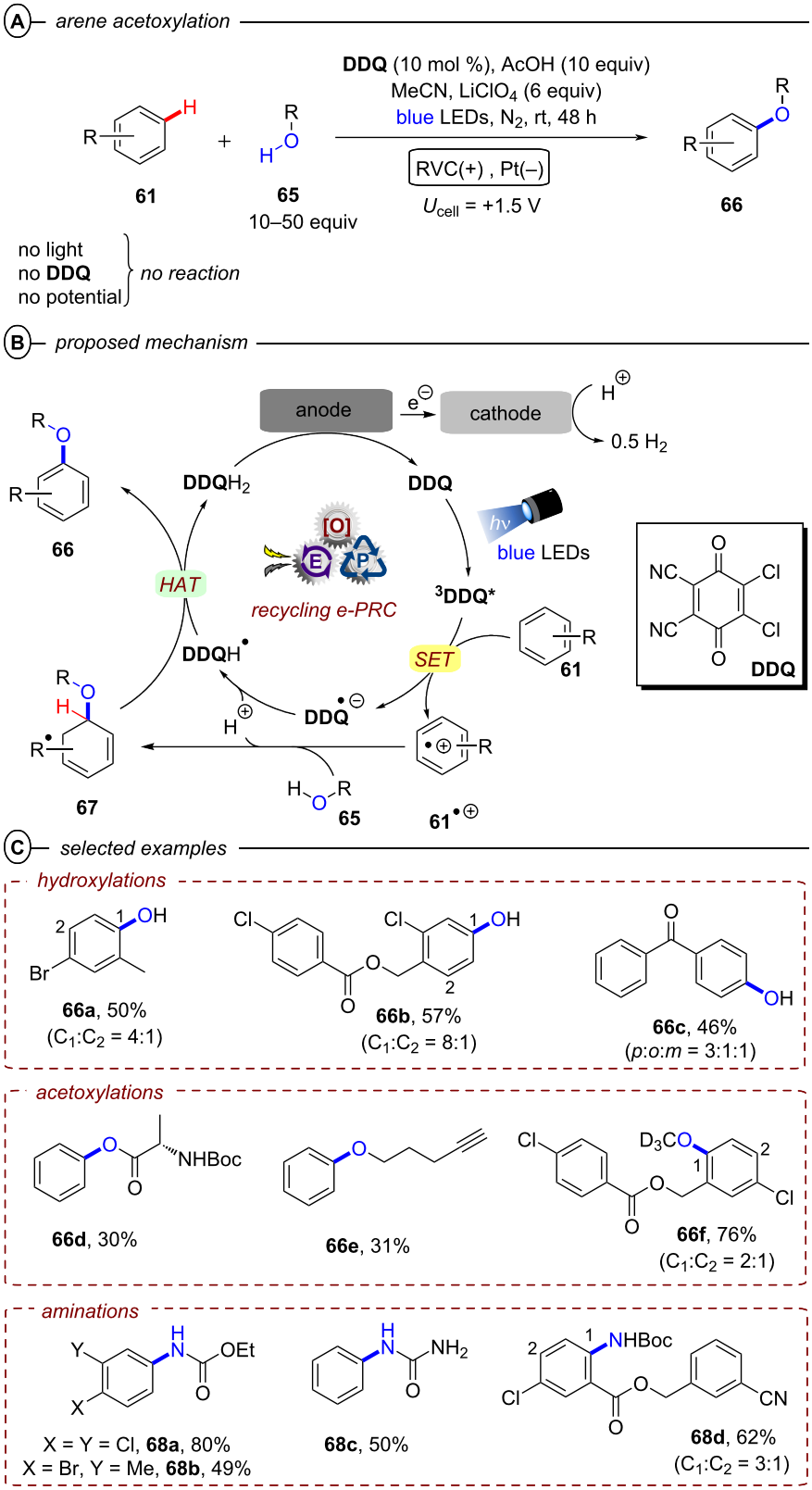

Figure 39: A) Recycling e-PRC C(sp^2)–H acetoxylation of arenes using **DDQ** as a photocatalyst. B) Proposed catalytic cycle. C) Selected examples from the scope.

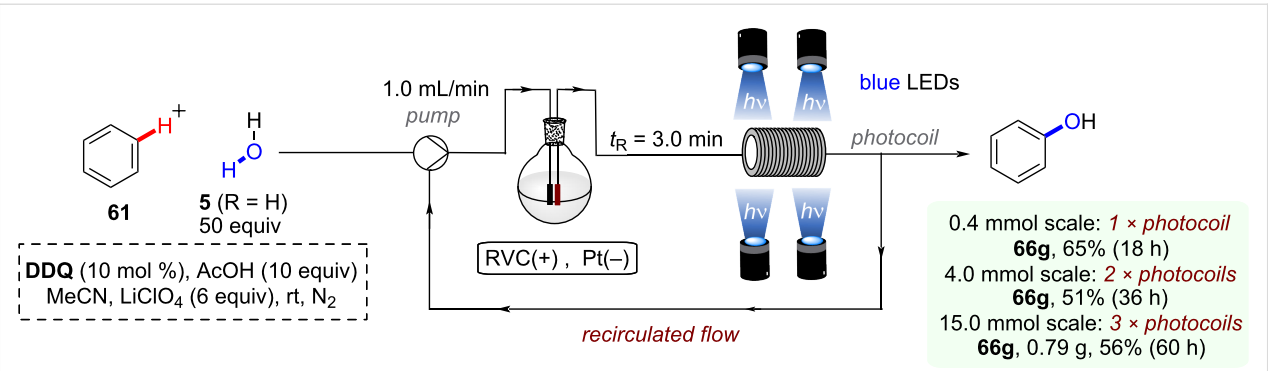

Figure 40: Gram scale hydroxylation of benzene in a recirculated flow setup.

cording to the authors, $LiClO_4$ electrolyte modifies the stability of cationic intermediates and the addition of H_2O to **73**$^{\bullet+}$ or **74** affords **71'** and **71**, respectively (Figure 41B).

Lambert and co-workers extended their radical ion e-PRC protocol toward oxygenation of multiple C–H bonds of alkylarenes simultaneously. This is an especially important target transformation, given the ubiquity of polyoxygenated molecules both in nature and in pharmaceutically active compounds [167-169]. At the same time, undesirable overoxidation reactions are highly likely. The control of oxidative chemoselectivity is also complex, although much progress has been made in the field of directed C–H oxidations [170-172]. The Lambert group found that treating alkylarenes **75** and **76** in the presence of **TAC**$^+$, acetic acid, acetic anhydride and a strong acid like trifluoroacetic acid (TFA) or trifluoromethanesulfonic acid (TfOH) under PEC conditions led to dioxygenated or trioxygenated products **77** and **78** (Figure 42A) [173]. The reactions were carried out in an undivided cell under 5 mA constant current and irradiation by CFL light bulbs. In the mechanism, substrate **76** bearing an arene as a redox-active substituent undergoes SET oxidation by photoexcited radical dication *$\mathbf{TAC}^{\bullet 2+}$, leading to the radical cation **76**$^{\bullet+}$. Following deprotonation and further SET oxidation (by anode or by $\mathbf{TAC}^{\bullet 2+}$) monooxygenated intermediate **79** is generated. Under acidic conditions, **79** undergoes slow and reversible elimination (E_1) to generate olefin **80a** (Figure 42B). Thanks to its conjugation with the arene moiety, **80a** can be further oxidized to form the dioxygenated product **77**. In support of this hypothesis, the reaction of **75** (R^1 = OAc, R^2 = Et) resulted in the formation of its corresponding dioxygenated product in 51% yield under the reaction conditions. Finally, if another C–H bond is present, another elimination/oxidation sequence occurs to yield the trioxygenated species **78** via **80b**. Regarding the reaction scope, the model reaction employed ethylbenzene and used TFA as a proton source, obtaining the product **77a** (Figure 42C). Then, a plethora of unbranched alkylarenes were examined, proving that in some cases a higher yield is obtained with a hydrolytic workup to generate a 1,2-diol like **77b** (the diastereomeric ratio favors the *anti*-isomer).

Once the efficiency of the dioxygenation protocol was established – even employing large scale reactions (2.5 g for **77c**) – the authors expanded the protocol to contiguous C–H trioxygenation within a single reaction flask, that was never reported before. Since E_1-type elimination is the key step in the mechanism, branched substrates were generally employed because they are more prone to elimination processes than unbranched ones, and so more capable to be further oxidized after the initial dioxygenation. Products **78a–f** were obtained in modest to good yields (36–63%) using TfOH as the proton source and **78b** could be accessed on a gram scale (1.86 g) in a scale-up batch experiment. Finally, trifluoroacetamides were exploited as an alternative redox-active substituent. In particular, **81a** was obtained as a mixture of diasteroisomers among which single crystal X-ray analysis confirmed the *cis-trans* stereoisomer as the major one. Moreover, 4-alkylated piperidine derivatives were successfully employed to yield products like **81b**; when comparing to **81a** one can see how the diastereoselectivity was influenced by alkyl substitutents on the piperidine.

Recently, Xu and co-workers published the first example of an asymmetric synthetic PEC reaction, achieving the cyanation of benzylic C–H bonds by employing an additional chiral [Cu] catalyst, formed in situ from $Cu(acac)_2$, TMSCN and a serine-derived bisoxazoline ligand **L1*** [174,175] (Figure 43A) [32]. Anthraquinone-2,6-disulfonate (**AQDS**) was used as a photocatalyst, where authors claimed the disulfonate groups promoted solubility, presumably by decreasing photocatalyst self-aggregation as found by the Barham group for a similar **DCA**-type system [176]. The PEC strategy described represents a key starting point for accessing chiral structures [174,177-180] via activation of benzylic C–H bonds in the absence of chemical oxidants or directing groups [181-183]. According to the

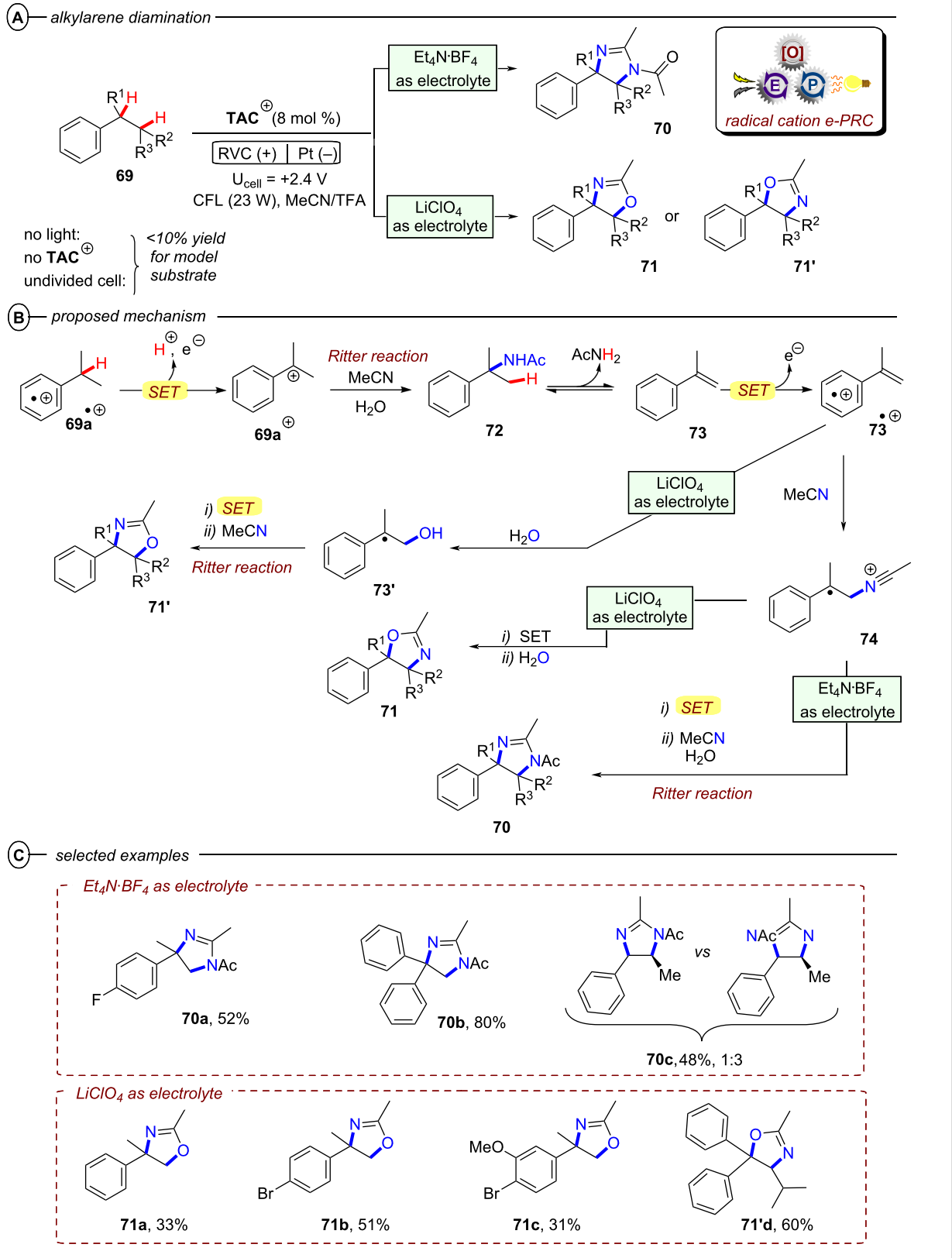

Figure 41: A) Radical ion e-PRC vicinal diamination of alkylarenes using **TAC**$^+$ as an electro-activated photocatalyst. B) Proposed catalytic cycle and electrolyte influence. C) Selected examples from the substrate scope.

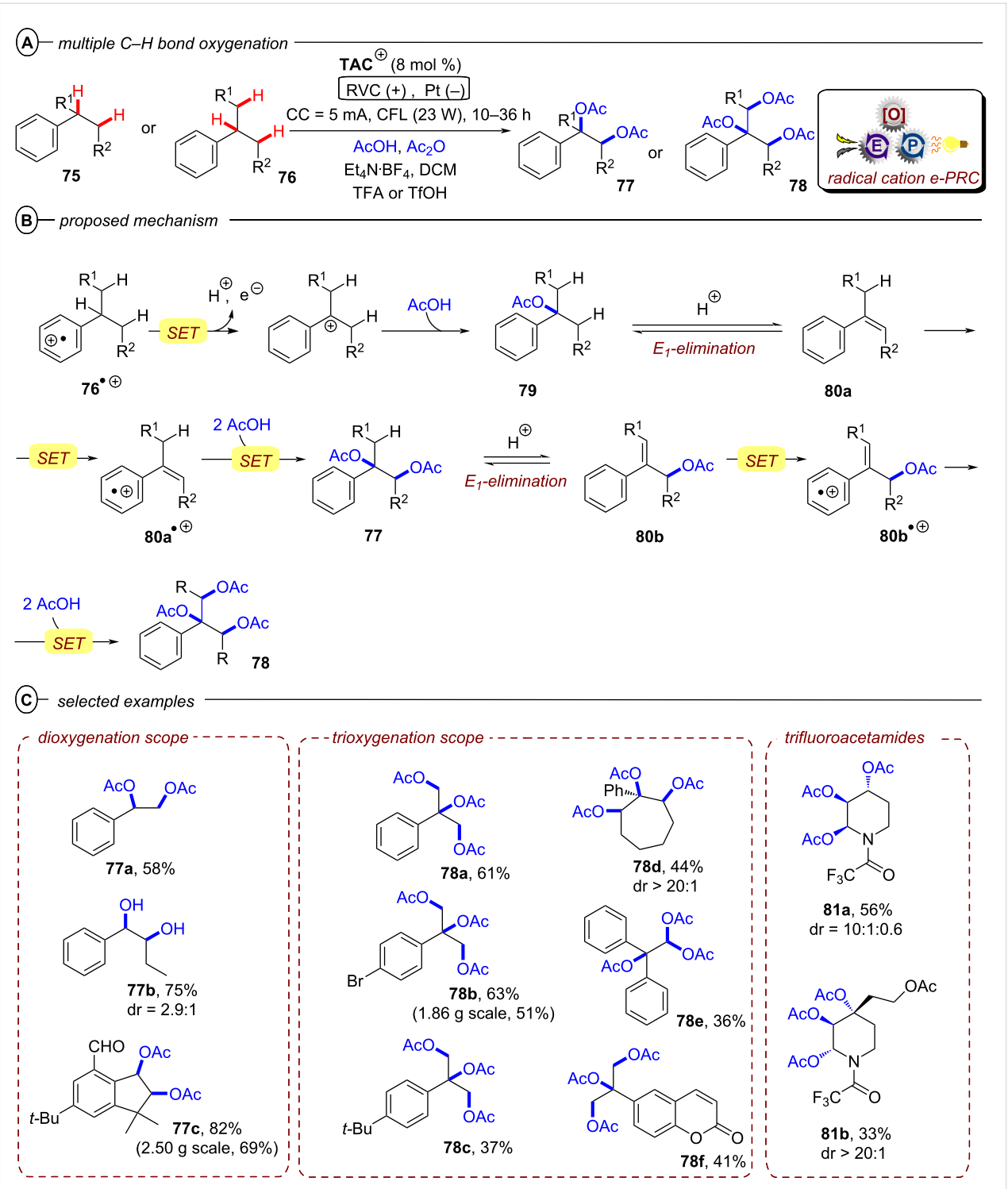

Figure 42: A) Sequential oxygenation of multiple adjacent C–H bonds under radical ion e-PRC using **TAC⁺** as an electro-activated photocatalyst. B) Proposed mechanism. C) Selected examples from the substrate scope.

authors, the high site selectivity derived from cleaving benzylic C–H bonds in a two-step sequential electron transfer/proton transfer mechanism instead of a single step HAT mechanism [184-187]. For the model substrate **82a**, the reaction with (R)-**L1***, the enantiomer of **L1***, was tested, resulting in a comparable result for the enantiomeric product. Also, a gram-scale process was evaluated, yielding **83a** in good yield and enantioselectivity (82% yield and 91% ee). With the optimized

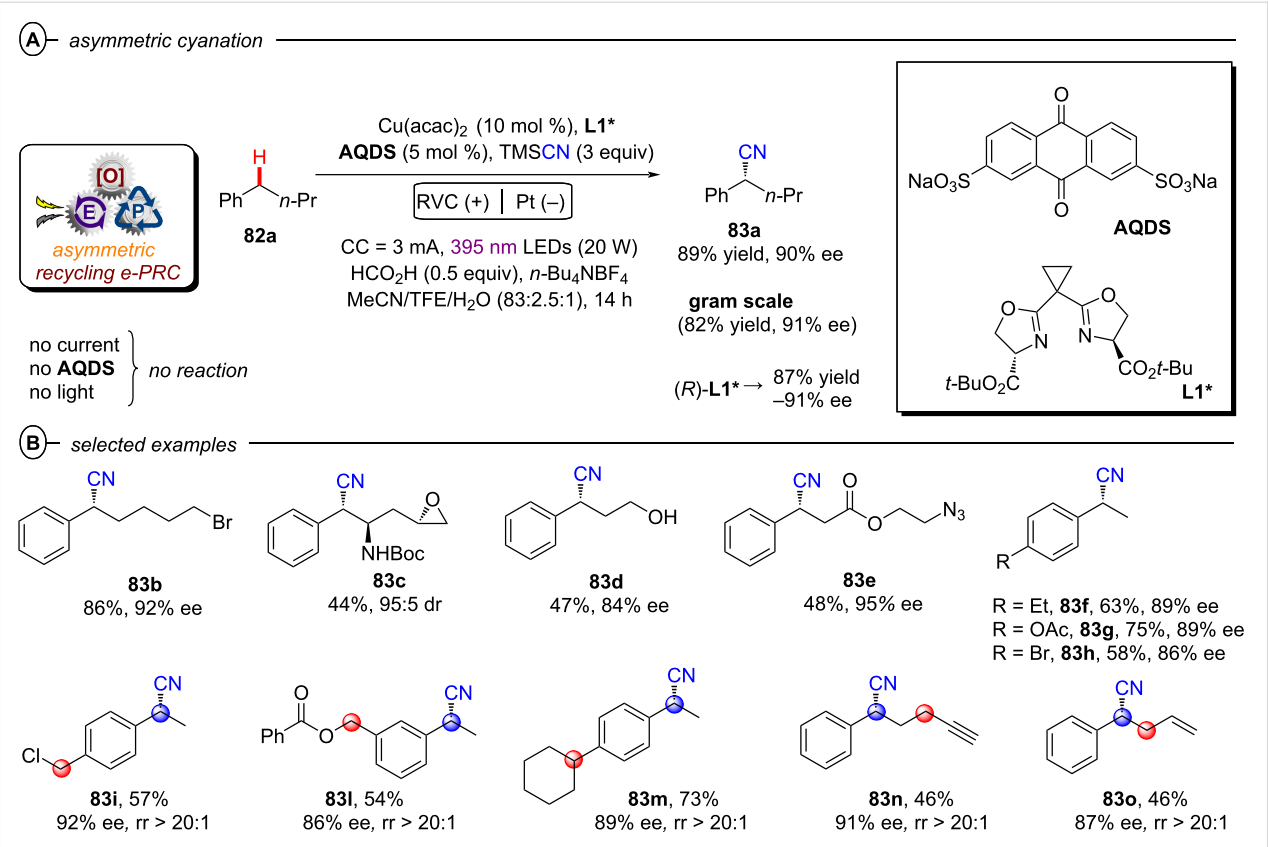

Figure 43: A) Enantioselective recycling e-PRC cyanation of benzylic C–H bonds using **ADQS** as photocatalyst. B) Selected examples from the substrate scope.

conditions in hand, a wide number of substrates were analyzed. Alkyl bromides (**83b**), epoxides (**83c**), alcohols (**83d**) and alkyl azides (**83e**) were all tolerated, resulting in the desired products in moderate to high yields (44–86% in Figure 43B). Once established that the method could be applied to substrates bearing different functional groups, Xu and co-workers shifted their focus to analyze arene electronic properties and substrates with multiple potential reactive C–H bonds. Regarding the first challenge, both electron-rich and electron-deficient alkylarenes were well-tolerated, as evidenced by the results presented in Figure 43B for **83f–h**. Turning to the site selectivity, a preference was found for cyanation of the most electron-rich benzylic position. This preference allowed the functionalization of stronger C(sp^3)–H bonds, such as those in ethyl groups compared to the same secondary benzylic sites weakened with α-electron-withdrawing groups (Cl and acetyl groups in **83i–l**, respectively).

The reaction also displayed selectivity for the less hindered position, as exemplified by the absence of cyanation at the sterically more hindered tertiary benzylic carbon (**83m**) [188-191]. Furthermore, benzylic C(sp^3)–H bonds were favored over their propargylic (**83n**) and allylic (**83o**) counterparts. The proposed mechanism for the enantioselective C(sp^3)–H cyanation is composed of two relay catalytic cycles in tandem: a "site-selective C–H bond cleavage" cycle and an "enantioselective C–C bond formation" cycle (Figure 44). In the former cycle, photoexcitation of **AQDS** generates ***AQDS** as a potent photooxidant ($^*E_{1/2}$ = +2.00 V vs SCE) [192], which engages alkylarene **82** in SET to yield an radical ion pair [$\mathbf{AQDS}^{\bullet-}$, $\mathbf{82}^{\bullet+}$] [193,194]. Proton transfer between these species affords benzylic radical **84** and **AQDS-H**, where oxidation of the latter (by anode or by (**L1***)CuI$(CN)_2$) regenerates the catalyst and liberates a proton. The formation of the benzylic radical intermediate was confirmed by trapping experiments with an allyl sulfone, which gave a benzylic allylation product. At this point, the intermediate **84** is intercepted by the chiral copper complex (**L1***)$Cu^{II}(CN)_2$ to generate a Cu^{III} species **85**, which undergoes enantioselective reductive elimination [185] to yield the benzylic nitrile **83** and the reduced catalyst (**L1***)CuI$(CN)_2$. The latter is promptly oxidized at the anode surface.

In an extension of this method, Xu and co-workers reported a PEC enantioselective decarboxylative cyanation using Ce(OTf) and Cu$(acac)_2$ as catalysts and **L1*** as chiral ligand starting from benzylic carboxylic acid like **86a** (Figure 45A) [33]. In the

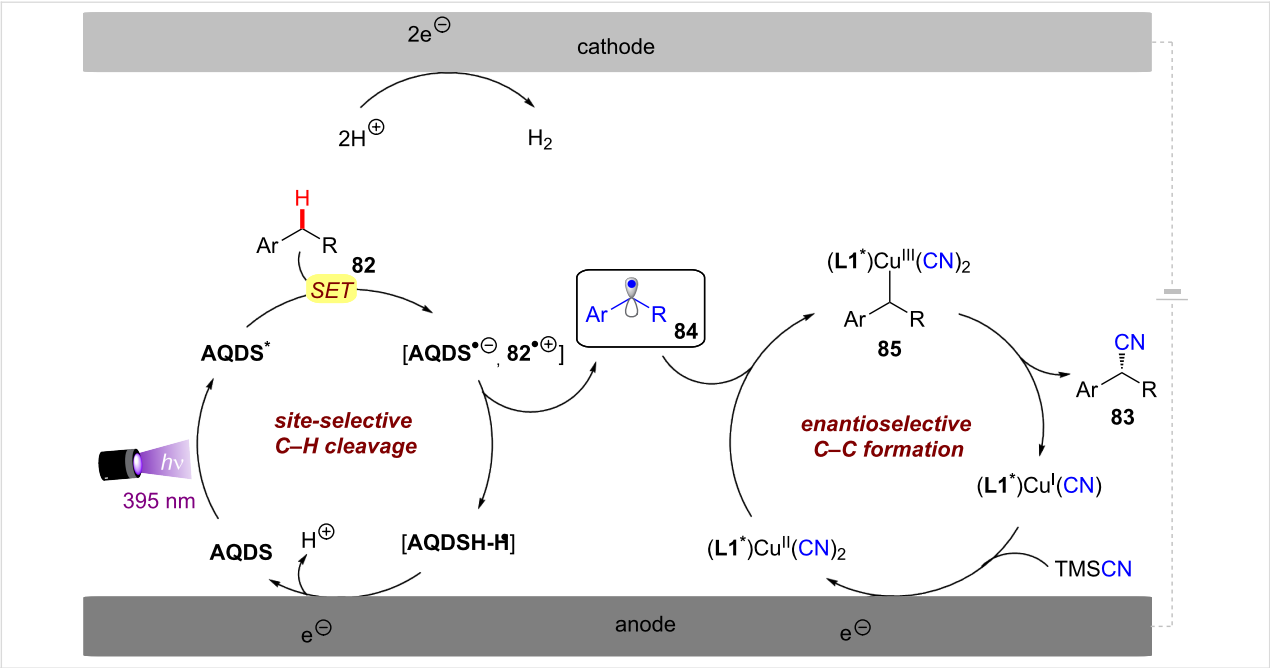

Figure 44: Proposed tandem mechanism by Xu and co-workers.

mechanism, it is well known in the literature that cerium salts are converted to $CeCl_6^{3-}$ in the presence of a chloride source (*n*-Bu_4N·Cl, in this case). The latter is oxidized at the anode to $CeCl_6^{2-}$ (Figure 45B). Then, the coordination of the carboxylate **86** and the photoinduced LMCT process regenerates Ce(III) and leads to the benzylic radical **84**. Thereafter, the radical species then undergoes the same process for enantioselective cyanation proposed in Figure 44, to yield the reaction product **83**.

The scope of the PEC decarboxylation cyanation reaction was then explored with the optimized conditions. In particular, *para*-substituents of varying electronics at the aryl group such as OMe, SMe, and F were all tolerated (**83b'**–**d'**, Figure 45C). Good yields were obtained with *ortho*- and *meta*-substituted rings (**83e'**–**g'**) and also alkyl side chains with substituents (amide and chloride) were compatible (**83h'**,**i'**). A non-benzylic substrate was also tested, resulting in an efficient decarboxylative reaction but with no stereoselectivity (**83l'**). Finally, a gram scale reaction of the model substrate **86a** was conducted to obtain the product **83a'** in 90% yield and 87% ee. It is worth pointing out that an altogether highly similar PEC procedure for asymmetric cyanation has also been reported by Liu and co-workers (Figure 46A) [195]. The authors employed the bis-oxazoline (Box) ligand **L2*** and $Cu(CH_3CN)_4BF_4$ as the catalyst, under constant current conditions with reticulated vitreous carbon (RVC) as the anode and Pt/Ti as the cathode in an undivided cell. As photocatalyst, an array of anthraquinone-type photosensitizers $\mathbf{AQ^R}$ were tested (R = Cl, OMe, Me and CF_3), affording enantioselective cyanation products in good to excellent yields (50–94%) and ee (73–90%) values starting from both electron-rich and electron-poor (hetero)arenes.

Similarly, after the pioneering work of Xu, a closely-related decarboxylative cyanation protocol has been reported by Zhang and co-workers, who employed copper(II) hexafluoroacetylacetonate ($Cu(hfacac)_2$), commercially inexpensive and earth-abundant $CeCl_3$ and the box ligand **L2*** as catalysts (Figure 46B) [196].

***Aryl olefins activation*:** Among the many classical methods used to achieve olefin dioxygenations [197-199], those using transition metals, especially osmium, are undoubtedly the most widely used in organic synthesis [200-205]. However, the problems associated with the use of such transition metals, including issues of toxicity and expense, are widely known. For this reason, there has been a large interest to develop transition metal-free alternative methods that overcome the expense and toxicity of certain metal reagents or catalysts [206-211]. In this regard, electrochemistry has been illustrated as a sustainable synthetic alternative that does not require stoichiometric oxidizing agents [212-215]. Although oftentimes electrochemistry is technically not 'transition metal-free', the metal electrode is a heterogeneous surface that is easily separated post-reaction and reused.

One of the main problems with electrolysis is that applied anodic potential can encourage overoxidation of olefins, leading

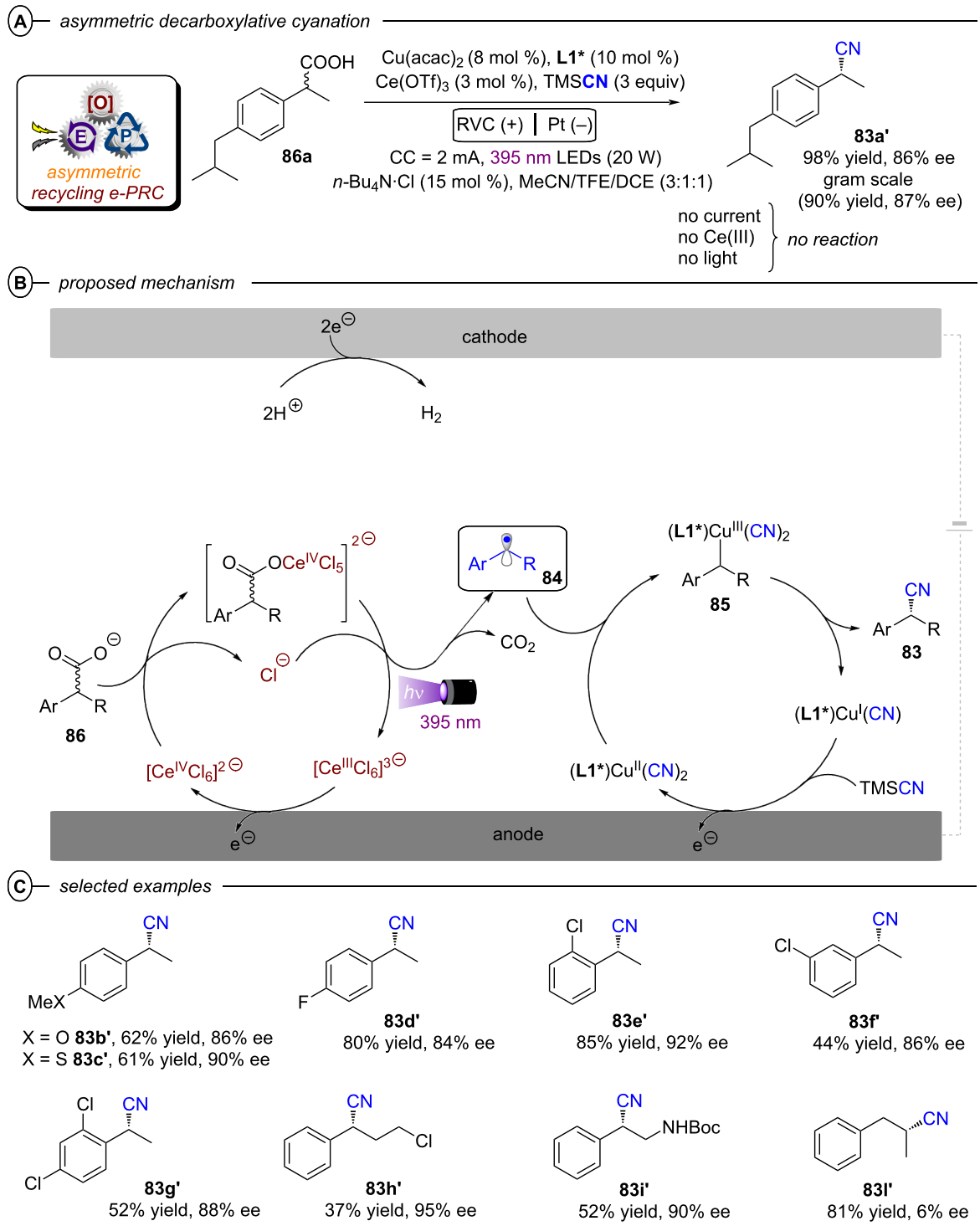

Figure 45: A) Enantioselective recycling e-PRC decarboxylative cyanation using $Cu(acac)_2$, $Ce(OTf)_3$ and a box ligand as catalysts. B) Proposed tandem mechanism. C) Selected examples from the substrate scope.

even to undesirable oligomerization processes. This issue can be easily overcome with e-PRC, where the high requisite potential is generated transiently in the form of a photoexcited state in bulk solution. An initial demonstration of the potential of merging electrochemistry and photochemistry in this field is the acetoxyhydroxylation protocol for aromatic olefins reported by Lambert and Huang (Figure 47A) [216]. They used radical ion e-PRC employing $\mathbf{TAC}^+$ as a catalyst to engage a number of

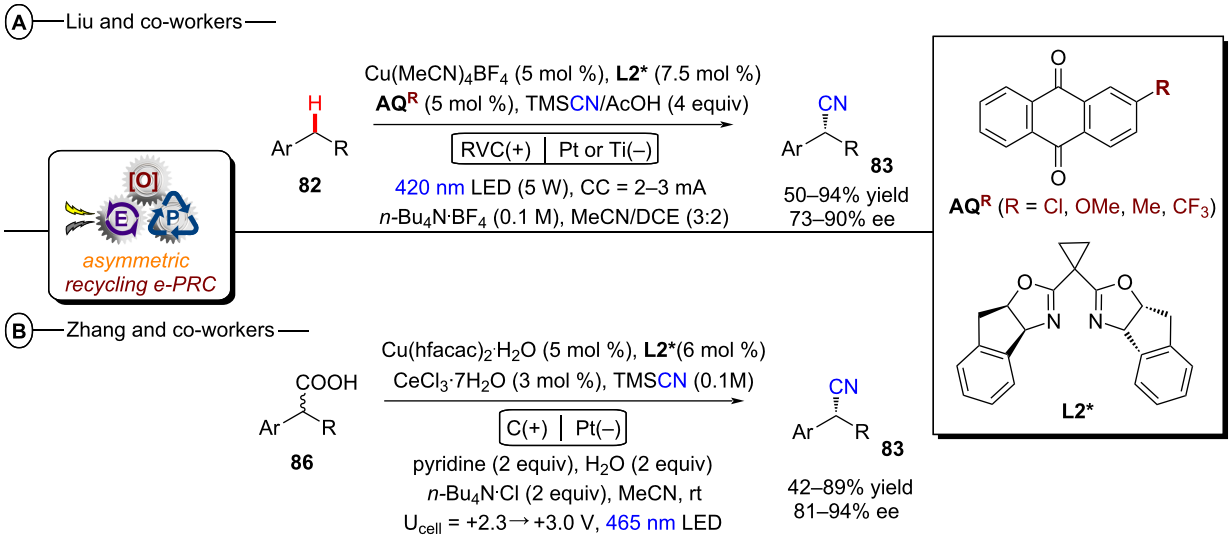

Figure 46: A) Enantioselective recycling e-PRC benzylic cyanation using $Cu(MeCN)_4BF_4$, box ligand and anthraquinone derivatives as catalysts. B) Enantioselective recycling e-PRC decarboxylative cyanation of benzylic carboxylic acids using $Cu(hfacac)_2$, box ligand and $CeCl_3$ as catalysts.

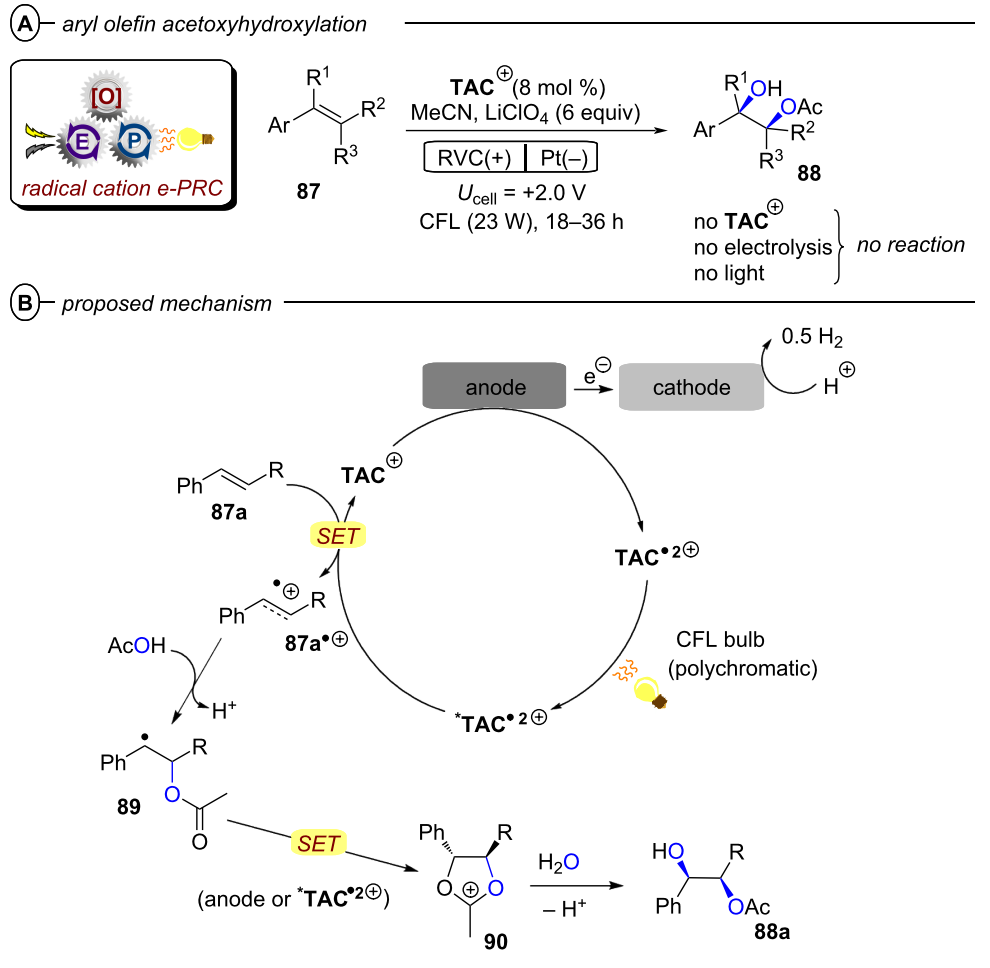

Figure 47: A) Radical ion e-PRC acetoxyhydroxylation of aryl olefins using **TAC⁺** as an electro-activated photocatalyst. B) Proposed mechanism.

activated olefins (benzylic or vinylic substituents), forming acetoxyhydroxylated products **88**. In the mechanism, olefin **87a** is oxidized by ***TAC**$^{\bullet 2+}$ to its radical cation **87a**$^{\bullet +}$. Nucleophilic addition of AcOH to the latter yields benzylic radical **89** (Figure 47B), whose SET oxidation – either by anodic potential or by ***TAC**$^{\bullet 2+}$ – induces an intramolecular cyclization to **90**. Hydrolysis of the cyclic intermediate releases the reaction product **88a**. The optimized conditions allowed hydroxyacetoxylation of different kind of cyclic alkenes with high levels of *syn*-diastereoselectivity (**88b**–**g**, Figure 48), demonstrating the method's formidable tolerance to a range of electronically different substituents and even for conjugated systems such as **88e**. Benzylic groups, alcohols and aldehydes were all tolerated (**88h**–**l**). For open-chain substrates a boronic ester, a product-bearing styrene and different heterocycles including furan and indole were all well-tolerated in the syntheses of **88m**–**p**. In addition to the use of acetic acid to generate hydroxyacetate products, the authors tested other acids, obtaining the products **88q**,**r** in good to high yields (55–80%). Finally, scalability of the method was demonstrated up to multigram scales (up to 50 mmol) via a continuous flow approach. Multigram quantities of products **88b** (8.44 g), **88s** (2.16 g) and **88t** (3.73 g) were accessed using a recirculated flow setup depicted in Figure 49, in which the solution was circulated through Teflon tubes exposed to three CFL bulbs for 20–38 h with a residence time of 3 minutes 'per pass'.

Lambert's group also described a method for the regiodivergent aminooxygenation of aryl olefins under similar PEC conditions with **TAC**$^{+}$ as catalyst (Figure 50A) [217]. This protocol forms aryl-substituted 1,2-aminoalcohols of both regioisomeric configurations **91** and **92** that are important architectural motifs in many complex molecules [218], including natural products [219,220], chiral auxiliaries and ligands [221]. In the proposed mechanism (Figure 50B), oxidative SET activation of alkene **87b** occurs by the electrochemically activated ***TAC**$^{\bullet 2+}$. Radical cation **87b**$^{\bullet +}$ can be trapped by water leading to the radical **94a**, whose SET oxidation (either by ***TAC**$^{\bullet 2+}$ or the anode) and nucleophilic trapping by MeCN yields the intermediate **96a** through the intermediate **95a** (Figure 50C). Intramolecular addition of the hydroxyl group to the nitrilium ion leads to the oxazoline product **91a**. According to the authors, water is competitive as the second nucleophile, leading to formation of diol **97a**, particularly when present in large excess (dashed grey path in Figure 50B). On the other hand, the use of urethane **93** as nucleophile instead of water leads to the formation of radical **98a** via trapping of radical cation **87b**$^{\bullet +}$. Oxidation of **98a** leads to cyclization at the carbamate carbonyl oxygen, furnishing product **92a**. For the reaction with water as nucleophile, various cyclic and acyclic alkenes were found to undergo efficient aminooxygenations with high levels of *syn* diastereoselectivity (**91b**–**d,** Figure 50C) and in good yields (58–61%). Furthermore, reaction conditions were well-tolerated by a wide range

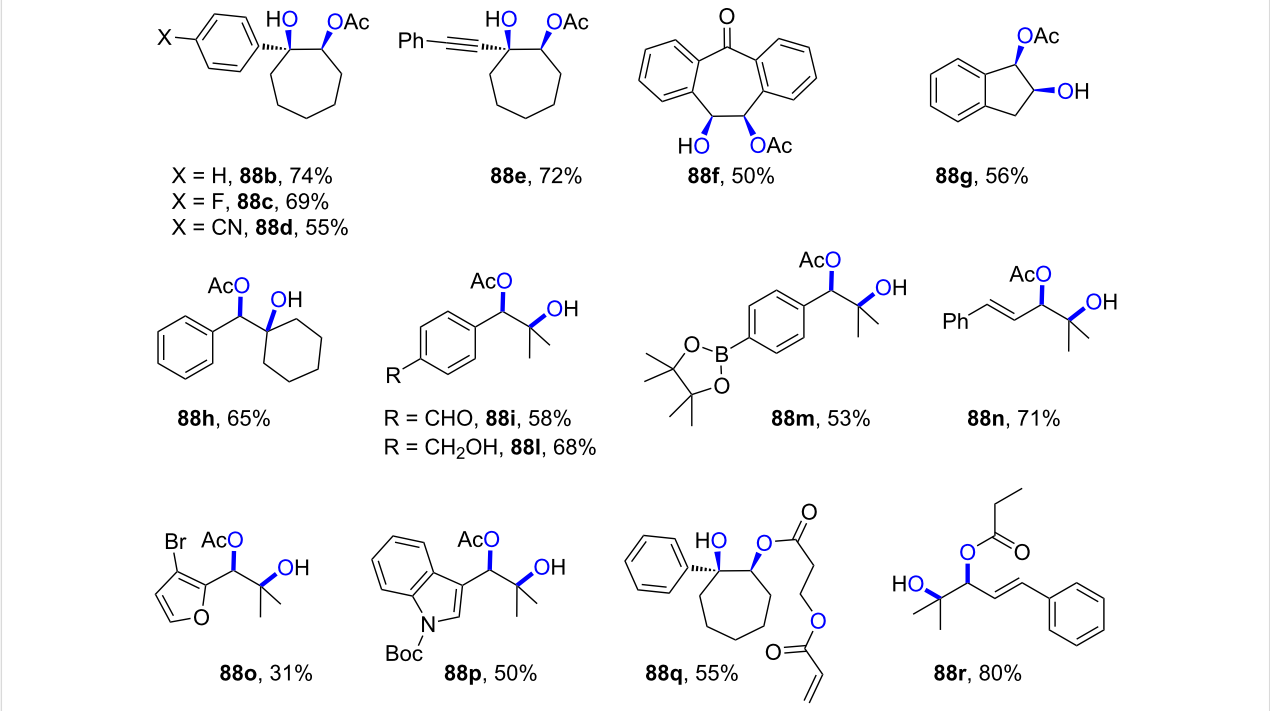

Figure 48: Selected examples from the substrate scope.

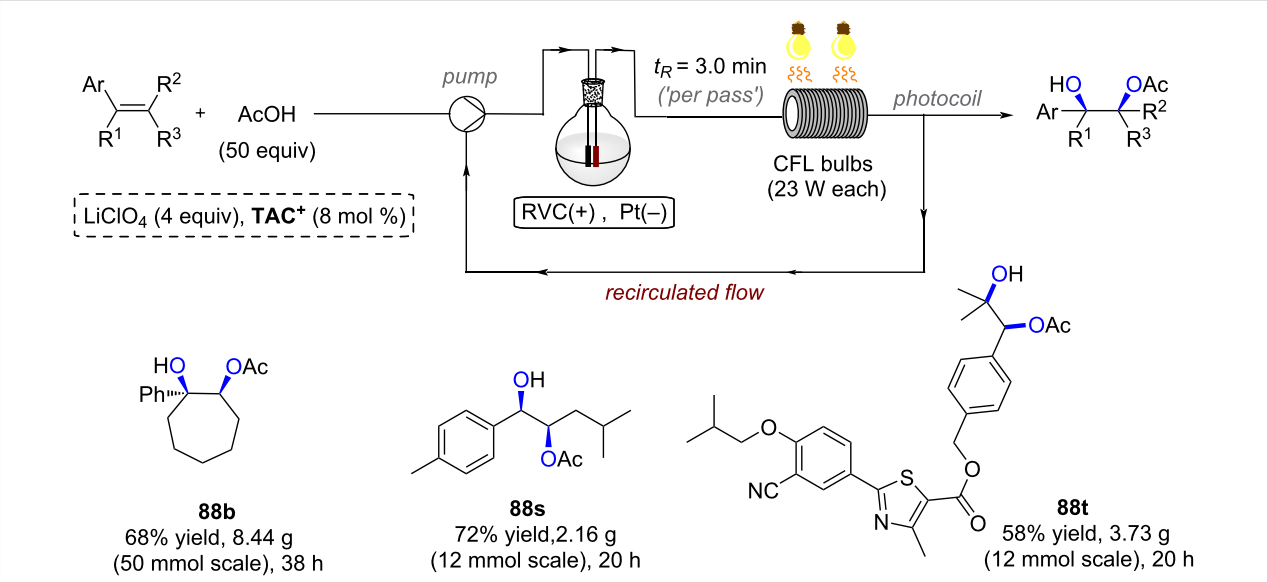

Figure 49: Photoelectrochemical acetoxyhydroxylation in a recirculated flow setup.

of aryl olefins bearing different functional groups, such as fluorine and alkyne (**91e**,**f**). An intriguing example from the scope involves the utilization of 1,3-dienes as the starting material, which exclusively undergoes functionalization at the olefin position distant from the aromatic ring (**91g**,**h**). The authors then switched the focus to the regioisomeric products **92** using **93** as reactant. Again, a variety of 1,2-disubstituted and trisubstituted were tested (**92b–f**, Figure 50C), leading to the products in good to high yields (65–86%).

3.1.2 Heteroarene activation: The radical-mediated C–H Minisci-type [222] functionalization of heteroarenes like **99** enables rapid construction of 2-alkyl-substituted heteroaromatic building blocks [223], which are found in a variety of natural products, organic materials, small molecule drugs, and ligands [224]. Carbon-centered radicals can be generated under photoelectrochemical conditions from various precursors. In one of the seminal examples of contemporary synthetic PEC, Xu and co-workers used trifluoroborates under recycling PRC conditions with Fukuzumi's catalyst [225] ***Mes-Acr**$^+$ (Figure 51A) [226]. As aforementioned (vide supra, Figure 34B), irradiation of **Mes-Acr**$^+$ produces its highly oxidizing photoexcited state, ***Mes-Acr**$^+$ ($^*E_{1/2}$ = +2.06 V vs SCE) [227-229]. SET between the latter and organotrifluoroborate **100** generates the acridinyl radical **Mes-Acr**$^•$ and an alkyl radical (Figure 51B) [230]. **Mes-Acr**$^•$ is then oxidized on the anode surface to regenerate **Mes-Acr**$^+$ in the typical recycling e-PRC manifold. The resulting alkyl radical adds to the protonated heteroarene **99**-H at the 2-position to give the radical cation **102a**, which is then deprotonated affording a C-radical intermediate **103a** [231]. A subsequent deprotonation affords the desired protonated product **101a**-H. A large range of heteroarenes were used as radical acceptors, including isoquinolines, phenanthridines, phthalazines, benzothiazoles acridines and purines (**41a–e**, Figure 51C). The conditions employed tolerated amine, alcohol, olefin and alkyne functional groups, in both the heterocyclic partner and radical precursor.

Carbon-centered radicals can be also directly generated from carboxylic acids, which are inexpensive, stable and nontoxic feedstocks [89,232-236]. The carboxylate group upon oxidative SET evolves in the form of CO_2, thus acting as a traceless leaving group. Xu and co-workers leveraged this by reporting a decarboxylative C–H alkylation of heteroarenes **99** under PEC conditions with $CeCl_3·7H_2O$ as catalyst (Figure 52A) [237]. The reaction begins with the anodic oxidation of the catalytic precursor Ce^{III} to Ce^{IV}, followed by the coordination of the latter by the carboxylic acid **104a** to form complex **104a'** (Figure 52B).

Upon photoexcitation, **104a'** undergoes a ligand–metal charge transfer (LMCT) and cleavage to regenerate Ce^{III} and yield carboxyl radical **105a**, which decarboxylates leading to alkyl radical **106a** [238,239]. Addition of the resulting alkyl radical to protonated **99**-H at the 2- position affords radical cation **107**. This transient species loses a proton to give radical **108**, whose SET oxidation furnishes the protonated product **101f**-H. Several different examples of carboxylic acids were tolerated by the reaction conditions (primary, secondary, tertiary, α-alkoxy and aliphatic, **101f–j** in Figure 52C). A limitation is that the 4-position of the heteroarene must be blocked to prevent competing radical addition.

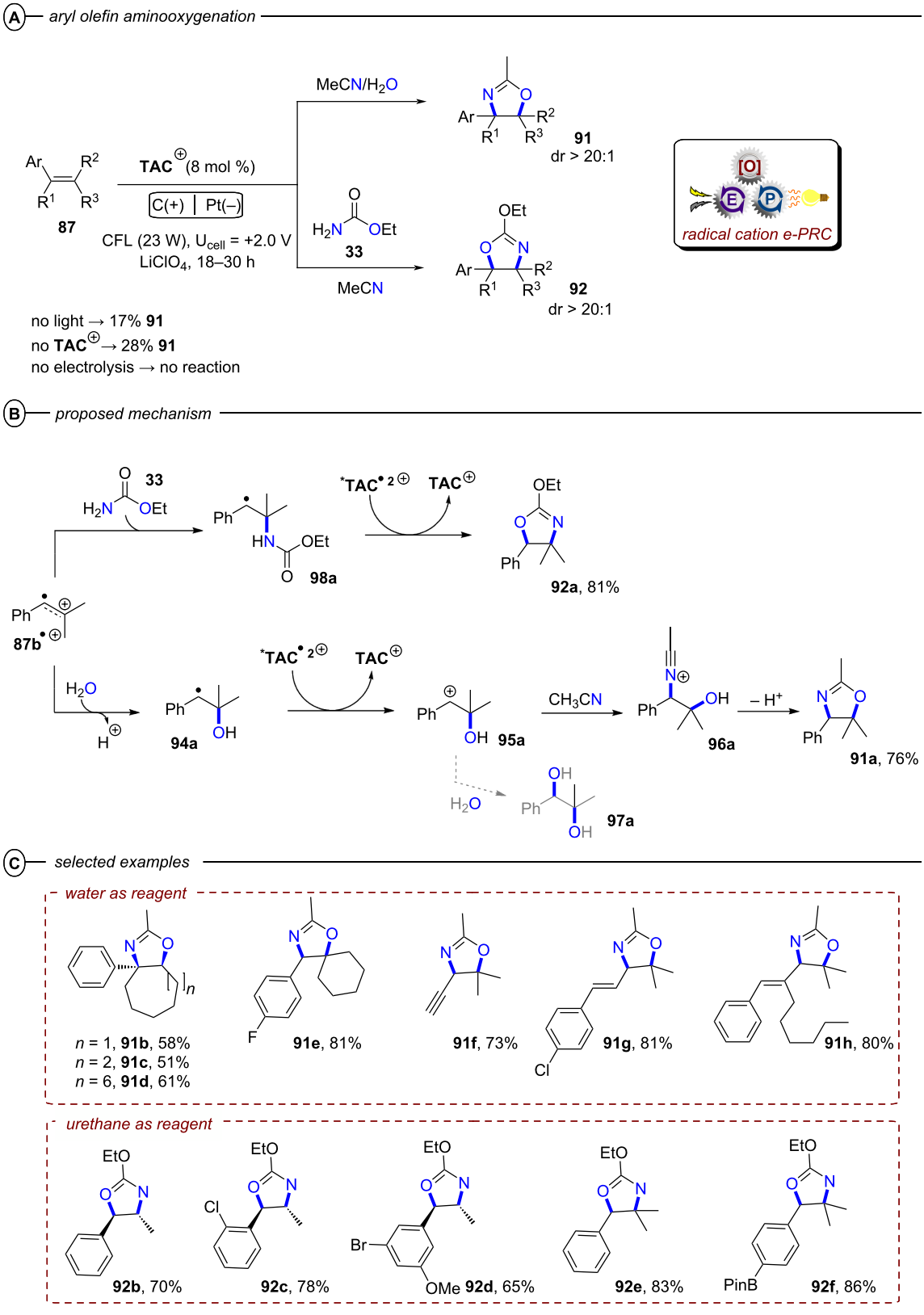

Figure 50: A) Radical ion e-PRC aminooxygenation of aryl olefins using **TAC⁺** as an electro-activated photocatalyst. B) Proposed mechanism for the synthesis of oxazolines and the influence of nucleophile. C) Selected examples from the scope.

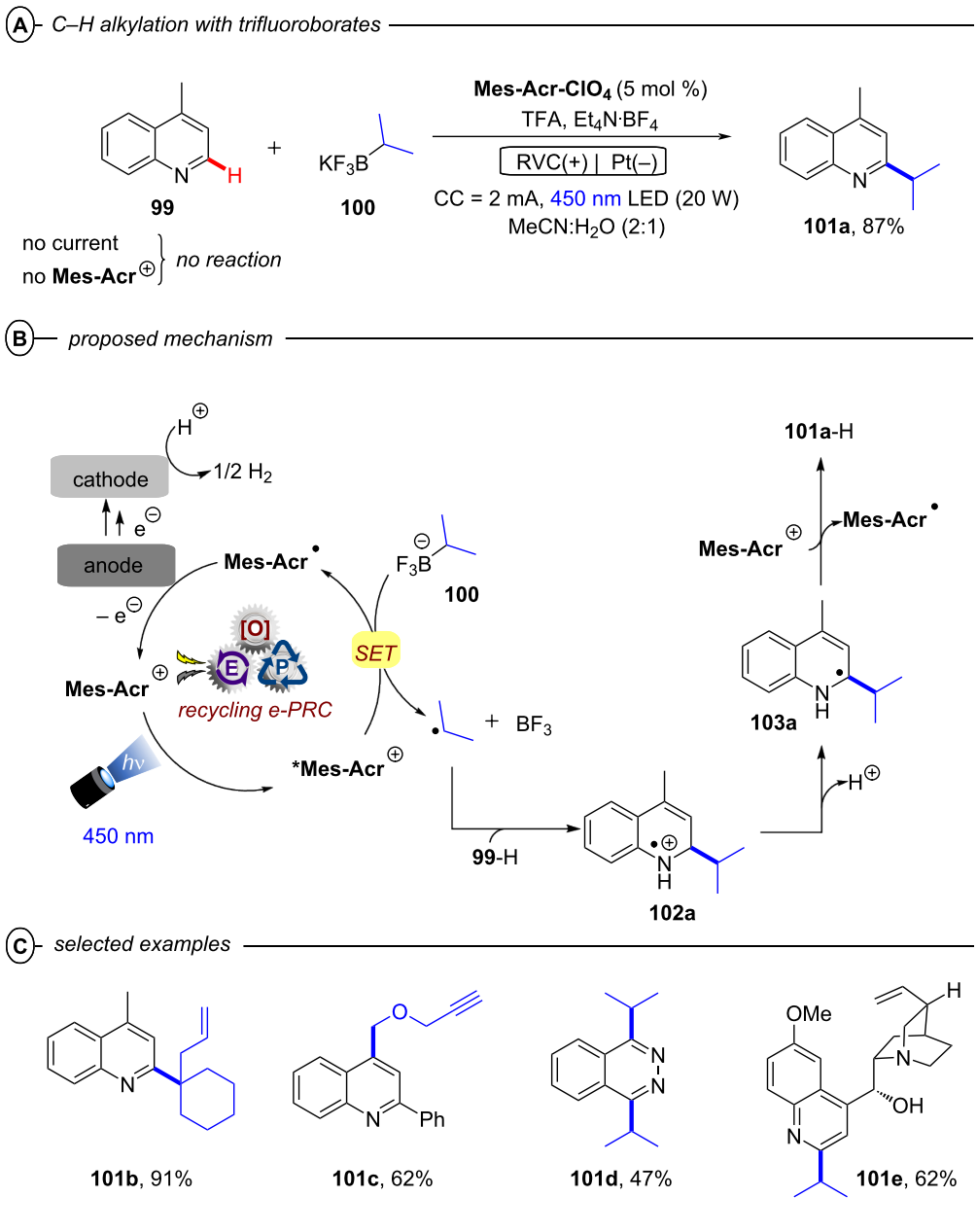

Figure 51: A) Recycling e-PRC C–H alkylation of heteroarenes with organic trifluoroborates using **Mes-Acr**$^+$ as photocatalyst. B) Proposed catalytic cycle. C) Selected examples from the substrate scope.

A very similar protocol was reported by the Wang's group [240], which employs a Fe^{II}-based photoredox catalyst for decarboxylative C–H alkylation of quinoxalin-2(1*H*)-ones **109** (Figure 53A). The initial stages of the mechanism involve, as observed for cerium (vide supra), the generation of the photoactive Fe^{III}–carboxylate complex **104b'** (Figure 53B) [99]. The photoinduced (435–445 nm) LMCT process leads to **105b**, the precursor of the reactive alkyl radical **106b** via decarboxylation. The C-centered radical was observed by HRMS via TEMPO or BHT radical trapping experiments when R = adamantyl. Coupling of this radical with **109** generates intermediate **111**, which via a 1,2-*H* shift yields **112**. Finally, anodic oxidation and deprotonation affords the reaction product **110**. Different radical acceptors with halogenated (F, Cl and Br) aromatic rings were well-tolerated under the reaction conditions, resulting in products **110b–d** in high yields (82–91%, Figure 53C). Both secondary and tertiary alkyl carboxylic acids led to desired products **110e–g** in good to excellent yields (63–91%).

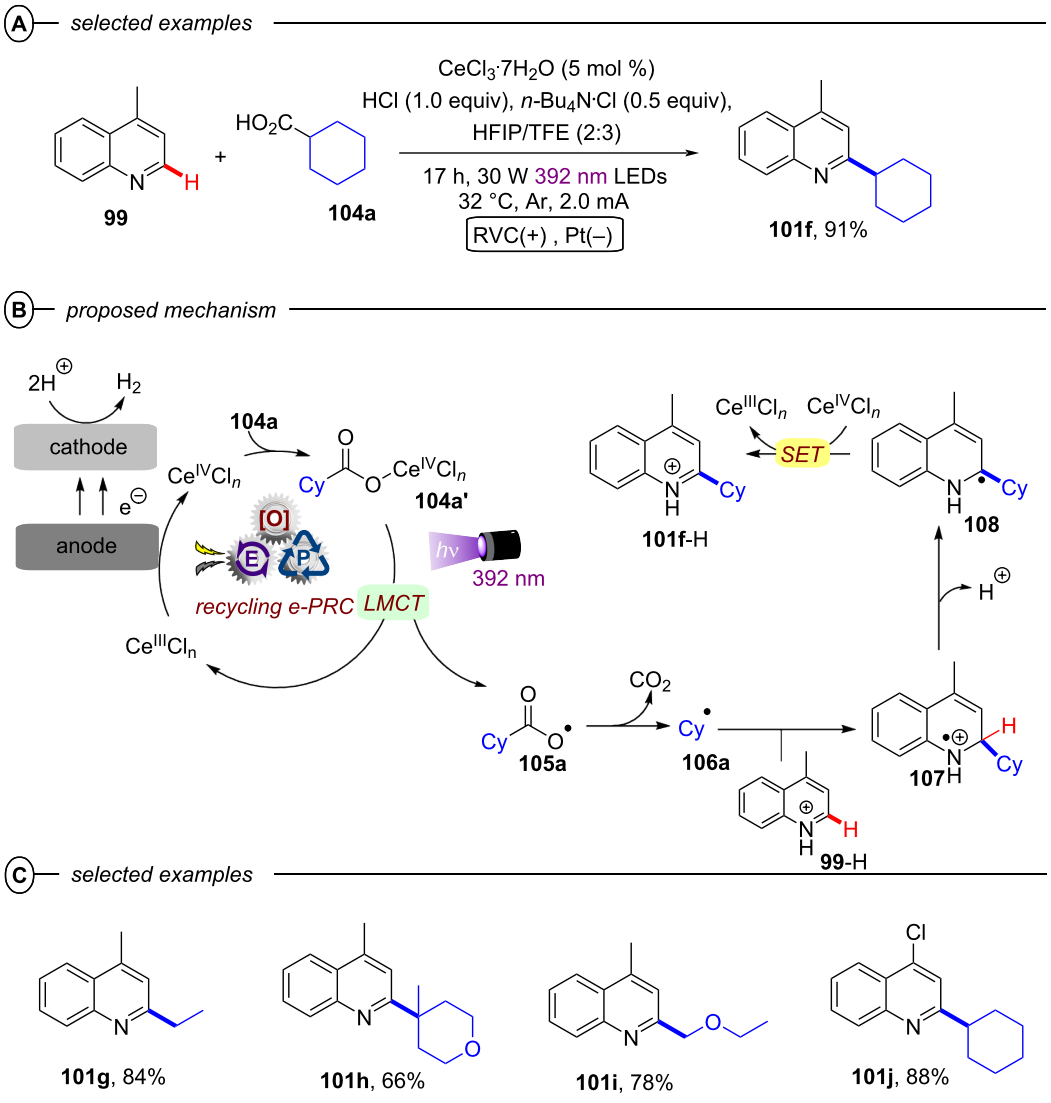

Figure 52: A) Recycling e-PRC decarboxylative C–H alkylation of heteroarenes using $CeCl_3·7H_2O$ as catalyst. B) Proposed mechanism. C) Selected examples from the substrate scope.

The reports of Xu and co-workers as well as Wang and co-workers prove that LMCT is an effective, economical and eco-friendly strategy for homolytic cleavage of complexes of earth-abundant first-row and lanthanide metals such as Ni, Cu, Fe and Ce, to generate reactive radicals for couplings under PEC conditions [241], as well as under conPET conditions (vide supra, Figure 20, Fe-based catalyst).

Xu and co-workers extended their previous alkylation method (vide supra, Figure 52) to alkyl oxalates **113** as precursors to alkyl radicals in the absence of any transition metal catalyst (Figure 54A) [242]. The alkyl oxalate **113a** reductively quenches the photoexcited catalyst ***4CzIPN** ($*E_{1/2}$ = +1.35 V vs SCE) to afford **4CzIPN**$^{•-}$ and the alkyl radical **106c** after double decarboxylation (Figure 54B) [243]. Addition of the latter to the protonated heterocycle **99**-H produces radical cation **107**, which undergoes an SET reduction by **4CzIPN**$^{•-}$ to obtain 1,2-dihydroquinoline **114** with concomitant regeneration of catalyst. Lastly, **114** is SET oxidated at the anode to furnish product **101f**-H. While the reaction was suitable for various examples of secondary and tertiary oxalates (**101k–o**, Figure 54C), primary oxalates were ineffective alkyl radical precursors.

Xu's group also deepened the application of decarboxylative radical formation in a PEC carbamoylation of heteroarenes

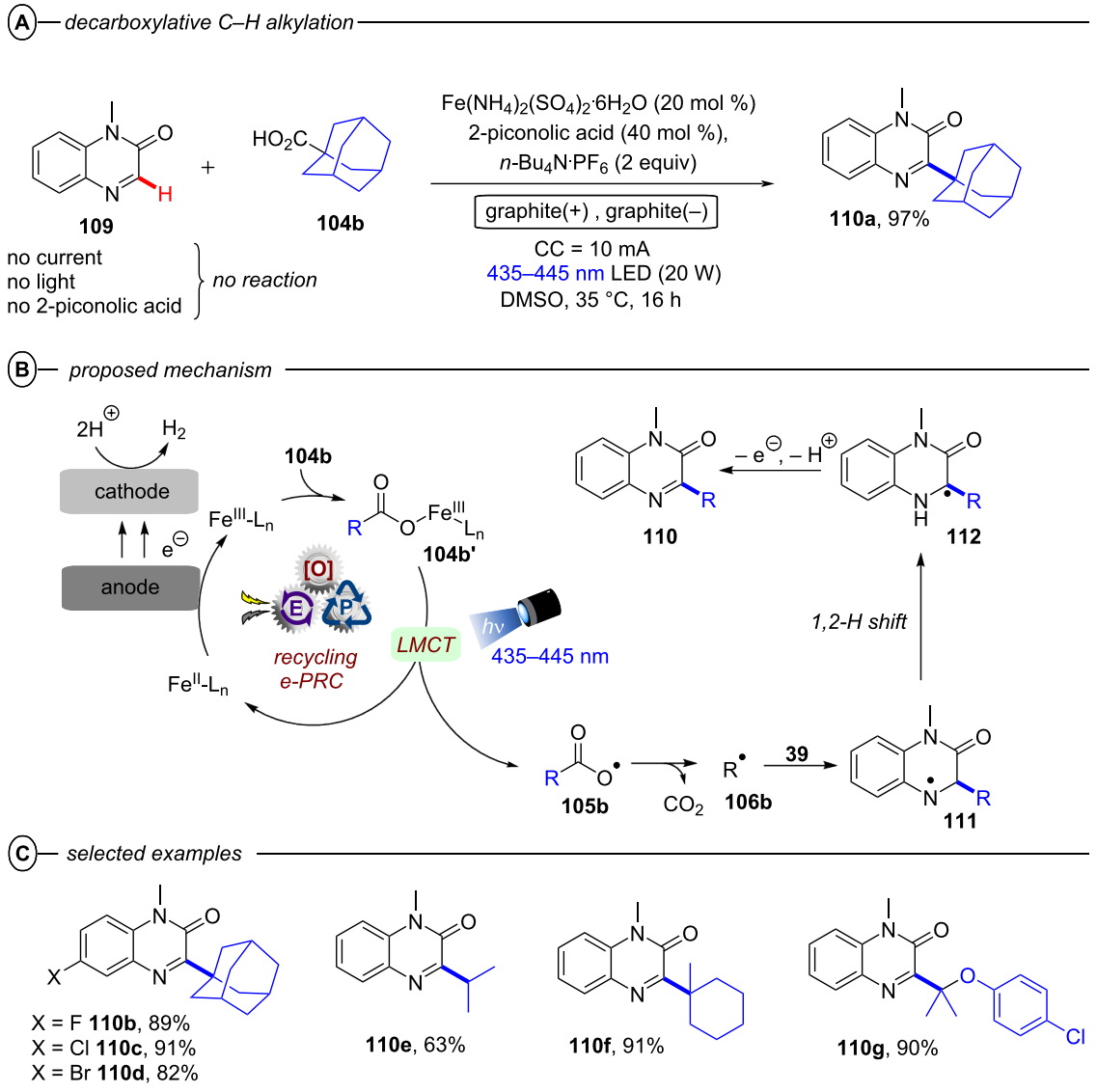

Figure 53: A) Recycling e-PRC decarboxylative C–H alkylation of heteroarenes using $Fe(NH_4)_2(SO_4)_2·6H_2O$ as catalyst. B) Proposed mechanism. C) Selected examples from the substrate scope.

using **4CzIPN** as photocatalyst (Figure 55A) [237]. The latter, upon photoexcitation (455 nm), oxidates the oxamate **115** in a SET process leading to the carbamoyl radical **117** through decarboxylation (Figure 55B). The reactive radical adds to protonated heteroarene **99**-H resulting in radical cation **118**, SET reduction of which (by **4CzIPN**$^{\bullet-}$, or by the cathode) affords **119**. The latter intermediate was detected in a HRMS experiment when R = NHCy. Finally, oxidation of dihydroquinoline **119** yielded the protonated product **56**-H. Alternatively, the authors proposed deprotonation of **118** affords radical **120** which could be oxidized by ground-state **4CzIPN** or by the anode (grey dashed mechanism). The substrate scope featured various examples of oxamic acids (bearing primary, secondary and tertiary *N*-substituents) and various electron-deficient N-heteroarenes (affording compounds such as **116b–e**) (Figure 55C).

Another important vehicle to access Minisci reactive pathways is a direct C(sp^3)–H bond activation via HAT, a method capable to generate radicals that are hard to obtain from photocatalytic SET or electrochemical transformations [244-246]. Conceptually relating to the conPET report of Meyer, Hu and co-workers (vide supra, Figure 33), the Xu group utilized PEC to access chlorine radicals (Cl$^{\bullet}$) under remarkably accessible reaction conditions, furnishing HAT agents to afford C(sp^2)–H alkylations of heterocycles like 2-phenylquinoline

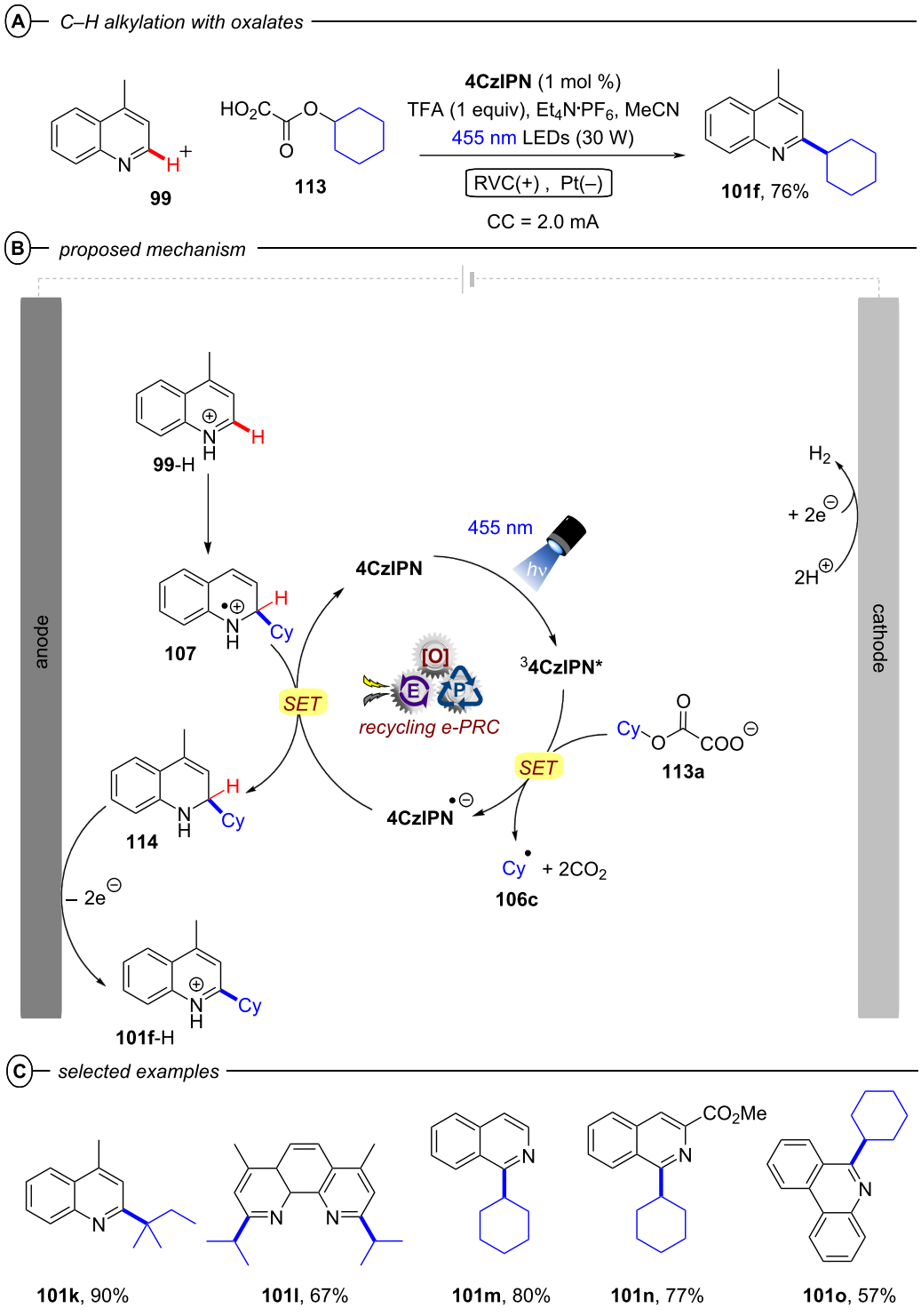

Figure 54: A) Recycling e-PRC C–H alkylation of heteroarenes with alkyl oxalates and **4CzIPN** as photocatalyst. B) Proposed mechanism. C) Selected examples from the substrate scope.

121 (Figure 56A) [141]. Anodic oxidation of chloride generates chlorine (Cl_2). Subsequential light irradiation homolytically cleaves Cl_2 (Figure 56B) and regulates a steady-state concentration of $Cl^{\bullet}$ [247]. Then, $Cl^{\bullet}$ engages unactivated C(sp^3)–H bonds such as those of cyclohexane (**122a**), affording C-radicals (such as **122a**$^{\bullet}$).

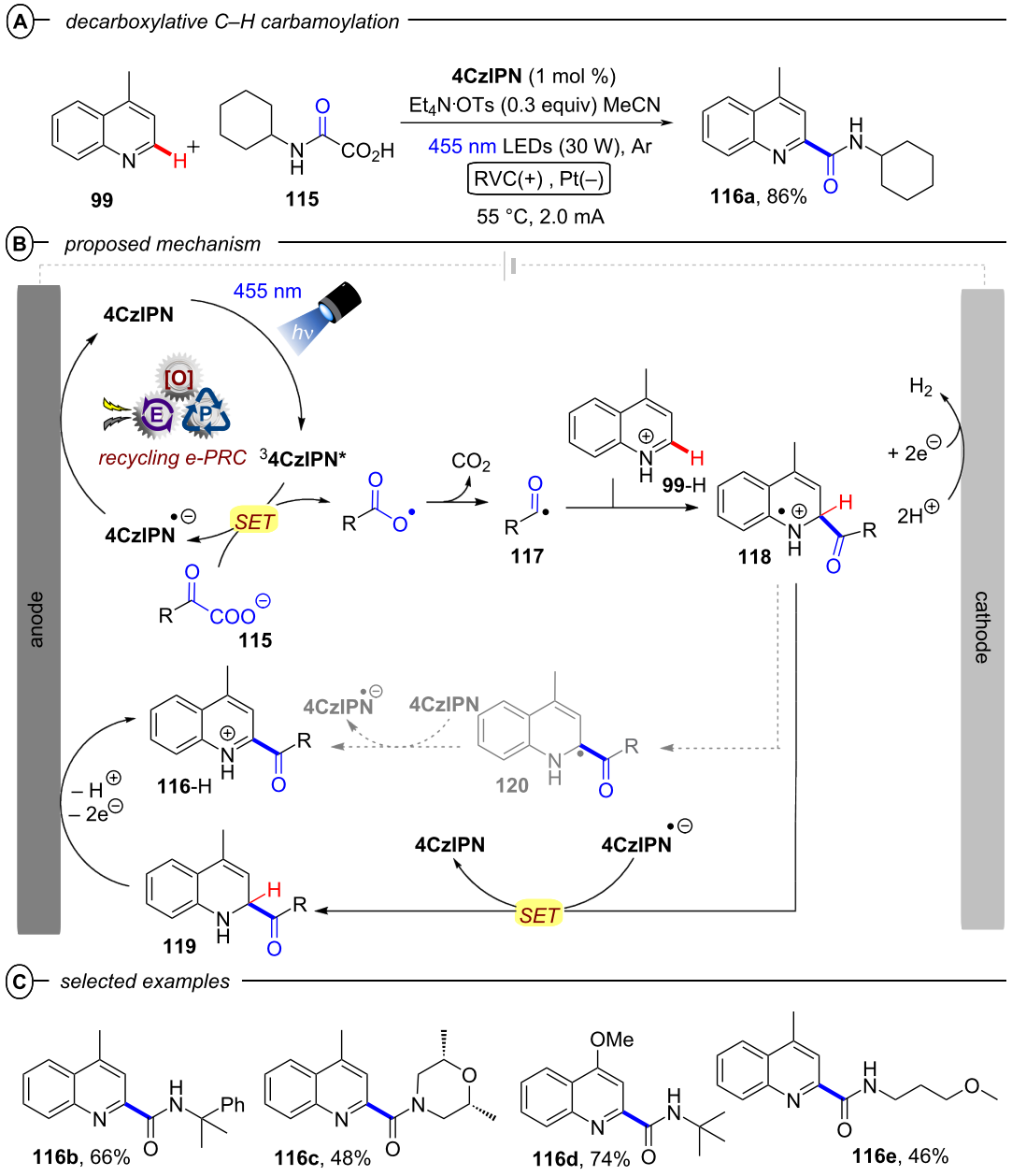

Figure 55: A) Recycling e-PRC decarboxylative C–H carbamoylation of heteroarenes using **4CzIPN** as photocatalyst. B) Proposed mechanism. C) Selected examples from the substrate scope.

The high bond dissociation enthalpy (BDE) of HCl (102 kcal mol^{-1}) ensures that $Cl^{\bullet}$ can react with a plethora of activated and unactivated aliphatic C–H bonds [139,140,248-250]. The C-radical reacts with the heteroaromatic compound **121** to yield a radical cation intermediate **123**, which can then undergo rearomatization to furnish the protonated product **101p**-H. Corroborating the intermediacy of a cyclohexanyl radical, the authors conducted a control experiment using an allylic phenyl sulfone **121'** as reactant and detected the allylic radical substitution product **101'** (Figure 56C). Continuous generation of Cl_2 by anodic oxidation and its photolysis avoids the direct use of toxic Cl_2 gas and regulates a manageable low concentration at any given time [251].

The substrate scope was relatively broad with regard to both radical precursors and heteroarenes, tolerating many sensitive functional groups and affording products such as **101q–w** generally in moderate to high yields (45–83%) (Figure 57A). The

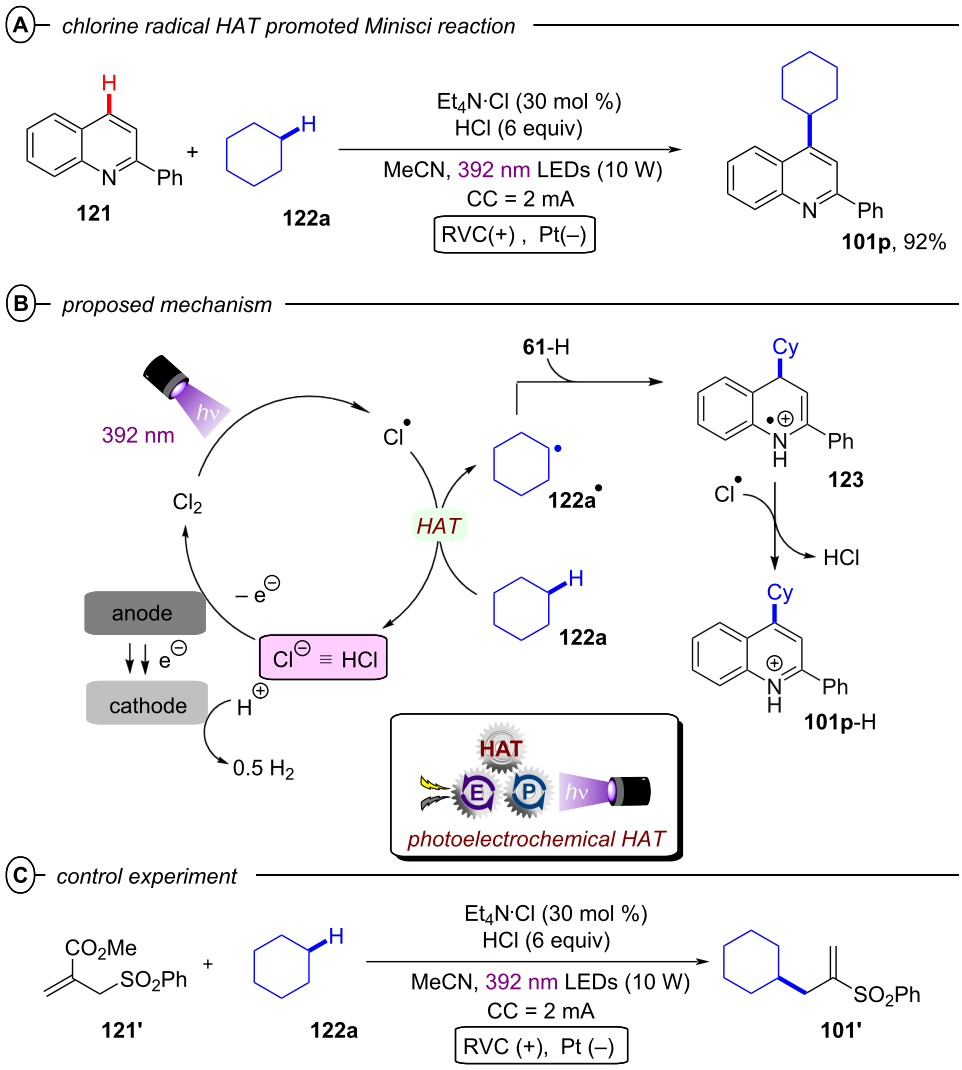

Figure 56: A) Photoelectrochemical HAT-mediated hydrocarbon activation via the chlorine radical. B) Proposed mechanism. C) Trapping experiment of the proposed radical with an allylic sulfone.

authors achieved synthesis of **101z** on a gram and even decagram scale by employing a recirculated semi-continuous flow setup (Figure 57B).

A seminal report in the photoelectrochemical HAT field was made by Ravelli and co-workers in a cross-dehydrogenative coupling (CDC) of benziothiazoles **124** and aliphatic C–H bonds (e.g., cyclohexane **122a** in Figure 58A) [252] using tetrabutylammonium decatungstate (**TBADT**, $(n\text{-}Bu_4N)_4[W_{10}O_{32}]$) [253]. The authors studied a plausible mechanism through kinetic analysis and laser flash photolysis (LFP). In particular, the excited state of **TBADT** is generated upon light irradiation (Figure 58B). ***TBADT** can activate unactivated C(sp^3)–H bonds (such as those of cyclohexane **122**) via HAT to yield the carbon-centered radical **122a**$^{\bullet}$, which adds to the 2-position of benzothiazole **124** to generate the radical intermediate **126**. The authors then proposed two different pathways to access the target coupling product **125a**. Firstly, **126** undergoes to a back-HAT (*b*-HAT) from the reduced form of the catalyst, **TBADT**-H to generate the compound **127**, that affords the product through a photochemical oxidative cascade process where ***TBADT** acts as the oxidant. In the second possibility, **126** can undergo a proton-mediated spin center shift (SCS) process to give **128** and then **TBADT** serves as reductant to regenerate aromacity. Regarding the substrate scope, different benzothiazoles and C(sp^3) radical precursors were envisioned, affording coupling products such as **125b–f** in moderate to high yields (47–88%, Figure 58C).

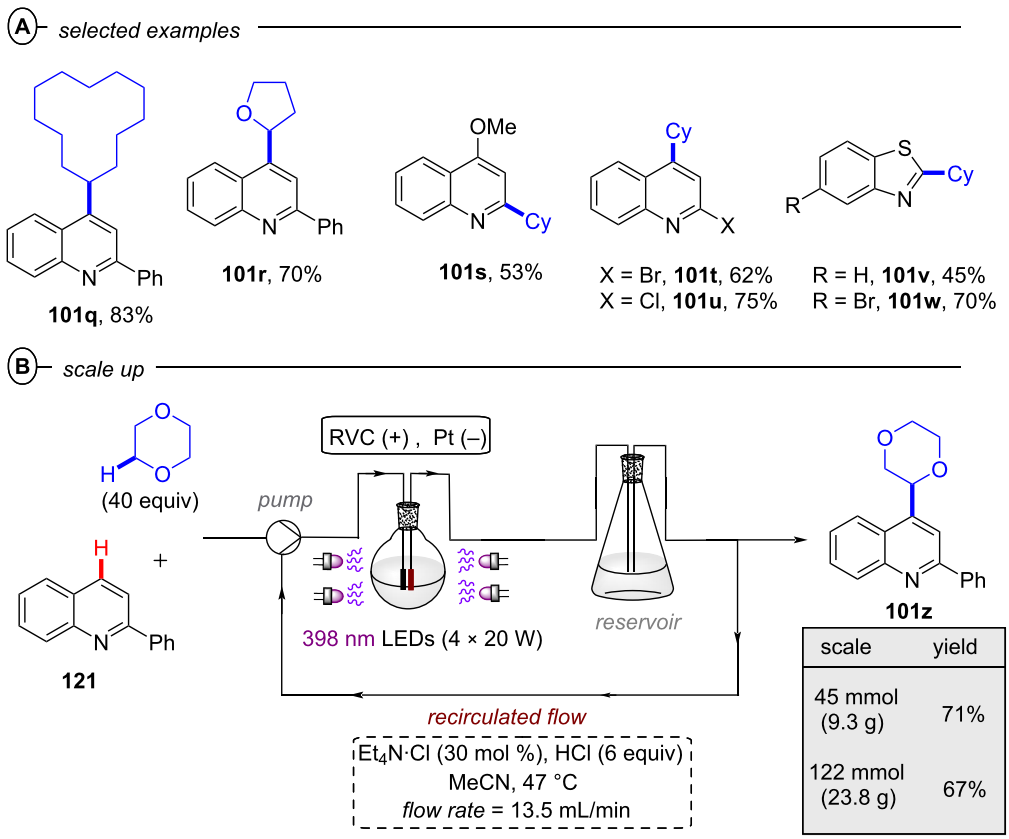

Figure 57: A) Selected examples from the substrate scope. B) Gram and decagram scale semi-continuous flow PEC HAT activation of 1,4-dioxane and its Minisci-type reaction.

Lastly, Lambert and co-workers reported a PEC protocol for coupling alkyl ethers **129** with isoquinoline derivatives **130** involving **TAC**$^+$ as catalyst (Figure 59A) [254]. As usual, **TAC**$^+$ initially undergoes anodic oxidation and then photoexcitation to afford ***TAC**$^{\bullet 2+}$ (Figure 59B). Rather than SET oxidation of the substrate, authors proposed HAT (supported by kinetic isotopic effect of $k_{H/D}$ = 3.0) directly from the tetrahydrofuran **129a** to ***TAC**$^{\bullet 2+}$ to generate the corresponding radical **129a**$^\bullet$ and the protonated form of the photocatalyst **TAC-H**$^{2+}$. At this stage, carbon-centered radical **129a**$^\bullet$ can undergo coupling reaction with **130a** to yield the intermediate **132**. Subsequently, a second oxidation occurs via ***TAC**$^{\bullet 2+}$ along with the loss of a proton, resulting in the formation of the target product **131a**. According to the authors, it is not possible to completely exclude SET activation of the ether partner (the KIE could also be attributed to deprotonation of the ether radical cation), nor possible to rule out the alternative pathway from C-centered radical **129a**$^\bullet$ by SET oxidation to the oxocarbenium **129'** followed by nucleophilic addition of **130a** (grey dashed pathway in Figure 59B). With the optimized conditions in hand, a variety of isoquinoline partners tested with **129a**, giving rise to products like **131a–c** in very good to high yields (72–81%) (Figure 60).

Regarding the regioselectivity using different ethers, 2-methyltetrahydrofuran generated single regioisomers such as **131d**. Interestingly, while a notable regioselectivity for primary over tertiary C−H ethers bonds was observed (**131e** and **131f**), the competition between primary and secondary C−H bonds resulted in substitution at the secondary position (**131g**). Thus, in the latter case, the greater stability of the intermediate radical outweighed the steric difference. The authors extended the method to vinyl sulfones (**133a–c**) – due to ease of removing the phenylsulfonyl group – and to azoles (**134a–c**).

3.1.3 Alkene and alkyne activation: ***Alkene activation*:** Benzimidazo-fused isoquinolines are recurrent motifs in many pharmaceutical products (e.g., antidiabetic and antitumor agents) and advanced organic materials (e.g., organic electronics and organic colorant, the so-called 'carbonyl-dyes') [255,256]. Classical methods for obtaining these motifs consist of high-temperature (130–150 °C) condensation reactions [257], or

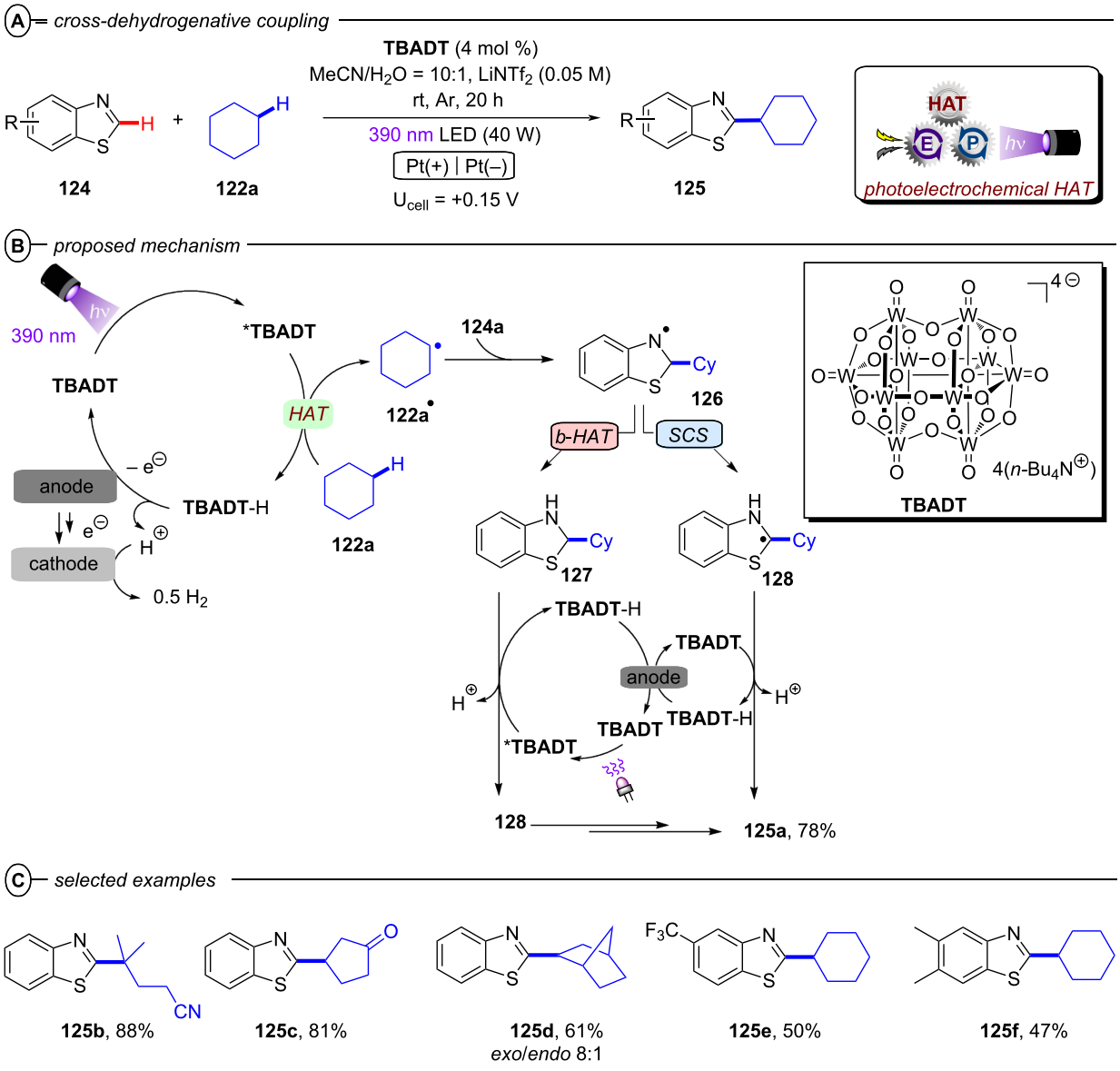

Figure 58: A) Photoelectrochemical HAT-mediated dehydrogenative coupling of benzothiazoles with aliphatic C–H bonds using **TBADT** as catalyst. B) Proposed mechanism. C) Selected examples from the substrate scope.

milder yet more expensive rhodium-based catalyzed [4 + 2] annulation conditions [258]. Owing to these drawbacks, the development of new cutting-edge strategies for their synthesis has therefore attracted interest. Several protocols have been reported in recent years, showing how these motifs can be obtained from radical addition/cyclization cascade processes [259,260]. Aliphatic carboxylic acids [261], alkyl boronic acids [262], *N*-hydroxyphthalimide esters (NHPI esters) [263,264] or Katrizky salts [265] can all be used as radical precursors under photoredox or electrochemical conditions. Naturally, these are not so atom economical and the use of non-prefunctionalized alkyl radical precursors would increase atom economy. Although a step in this direction has been taken by the group of Wei and co-workers [266], a potentially explosive peroxide radical was necessary. However, recently, Xu, Zeng and co-workers reported an interesting PEC cerium-catalyzed radical addition/cyclization process for the incorporation of unactivated alkanes **136** as radical precursors [267], by exploiting a PEC HAT to generate an alkyl radical directly from the unactivated alkane (as described previously by Xu, Ravelli and Lambert; Figures 56–59). This generated alkylated benzimidazo-fused isoquinolinones and other correlated N-bearing cycles **77** starting from compounds like **135** (Figure 61A) [267].

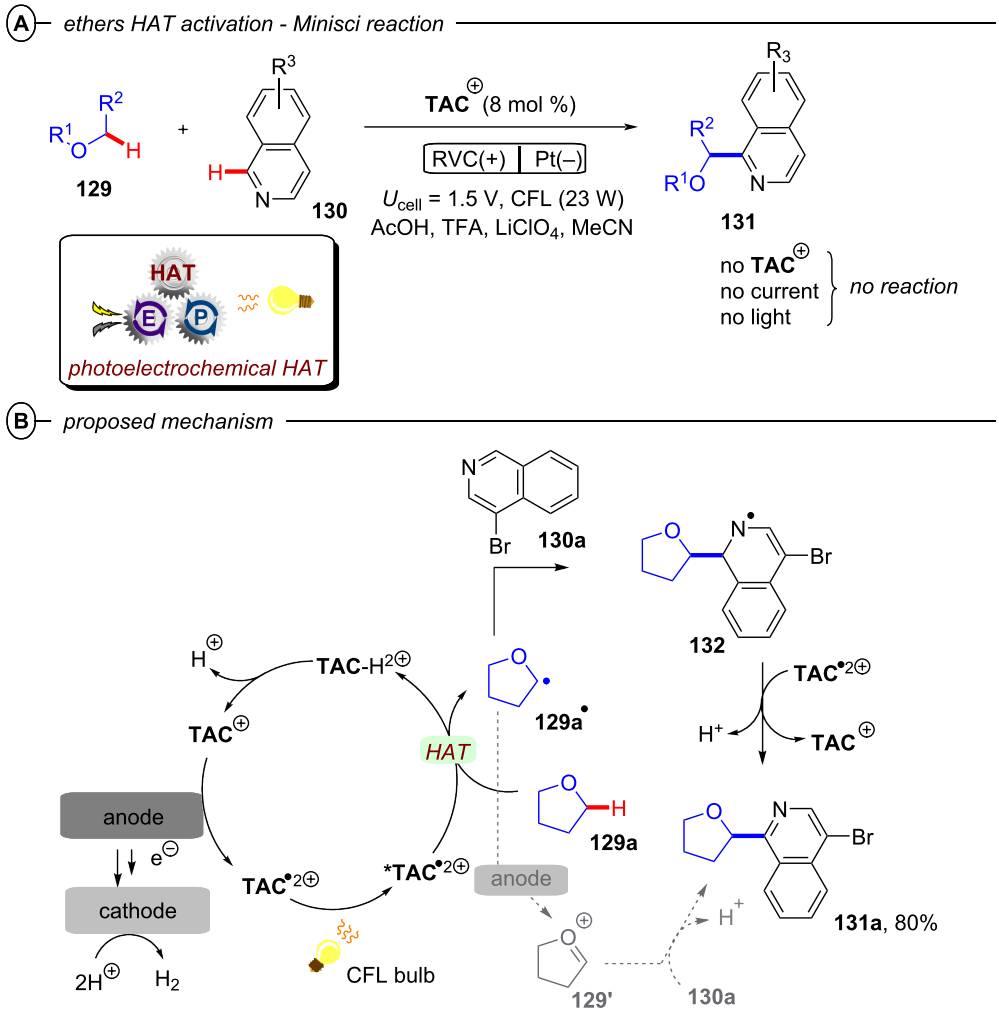

Figure 59: A) Photoelectrochemical HAT activation of ethers using electro-activated **TAC⁺** as photocatalyst. B) Proposed mechanism. C) Selected examples from the substrate scope.

The proposed mechanism was supported by kinetic isotope effect (KIE) experiments, cyclic voltammograms (CV), UV–vis spectroscopy and comparisons with previous reports [238,268,269]. Anodic oxidation of Ce^{III} in the presence of *n*-Bu_4N·Cl and MeOH was proposed to afford the complex MeO–$Ce^{IV}Cl_{n-1}$, which undergoes homolytic cleavage through a ligand to metal charge transfer (LMCT) under 405 nm LED irradiation. The authors claimed formation of MeO$^\bullet$ (Figure 61B), rather than Cl$^\bullet$, on the basis that other alcohols such as hexafluoroisopropanol (HFIP), CF_3CH_2OH and CCl_3CH_2OH led to lower product yields. At this point, the HAT process from cyclohexane to electrophilic MeO$^\bullet$ affords the cyclohexyl radical, which undergoes radical addition to the double bond of **135a** to yield intermediate **138**, which can then cyclize to **139**. Finally, SET oxidation of the latter by Ce(IV) and subsequential deprotonation of **140** generates the benzimidazo-fused isoquinolinone **137a**. The alternative possibility of LMCT to afford Cl$^\bullet$ cannot be excluded (grey pathway in Figure 61B), especially since i) a 13% product yield was observed for the model reaction without MeOH and ii) different electrolytes like *n*-Bu_4N·Br or *n*-Bu_4N·I led to the model reaction product in only low or trace yield.

Regarding the substrate scope, the authors demonstrated that both secondary and tertiary C(sp^3)–H-bearing compounds were successfully incorporated to afford the products in moderate to good yields (49–56% for **137b** and **137c** in Figure 61C). Then, the scope of *N*-methacryloyl-2-phenylbenzoimidazoles was explored, e.g., with 1-chloroadamantane or cyclohexane, resulting in products such as **137d** and **137e** in moderate to good yields (49–66%).

***Alkyne activation*:** α,α-Dihaloalkyl derivatives play a fundamental role in pharmaceuticals and natural products like AML

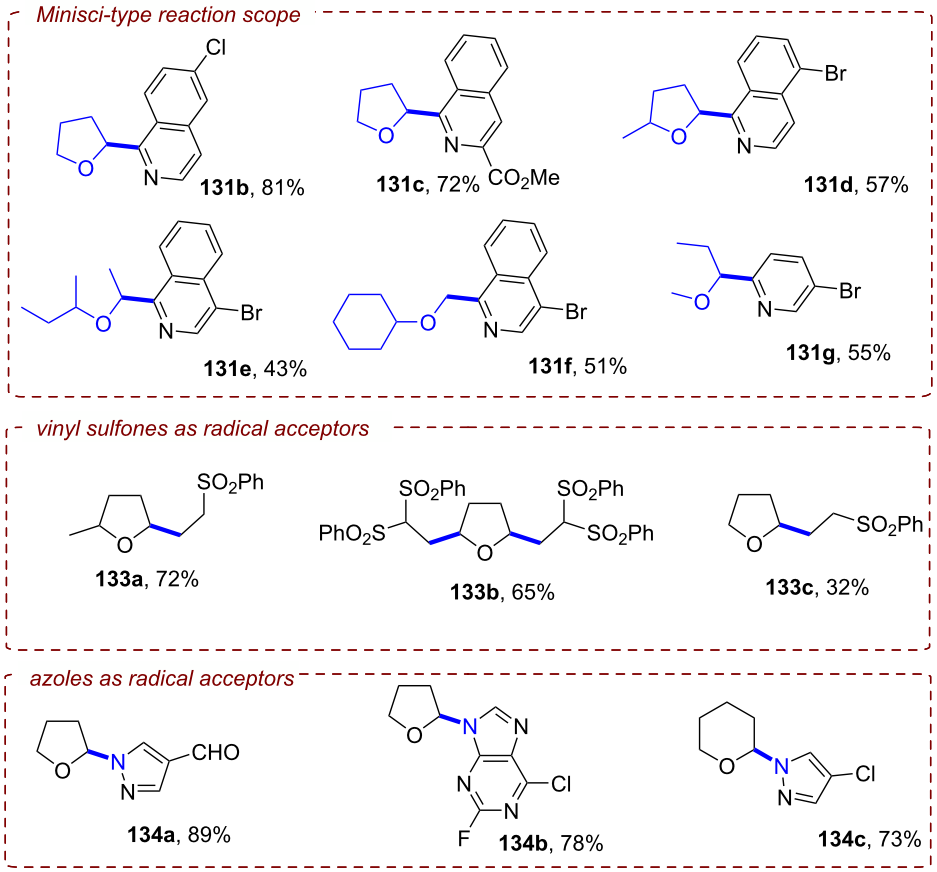

Figure 60: Selected examples from the substrate scope.

inhibitors and antiviral drugs [270-272]. They constitute important building blocks in the synthesis of various chemical intermediates like cyclopropanes and 2-keto(hetero)aryl benzox(thio)azoles [273-275]. Methods for their synthetic access have garnered attention, the most straightforward of which is the direct oxydichlorination of alkynes. There are excellent examples of this process in the literature [276-280], but all suffer from several limitations. Among them are the use of excess strong chemical oxidants, divided cell direct electrolysis (high cell resistance), strongly acidic conditions or atom uneconomical chlorinating agents like *N*-chlorosuccinimide (NCS).

Hence, Chen and co-workers reported a *d*PEC oxydichlorination starting from alkynes such as **141**, catalyzed by $CeCl_3$ under PEC conditions (Figure 62A) [281]. The optimized conditions employed $LiClO_4$ as electrolyte and $MgCl_2{\cdot}6H_2O$ as a source of $Cl^•$ (a much cheaper and more atom economical source in comparison to NCS) in a mixed MeCN/water solvent. The authors examined numerous arylalkynes and observed that ethynylbenzene and substrates bearing benzylic alkyl substituents were successful (**142a**,**b**, Figure 62B). Both electron-rich and -poor substituents were tolerated affording products in very good yields (73–78% for **142c**,**d**), while 4-MeO-substituted phenylacetylene mostly polymerized and only gave a modest product yield (**142e**). The method was also tested on an aliphatic substrate (4-phenyl-1-butyne), resulting in the product **142f** in 26% yield. Although the authors did not investigate further the reactivity between aromatic and aliphatic alkynes, it is proposed that the low efficiency of the latter is due to the absence of the aromatic ring to stabilize the reactive intermediate **143a** or **141a**$^•$ (Figure 63). Internal acetylenes were also successful, affording alkyl-substituted dichloroketones such as **142g**. A series of electron-poor functional groups (halogen, trifluoromethyl) were compatible (**142h**,**i**), a diarylalkyne and propargylic alcohol were tolerated (**142l**,**m**).

Concerning the mechanism, the authors proposed anodic oxidation of $CeCl_3$ to a $[Ce^{IV}Cl_m]$ species, followed by release of $Cl^•$ via photoinduced LMCT (Figure 63). Trapping of $Cl^•$ by the alkyne **141a** affords alkene radical intermediate **141a**$^•$, whose oxidation leads to carbocation **141a**$^+$. Subsequential nucleophilic addition of water and deprotonation was invoked to access enol **143a**. The latter is transformed to enol radical

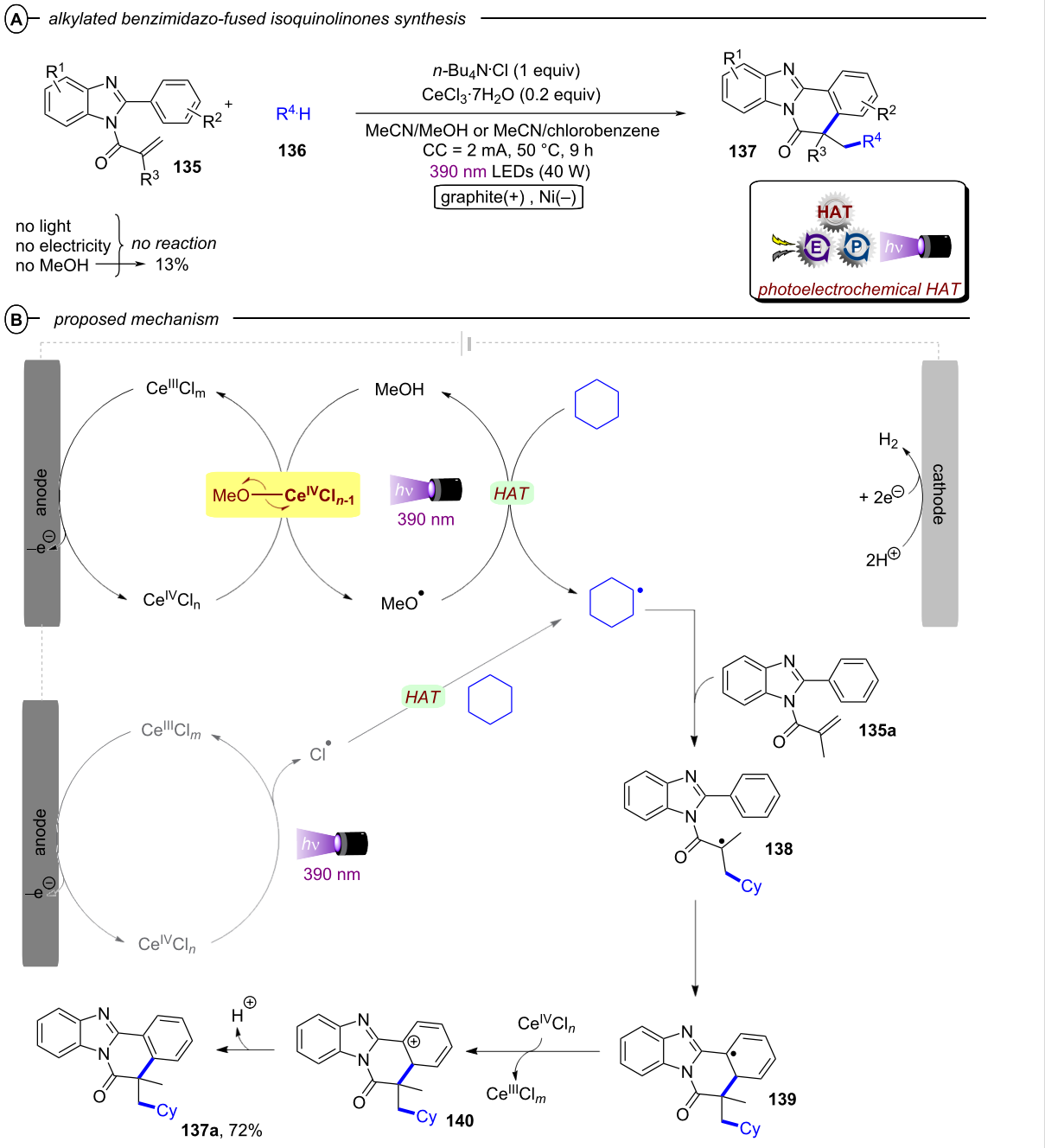

Figure 61: A) Photoelectrochemical HAT-mediated synthesis of alkylated benzimidazo-fused isoquinolinones using $CeCl_3$ as catalyst. B) Proposed mechanism. C) Selected examples from the substrate scope.

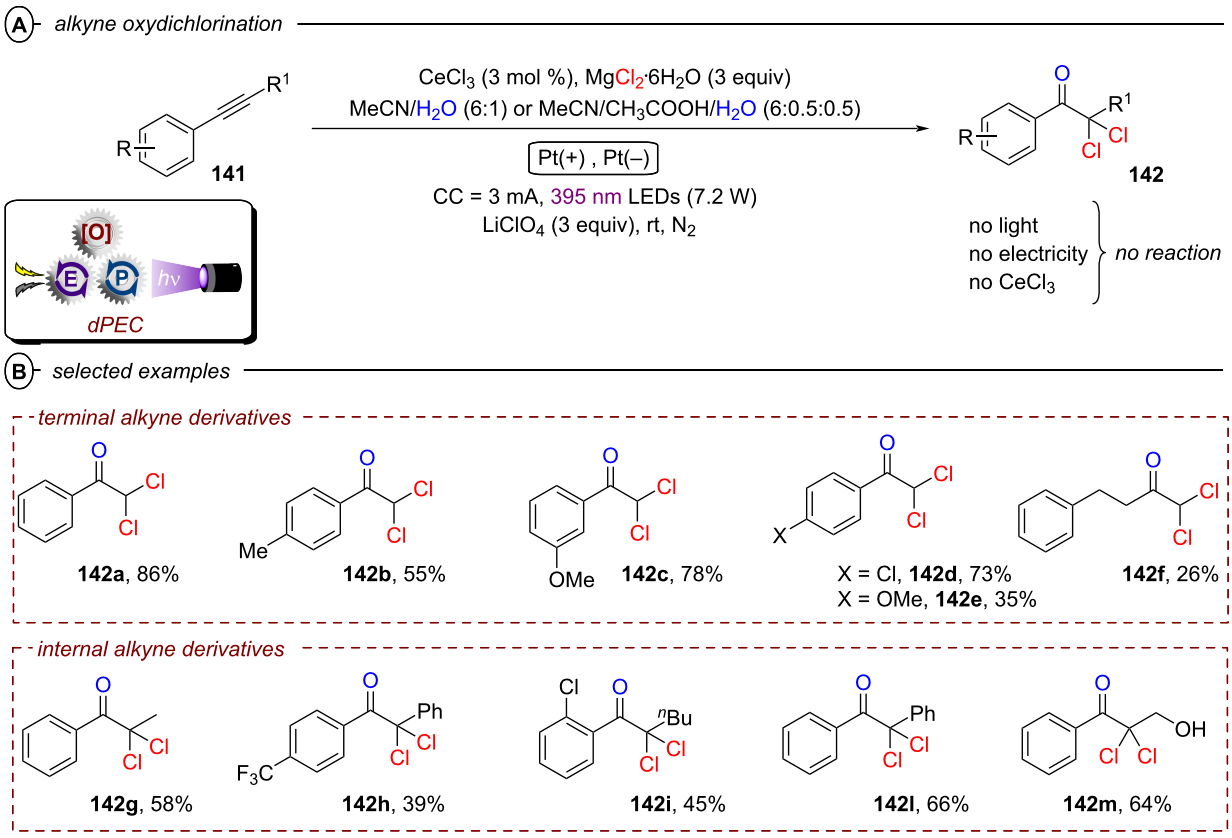

Figure 62: A) Decoupled photoelectrochemical cerium-catalyzed oxydichlorination of alkynes using $CeCl_3$ as catalyst. B) Selected examples from the substrate scope.

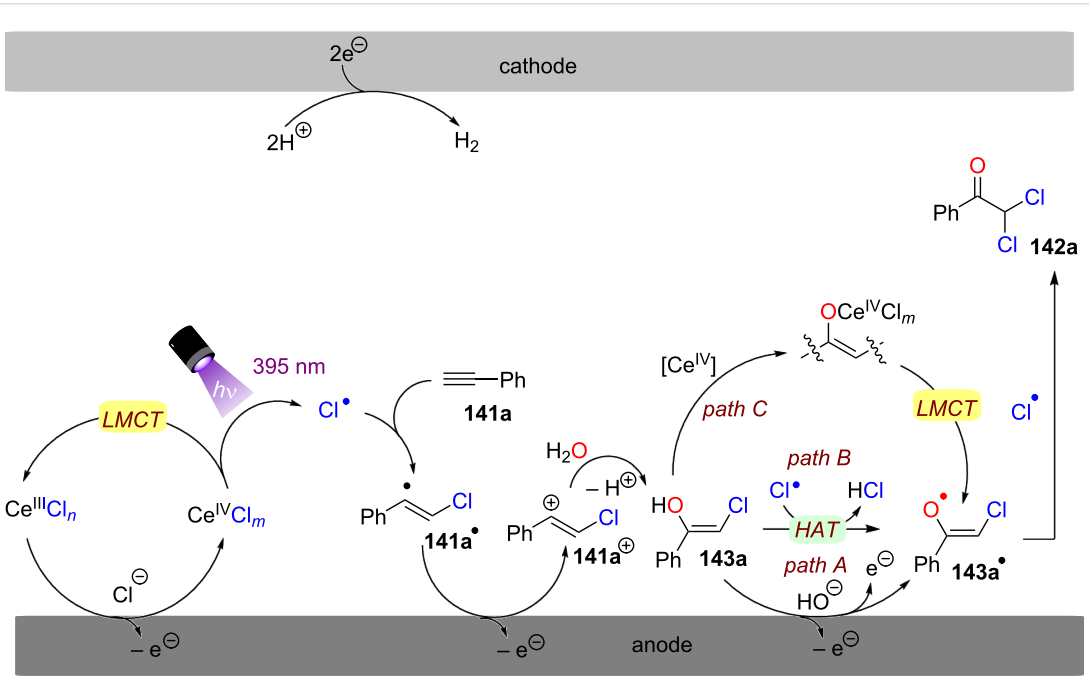

Figure 63: Proposed decoupled photoelectrochemical mechanism.

143a• via a tandem process of deprotonation and anodic oxidation (*path A*). The final product **142a** is formed via chlorine radical termination with **143a**•. Alternatively, the process **143a** → **143a**• could be achieved either by the HAT reactivity of Cl• (*path B*) or the LMCT activity of a Ce^{IV} enolate (*path C*).

3.1.4 (Hetero)cycles activation: The selective cleavage and functionalization of C–C bonds is a strategy of growing importance in organic synthesis [282-284]. In particular, the β-scission of C–C bonds in alcohols has proven a key target owing to the privileged abundance of these moeities in biomass chemical feedstocks [285,286]. The key driving force for β-scission is the formation of a strong C=O bond from an alkoxy radical, which is challenging to generate due to its high O–H bond dissociation energy (≈105 kcal mol^{-1}). Strong, stoichiometric chemical oxidants such as bromine, hypervalent iodine agents or Selectfluor® have been previously used to achieve this [287-291]. Thus, the development of milder and greener protocols without stoichiometric oxidants is desirable and one such reported approach leverages PEC.

Onomura and co-workers first realized a PEC ring-opening bromination of unstrained *tert*-cycloalkanols **144** to afford ω-bromo-substituted ketones **145** by using $MgBr_2·6H_2O$ as a source of Br^+ (Figure 64A) [292]. This paper contributes to the vast field of halogenated ketone synthesis, which is important since these compounds constitute versatile building blocks in the formation of various heterocyclic compounds (e.g., cyclic imines) [293-295], functional materials (e.g., conjugated polymers and liquid crystal dimers and trimers) [296-298] and biologically-active molecules (e.g., 5-HT4 receptor agonists and 5-HT7 receptor ligands) [299-301]. The optimized conditions

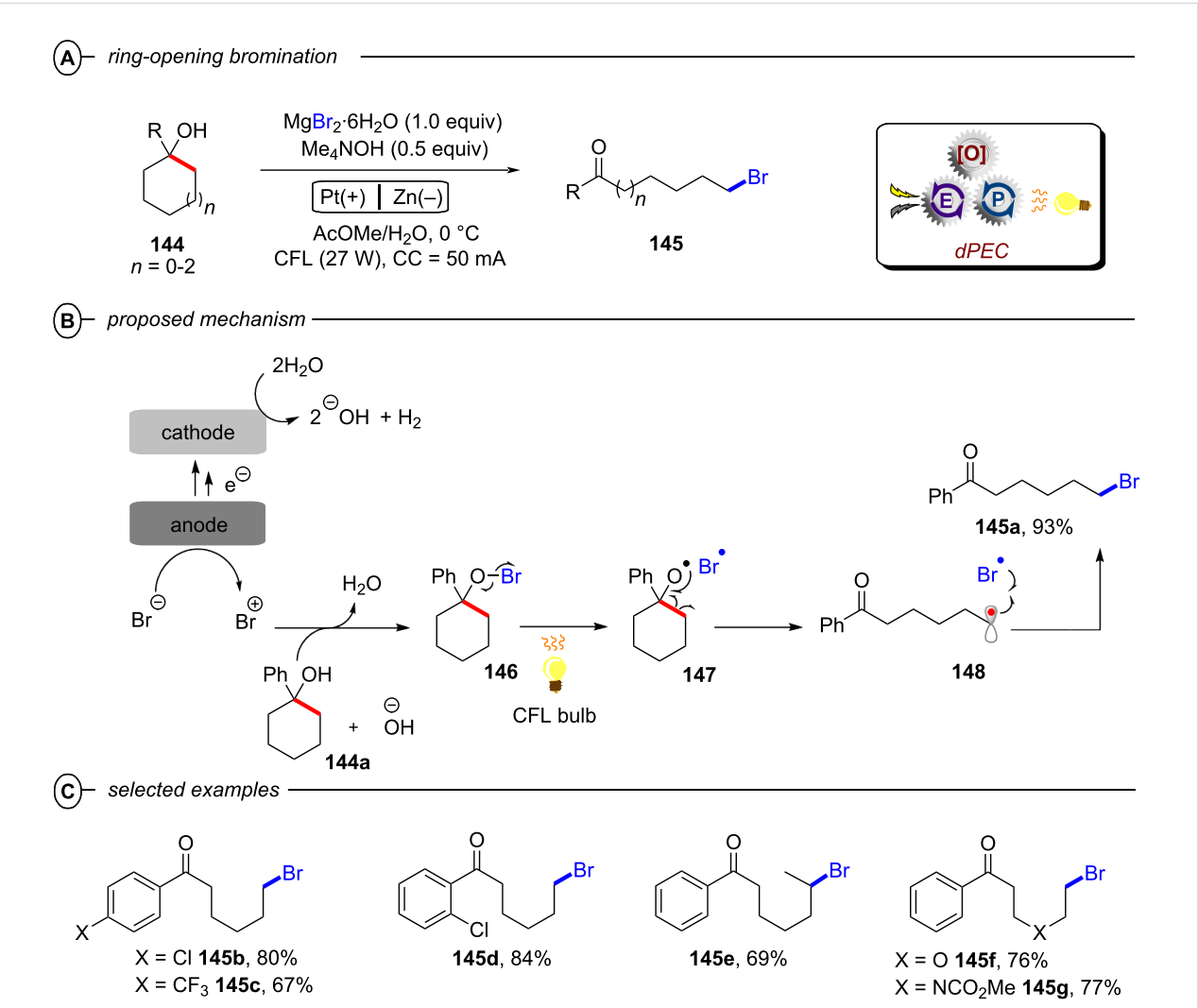

Figure 64: A) Decoupled photoelectrochemical ring-opening bromination of tertiary cycloalkanols using $MgBr_2$ as Br^+ source. B) Proposed mechanism. C) Selected examples from the substrate scope.

reported by the authors consist of Me_4NOH as both a base and phase transfer catalyst (PTC) in a mixture of AcOMe/H_2O at 0 °C using an undivided cell and a CFL bulb (27 W).

In the mechanism, the bromide ion is SET oxidized (twice) at the anode to generate the bromine cation species (Figure 64B). The reaction between the latter and the starting material **144a** yields a hypobromite intermediate **146**, which can undergo light-promoted homolytic cleavage of the O−Br bond to generate the alkoxy radical **147**. Then, the latter is trapped by a bromo radical (or other hypobromite species) to afford the radical carbon intermediate **148**, which reacts with $Br^{\bullet}$ to yield the ω-bromoketone **145a**. Regarding the substrate scope, cyclohexanols bearing an electron-withdrawing group such as chloro (**145b**) or trifluoromethyl (**145c**) afford the target product in good to high yields (67–80% in Figure 64C). The steric hindrance of an *ortho*-Cl atom did not compromise the yield of **145d**. Unsymmetrical substrates led selectively to the products like **145e** via regioselective β-scission to generate the more stable (secondary) alkyl radical. Finally, tetrahydropyranol and piperidinol derivatives were successfully transformed into the desired products in very good yields (76–77% for **145f,g**).

Subsequently, Lei and co-workers reported a redox-neutral PEC method for ring opening functionalization of cycloalkanols **149** or **150** using $CeCl_3$ as catalyst (Figure 65A) [268]. Their protocol allowed cleavage of cycloalkanols with different sizes and tolerated a vast range of functional groups, allowing the scope of downstream functionalization to be notably broadened beyond bromination. Mechanistically, $CeCl_3$ is solubilized in MeCN with the help of $Et_4N{\cdot}Cl$, leading to a $[Ce^{III}Cl_6]^{3-}$ complex which was identified as the active catalyst state (Figure 65B). The latter is oxidized at the anode to Ce(IV), which immediately reacts with the cyclic alcohol **150a** to yield a Ce(IV)-alkoxide species via ligand exchange in the presence of base. Thereafter, the Ce(IV)-alkoxide undergoes a photoin-

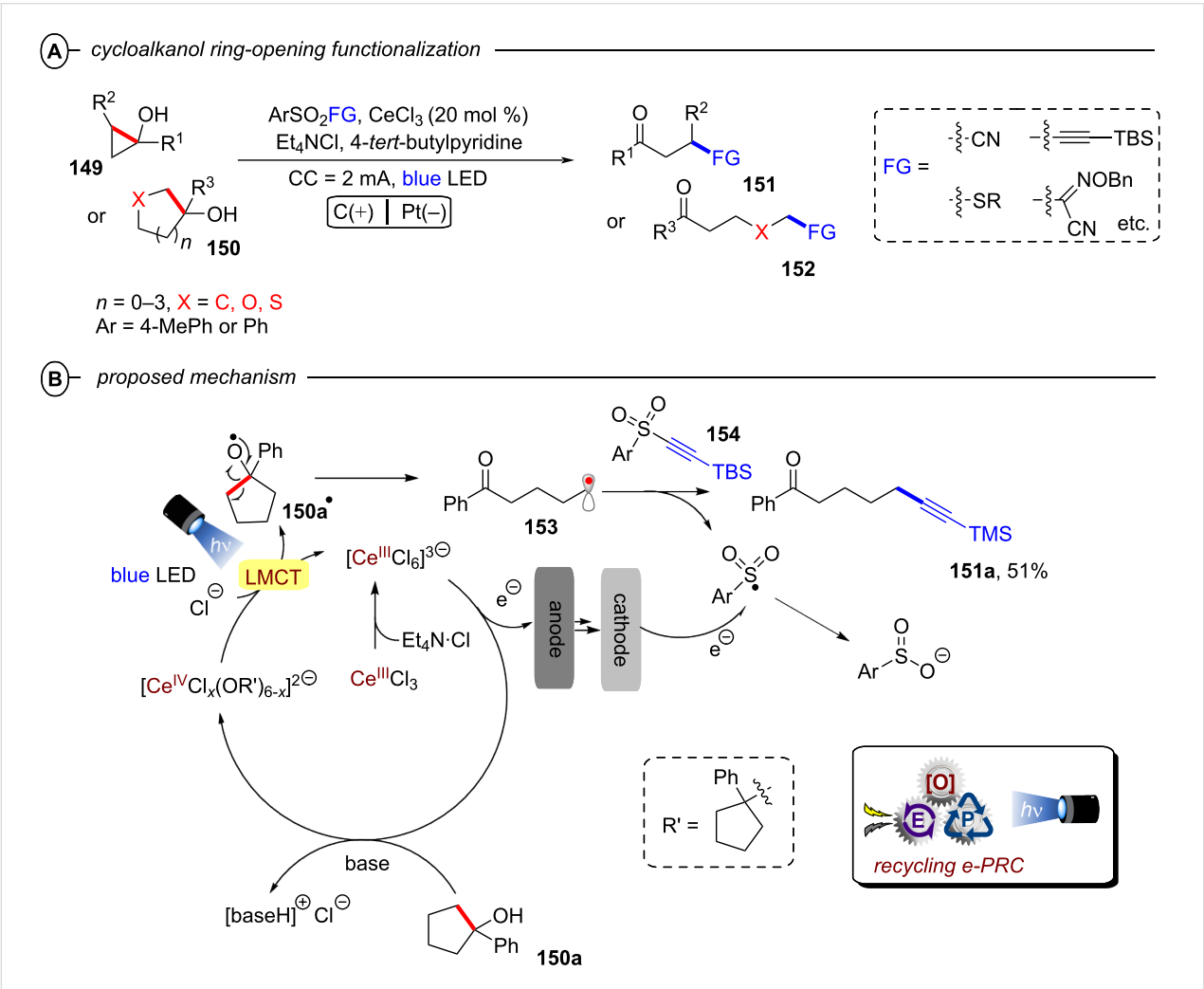

Figure 65: A) Recycling e-PRC ring-opening functionalization of cycloalkanols using $CeCl_3$ as catalyst. B) Proposed mechanism.

duced LMCT homolysis process to form radical **150a**$^{\bullet}$ and regenerate the $[Ce^{III}Cl_6]^{3-}$ complex. The former undergoes β-scission to break the C–C bond, resulting in radical **153**. Radical addition–elimination of **153** to the arylsulfonyl compound (such as *tert*-butyldimethyl(tosylethynyl)silane **154** in Figure 65B) generates product **151a** and liberates the sulfonyl radical, which is then reduced at the cathode to form a nontoxic benzenesulfonate. Therefore, and notably, this reaction occurs in an overall redox neutral fashion.

The optimized conditions were applied to cycloalkanols of different ring sizes – from a three-membered ring to a seven-membered ring – in an overall fragmentative cyanation reaction affording the desired products (**151b**–**e**) in moderate to good yields (53–67% in Figure 66). Electron-donating groups and electron withdrawing groups (**151f**–**h**) were all tolerated. Interestingly, heterocyclic alcohols were tolerated, giving the desired products **152a**,**d** in moderate to high yields (43–82%). Together with the protocol of Onomura and co-workers (Figure 64), this shows how PEC provides an oxidative platform for engaging cyclic alcohols and amines that is complementary to the reductive conPET strategy for the carboxylative ring-opening of cyclic amines (vide supra, Figure 22). Finally, the protocol could be extended to engage intermediate **153** in downstream alkynylations (**151i**–**n**), thioetherifications (**152e**–**g**), chlorinations (**151o**), alkenylations (**151p**), arylations (**151q**) and reactions with oximes (**152h**–**l**), demonstrating a notably broad scope of applications.

3.2 Reductive activation

3.2.1 Arene C(sp^2)–X activation: As mentioned in the introduction (vide supra), a key focus of PRC in recent years and justification in the efforts to merge photo- and electrochemistry has been on the development of novel approaches for achieving extreme reduction potentials (E^{p}_{red} < −2 V vs SCE) without using dissolving alkali metals. While the concomitant conPET approach represented an important initial step towards a safe and chemoselective protocol, it has certain limitations that need to be addressed. These limitations include i) the need for multiple photons which are expensive to generate, ii) the requirement for a carefully balanced system in which both catalyst oxidation states absorb light and undergo PET processes under the same reaction conditions, iii) the interference of by-products from sacrificial electron donors in the reaction pathway (and their separation from the desired products). A typical example of the latter is a trialkylamine such as Et_3N, which can i) limit the steady-state concentration of (radical anion) reductive photocatalyst/hinder downstream reactivity by back elec-

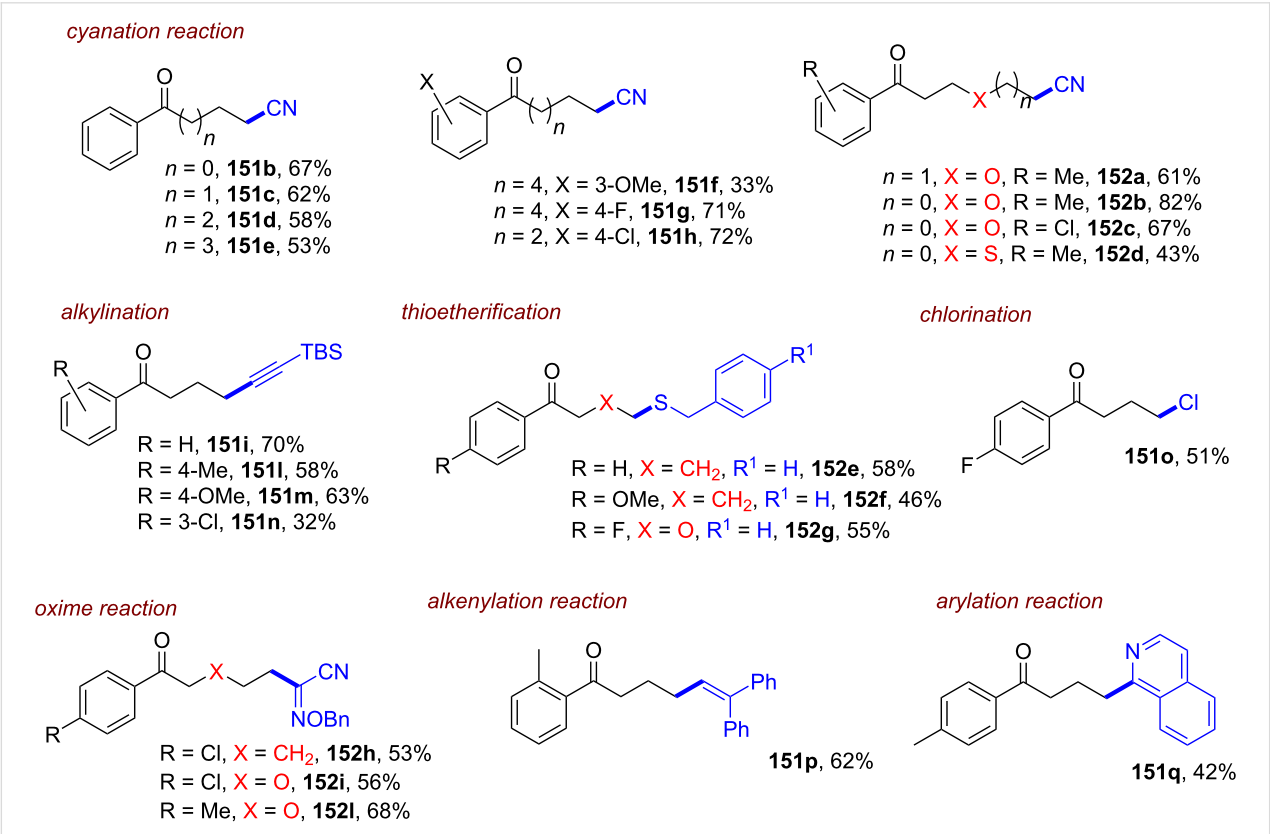

Figure 66: Selected examples from the substrate scope of the PEC ring-opening functionalization.

tron transfer to $Et_3N^{\bullet+}$, ii) promote intermediate radical quenching via HAT (either involving $Et_3N^{\bullet+}$ or the derived α-amino radical), iii) effect other pathways like XAT (from the derived α-amino radical).

Therefore, researchers identified electrochemistry as a direct and more flexible alternative for generating a high steady-state concentration of (radical anion) reductive photocatalyst from its neutral precursor via cathode reduction. By using a divided cell configuration, the risk of interference from oxidized byproducts can be suppressed or entirely eliminated.

With this idea in mind, Lambert, Lin and co-workers reported a radical ion e-PRC reduction of chloro- and bromoarenes **155** using 9,10-dicyanoanthracene (**DCA**) as catalyst (Figure 67A) [302]. In their mechanistic proposal, the **DCA** catalyst undergoes cathodic reduction to generate **DCA**$^{\bullet-}$, which is then photoexcited to afford a powerful reductant [52]. The authors proposed that ***DCA**$^{\bullet-}$ can donate an electron to the aryl halide **155** to furnish intermediate **155**$^{\bullet-}$ and to regenerate the **DCA** catalyst (Figure 67B). Aryl halide radical anion **155**$^{\bullet-}$ then undergoes mesolytic C(sp^2)–X cleavage to form an aryl radical that is trapped by an electrophile (B_2Pin_2, (Het)Ar or Sn_2Me_6 respectively) to furnish the target products. The authors could not rule out the possibility of a photoinduced reductive quenching of **DCA** at the cathode to form **DCA**$^{\bullet-}$ (grey pathway in Figure 67B). However, this seems implausible because i) **DCA** is not efficiently excited by the blue LEDs and ii) the Beer–Lambert dependence would dictate light penetration only in the bulk solution within a thin film at the reactor walls, shielding transmission of light to the electrode. Remarkably, electron-rich aryl halides like 4-bromo- and 4-choroanisole could be reductively engaged in SET, leading to their corresponding borylated (**156a**,**b**), (hetero)coupled (**157a**) and stannylated products (**158a**) (Figure 67C). Without delving into the details of substrate scope that was concisely described in a previous review [28], it is interesting to further elaborate on the mechanism and to compare with the conPET report (vide supra, Figure 9).

According to the estimation of the authors made by the Rehm–Weller equation [303], ***DCA**$^{\bullet-}$ displays an exceptionally high reducing potential of $^*E_{1/2}$ = −3.2 V vs SCE. However, this value is ≈0.6 V more negative than the value calculated by Jacobi von Wangelin, Pérez-Ruiz and co-workers [52] and recently by Vauthey and co-workers [53] (section 2.1.1, vide supra). The difference lies in the fact that the −3.2 V value was calculated on the basis of an excited-state energy of 2.38 eV (and not the D_1 state energy of 1.75 eV) extracted from the absorption and emission spectra presented in the work of Eriksen [304], which was later found to be associated with a follow-up reaction product of **DCA**$^{\bullet-}$ (discussed below). This follow-up reaction product was also responsible for the nanosecond lifetime (13.5 ns) that was incorrectly ascribed to ***DCA**$^{\bullet-}$ ($\tau \neq 13.5$ ns), with the correct picosecond lifetime being later reported by Vauthey ($\tau \approx 3$ ps).

Photophysical properties aside, a very interesting aspect is that the conceptually analogous conPET protocal using **DCA** (vide supra, Figure 9) [52] *did not achieve reductive activation of electron-rich aryl halides like haloanisoles* (affording – at most – 6% yield). Since this discrepancy between the reports has not been previously addressed, we propose two different explanations:

i) the steady-state concentration of **DCA**$^{\bullet-}$ generated under e-PRC favors a preassembly with the substrate, that may enable access to higher order excited states ($D_{n>1}$) of ***DCA**$^{\bullet-}$ and/or facilitate cleavage of [Ar−X]$^{\bullet-}$ that is likely rate-determining;

ii) the active species involved in the process was not the radical anion species ***DCA**$^{\bullet-}$, but rather a 10-cyanoanthrolate species (**159** in Figure 67B). The 10-cyanoanthrolate is known to form in quantitative yield during cathodic reduction of **DCA** without rigorous exclusion of oxygen [305,306], and gradually further transforms to anthraquinone (which Lambert, Lin and co-workers reported was also a successful catalyst precursor, albeit affording a lower yield of product compared to the **DCA** precursor). The brown color and UV–vis bands of the reaction mixture reported by Lambert, Lin and co-workers [302] corresponds better with the 10-cyanoanthrolate spectra of Breslin and Fox [305] than with the purple color and UV–vis bands of **DCA**$^{\bullet-}$.

However, although the formation of 10-cyanoanthrolate in the reaction of Lambert, Lin and co-workers is obvious, there is no evidence to suggest its excited state is reductive enough to engage the electron-rich aryl halides. König and co-workers reported a 9-anthrolate photocatalyst without substituents at the 10-position that could only engage electron-poor aryl chlorides [307]. Having a 10-cyano substituent would stabilize the anthrolate further and thus render its excited state even less reducing.

Overall, we conclude based on the evidence available so far that either ***DCA**$^{\bullet-}$ ($D_{n>1}$) is the active catalyst via a preassembly with the aryl halide, or 10-cyanoanthrolate preassembles with the aryl halide in a manner that accelerates cleavage of [Ar−X]$^{\bullet-}$.

Simultaneously to the report of Lambert, Lin and co-workers, Wickens and co-workers reported a noteworthy investigation on

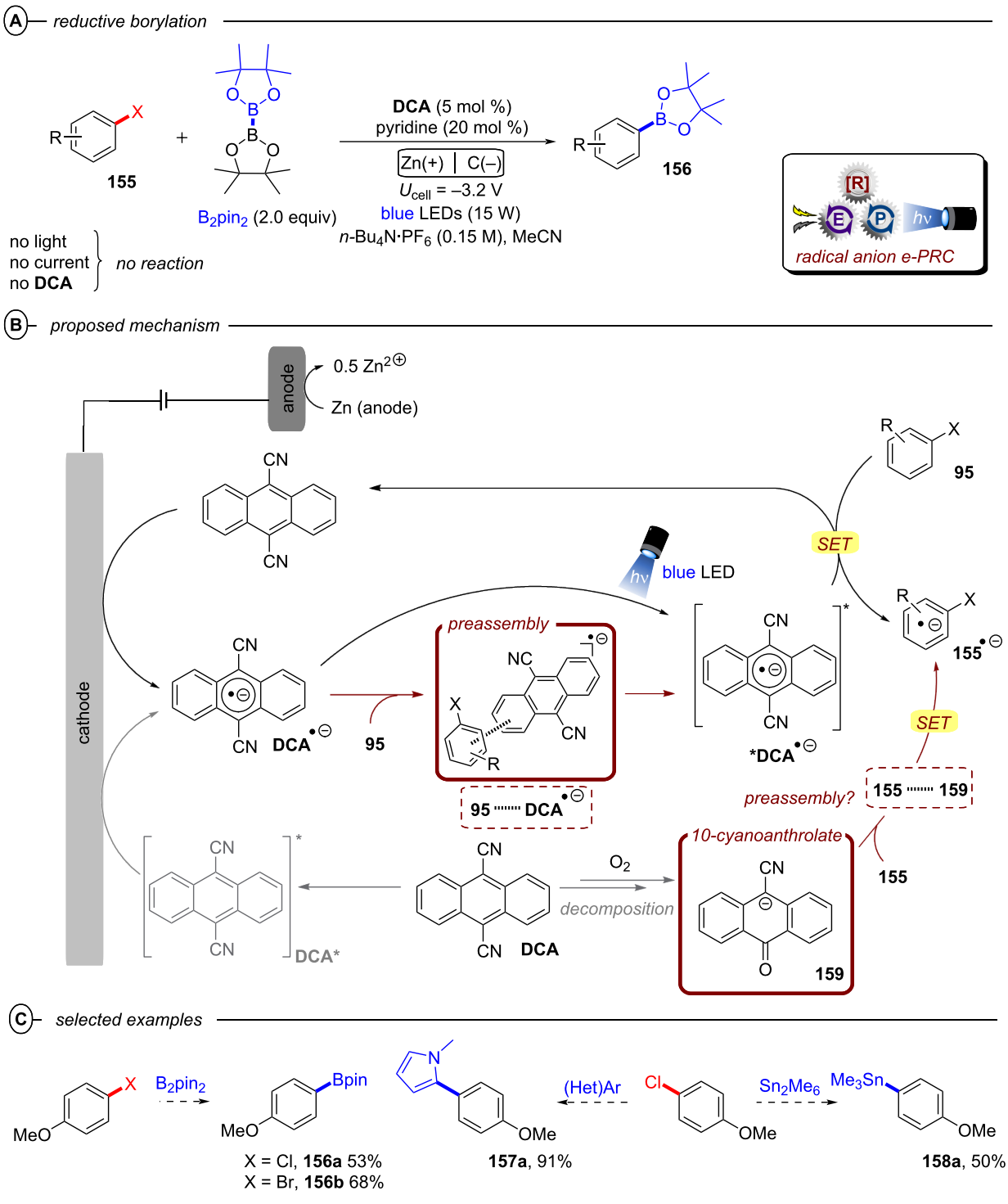

Figure 67: A) Radical ion e-PRC reduction of chloro- and bromoarenes using **DCA** as catalyst and various acceptors as trapping agents. B) Proposed mechanistic pathways (by authors, black/grey arrows; by us, burgandy arrows). C) Selected examples from the substrate scope.

the reductive dehalogenation and activation of aryl halides [308]. Initially, the authors investigated the dehalogenation reaction of 4-bromobiphenyl **160** (E^{p}_{red} = −2.40 V vs SCE), as depicted in Figure 68A [308]. Four arylimide catalysts were tested under appropriate conditions of constant potential and visible light (Figure 68A). Perylene diimide (**PDI**, $E_{1/2}$ = −0.43 V vs SCE) was found to be poorly effective (<5%) in the reaction, whereas the naphthalene-based analogues,

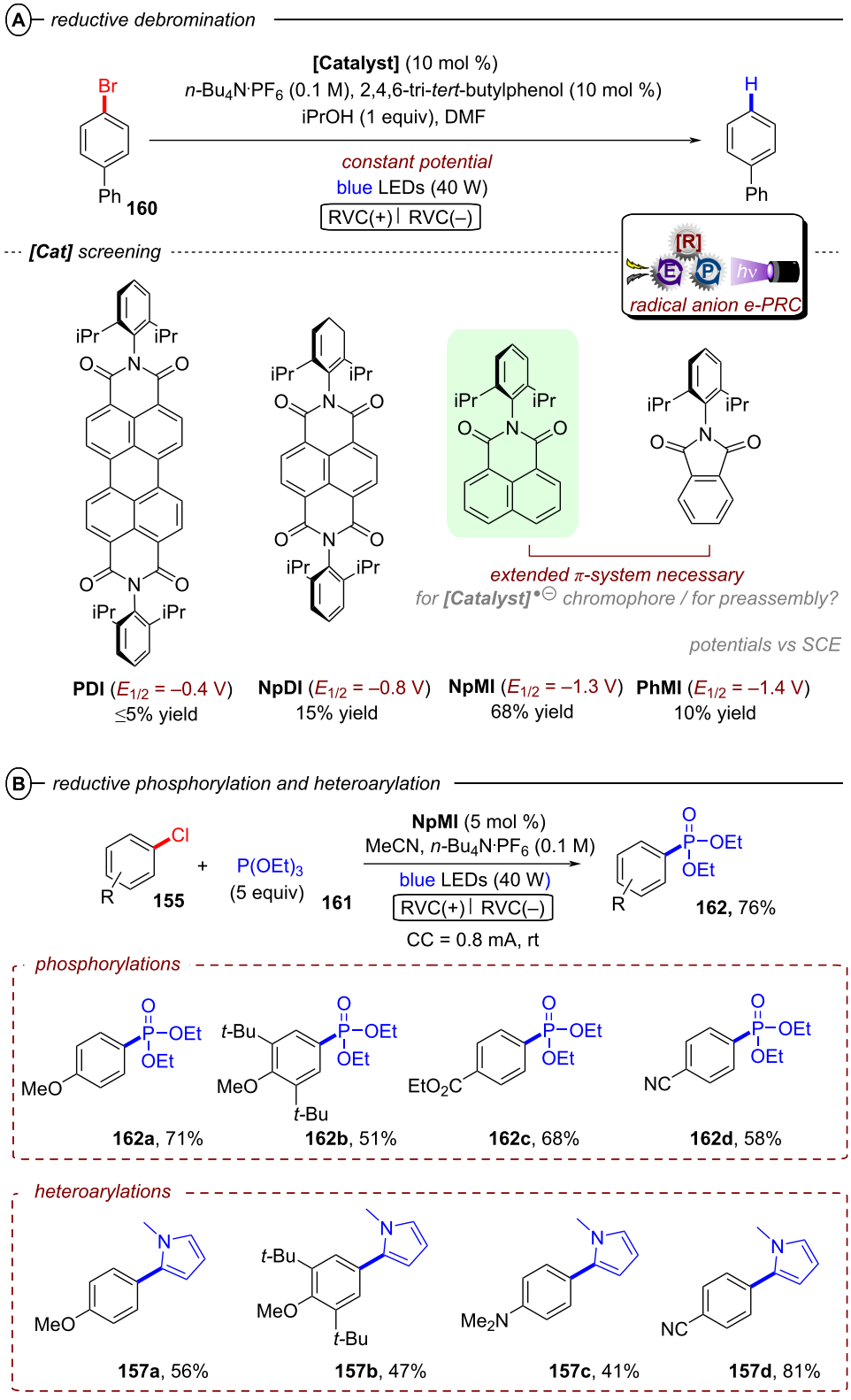

Figure 68: A) Screening of different phthalimide derivatives as catalyst for the e-PRC reduction of aryl halides. B) e-PRC Arbuzov reaction of aryl chlorides using **NpMI** as catalyst (top) and selected examples (bottom).

NpDI ($E_{1/2}$ = −0.8 V vs SCE) and **NpMI** ($E_{1/2}$ = −1.32 V vs SCE), exhibited much improved yields (15% and 68%, respectively). This finding is intriguing since the reactivity of **PDI** was known both under electrochemical and photochemical conditions (after excitation with two photons, vide supra) [15,309], whereas the reactivities of **NpDI** and **NpMI** derivatives were previously little explored, despite photophysical experiments indicating they would furnish more potent reductants by electron-priming [310]. The screening of catalysts concluded with the phthalimide derivative **PhMI** ($E_{1/2}$ = −1.4 V vs SCE), which was far less effective than **NpMI** despite a comparable redox potential. The extended naphthalene π-system is clearly necessary (either for photoexcitation or to promote a preassembly with the target substrate).

Thus, the Wickens group employed **NpMI** as catalyst for an e-PRC Arbuzov reaction [311], beginning with aryl chlorides (**155** in Figure 68B) [308]. Generally, the photo-Arbuzov reaction refers to a carbon–phosphorus bond-forming reaction that proceeds through an aryl radical intermediate to generate a pentavalent phosphorus species (vide supra, section 2.1.1) [312]. Wickens' group utilized triethylphosphite **161** to trap the aryl radical generated via SET to the chloride from the radical anion ***NpMI**$^{\bullet-}$ (*$E_{1/2}$ = −2.81 V vs SCE), the latter of which was generated by cathodic reduction and photoexcitation (Figure 68B).

Aryl chloride substrates bearing potentially sensitive functional groups such as esters (**162c**) and nitriles (**162d**) were suitable for SET phosphorylation. Overall, good yields of products were observed, providing a PEC strategy that is complementary to the subsequently reported conPET method (discussed vide supra, Figure 11). The method was expanded to heteroarylations using *N*-methylpyrrole as the trapping reagent, affording products **157a**–**d** in moderate to high yields (41–81%).

In particular, the reaction successfully engaged 4-chloroanisole (**162a**) and an even electron-richer aryl chloride (E^{p}_{red} = −3.4 V vs SCE) was converted (**162b**). This result indicates that ***NpMI**$^{\bullet-}$ possesses a reductive redox power that is i) comparable to the photoactive species in the study of Lambert, Lin and co-workers [302] and ii) comparable to that of Li^0 (−3.3 V vs SCE). Finally, both reports from the groups of Lambert/Lin and Wickens found that e-PRC gave higher preparative yields compared to direct electrolysis conditions [313], and dehalogenation was not observed, demonstrating the key selectivity benefit of e-PRC compared to electrolysis alone.

Following their investigation of the e-PRC reductive activation of arenes, Wickens and co-workers extended their methodology for reducing aryl halides to the reduction of aryl pseudohalides such as trialkylanilinium salts **163** and phosphonated phenols **164** (Figure 69) [314]. Initially, they screened various precatalysts that might, upon electro-activation and photoexcitation, serve as potent reductants to convert *N*,*N*,*N*-trimethylanilinium salt **163a** to benzene. Among the tested species, **NpMI** and its derivatives, such as **NpImz**, led to acceptable yields of benzene (41–42%). Precursors to persistent organic radical anions, including phenazine (**PZ**), fluorescein (**FC**), and 9*H*-fluoren-9-one (**FL**), generated similar yields of the product (34–45%). By contrast, employing isophtaionitrile scaffolds led to a substantial improvement in yield, with 1,2,3,5-tetrakis(carbazol-9-yl)-4,6-dicyanobenzene (**4-CzIPN**) [315] resulting in a 65% yield, while **4-DPAIPN** [316] gave the highest (98%) yield of benzene. Consequently, the latter compound was selected for the subsequent experiments, wherein C(sp^2)–N and C(sp^2)–O cleavage processes were performed using a constant potential of −1.6 V and 405 nm (Figure 70A).

The reaction conditions were well-tolerated by free alcohols (**165b**), esters (**165c**), and ethers, enabling C(sp^2)–N reduction in moderate to excellent yields (50–98%). In addition, despite the deep reduction potentials of phenol derivatives (E^{p}_{red} < −2.7 V vs SCE), a wide range of phosphate esters with base-sensitive functional groups yielded the products **165e**–**h** in moderate to excellent yields (46–97%) (Figure 70B). Aryl radical intermediates derived from anilinium salts and phosphonate esters could also be intercepted by trapping agents. The C(sp^2)–N and C(sp^2)–O precursors were found to undergo borylations, phosphonylations, and heteroarylations, affording products **162e,f**, **157e**, and **156c**.

Lastly, Bardagi and co-workers conducted a direct comparison of reductive aryl halide coupling reactions mediated by conPET and radical ion e-PRC [317]. Specifically, they investigated a family of naphthalene diimides (**NDI**) as (electro-activated) photocatalysts for the reductive coupling of 4-bromobenzonitrile (**166**) with benzene. The authors synthesized a range of diimides from commercially available naphthalene-1,4,5,8-tetracarboxylic acid dianhydride (**NDA**) and a variety of amines, leading to **NDI1**–**5** shown in Figure 71A [318]. Under conPET conditions, DIPEA served as a sacrificial electron donor and DMSO as a solvent. Intriguingly, all catalysts promoted the cross-coupling, with **NDI2** delivering the highest yield of **167** (32%) after 48 h, and benzonitrile (**168**, 23% yield) as a byproduct. Encouraged by these results, the authors tested the same catalyst under e-PRC conditions, evaluating both constant current and potential conditions in a divided cell setup with graphite and platinum electrodes. The optimal conditions involved a constant current of −56 μA (employing a potential cutoff E^0 < −1.06 V) or a constant potential of −0.56 V. After 48 h, conditions afforded **167** with a yield of 25–27% and only

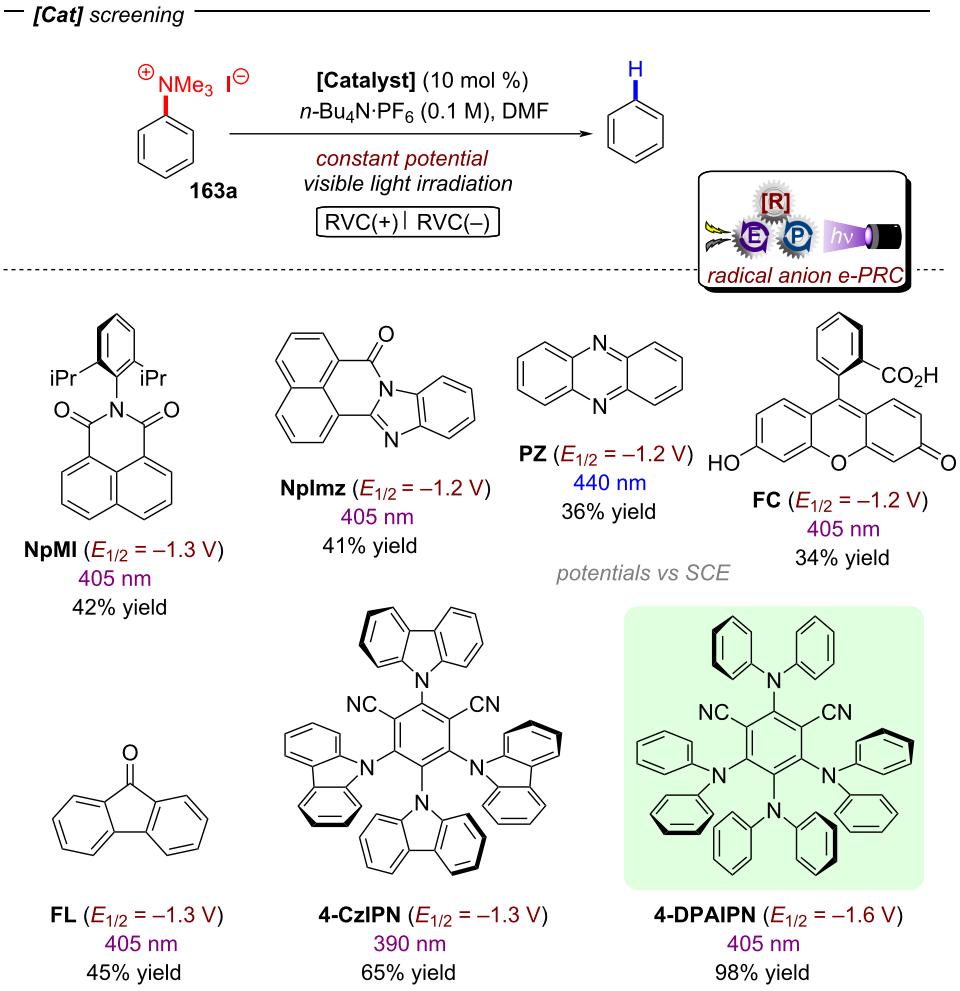

Figure 69: Screening of different organic catalysts for the e-PRC reduction of trialkylanilium salts.

6% of benzonitrile. These findings led the authors to conclude that both conPET and e-PRC approaches are comparably effective for such reductive couplings of aryl halides in terms of yields. While a conPET process requires a simpler setup, the e-PRC method improves the selectivity with respect to hydrodehalogenation (presumably due to the absence of DIPEA$^{\bullet+}$ as a H atom donor).

Regarding the mechanistic comparison (Figure 71B), blue LED irradiation of **NDI** in the presence of DIPEA generated **NDI**$^{\bullet-}$ via the conPET pathway, while cathodic reduction was employed in the e-PRC approach. The authors reported that the concentration of **NDI1**$^{\bullet-}$ was ≈5 × 10^{-5} M, indicating that PET from DIPEA to **NDI1*** was efficient and BET were sufficiently slow to ensure build up of a stable concentration of the radical anion in the solution. Interestingly, electrochemical generation of **NDI1**$^{\bullet-}$ led to even higher concentrations (≈0.7–2.0 × 10^{-4} M), possibly due to the absence of sacrificial electron donors in the cathodic chamber which prevented BET. Following photoexcitation, the authors proposed SET from *__NDI__$^{\bullet-}$ to **166** (E^{p}_{red} = −1.94 V vs SCE). This step was feasible, considering the estimated reduction potential of *__NDI3__$^{\bullet-}$ (*$E_{1/2}$ = −2.14 V vs SCE) based on $E_{0\text{-}0}$ = −1.64 V [310]. After this crucial step, rapid mesolytic cleavage of [**166**]$^{\bullet-}$ occurred ($10^{9–11}$ s^{-1}) [76] to yield the aryl radical, which could either i) abstract a H atom from the solvent (or DIPEA$^{\bullet+}$) to generate byproduct benzonitrile (*grey path*) or ii) undergo homolytic aromatic substitution (HAS) with benzene to ultimately furnish coupling product **167**.

3.2.2 C(sp^3)–X activation: C(sp^3)–O bond cleavages are high priority targets, since alcohols are widely abundant feedstocks deriving from nature and industrial hydroformylation processes. Classically, this is achieved by elimination (acid- or base-catalyzed) that can require high temperatures and do not tolerate sensitive functional groups, requiring additional protection steps

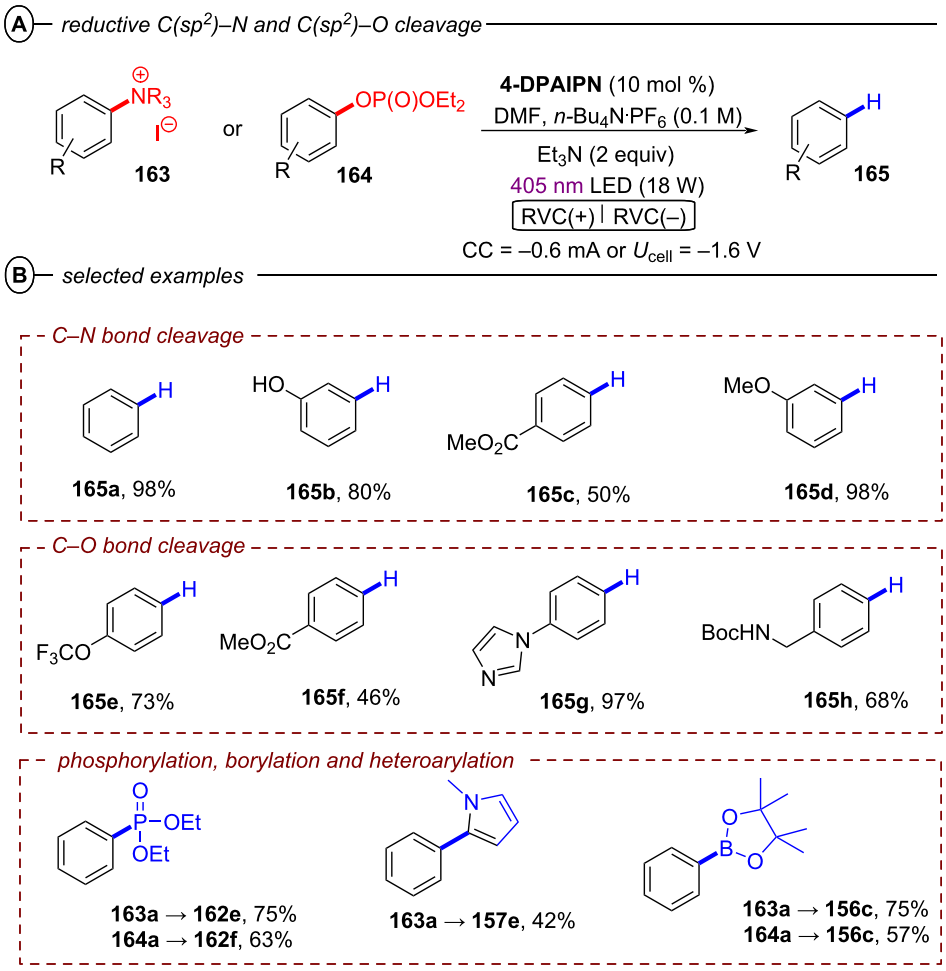

Figure 70: A) e-PRC reduction of phosphonated phenols and anilinium salts. B) Selected examples from the substrate scope.

elsewhere in the molecule. Within this context, Barham, König and co-workers reported the first e-PRC reductive cleavage of an aliphatic C(sp^3)–X bond – namely C(sp^3)–O bonds of phosphinates of alkyl alcohols **169** – giving rise to olefins or deoxygenated products (Figure 72A) [319]. Here, *N*-(*para*-butoxyphenyl)naphthalene monoimide (***n*-BuO-NpMI**) was employed as an electro-activated photocatalyst, affording either i) olefination products **170** in a Corey–Winter-type process if there is a leaving group 'X' α- to the alcohol (X = Cl, Br), or ii) deoxygenation products **171** when X = H as a mild and tin-free alternative to the Barton–McCombie process [320,321].

In the mechanism, ***n*-BuO-NpMI** is reduced at the cathode and its radical anion ***n*-BuO-NpMI]$^{\bullet-}$** engages phosphinate **169** in a preassembly. Photoexcitation affords a potent reductant, ***[*n*-BuO-NpMI]$^{\bullet-}$** ($^*E_{1/2}$ = −2.8 V vs SCE) (Figure 72B). SET reduction of phospinate **169** (E^p_{red} = −2.4 to −2.6 V vs SCE) affords radical anion **171$^{\bullet-}$**, effecting C(sp^3)–O bond cleavage (which is likely facilitated by the assembly) to liberate the phosphinate and generate C(sp^3) radical **172**. A further SET reduction (either by the cathode or by ***n*-BuO-NpMI$^{\bullet-}$**) provides carbanion **173** in a radical polar crossover [322,323]. With the optimized conditions in hand, the authors explored a wide range of olefination reactions (Figure 73).

Symmetrical and unsymmetrical *Z*-stilbenes **170a–c** were obtained in high yields with a tandem reduction/isomerization process under the PEC conditions. Interestingly, this represents the first example of a radical ion catalytic system that functions both as a potent SET reductant and in a subsequent *E*/*Z* isomerization. Cyclic olefins could be readily accessed, giving products **170d–g** in good to high yields (69–73%). This is an important achievement since such types of internal olefins are difficult to access with classical olefination reactions and typically require acid-/base-catalyzed eliminations whose site-selectivity is hard to control. For example, while terminal olefin **170h** was

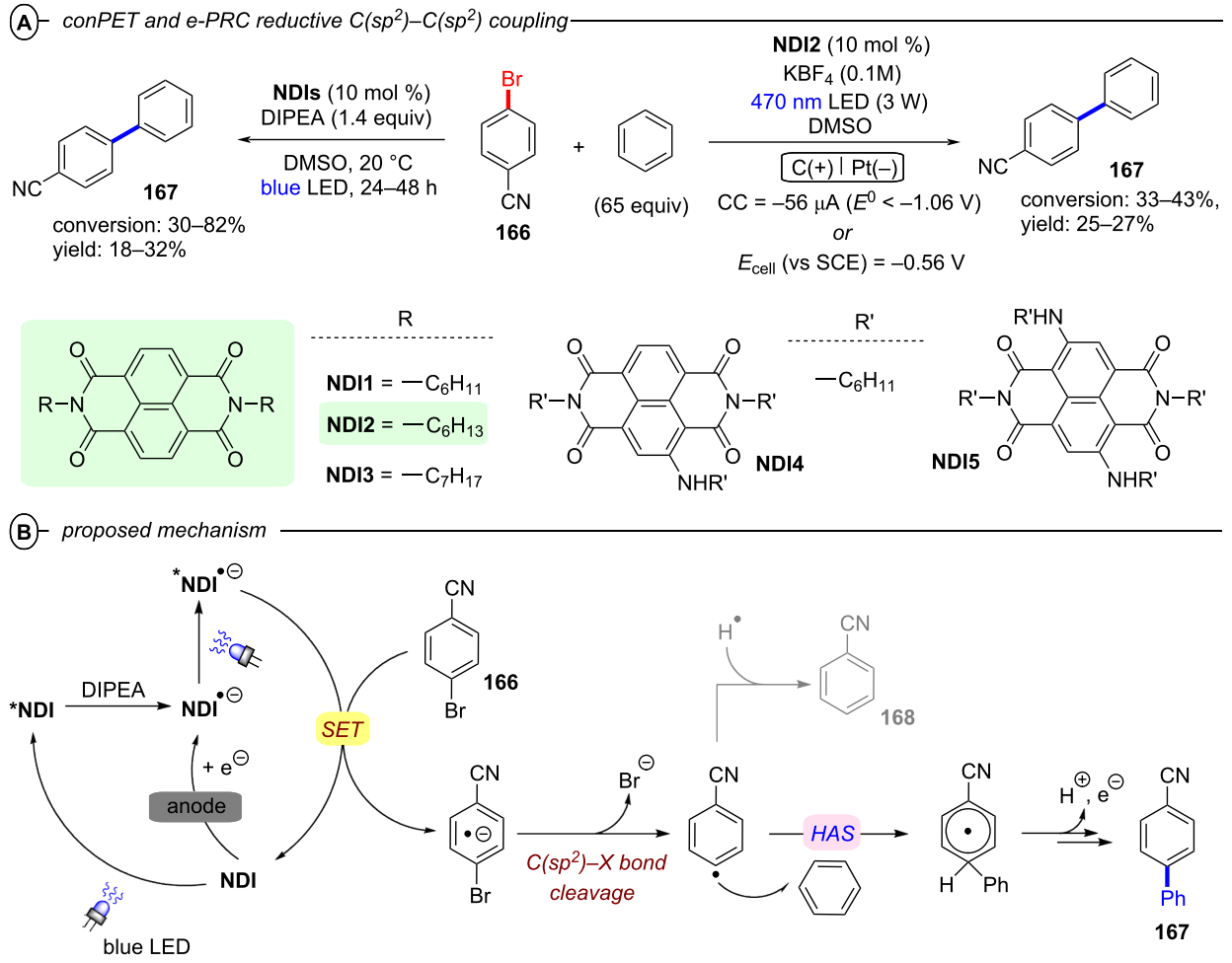

Figure 71: A) ConPET and e-PRC reduction of 4-bromobenzonitrile using a naphthalene diimide (**NDI**) precatalyst and aryl radical coupling with benzene. B) Proposed mechanism for conPET and e-PRC protocols.

obtained by the e-PRC method, conventional dehydration of the corresponding tertiary alcohol would lead to the most substituted double C–C bond.

Interestingly, despite the deeply reducing electro-activated photocatalyst, the reaction tolerated reductively labile substituents such as Ar–CF_3 (**170i**) and Ar–$OP(OR)_2$ (**170l**, reductive cleavage of which was later reported by Wickens and co-workers using ***[4-DPAIPN]**$^{\bullet-}$, vide supra, Figure 70). *The authors thus questioned whether even halogens could be tolerated, which would go against all expectations from all the aforementioned conPET and e-PRC reports*. For this purpose, phosphinates with either Ar–Cl or Ar–Br substituents were tested and products **170m–o** were generated in modest to good yields (39–69%). Only traces of dehalogenated styrene were observed, which was highly surprising i) in contrast to the reports of Wickens and Lin/Lambert (vide supra), ii) given the potent reductive power of ***[*n*-BuO-NpMI]**$^{\bullet-}$ and iii) despite the similar redox potentials of phosphinates and aryl halides (E^{p}_{red} = −2.4 V for 4-bromobiphenyl [308]). The authors' computational, spectroscopic and catalyst structural variation experiments (i.e., **NpMI** did not work) revealed that the *N*-aniline moiety of the radical anion catalyst engages in an intimate and selective preassembly with target substrates, facilitating a rate determining C(sp^3)–O cleavage step and ensuring redox chemoselectivity over dehalogenations/other reductive cleavages. The preference for a π-stacking preassembly of the *N*-aniline moiety of ***n*-BuO-NpMI**$^{\bullet-}$ at the diarylphosphinate group, rather than the aryl halide, could rationalize the tolerance of aryl halides. Finally, styrene-forming substrates containing a longer-chain aliphatic or a benzyl group retained high *E*-isomer selectivity (**170p,q**). e-PRC deoxygenations were also achieved, affording 1,2-diphenylethane **171a** and limonene **171b**.

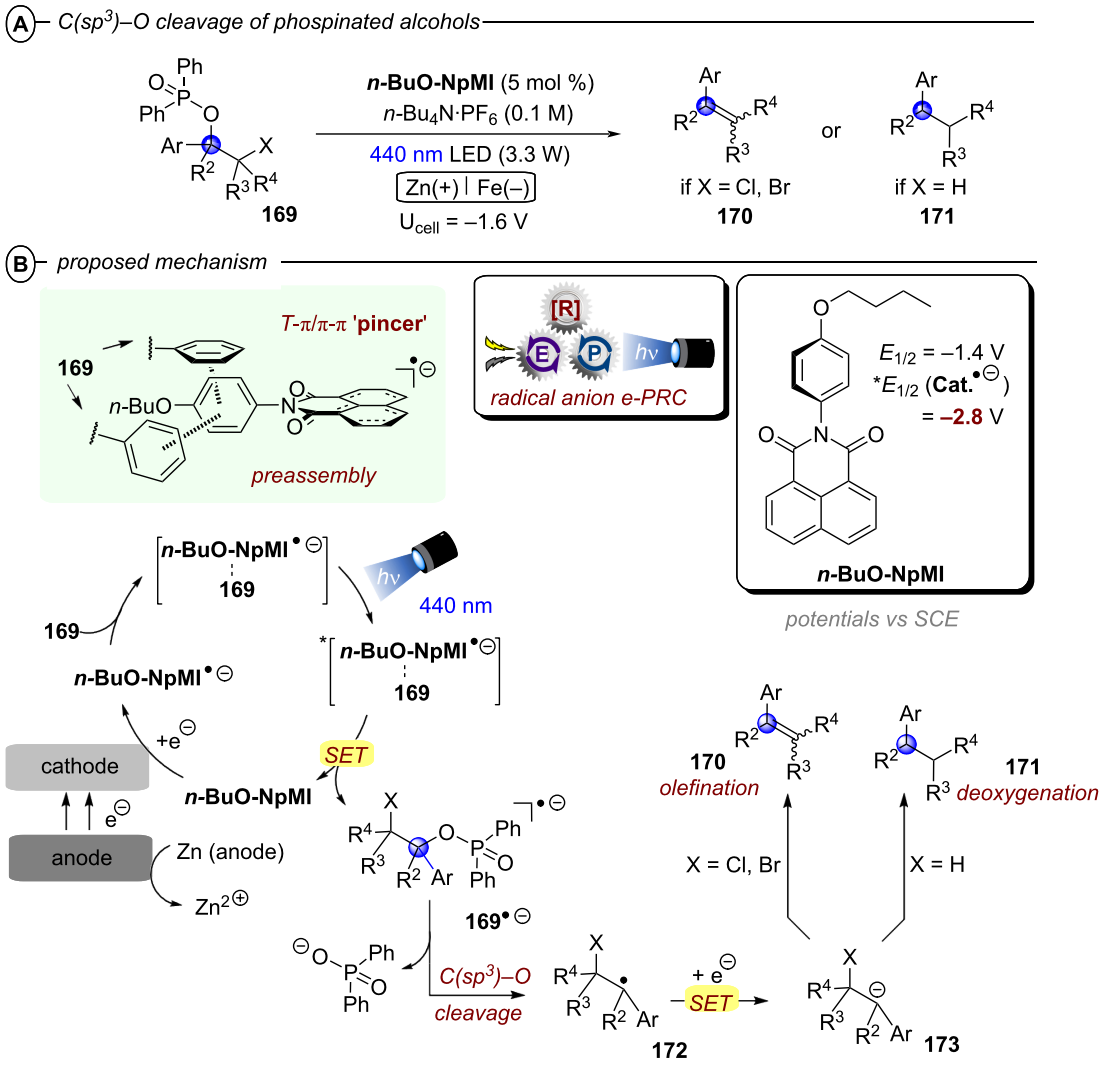

Figure 72: A) Radical ion e-PRC reduction of phosphinated aliphatic alcohols with ***n*-BuO-NpMI** as catalyst. B) Catalytic cycle including proposed preassembly.

Analogously to Mikaye's conPET study (vide supra, section 2.1.4), the authors observed a nanosecond-lived emitting state with an $E_{0\text{-}0}$ value (56.6 kcal mol^{-1}) similar to the triplet energy of the *E*-stilbene (51 kcal mol^{-1}), which rationalized the Z-stilbene formation by an energy transfer *E*/*Z*-photoisomerization pathway. This was ascribed to a quartet state ^{*4}[***n*-BuO-NpMI**$^{\bullet-}$], arising from ISC from the doublet state ^{*2}[***n*-BuO-NpMI**$^{\bullet-}$]. The possibility of a closed-shell decomposition product of the catalyst with a similar singlet excited state lifetime (as reported by Nocera and co-workers) functioning in the *E*/*Z*-stilbene photoisomerism cannot be fully ruled out [324]. However, the emitting species/a closed-shell decomposition species can be excluded as the SET reductant since i) its TCSPC lifetime was not quenched by phosphinate esters, ii) the clear influence of the *N*-aniline substituent, electronically disconnected from the naphthalene moiety which is where the transformation to the closed-shell decomposed catalyst occurs.

Shifting focus away from C(sp^3)–O cleavages to C(sp^3)–Cl cleavages, the direct generation of R$^\bullet$ from alkyl halides – that are challenging to reduce [325,326] – is a crucial aspect in modern chemical transformations [327-332] that allows i) to avoid issues with traditional alkylation and ii) to open a complementary radical reactive mode. Hence, there has been a considerable interest in expanding the pool of alkyl halides compatible with this type of transformation [325,333,334]. Peters and co-worker reported how a dicopper diamond-type complex (referred to as **[Cu$_2$]** in Figure 74A), previously developed in their laboratory [335], served as an interesting electro-recycled

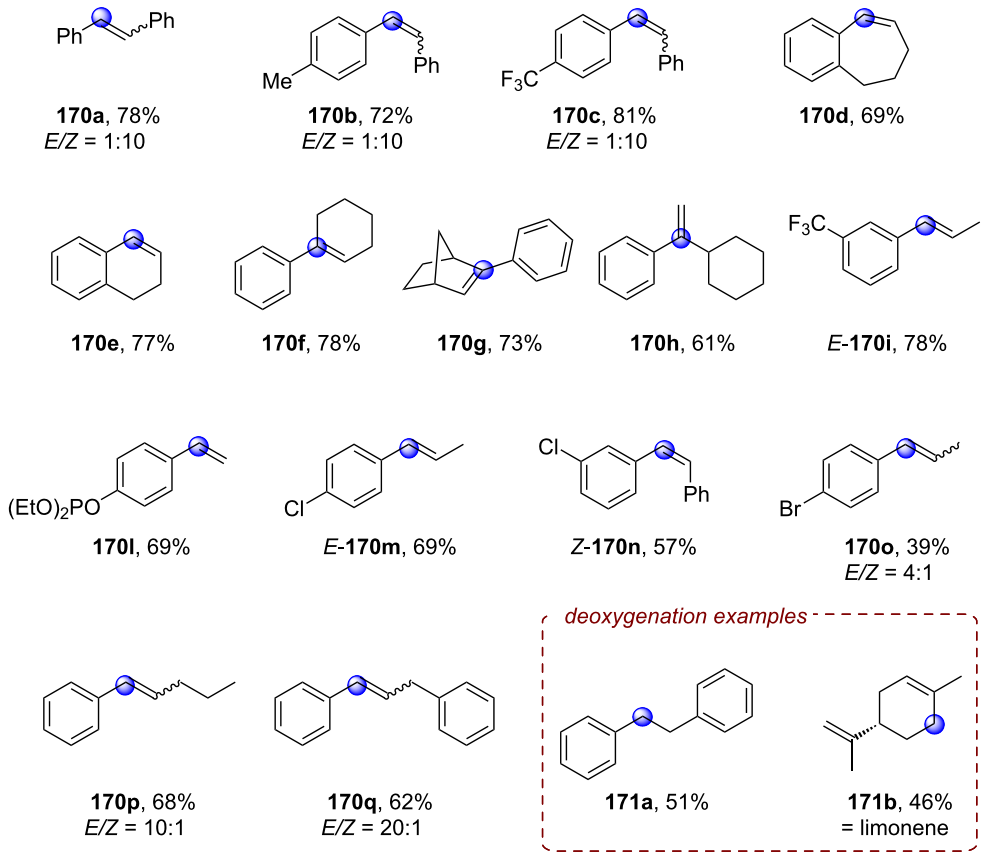

Figure 73: Selected examples from the substrate scope.

photoredox catalyst for the reductive dimerization of benzylic chlorides **174** (Figure 74A) [336]. According to the authors, this specific catalyst was ideal for reductive processes owing to i) its charge delocalization over the $Cu_2(\mu\text{-}N)_2$ core, ii) the steric shieldng of the isobutyl and *tert*-butyl groups which renders the one-electron oxidized state $\mathbf{[Cu_2]^+}$ non-nucleophilic, avoiding undesirable reactions of the benzylic radical and the ligands.

The authors proposed a mechanism based on Stern–Volmer (SV) and time-resolved luminescence spectroscopy experiments. Firstly, $\mathbf{[Cu_2]}$ is photoactivated to generate a potent excited-state reductant, $^*\mathbf{[Cu_2]}$ ($^*E_{1/2}$ = −2.7 V vs SCE). SET reduction of benzyl chloride **174** (R = Me, E^p_{red} = −2.5 V vs SCE) yields benzylic radical **174•** and the ground state oxidized catalyst $\mathbf{[Cu_2]^+}$ (Figure 74B). Dimerization of **174•** generates coupling product **170**, while $\mathbf{[Cu_2]^+}$ is reduced at the cathode to complete a recycling e-PRC process. Under the optimized reaction conditions, $LiNTf_2$ serves two roles: i) a supporting electrolyte, and ii) a chloride scavenger; since the chloride byproduct from reductive C–Cl bond cleavage can interfere with $\mathbf{[Cu_2]^+}$. This undesirable reaction between catalyst and chloride was confirmed by observing the color change of a solution containing $\mathbf{[Cu]^+}$ with or without LiCl. Without the addition of the chloride source, the solution appeared brown in DME, a color attributed to the active form of the catalyst. In the presence of LiCl, a loss of red-brown color occurred over several hours, resulting in a yellow solution and inactive catalyst. The optimal reaction conditions tolerated electron-withdrawing groups *para*- to the benzylic chloride such as esters and nitriles (**170a**,**b**, Figure 74C) as well as electron-donating groups like methyl, methoxy (**170c**,**d**) and alkynyl (**170e**) groups. Secondary and tertiary benzylic chlorides were successfully reductively dimerized, affording the products **170f**–**h** in good yields. However, the transformation was limited to homodimerizations and no crossed dimerizations were achieved.

Finally, a C(sp^3)–N bond cleavage was achieved by the group of Chen and co-workers, complementing the well-explored field of PEC alkylation of heteroarenes (vide supra, section 3.1.2). The authors employed *d*PEC deamination (Figure 75A) in a reductive process [337] that cleaved Katritzky salts **177** [338-340] to generate alkyl radicals. Broadly speaking, SET reduction of **177** produces species **177'**, followed by exothermic fragmentation that provides alkyl species **179** (Figure 75B-*i*). However, compared to endothermic addition of radicals to heterocycles, exothermic radical coupling with precursor **177'** is often ob-

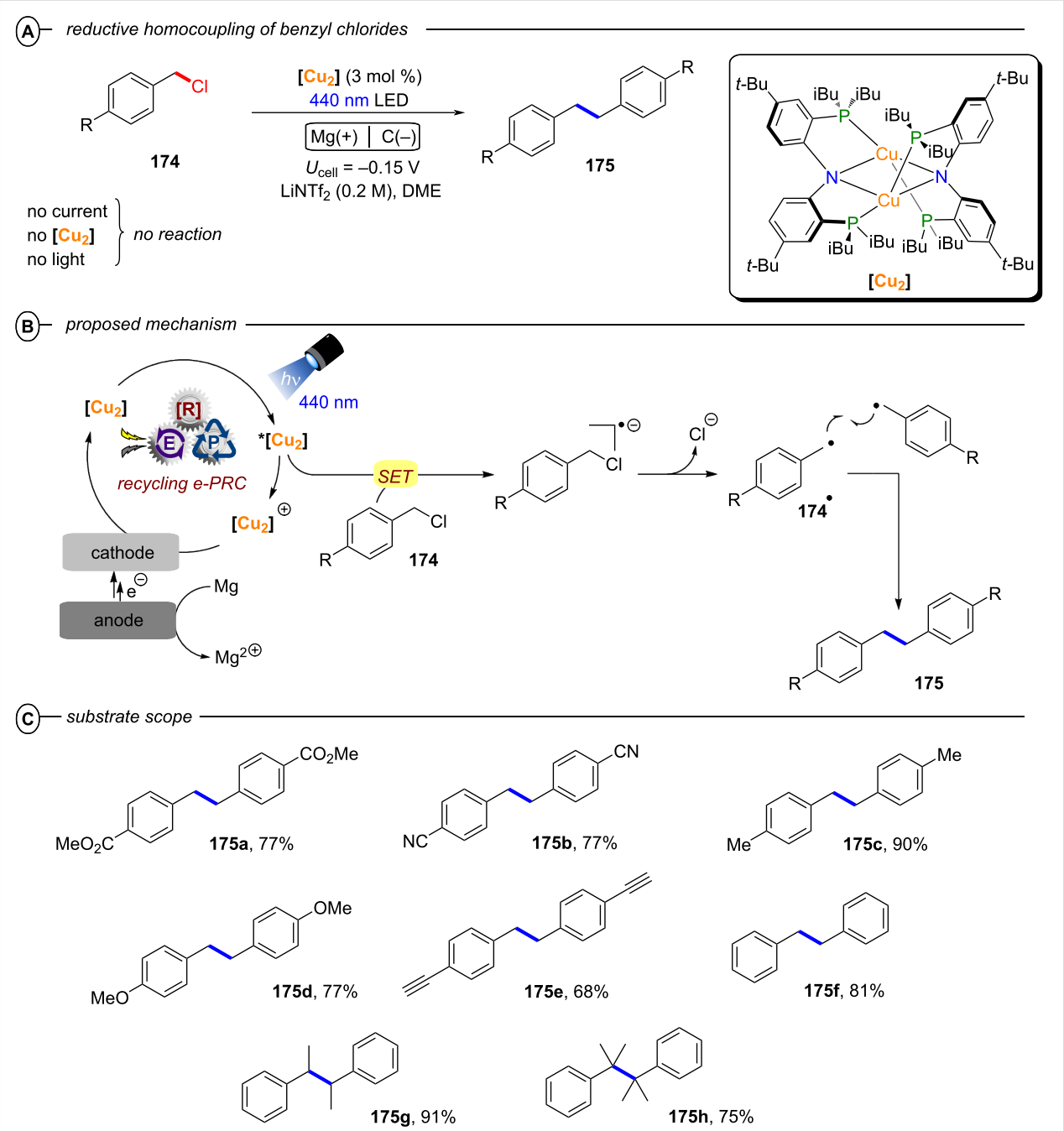

Figure 74: A) Recycling e-PRC reductive dimerization of benzylic chlorides using a [Cu$_2$] catalyst. B) Proposed mechanism. C) Substrate scope.

served thus inhibiting the target reaction (Figure 75B-*ii*) [341,342]. Despite the less than encouraging premises [343], Chen and co-workers managed to develop a deaminative *d*PEC C–H alkylation method for quinoline **176** using Ru(bpy)$_3$·6H$_2$O as a photocatalyst, obtaining the products in good yields with minimum quantities of byproduct **180** (Figure 75B). According to the authors, constant potential conditions were indispensable to selectively reduce the Katritzky salts and not the quinolines and/or the products.

As shown in Figure 75C, when **176** was substituted at the 2-position, alkylation selectively occurred at the 4-position (such as in **178a**), while 2-position was regioselectivity obtained starting from 4-position substituted starting materials (such as **178g**). Regarding the quinoline derivatives scope, electron-donating groups such as methoxy or *tert*-butyl worked well with different acceptors (**178b**,**c** in Figure 75C). Weakly electron-withdrawing functionalities, for example, fluoro- and chloro-substituted substrates, worked smoothly (**178d** and **178e**) and bromo-

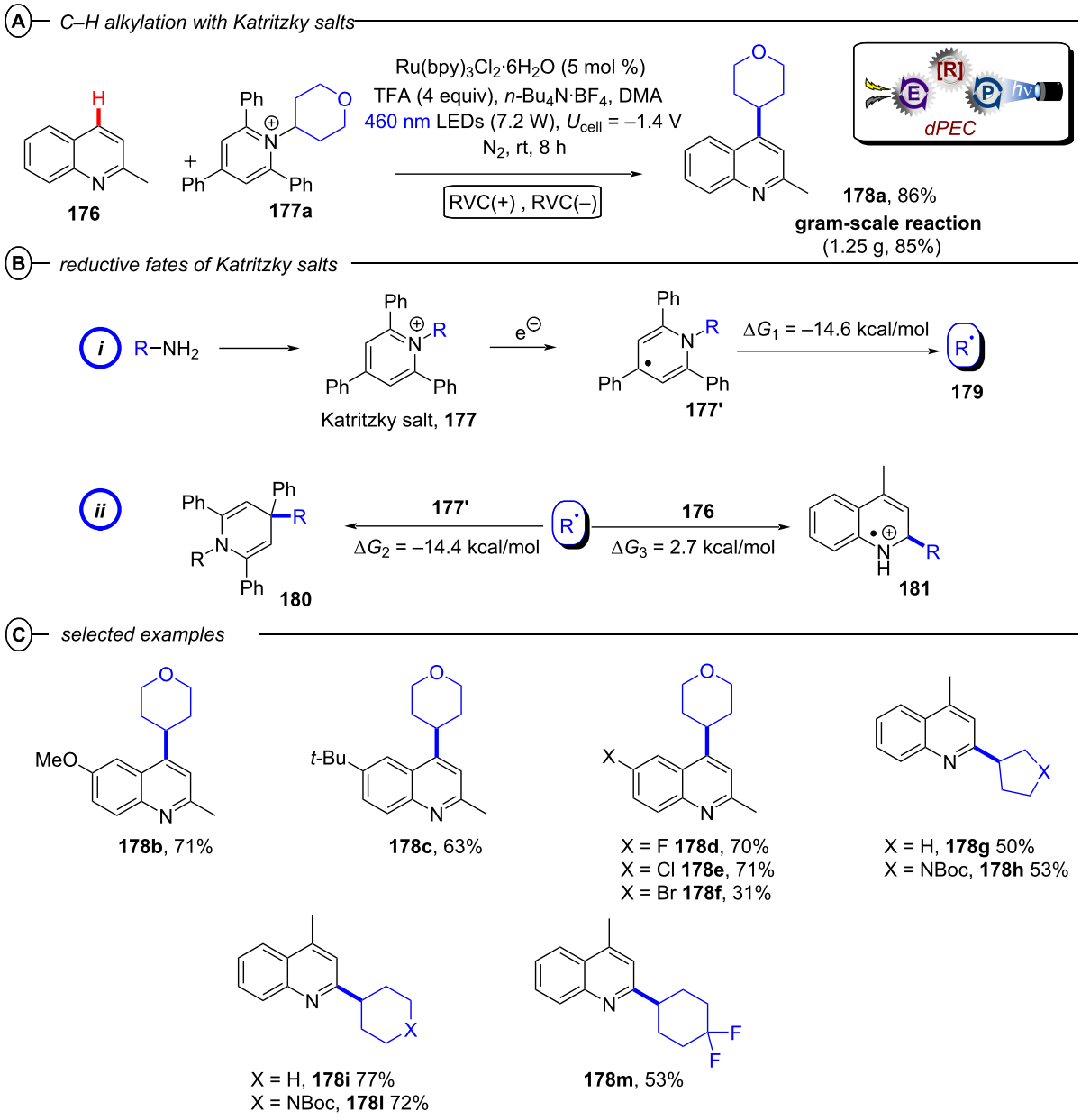

Figure 75: A) Decoupled photoelectrochemical C–H alkylation of heteroarenes through deamination of Katritzky salts. B) Alkyl radical generation and competing pathways for the downstream radical chemistry. C) Selected examples from the substrate scope.

substituted substrates provided the corresponding product in moderate yields accompanied by a debromination byproduct (**178f**). Then, several alkyl partners were tested, resulting in products such as **178g–m** using cyclopentyl- and cyclohexyl-derivatives. Finally, the authors successfully scaled the process in a batch set-up for the model substrate, obtaining **178a** on a 6.5 mmol scale with 85% yield. Through detailed investigations (CV analysis, spectrometric analysis, UV–vis and quenching studies) the authors proposed a *d*PEC mechanism (Figure 76).

Firstly, cathodic reduction of the Katritzky salt **177a** produces the persistent radical species **177a'**, followed by its exothermic fragmentation to generate alkyl radical **179a**, whose BHT complex was observed in GC–MS analysis by the authors. The latter incurred endothermic radical addition to the protonated quinoline **176**-H, leading to the radical **181a**, whose SET reduction by excited state $*[Ru^{II}(bpy)_3]$ delivers the intermediate **182** (detected by HRMS) and regenerates $[Ru^{III}(bpy)_3]$. The protonated product **178a**-H is obtained through anodic oxidation of **182** (black path). Alternatively, the authors proposed deproton-

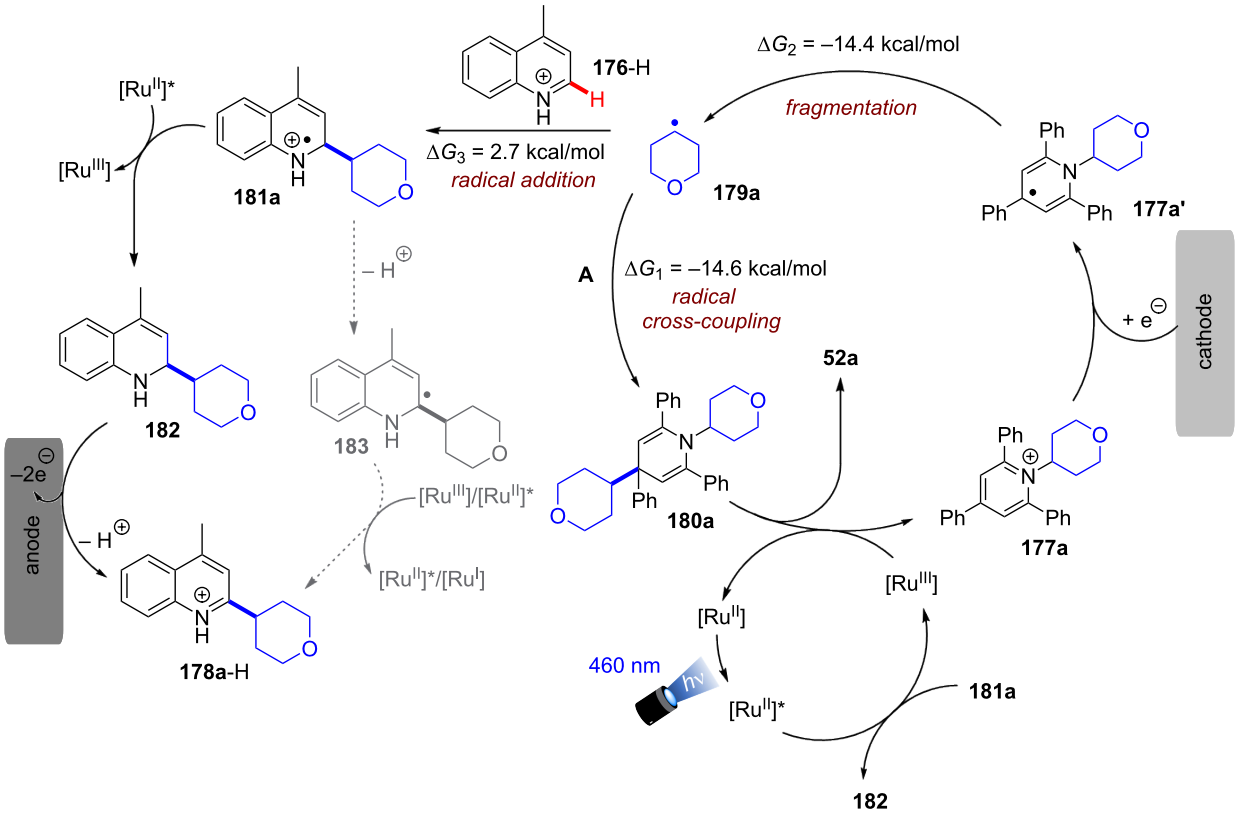

Figure 76: Proposed mechanism by Chen and co-workers.

ation of **181a** would afford radical **183**, which could be oxidized by ***[Ru^{II}(bpy)$_3$]** or **[Ru^{III}(bpy)$_3$]** (grey-dashed path). Lastly, although during the electrolysis considerable quantities of radical exergonic cross-coupling product **180a** are obtained, which can be oxidized by the **[Ru^{III}]** species to regenerate **177a**.

Summary and Outlook

The Review reported consecutive photoinduced electron transfer and synthetic photoelectrochemistry (with a focus on electro-activated photoredox catalysis) as two promising fields that offer unique advantages and challenges to overcome the energetic limitations of photoredox catalysis. While both approaches involve SET reactions of the excited state of a photocatalyst and organic substrates, they differ in the generation of the active catalyst species and the reaction mechanism. In particular, we propose the most significant difference between the two techniques is *the steady-state concentration of in situ-generated radical ion catalyst* (generally lower for conPET due to the less efficient PET generation and the propensity for back-electron transfer). This heavily influences the chemoselectivity and ability of the catalyst to preassemble with target substrates.

Also, the profile of catalyst voltammograms might have interesting implications on the choice of conPET/e-PRC and the resulting reactivity. Catalysts with fully reversible voltammograms are generally required for e-PRC, permitting high steady-state concentrations of the active photocatalyst. On the other hand, catalysts exhibiting irreversible (or quasi-reversible) voltammograms might be employable in conPET due to the regulation of a lower steady-state concentration of the active photocatalyst by competing PET generation/BET reversion processes. The peculiarities of each method make them perfectly complementary: conPET in the oxidative direction is less explored than in the reductive direction, probably due to the lack of colored precursors to oxidative photocatalysts. On the other hand, e-PRC boasts a lot of examples for oxidative activations of organic functionalities – likely owing to the hydrogen evolution reaction (HER) as the ideal reductive counter reaction – yet less so for the reductive direction (possibly due to complications derived from sacrificial anode materials or the competing oxygen evolution reaction).

Regarding the initial ‘inhibition barrier’ for experimental application in academia and industry, conPET appears more easily accessible and scalable. However, considering that i) photons

cost more than electrons and ii) the cost of sacrificial chemical additives, PEC is ultimately the superior technology for industrial applications once standardized (flow) reactors can be developed to i) bring light and current/potential into the same flow path, ii) eliminate supporting electrolyte and iii) render robust, reproducible processes. Although the lack of tailor-made reactors has hampered the advancement of 'single pass flow' PEC protocols, several examples of gram-scale reactions in batch or recirculated flow are already present.

In conclusion, further developments of both techniques are desirable. These include for conPET i) the expansion of oxidative activations pool, ii) the exploration of neutral radical photocatalysts, and iii) the development of 'redox neutral' conPET reactions that consolidate both redox-activated partners into a single product (surprisingly, this is yet to be achieved). Regarding e-PRC, cutting-edge technologies to establish truly scalable processes are required. Of high priority in both e-PRC and conPET reactions is conducting further investigations into the mechanism. In particular, noncovalent aggregations of photocatalysts and substrates is a topic receiving increasing attention in the literature [344,345], and – specifically for radical ion photocatalysis – further investigations into catalyst-substrate pre-association are urgently needed to i) explain unexpected wavelength dependencies and ii) to rationalize how ultrashort-lived excited states can provide productive photochemistry. Transformation of the species designated 'catalyst' (to another photoactive catalyst) and how this is influenced by reaction conditions/concentration (conPET/e-PRC) is also a priority topic for investigation. Such investigations will provide better understanding of these techniques and could potentially lead to the discovery of more efficient and selective catalysts.

Funding

M. L. and J. P. B. are members of the Elite Network of Bavaria Doctoral College: "IDK Chemical Catalysis with Photonic or Electric Energy Input" and M. L. is grateful to the College for financial support. S. S. is grateful for funding provided by the University of Regensburg and the SynCat programme of the Elite Network of Bavaria. J. P. B. acknowledges funding provided by the Alexander von Humboldt Foundation within the framework of the Sofja Kovalevskaja Award endowed by the German Federal Ministry of Education and Research. J. P. B. is an associated member of DFG TRR 325 'Assembly Controlled Chemical Photocatalysis' (444632635) and thanks other members of the TRR for insightful discussions.

ORCID® iDs

Mattia Lepori - https://orcid.org/0009-0001-7576-8634
Simon Schmid - https://orcid.org/0009-0001-0436-5491
Joshua P. Barham - https://orcid.org/0000-0003-1675-9399

References

1. Ashby, E. C. *Acc. Chem. Res.* **1988,** *21,* 414–421. doi:10.1021/ar00155a005
2. Zhang, N.; Samanta, S. R.; Rosen, B. M.; Percec, V. *Chem. Rev.* **2014,** *114,* 5848–5958. doi:10.1021/cr400689s
3. Broggi, J.; Terme, T.; Vanelle, P. *Angew. Chem., Int. Ed.* **2014,** *53,* 384–413. doi:10.1002/anie.201209060
4. van der Vlugt, J. I. *Chem. – Eur. J.* **2019,** *25,* 2651–2662. doi:10.1002/chem.201802606
5. Plesniak, M. P.; Huang, H.-M.; Procter, D. J. *Nat. Rev. Chem.* **2017,** *1,* 0077. doi:10.1038/s41570-017-0077
6. Zhang, C.; Tang, C.; Jiao, N. *Chem. Soc. Rev.* **2012,** *41,* 3464. doi:10.1039/c2cs15323h
7. Chuang, K. V.; Xu, C.; Reisman, S. E. *Science* **2016,** *353,* 912–915. doi:10.1126/science.aag1028
8. He, C.; Stratton, T. P.; Baran, P. S. *J. Am. Chem. Soc.* **2019,** *141,* 29–32. doi:10.1021/jacs.8b13029
9. Joshi, D. K.; Sutton, J. W.; Carver, S.; Blanchard, J. P. *Org. Process Res. Dev.* **2005,** *9,* 997–1002. doi:10.1021/op050155x
10. Evans, W. J.; Lee, D. S.; Rego, D. B.; Perotti, J. M.; Kozimor, S. A.; Moore, E. K.; Ziller, J. W. *J. Am. Chem. Soc.* **2004,** *126,* 14574–14582. doi:10.1021/ja046047s
11. Arias-Rotondo, D. M.; McCusker, J. K. *Chem. Soc. Rev.* **2016,** *45,* 5803–5820. doi:10.1039/c6cs00526h
12. Roth, H. G.; Romero, N. A.; Nicewicz, D. A. *Synlett* **2015,** *27,* 714–723. doi:10.1055/s-0035-1561297
13. Nelson, N.; Ben-Shem, A. *Nat. Rev. Mol. Cell Biol.* **2004,** *5,* 971–982. doi:10.1038/nrm1525
14. Govindjee; Shevela, D.; Björn, L. O. *Photosynth. Res.* **2017,** *133,* 5–15. doi:10.1007/s11120-016-0333-z
15. Ghosh, I.; Ghosh, T.; Bardagi, J. I.; König, B. *Science* **2014,** *346,* 725–728. doi:10.1126/science.1258232
16. Rombach, D.; Wagenknecht, H.-A. *ChemCatChem* **2018,** *10,* 2955–2961. doi:10.1002/cctc.201800501
17. Glaser, F.; Kerzig, C.; Wenger, O. S. *Angew. Chem., Int. Ed.* **2020,** *59,* 10266–10284. doi:10.1002/anie.201915762
18. Ghosh, I.; Shaikh, R. S.; König, B. *Angew. Chem., Int. Ed.* **2017,** *56,* 8544–8549. doi:10.1002/anie.201703004
19. Coles, M. S.; Quach, G.; Beves, J. E.; Moore, E. G. *Angew. Chem., Int. Ed.* **2020,** *59,* 9522–9526. doi:10.1002/anie.201916359
20. Glaser, F.; Kerzig, C.; Wenger, O. S. *Chem. Sci.* **2021,** *12,* 9922–9933. doi:10.1039/d1sc02085d
21. Kerzig, C.; Goez, M. *Chem. Sci.* **2016,** *7,* 3862–3868. doi:10.1039/c5sc04800a
22. Horn, E. J.; Rosen, B. R.; Baran, P. S. *ACS Cent. Sci.* **2016,** *2,* 302–308. doi:10.1021/acscentsci.6b00091
23. Meyer, T. H.; Choi, I.; Tian, C.; Ackermann, L. *Chem* **2020,** *6,* 2484–2496. doi:10.1016/j.chempr.2020.08.025
24. Moeller, K. D. *Tetrahedron* **2000,** *56,* 9527–9554. doi:10.1016/s0040-4020(00)00840-1
25. Wiebe, A.; Gieshoff, T.; Möhle, S.; Rodrigo, E.; Zirbes, M.; Waldvogel, S. R. *Angew. Chem., Int. Ed.* **2018,** *57,* 5594–5619. doi:10.1002/anie.201711060
26. Yan, M.; Kawamata, Y.; Baran, P. S. *Chem. Rev.* **2017,** *117,* 13230–13319. doi:10.1021/acs.chemrev.7b00397

27. Kawamata, Y.; Hayashi, K.; Carlson, E.; Shaji, S.; Waldmann, D.; Simmons, B. J.; Edwards, J. T.; Zapf, C. W.; Saito, M.; Baran, P. S. *J. Am. Chem. Soc.* **2021,** *143,* 16580–16588. doi:10.1021/jacs.1c06572
28. Barham, J. P.; König, B. *Angew. Chem., Int. Ed.* **2020,** *59,* 11732–11747. doi:10.1002/anie.201913767
29. Wu, S.; Kaur, J.; Karl, T. A.; Tian, X.; Barham, J. P. *Angew. Chem., Int. Ed.* **2022,** *61,* e202107811. doi:10.1002/anie.202107811
30. Pitzer, L.; Schwarz, J. L.; Glorius, F. *Chem. Sci.* **2019,** *10,* 8285–8291. doi:10.1039/c9sc03359a
31. Wiles, R. J.; Molander, G. A. *Isr. J. Chem.* **2020,** *60,* 281–293. doi:10.1002/ijch.201900166
32. Cai, C.-Y.; Lai, X.-L.; Wang, Y.; Hu, H.-H.; Song, J.; Yang, Y.; Wang, C.; Xu, H.-C. *Nat. Catal.* **2022,** *5,* 943–951. doi:10.1038/s41929-022-00855-7
33. Lai, X.-L.; Chen, M.; Wang, Y.; Song, J.; Xu, H.-C. *J. Am. Chem. Soc.* **2022,** *144,* 20201–20206. doi:10.1021/jacs.2c09050
34. Kalyani, D.; McMurtrey, K. B.; Neufeldt, S. R.; Sanford, M. S. *J. Am. Chem. Soc.* **2011,** *133,* 18566–18569. doi:10.1021/ja208068w
35. Nguyen, J. D.; Tucker, J. W.; Konieczynska, M. D.; Stephenson, C. R. J. *J. Am. Chem. Soc.* **2011,** *133,* 4160–4163. doi:10.1021/ja108560e
36. Hari, D. P.; König, B. *Angew. Chem., Int. Ed.* **2013,** *52,* 4734–4743. doi:10.1002/anie.201210276
37. Huang, L.; Ackerman, L. K. G.; Kang, K.; Parsons, A. M.; Weix, D. J. *J. Am. Chem. Soc.* **2019,** *141,* 10978–10983. doi:10.1021/jacs.9b05461
38. Li, Y.; Ye, Z.; Lin, Y.-M.; Liu, Y.; Zhang, Y.; Gong, L. *Nat. Commun.* **2021,** *12,* 2894. doi:10.1038/s41467-021-23255-0
39. Magagnano, G.; Gualandi, A.; Marchini, M.; Mengozzi, L.; Ceroni, P.; Cozzi, P. G. *Chem. Commun.* **2017,** *53,* 1591–1594. doi:10.1039/c6cc09387f
40. Zeman, C. J., IV; Kim, S.; Zhang, F.; Schanze, K. S. *J. Am. Chem. Soc.* **2020,** *142,* 2204–2207. doi:10.1021/jacs.9b13027
41. Gong, H.-X.; Cao, Z.; Li, M.-H.; Liao, S.-H.; Lin, M.-J. *Org. Chem. Front.* **2018,** *5,* 2296–2302. doi:10.1039/c8qo00445e
42. Zeng, L.; Liu, T.; He, C.; Shi, D.; Zhang, F.; Duan, C. *J. Am. Chem. Soc.* **2016,** *138,* 3958–3961. doi:10.1021/jacs.5b12931
43. Shang, J.; Tang, H.; Ji, H.; Ma, W.; Chen, C.; Zhao, J. *Chin. J. Catal.* **2017,** *38,* 2094–2101. doi:10.1016/s1872-2067(17)62960-7
44. Caby, S.; Marín Oliva, L.; Bardagi, J. I. *J. Org. Chem.* **2023,** *88,* 711–716. doi:10.1021/acs.joc.2c02172
45. Ghosh, I.; König, B. *Angew. Chem., Int. Ed.* **2016,** *55,* 7676–7679. doi:10.1002/anie.201602349
46. Das, A.; Ghosh, I.; König, B. *Chem. Commun.* **2016,** *52,* 8695–8698. doi:10.1039/c6cc04366f
47. Shaikh, R. S.; Düsel, S. J. S.; König, B. *ACS Catal.* **2016,** *6,* 8410–8414. doi:10.1021/acscatal.6b02591
48. Eggins, B. R.; Robertson, P. K. J. *J. Chem. Soc., Faraday Trans.* **1994,** *90,* 2249–2256. doi:10.1039/ft9949002249
49. Nelleborg, P.; Lund, H.; Eriksen, J. *Tetrahedron Lett.* **1985,** *26,* 1773–1776. doi:10.1016/s0040-4039(00)98335-7
50. Cervantes-González, J.; Vosburg, D. A.; Mora-Rodriguez, S. E.; Vázquez, M. A.; Zepeda, L. G.; Villegas Gómez, C.; Lagunas-Rivera, S. *ChemCatChem* **2020,** *12,* 3811–3827. doi:10.1002/cctc.202000376
51. Bardagi, J. I.; Ghosh, I.; Schmalzbauer, M.; Ghosh, T.; König, B. *Eur. J. Org. Chem.* **2018,** 34–40. doi:10.1002/ejoc.201701461
52. Neumeier, M.; Sampedro, D.; Májek, M.; de la Peña O'Shea, V. A.; Jacobi von Wangelin, A.; Pérez-Ruiz, R. *Chem. – Eur. J.* **2018,** *24,* 105–108. doi:10.1002/chem.201705326
53. Beckwith, J. S.; Aster, A.; Vauthey, E. *Phys. Chem. Chem. Phys.* **2022,** *24,* 568–577. doi:10.1039/d1cp04014f
54. MacKenzie, I. A.; Wang, L.; Onuska, N. P. R.; Williams, O. F.; Begam, K.; Moran, A. M.; Dunietz, B. D.; Nicewicz, D. A. *Nature* **2020,** *580,* 76–80. doi:10.1038/s41586-020-2131-1
55. Chmiel, A. F.; Williams, O. P.; Chernowsky, C. P.; Yeung, C. S.; Wickens, Z. K. *J. Am. Chem. Soc.* **2021,** *143,* 10882–10889. doi:10.1021/jacs.1c05988
56. Hu, J.; Wang, J.; Nguyen, T. H.; Zheng, N. *Beilstein J. Org. Chem.* **2013,** *9,* 1977–2001. doi:10.3762/bjoc.9.234
57. Xu, J.; Cao, J.; Wu, X.; Wang, H.; Yang, X.; Tang, X.; Toh, R. W.; Zhou, R.; Yeow, E. K. L.; Wu, J. *J. Am. Chem. Soc.* **2021,** *143,* 13266–13273. doi:10.1021/jacs.1c05994
58. Hwang, L. K.; Na, Y.; Lee, J.; Do, Y.; Chang, S. *Angew. Chem., Int. Ed.* **2005,** *44,* 6166–6169. doi:10.1002/anie.200501582
59. Hilton, M. C.; Dolewski, R. D.; McNally, A. *J. Am. Chem. Soc.* **2016,** *138,* 13806–13809. doi:10.1021/jacs.6b08662
60. Toda, Y.; Komiyama, Y.; Kikuchi, A.; Suga, H. *ACS Catal.* **2016,** *6,* 6906–6910. doi:10.1021/acscatal.6b02265
61. Manabe, K. *Tetrahedron Lett.* **1998,** *39,* 5807–5810. doi:10.1016/s0040-4039(98)01181-2
62. Marcoux, D.; Charette, A. B. *J. Org. Chem.* **2008,** *73,* 590–593. doi:10.1021/jo702355c
63. Marcoux, D.; Charette, A. B. *Adv. Synth. Catal.* **2008,** *350,* 2967–2974. doi:10.1002/adsc.200800542
64. Huang, W.; Zhong, C.-H. *ACS Omega* **2019,** *4,* 6690–6696. doi:10.1021/acsomega.9b00568
65. Flynn, A. R.; McDaniel, K. A.; Hughes, M. E.; Vogt, D. B.; Jui, N. T. *J. Am. Chem. Soc.* **2020,** *142,* 9163–9168. doi:10.1021/jacs.0c03926
66. Koppenol, W. H.; Rush, J. D. *J. Phys. Chem.* **1987,** *91,* 4429–4430. doi:10.1021/j100300a045
67. Kasha, M. *Discuss. Faraday Soc.* **1950,** *9,* 14–19. doi:10.1039/df9500900014
68. Fox, M. A. *Chem. Rev.* **1979,** *79,* 253–273. doi:10.1021/cr60319a002
69. Demchenko, A. P.; Tomin, V. I.; Chou, P.-T. *Chem. Rev.* **2017,** *117,* 13353–13381. doi:10.1021/acs.chemrev.7b00110
70. Seegerer, A.; Nitschke, P.; Gschwind, R. M. *Angew. Chem., Int. Ed.* **2018,** *57,* 7493–7496. doi:10.1002/anie.201801250
71. Brandl, F.; Bergwinkl, S.; Allacher, C.; Dick, B. *Chem. – Eur. J.* **2020,** *26,* 7946–7954. doi:10.1002/chem.201905167
72. Jeong, D. Y.; Lee, D. S.; Lee, H. L.; Nah, S.; Lee, J. Y.; Cho, E. J.; You, Y. *ACS Catal.* **2022,** *12,* 6047–6059. doi:10.1021/acscatal.2c00763
73. Marcus, R. A. *Annu. Rev. Phys. Chem.* **1964,** *15,* 155–196. doi:10.1146/annurev.pc.15.100164.001103
74. Turró, C.; Zaleski, J. M.; Karabatsos, Y. M.; Nocera, D. G. *J. Am. Chem. Soc.* **1996,** *118,* 6060–6067. doi:10.1021/ja960575p
75. Li, H.; Tang, X.; Pang, J. H.; Wu, X.; Yeow, E. K. L.; Wu, J.; Chiba, S. *J. Am. Chem. Soc.* **2021,** *143,* 481–487. doi:10.1021/jacs.0c11968
76. Costentin, C.; Robert, M.; Savéant, J.-M. *J. Am. Chem. Soc.* **2004,** *126,* 16051–16057. doi:10.1021/ja045989u
77. Connell, T. U.; Fraser, C. L.; Czyz, M. L.; Smith, Z. M.; Hayne, D. J.; Doeven, E. H.; Agugiaro, J.; Wilson, D. J. D.; Adcock, J. L.; Scully, A. D.; Gómez, D. E.; Barnett, N. W.; Polyzos, A.; Francis, P. S. *J. Am. Chem. Soc.* **2019,** *141,* 17646–17658. doi:10.1021/jacs.9b07370

78. van As, D. J.; Connell, T. U.; Brzozowski, M.; Scully, A. D.; Polyzos, A. *Org. Lett.* **2018,** *20,* 905–908. doi:10.1021/acs.orglett.7b03565
79. Forni, J. A.; Micic, N.; Connell, T. U.; Weragoda, G.; Polyzos, A. *Angew. Chem., Int. Ed.* **2020,** *59,* 18646–18654. doi:10.1002/anie.202006720
80. Isidro-Llobet, A.; Kenworthy, M. N.; Mukherjee, S.; Kopach, M. E.; Wegner, K.; Gallou, F.; Smith, A. G.; Roschangar, F. *J. Org. Chem.* **2019,** *84,* 4615–4628. doi:10.1021/acs.joc.8b03001
81. Humphrey, J. M.; Chamberlin, A. R. *Chem. Rev.* **1997,** *97,* 2243–2266. doi:10.1021/cr950005s
82. Brennführer, A.; Neumann, H.; Beller, M. *Angew. Chem., Int. Ed.* **2009,** *48,* 4114–4133. doi:10.1002/anie.200900013
83. Shen, C.; Wu, X.-F. *Chem. – Eur. J.* **2017,** *23,* 2973–2987. doi:10.1002/chem.201603623
84. Sumino, S.; Fusano, A.; Fukuyama, T.; Ryu, I. *Acc. Chem. Res.* **2014,** *47,* 1563–1574. doi:10.1021/ar500035q
85. Kawamoto, T.; Matsubara, H.; Fukuyama, T.; Ryu, I. *Chem. Lett.* **2018,** *47,* 1169–1171. doi:10.1246/cl.180599
86. Vasudevan, D. *Russ. J. Electrochem.* **2005,** *41,* 310–314. doi:10.1007/s11175-005-0067-2
87. Isse, A. A.; Lin, C. Y.; Coote, M. L.; Gennaro, A. *J. Phys. Chem. B* **2011,** *115,* 678–684. doi:10.1021/jp109613t
88. Dolbier, W. R. Fluorinated Free Radicals. *Organofluorine Chemistry;* Topics in Current Chemistry, Vol. 192; Springer: Berlin, Heidelberg, 1997; pp 97–163. doi:10.1007/bfb0119266
89. Crespi, S.; Fagnoni, M. *Chem. Rev.* **2020,** *120,* 9790–9833. doi:10.1021/acs.chemrev.0c00278
90. Shimkin, K. W.; Watson, D. A. *Beilstein J. Org. Chem.* **2015,** *11,* 2278–2288. doi:10.3762/bjoc.11.248
91. Chatterjee, T.; Iqbal, N.; You, Y.; Cho, E. J. *Acc. Chem. Res.* **2016,** *49,* 2284–2294. doi:10.1021/acs.accounts.6b00248
92. Rosso, C.; Filippini, G.; Cozzi, P. G.; Gualandi, A.; Prato, M. *ChemPhotoChem* **2019,** *3,* 193–197. doi:10.1002/cptc.201900018
93. Médebielle, M.; Pinson, J.; Savéant, J.-M. *J. Am. Chem. Soc.* **1991,** *113,* 6872–6879. doi:10.1021/ja00018a025
94. Ilic, A.; Schwarz, J.; Johnson, C.; de Groot, L. H. M.; Kaufhold, S.; Lomoth, R.; Wärnmark, K. *Chem. Sci.* **2022,** *13,* 9165–9175. doi:10.1039/d2sc02122f
95. Liu, Y.; Persson, P.; Sundström, V.; Wärnmark, K. *Acc. Chem. Res.* **2016,** *49,* 1477–1485. doi:10.1021/acs.accounts.6b00186
96. Miller, J. N.; McCusker, J. K. *Chem. Sci.* **2020,** *11,* 5191–5204. doi:10.1039/d0sc01506g
97. Liu, Y.; Harlang, T.; Canton, S. E.; Chábera, P.; Suárez-Alcántara, K.; Fleckhaus, A.; Vithanage, D. A.; Göransson, E.; Corani, A.; Lomoth, R.; Sundström, V.; Wärnmark, K. *Chem. Commun.* **2013,** *49,* 6412. doi:10.1039/c3cc43833c
98. Rosemann, N. W.; Chábera, P.; Prakash, O.; Kaufhold, S.; Wärnmark, K.; Yartsev, A.; Persson, P. *J. Am. Chem. Soc.* **2020,** *142,* 8565–8569. doi:10.1021/jacs.0c00755
99. Woodhouse, M. D.; McCusker, J. K. *J. Am. Chem. Soc.* **2020,** *142,* 16229–16233. doi:10.1021/jacs.0c08389
100. Aydogan, A.; Bangle, R. E.; Cadranel, A.; Turlington, M. D.; Conroy, D. T.; Cauët, E.; Singleton, M. L.; Meyer, G. J.; Sampaio, R. N.; Elias, B.; Troian-Gautier, L. *J. Am. Chem. Soc.* **2021,** *143,* 15661–15673. doi:10.1021/jacs.1c06081
101. Constantin, T.; Zanini, M.; Regni, A.; Sheikh, N. S.; Juliá, F.; Leonori, D. *Science* **2020,** *367,* 1021–1026. doi:10.1126/science.aba2419
102. Chen, L.; Qu, Q.; Ran, C.-K.; Wang, W.; Zhang, W.; He, Y.; Liao, L.-L.; Ye, J.-H.; Yu, D.-G. *Angew. Chem., Int. Ed.* **2023,** *62,* e202217918. doi:10.1002/anie.202217918
103. Odom, A. L. *Dalton Trans.* **2005,** 225–233. doi:10.1039/b415701j
104. Weiser, M.; Hermann, S.; Penner, A.; Wagenknecht, H.-A. *Beilstein J. Org. Chem.* **2015,** *11,* 568–575. doi:10.3762/bjoc.11.62
105. Wang, H.; Man, Y.; Xiang, Y.; Wang, K.; Li, N.; Tang, B. *Chem. Commun.* **2019,** *55,* 11426–11429. doi:10.1039/c9cc05902d
106. Czyz, M. L.; Taylor, M. S.; Horngren, T. H.; Polyzos, A. *ACS Catal.* **2021,** *11,* 5472–5480. doi:10.1021/acscatal.1c01000
107. Birch, A. J. *Nature* **1946,** *158,* 585. doi:10.1038/158585c0
108. Birch, A. J. *Q. Rev., Chem. Soc.* **1950,** *4,* 69–93. doi:10.1039/qr9500400069
109. Fuchs, J. R.; Mitchell, M. L.; Shabangi, M.; Flowers, R. A., II. *Tetrahedron Lett.* **1997,** *38,* 8157–8158. doi:10.1016/s0040-4039(97)10222-2
110. Lei, P.; Ding, Y.; Zhang, X.; Adijiang, A.; Li, H.; Ling, Y.; An, J. *Org. Lett.* **2018,** *20,* 3439–3442. doi:10.1021/acs.orglett.8b00891
111. Yoo, B. I.; Kim, Y. J.; You, Y.; Yang, J. W.; Kim, S. W. *J. Org. Chem.* **2018,** *83,* 13847–13853. doi:10.1021/acs.joc.8b02094
112. Giustra, Z. X.; Ishibashi, J. S. A.; Liu, S.-Y. *Coord. Chem. Rev.* **2016,** *314,* 134–181. doi:10.1016/j.ccr.2015.11.006
113. Peters, B. K.; Rodriguez, K. X.; Reisberg, S. H.; Beil, S. B.; Hickey, D. P.; Kawamata, Y.; Collins, M.; Starr, J.; Chen, L.; Udyavara, S.; Klunder, K.; Gorey, T. J.; Anderson, S. L.; Neurock, M.; Minteer, S. D.; Baran, P. S. *Science* **2019,** *363,* 838–845. doi:10.1126/science.aav5606
114. Mizuno, K.; Okamoto, H.; Pac, C.; Sakurai, H. *J. Chem. Soc., Chem. Commun.* **1975,** 839. doi:10.1039/c39750000839
115. Yasuda, M.; Pac, C.; Sakurai, H. *J. Org. Chem.* **1981,** *46,* 788–792. doi:10.1021/jo00317a028
116. Yoshimi, Y.; Ishise, A.; Oda, H.; Moriguchi, Y.; Kanezaki, H.; Nakaya, Y.; Katsuno, K.; Itou, T.; Inagaki, S.; Morita, T.; Hatanaka, M. *Tetrahedron Lett.* **2008,** *49,* 3400–3404. doi:10.1016/j.tetlet.2008.03.123
117. Li, G.-X.; Morales-Rivera, C. A.; Wang, Y.; Gao, F.; He, G.; Liu, P.; Chen, G. *Chem. Sci.* **2016,** *7,* 6407–6412. doi:10.1039/c6sc02653b
118. Meerholz, K.; Heinze, J. *J. Am. Chem. Soc.* **1989,** *111,* 2325–2326. doi:10.1021/ja00188a069
119. Chatterjee, A.; König, B. *Angew. Chem., Int. Ed.* **2019,** *58,* 14289–14294. doi:10.1002/anie.201905485
120. Cole, J. P.; Chen, D.-F.; Kudisch, M.; Pearson, R. M.; Lim, C.-H.; Miyake, G. M. *J. Am. Chem. Soc.* **2020,** *142,* 13573–13581. doi:10.1021/jacs.0c05899
121. Glaser, F.; Wenger, O. S. *JACS Au* **2022,** *2,* 1488–1503. doi:10.1021/jacsau.2c00265
122. Ravetz, B. D.; Pun, A. B.; Churchill, E. M.; Congreve, D. N.; Rovis, T.; Campos, L. M. *Nature* **2019,** *565,* 343–346. doi:10.1038/s41586-018-0835-2
123. Soika, J.; McLaughlin, C.; Neveselý, T.; Daniliuc, C. G.; Molloy, J. J.; Gilmour, R. *ACS Catal.* **2022,** *12,* 10047–10056. doi:10.1021/acscatal.2c02991
124. Das, S.; Natarajan, P.; König, B. *Chem. – Eur. J.* **2017,** *23,* 18161–18165. doi:10.1002/chem.201705442
125. Sheridan, T.; Yayla, H. G.; Lian, Y.; Genovino, J.; Monck, N.; Burton, J. W. *Eur. J. Org. Chem.* **2020,** 2766–2770. doi:10.1002/ejoc.202000337
126. Natarajan, P.; König, B. *Eur. J. Org. Chem.* **2021,** 2145–2161. doi:10.1002/ejoc.202100011

127. Braude, E. A.; Brook, A. G.; Linstead, R. P. *J. Chem. Soc.* **1954,** 3569. doi:10.1039/jr9540003569
128. Christensen, J. A.; Phelan, B. T.; Chaudhuri, S.; Acharya, A.; Batista, V. S.; Wasielewski, M. R. *J. Am. Chem. Soc.* **2018,** *140,* 5290–5299. doi:10.1021/jacs.8b01778
129. McTeague, T. A.; Jamison, T. F. *Angew. Chem., Int. Ed.* **2016,** *55,* 15072–15075. doi:10.1002/anie.201608792
130. Rombach, D.; Wagenknecht, H.-A. *Synthesis* **2022,** *54,* 4883–4894. doi:10.1055/a-1877-5231
131. Rombach, D.; Wagenknecht, H.-A. *Angew. Chem., Int. Ed.* **2020,** *59,* 300–303. doi:10.1002/anie.201910830
132. Savoie, P. R.; Welch, J. T. *Chem. Rev.* **2015,** *115,* 1130–1190. doi:10.1021/cr500336u
133. Rombach, D.; Birenheide, B.; Wagenknecht, H.-A. *Chem. – Eur. J.* **2021,** *27,* 8088–8093. doi:10.1002/chem.202100767
134. Targos, K.; Williams, O. P.; Wickens, Z. K. *J. Am. Chem. Soc.* **2021,** *143,* 4125–4132. doi:10.1021/jacs.1c00399
135. Romero, N. A.; Margrey, K. A.; Tay, N. E.; Nicewicz, D. A. *Science* **2015,** *349,* 1326–1330. doi:10.1126/science.aac9895
136. Eberson, L.; Persson, O.; Hartshorn, M. P. *Angew. Chem., Int. Ed. Engl.* **1995,** *34,* 2268–2269. doi:10.1002/anie.199522681
137. Eberson, L.; Hartshorn, M. P.; Persson, O.; Radner, F. *Chem. Commun.* **1996,** 2105. doi:10.1039/cc9960002105
138. Ohkubo, K.; Fujimoto, A.; Fukuzumi, S. *Chem. Commun.* **2011,** *47,* 8515. doi:10.1039/c1cc12534f
139. Deng, H.-P.; Zhou, Q.; Wu, J. *Angew. Chem., Int. Ed.* **2018,** *57,* 12661–12665. doi:10.1002/anie.201804844
140. Rohe, S.; Morris, A. O.; McCallum, T.; Barriault, L. *Angew. Chem., Int. Ed.* **2018,** *57,* 15664–15669. doi:10.1002/anie.201810187
141. Xu, P.; Chen, P.-Y.; Xu, H.-C. *Angew. Chem., Int. Ed.* **2020,** *59,* 14275–14280. doi:10.1002/anie.202005724
142. Li, P.; Deetz, A. M.; Hu, J.; Meyer, G. J.; Hu, K. *J. Am. Chem. Soc.* **2022,** *144,* 17604–17610. doi:10.1021/jacs.2c07107
143. Hou, Z.-W.; Xu, H.-C. *ChemElectroChem* **2021,** *8,* 1571–1573. doi:10.1002/celc.202100272
144. Bandar, J. S.; Lambert, T. H. *Synthesis* **2013,** *45,* 2485–2498. doi:10.1055/s-0033-1338516
145. Gerson, F.; Plattner, G.; Yoshida, Z. *Mol. Phys.* **1971,** *21,* 1027–1032. doi:10.1080/00268977100102181
146. Johnson, R. W. *Tetrahedron Lett.* **1976,** *17,* 589–592. doi:10.1016/s0040-4039(00)77918-4
147. Weiss, R.; Schloter, K. *Tetrahedron Lett.* **1975,** *16,* 3491–3494. doi:10.1016/s0040-4039(00)91392-3
148. Huang, H.; Strater, Z. M.; Rauch, M.; Shee, J.; Sisto, T. J.; Nuckolls, C.; Lambert, T. H. *Angew. Chem., Int. Ed.* **2019,** *58,* 13318–13322. doi:10.1002/anie.201906381
149. Sevov, C. S.; Samaroo, S. K.; Sanford, M. S. *Adv. Energy Mater.* **2017,** *7,* 1602027. doi:10.1002/aenm.201602027
150. Silvi, M.; Verrier, C.; Rey, Y. P.; Buzzetti, L.; Melchiorre, P. *Nat. Chem.* **2017,** *9,* 868–873. doi:10.1038/nchem.2748
151. Pabon, R. A.; Bellville, D. J.; Bauld, N. L. *J. Am. Chem. Soc.* **1983,** *105,* 5158–5159. doi:10.1021/ja00353a065
152. Reynolds, D. W.; Lorenz, K. T.; Chiou, H. S.; Bellville, D. J.; Pabon, R. A.; Bauld, N. L. *J. Am. Chem. Soc.* **1987,** *109,* 4960–4968. doi:10.1021/ja00250a033
153. Jahn, U.; Aussieker, S. *Org. Lett.* **1999,** *1,* 849–852. doi:10.1021/ol990735c
154. Barham, J. P.; John, M. P.; Murphy, J. A. *J. Am. Chem. Soc.* **2016,** *138,* 15482–15487. doi:10.1021/jacs.6b09690
155. Wu, S.; Žurauskas, J.; Domański, M.; Hitzfeld, P. S.; Butera, V.; Scott, D. J.; Rehbein, J.; Kumar, A.; Thyrhaug, E.; Hauer, J.; Barham, J. P. *Org. Chem. Front.* **2021,** *8,* 1132–1142. doi:10.1039/d0qo01609h
156. Hagopian, L.; Koehler, G.; Walter, R. I. *J. Phys. Chem.* **1967,** *71,* 2290–2296. doi:10.1021/j100866a050
157. Kumar, A.; Malevich, P.; Mewes, L.; Wu, S.; Barham, J. P.; Hauer, J. *J. Chem. Phys.* **2023,** *158,* 144201. doi:10.1063/5.0142225
158. del Valle, J. C.; Catalán, J. *Phys. Chem. Chem. Phys.* **2019,** *21,* 10061–10069. doi:10.1039/c9cp00739c
159. Tseng, H.-W.; Shen, J.-Y.; Kuo, T.-Y.; Tu, T.-S.; Chen, Y.-A.; Demchenko, A. P.; Chou, P.-T. *Chem. Sci.* **2016,** *7,* 655–665. doi:10.1039/c5sc01945a
160. Brancato, G.; Signore, G.; Neyroz, P.; Polli, D.; Cerullo, G.; Abbandonato, G.; Nucara, L.; Barone, V.; Beltram, F.; Bizzarri, R. *J. Phys. Chem. B* **2015,** *119,* 6144–6154. doi:10.1021/acs.jpcb.5b01119
161. Huang, H.; Lambert, T. H. *Angew. Chem., Int. Ed.* **2021,** *60,* 11163–11167. doi:10.1002/anie.202100222
162. Shen, T.; Lambert, T. H. *Science* **2021,** *371,* 620–626. doi:10.1126/science.abf2798
163. Ritter, J. J.; Minieri, P. P. *J. Am. Chem. Soc.* **1948,** *70,* 4045–4048. doi:10.1021/ja01192a022
164. Ritter, J. J.; Kalish, J. *J. Am. Chem. Soc.* **1948,** *70,* 4048–4050. doi:10.1021/ja01192a023
165. de Lijser, H. J. P.; Arnold, D. R. *J. Org. Chem.* **1997,** *62,* 8432–8438. doi:10.1021/jo971197p
166. Metallinos, C.; Nerdinger, S.; Snieckus, V. *Org. Lett.* **1999,** *1,* 1183–1186. doi:10.1021/ol990846b
167. Que, L., Jr.; Tolman, W. B. *Nature* **2008,** *455,* 333–340. doi:10.1038/nature07371
168. Chen, M. S.; White, M. C. *Science* **2010,** *327,* 566–571. doi:10.1126/science.1183602
169. Horn, E. J.; Rosen, B. R.; Chen, Y.; Tang, J.; Chen, K.; Eastgate, M. D.; Baran, P. S. *Nature* **2016,** *533,* 77–81. doi:10.1038/nature17431
170. White, M. C.; Zhao, J. *J. Am. Chem. Soc.* **2018,** *140,* 13988–14009. doi:10.1021/jacs.8b05195
171. Huang, X.; Groves, J. T. *J. Biol. Inorg. Chem.* **2017,** *22,* 185–207. doi:10.1007/s00775-016-1414-3
172. Kawamata, Y.; Yan, M.; Liu, Z.; Bao, D.-H.; Chen, J.; Starr, J. T.; Baran, P. S. *J. Am. Chem. Soc.* **2017,** *139,* 7448–7451. doi:10.1021/jacs.7b03539
173. Shen, T.; Li, Y.-L.; Ye, K.-Y.; Lambert, T. H. *Nature* **2023,** *614,* 275–280. doi:10.1038/s41586-022-05608-x
174. Song, L.; Fu, N.; Ernst, B. G.; Lee, W. H.; Frederick, M. O.; DiStasio, R. A., Jr.; Lin, S. *Nat. Chem.* **2020,** *12,* 747–754. doi:10.1038/s41557-020-0469-5
175. Fu, N.; Song, L.; Liu, J.; Shen, Y.; Siu, J. C.; Lin, S. *J. Am. Chem. Soc.* **2019,** *141,* 14480–14485. doi:10.1021/jacs.9b03296
176. Mandigma, M. J. P.; Žurauskas, J.; MacGregor, C. I.; Edwards, L. J.; Shahin, A.; d'Heureuse, L.; Yip, P.; Birch, D. J. S.; Gruber, T.; Heilmann, J.; John, M. P.; Barham, J. P. *Chem. Sci.* **2022,** *13,* 1912–1924. doi:10.1039/d1sc05840a
177. Zhang, Z.; Zhang, X.; Nagib, D. A. *Chem* **2019,** *5,* 3127–3134. doi:10.1016/j.chempr.2019.09.010

178. Kamijo, S.; Hoshikawa, T.; Inoue, M. *Org. Lett.* **2011,** *13,* 5928–5931. doi:10.1021/ol202659e
179. Kim, K.; Lee, S.; Hong, S. H. *Org. Lett.* **2021,** *23,* 5501–5505. doi:10.1021/acs.orglett.1c01846
180. Zhang, W.; Wang, F.; McCann, S. D.; Wang, D.; Chen, P.; Stahl, S. S.; Liu, G. *Science* **2016,** *353,* 1014–1018. doi:10.1126/science.aaf7783
181. Lu, Q.; Glorius, F. *Angew. Chem., Int. Ed.* **2017,** *56,* 49–51. doi:10.1002/anie.201609105
182. Saint-Denis, T. G.; Zhu, R.-Y.; Chen, G.; Wu, Q.-F.; Yu, J.-Q. *Science* **2018,** *359,* eaao4798. doi:10.1126/science.aao4798
183. Zhang, C.; Li, Z.-L.; Gu, Q.-S.; Liu, X.-Y. *Nat. Commun.* **2021,** *12,* 475. doi:10.1038/s41467-020-20770-4
184. Capaldo, L.; Ravelli, D.; Fagnoni, M. *Chem. Rev.* **2022,** *122,* 1875–1924. doi:10.1021/acs.chemrev.1c00263
185. Zhang, W.; Wu, L.; Chen, P.; Liu, G. *Angew. Chem., Int. Ed.* **2019,** *58,* 6425–6429. doi:10.1002/anie.201902191
186. Fu, L.; Zhang, Z.; Chen, P.; Lin, Z.; Liu, G. *J. Am. Chem. Soc.* **2020,** *142,* 12493–12500. doi:10.1021/jacs.0c05373
187. Li, J.; Zhang, Z.; Wu, L.; Zhang, W.; Chen, P.; Lin, Z.; Liu, G. *Nature* **2019,** *574,* 516–521. doi:10.1038/s41586-019-1655-8
188. Hou, Z.-W.; Liu, D.-J.; Xiong, P.; Lai, X.-L.; Song, J.; Xu, H.-C. *Angew. Chem., Int. Ed.* **2021,** *60,* 2943–2947. doi:10.1002/anie.202013478
189. Shen, T.; Lambert, T. H. *J. Am. Chem. Soc.* **2021,** *143,* 8597–8602. doi:10.1021/jacs.1c03718
190. Baciocchi, E.; D'Acunzo, F.; Galli, C.; Lanzalunga, O. *J. Chem. Soc., Perkin Trans. 2* **1996,** 133–140. doi:10.1039/p29960000133
191. Baciocchi, E.; Bietti, M.; Lanzalunga, O. *Acc. Chem. Res.* **2000,** *33,* 243–251. doi:10.1021/ar980014y
192. Grampp, G.; Galán, M.; Sacher, M. *Ber. Bunsen-Ges.* **1995,** *99,* 111–117. doi:10.1002/bbpc.19950990204
193. Rathore, R.; Hubig, S. M.; Kochi, J. K. *J. Am. Chem. Soc.* **1997,** *119,* 11468–11480. doi:10.1021/ja971188y
194. Wagner, P. J.; Truman, R. J.; Puchalski, A. E.; Wake, R. *J. Am. Chem. Soc.* **1986,** *108,* 7727–7738. doi:10.1021/ja00284a041
195. Fan, W.; Zhao, X.; Deng, Y.; Chen, P.; Wang, F.; Liu, G. *J. Am. Chem. Soc.* **2022,** *144,* 21674–21682. doi:10.1021/jacs.2c09366
196. Yuan, Y.; Yang, J.; Zhang, J. *Chem. Sci.* **2023,** *14,* 705–710. doi:10.1039/d2sc05428k
197. Kolb, H. C.; VanNieuwenhze, M. S.; Sharpless, K. B. *Chem. Rev.* **1994,** *94,* 2483–2547. doi:10.1021/cr00032a009
198. Enthaler, S.; Company, A. *Chem. Soc. Rev.* **2011,** *40,* 4912. doi:10.1039/c1cs15085e
199. Crossley, S. W. M.; Obradors, C.; Martinez, R. M.; Shenvi, R. A. *Chem. Rev.* **2016,** *116,* 8912–9000. doi:10.1021/acs.chemrev.6b00334
200. Li, Y.; Song, D.; Dong, V. M. *J. Am. Chem. Soc.* **2008,** *130,* 2962–2964. doi:10.1021/ja711029u
201. Wang, A.; Jiang, H.; Chen, H. *J. Am. Chem. Soc.* **2009,** *131,* 3846–3847. doi:10.1021/ja900213d
202. Seayad, J.; Seayad, A. M.; Chai, C. L. L. *Org. Lett.* **2010,** *12,* 1412–1415. doi:10.1021/ol902813m
203. de Boer, J. W.; Brinksma, J.; Browne, W. R.; Meetsma, A.; Alsters, P. L.; Hage, R.; Feringa, B. L. *J. Am. Chem. Soc.* **2005,** *127,* 7990–7991. doi:10.1021/ja050990u
204. Chen, K.; Que, L., Jr. *Angew. Chem., Int. Ed.* **1999,** *38,* 2227–2229. doi:10.1002/(sici)1521-3773(19990802)38:15<2227::aid-anie2227>3.0.co;2-b
205. Costas, M.; Tipton, A. K.; Chen, K.; Jo, D.-H.; Que, L., Jr. *J. Am. Chem. Soc.* **2001,** *123,* 6722–6723. doi:10.1021/ja015601k
206. Rawling, M. J.; Tomkinson, N. C. O. *Org. Biomol. Chem.* **2013,** *11,* 1434–1440. doi:10.1039/c3ob27387c
207. Bag, R.; De, P. B.; Pradhan, S.; Punniyamurthy, T. *Eur. J. Org. Chem.* **2017,** 5424–5438. doi:10.1002/ejoc.201700512
208. Wöste, T. H.; Muñiz, K. *Synthesis* **2016,** *48,* 816–827. doi:10.1055/s-0035-1561313
209. Aertker, K.; Rama, R. J.; Opalach, J.; Muñiz, K. *Adv. Synth. Catal.* **2017,** *359,* 1290–1294. doi:10.1002/adsc.201601178
210. Walling, C.; El-Taliawi, G. M.; Amarnath, K. *J. Am. Chem. Soc.* **1984,** *106,* 7573–7578. doi:10.1021/ja00336a043
211. Yang, B.; Lu, Z. *Chem. Commun.* **2017,** *53,* 12634–12637. doi:10.1039/c7cc06745c
212. Yoshida, J.-i.; Kataoka, K.; Horcajada, R.; Nagaki, A. *Chem. Rev.* **2008,** *108,* 2265–2299. doi:10.1021/cr0680843
213. Francke, R.; Little, R. D. *Chem. Soc. Rev.* **2014,** *43,* 2492–2521. doi:10.1039/c3cs60464k
214. Torii, S.; Liu, P.; Bhuvaneswari, N.; Amatore, C.; Jutand, A. *J. Org. Chem.* **1996,** *61,* 3055–3060. doi:10.1021/jo952137r
215. Torii, S.; Liu, P.; Tanaka, H. *Chem. Lett.* **1995,** *24,* 319–320. doi:10.1246/cl.1995.319
216. Huang, H.; Lambert, T. H. *J. Am. Chem. Soc.* **2021,** *143,* 7247–7252. doi:10.1021/jacs.1c01967
217. Huang, H.; Lambert, T. H. *J. Am. Chem. Soc.* **2022,** *144,* 18803–18809. doi:10.1021/jacs.2c08951
218. Sata, N. U.; Fusetani, N. *Tetrahedron Lett.* **2000,** *41,* 489–492. doi:10.1016/s0040-4039(99)02098-5
219. Abraham, E.; Davies, S. G.; Millican, N. L.; Nicholson, R. L.; Roberts, P. M.; Smith, A. D. *Org. Biomol. Chem.* **2008,** *6,* 1655–1664. doi:10.1039/b801357h
220. Calder, E. D. D.; Zaed, A. M.; Sutherland, A. *J. Org. Chem.* **2013,** *78,* 7223–7233. doi:10.1021/jo401211j
221. Desimoni, G.; Faita, G.; Jørgensen, K. A. *Chem. Rev.* **2006,** *106,* 3561–3651. doi:10.1021/cr0505324
222. Minisci, F.; Fontana, F.; Vismara, E. *J. Heterocycl. Chem.* **1990,** *27,* 79–96. doi:10.1002/jhet.5570270107
223. Proctor, R. S. J.; Phipps, R. J. *Angew. Chem., Int. Ed.* **2019,** *58,* 13666–13699. doi:10.1002/anie.201900977
224. Gupta, R. R., Ed. *Bioactive Heterocycles V; Topics in Heterocyclic Chemistry*, Vol. 11; Springer: Berlin, Heidelberg, 2007.
225. Fukuzumi, S.; Ohkubo, K. *Org. Biomol. Chem.* **2014,** *12,* 6059–6071. doi:10.1039/c4ob00843j
226. Yan, H.; Hou, Z.-W.; Xu, H.-C. *Angew. Chem., Int. Ed.* **2019,** *58,* 4592–4595. doi:10.1002/anie.201814488
227. Fukuzumi, S.; Kotani, H.; Ohkubo, K.; Ogo, S.; Tkachenko, N. V.; Lemmetyinen, H. *J. Am. Chem. Soc.* **2004,** *126,* 1600–1601. doi:10.1021/ja038656q
228. Ohkubo, K.; Mizushima, K.; Iwata, R.; Souma, K.; Suzuki, N.; Fukuzumi, S. *Chem. Commun.* **2010,** *46,* 601–603. doi:10.1039/b920606j
229. Romero, N. A.; Nicewicz, D. A. *J. Am. Chem. Soc.* **2014,** *136,* 17024–17035. doi:10.1021/ja506228u
230. Matsui, J. K.; Primer, D. N.; Molander, G. A. *Chem. Sci.* **2017,** *8,* 3512–3522. doi:10.1039/c7sc00283a
231. Anne, A.; Hapiot, P.; Moiroux, J.; Neta, P.; Saveant, J. M. *J. Am. Chem. Soc.* **1992,** *114,* 4694–4701. doi:10.1021/ja00038a036

232. Li, C.; Wang, J.; Barton, L. M.; Yu, S.; Tian, M.; Peters, D. S.; Kumar, M.; Yu, A. W.; Johnson, K. A.; Chatterjee, A. K.; Yan, M.; Baran, P. S. *Science* **2017,** *356,* eaam7355. doi:10.1126/science.aam7355
233. Xiang, J.; Shang, M.; Kawamata, Y.; Lundberg, H.; Reisberg, S. H.; Chen, M.; Mykhailiuk, P.; Beutner, G.; Collins, M. R.; Davies, A.; Del Bel, M.; Gallego, G. M.; Spangler, J. E.; Starr, J.; Yang, S.; Blackmond, D. G.; Baran, P. S. *Nature* **2019,** *573,* 398–402. doi:10.1038/s41586-019-1539-y
234. Fawcett, A.; Pradeilles, J.; Wang, Y.; Mutsuga, T.; Myers, E. L.; Aggarwal, V. K. *Science* **2017,** *357,* 283–286. doi:10.1126/science.aan3679
235. Sun, X.; Chen, J.; Ritter, T. *Nat. Chem.* **2018,** *10,* 1229–1233. doi:10.1038/s41557-018-0142-4
236. Mao, R.; Frey, A.; Balon, J.; Hu, X. *Nat. Catal.* **2018,** *1,* 120–126. doi:10.1038/s41929-017-0023-z
237. Lai, X.-L.; Shu, X.-M.; Song, J.; Xu, H.-C. *Angew. Chem., Int. Ed.* **2020,** *59,* 10626–10632. doi:10.1002/anie.202002900
238. Hu, A.; Guo, J.-J.; Pan, H.; Zuo, Z. *Science* **2018,** *361,* 668–672. doi:10.1126/science.aat9750
239. Hu, A.; Guo, J.-J.; Pan, H.; Tang, H.; Gao, Z.; Zuo, Z. *J. Am. Chem. Soc.* **2018,** *140,* 1612–1616. doi:10.1021/jacs.7b13131
240. Niu, K.; Zhou, P.; Ding, L.; Hao, Y.; Liu, Y.; Song, H.; Wang, Q. *ACS Sustainable Chem. Eng.* **2021,** *9,* 16820–16828. doi:10.1021/acssuschemeng.1c06702
241. Abderrazak, Y.; Bhattacharyya, A.; Reiser, O. *Angew. Chem., Int. Ed.* **2021,** *60,* 21100–21115. doi:10.1002/anie.202100270
242. Xu, F.; Lai, X.-L.; Xu, H.-C. *Synlett* **2021,** *32,* 369–372. doi:10.1055/a-1296-8652
243. Nawrat, C. C.; Jamison, C. R.; Slutskyy, Y.; MacMillan, D. W. C.; Overman, L. E. *J. Am. Chem. Soc.* **2015,** *137,* 11270–11273. doi:10.1021/jacs.5b07678
244. Capaldo, L.; Ravelli, D. *Eur. J. Org. Chem.* **2017,** 2056–2071. doi:10.1002/ejoc.201601485
245. Green, S. A.; Crossley, S. W. M.; Matos, J. L. M.; Vásquez-Céspedes, S.; Shevick, S. L.; Shenvi, R. A. *Acc. Chem. Res.* **2018,** *51,* 2628–2640. doi:10.1021/acs.accounts.8b00337
246. Chu, J. C. K.; Rovis, T. *Angew. Chem., Int. Ed.* **2018,** *57,* 62–101. doi:10.1002/anie.201703743
247. Duncan, D. C.; Netzel, T. L.; Hill, C. L. *Inorg. Chem.* **1995,** *34,* 4640–4646. doi:10.1021/ic00122a021
248. Shields, B. J.; Doyle, A. G. *J. Am. Chem. Soc.* **2016,** *138,* 12719–12722. doi:10.1021/jacs.6b08397
249. Nielsen, M. K.; Shields, B. J.; Liu, J.; Williams, M. J.; Zacuto, M. J.; Doyle, A. G. *Angew. Chem., Int. Ed.* **2017,** *56,* 7191–7194. doi:10.1002/anie.201702079
250. Deng, H.-P.; Fan, X.-Z.; Chen, Z.-H.; Xu, Q.-H.; Wu, J. *J. Am. Chem. Soc.* **2017,** *139,* 13579–13584. doi:10.1021/jacs.7b08158
251. Fukuyama, T.; Tokizane, M.; Matsui, A.; Ryu, I. *React. Chem. Eng.* **2016,** *1,* 613–615. doi:10.1039/c6re00159a
252. Capaldo, L.; Quadri, L. L.; Merli, D.; Ravelli, D. *Chem. Commun.* **2021,** *57,* 4424–4427. doi:10.1039/d1cc01012c
253. Quattrini, M. C.; Fujii, S.; Yamada, K.; Fukuyama, T.; Ravelli, D.; Fagnoni, M.; Ryu, I. *Chem. Commun.* **2017,** *53,* 2335–2338. doi:10.1039/c6cc09725a
254. Huang, H.; Strater, Z. M.; Lambert, T. H. *J. Am. Chem. Soc.* **2020,** *142,* 1698–1703. doi:10.1021/jacs.9b11472
255. Alam, K.; Hong, S. W.; Oh, K. H.; Park, J. K. *Angew. Chem., Int. Ed.* **2017,** *56,* 13387–13391. doi:10.1002/anie.201705514
256. Taublaender, M. J.; Glöcklhofer, F.; Marchetti-Deschmann, M.; Unterlass, M. M. *Angew. Chem., Int. Ed.* **2018,** *57,* 12270–12274. doi:10.1002/anie.201801277
257. Nguyen, T. B.; Ermolenko, L.; Al-Mourabit, A. *Chem. Commun.* **2016,** *52,* 4914–4917. doi:10.1039/c6cc01436d
258. Mai, S.; Luo, Y.; Huang, X.; Shu, Z.; Li, B.; Lan, Y.; Song, Q. *Chem. Commun.* **2018,** *54,* 10240–10243. doi:10.1039/c8cc05390a
259. Liao, J.; Yang, X.; Ouyang, L.; Lai, Y.; Huang, J.; Luo, R. *Org. Chem. Front.* **2021,** *8,* 1345–1363. doi:10.1039/d0qo01453b
260. Scherübl, M.; Daniliuc, C. G.; Studer, A. *Angew. Chem., Int. Ed.* **2021,** *60,* 711–715. doi:10.1002/anie.202012654
261. Sun, K.; Li, S.-J.; Chen, X.-L.; Liu, Y.; Huang, X.-Q.; Wei, D.-H.; Qu, L.-B.; Zhao, Y.-F.; Yu, B. *Chem. Commun.* **2019,** *55,* 2861–2864. doi:10.1039/c8cc10243k
262. Yuan, Y.; Zheng, Y.; Xu, B.; Liao, J.; Bu, F.; Wang, S.; Hu, J.-G.; Lei, A. *ACS Catal.* **2020,** *10,* 6676–6681. doi:10.1021/acscatal.0c01324
263. Li, H.-C.; Sun, K.; Li, X.; Wang, S.-Y.; Chen, X.-L.; He, S.-Q.; Qu, L.-B.; Yu, B. *J. Org. Chem.* **2021,** *86,* 9055–9066. doi:10.1021/acs.joc.1c01022
264. Zhao, B.; Hammond, G. B.; Xu, B. *J. Org. Chem.* **2021,** *86,* 12851–12861. doi:10.1021/acs.joc.1c01486
265. Ramesh, V.; Gangadhar, M.; Nanubolu, J. B.; Adiyala, P. R. *J. Org. Chem.* **2021,** *86,* 12908–12921. doi:10.1021/acs.joc.1c01555
266. Li, J.-Z.; Mei, L.; Cai, X.-E.; Zhang, C.-C.; Cao, T.-T.; Huang, X.-J.; Liu, Y.-L.; Wei, W.-T. *Adv. Synth. Catal.* **2022,** *364,* 2080–2085. doi:10.1002/adsc.202200272
267. Tan, Z.; Jiang, Y.; Xu, K.; Zeng, C. *J. Catal.* **2023,** *417,* 473–480. doi:10.1016/j.jcat.2022.12.033
268. Yang, Z.; Yang, D.; Zhang, J.; Tan, C.; Li, J.; Wang, S.; Zhang, H.; Huang, Z.; Lei, A. *J. Am. Chem. Soc.* **2022,** *144,* 13895–13902. doi:10.1021/jacs.2c05520
269. Chang, L.; An, Q.; Duan, L.; Feng, K.; Zuo, Z. *Chem. Rev.* **2022,** *122,* 2429–2486. doi:10.1021/acs.chemrev.1c00256
270. Srivastava, S.; Bajpai, L. K.; Batra, S.; Bhaduri, A. P.; Maikhuri, J. P.; Gupta, G.; Dhar, J. D. *Bioorg. Med. Chem.* **1999,** *7,* 2607–2613. doi:10.1016/s0968-0896(99)00188-1
271. Qin, L.; Tian, Y.; Yu, Z.; Shi, D.; Wang, J.; Zhang, C.; Peng, R.; Chen, X.; Liu, C.; Chen, Y.; Huang, W.; Deng, W. *Oncotarget* **2016,** *7,* 1395–1407. doi:10.18632/oncotarget.6366
272. Xu, B.; Yu, Z.; Xiang, S.; Li, Y.; Zhang, S.-L.; He, Y. *Eur. J. Med. Chem.* **2018,** *155,* 275–284. doi:10.1016/j.ejmech.2018.06.012
273. Araki, S.; Hirashita, T.; Shimizu, K.; Ikeda, T.; Butsugan, Y. *Tetrahedron* **1996,** *52,* 2803–2816. doi:10.1016/0040-4020(96)00002-6
274. Safa, K. D.; Samani, S. P.; Tofangdarzadeh, S.; Hassanpour, A. *J. Organomet. Chem.* **2008,** *693,* 2004–2008. doi:10.1016/j.jorganchem.2008.02.032
275. Jiang, J.; Zou, H.; Dong, Q.; Wang, R.; Lu, L.; Zhu, Y.; He, W. *J. Org. Chem.* **2016,** *81,* 51–56. doi:10.1021/acs.joc.5b02093
276. Madabhushi, S.; Jillella, R.; Mallu, K. K. R.; Godala, K. R.; Vangipuram, V. S. *Tetrahedron Lett.* **2013,** *54,* 3993–3996. doi:10.1016/j.tetlet.2013.05.072
277. Meng, X.; Zhang, Y.; Luo, J.; Wang, F.; Cao, X.; Huang, S. *Org. Lett.* **2020,** *22,* 1169–1174. doi:10.1021/acs.orglett.0c00052
278. Li, Z.; Sun, Q.; Qian, P.; Hu, K.; Zha, Z.; Wang, Z. *Chin. Chem. Lett.* **2020,** *31,* 1855–1858. doi:10.1016/j.cclet.2020.02.030
279. Finck, L.; Brals, J.; Pavuluri, B.; Gallou, F.; Handa, S. *J. Org. Chem.* **2018,** *83,* 7366–7372. doi:10.1021/acs.joc.7b03143

280. Li, Y.; Mou, T.; Lu, L.; Jiang, X. *Chem. Commun.* **2019,** *55,* 14299–14302. doi:10.1039/c9cc07655g
281. Shao, D.; Wu, Y.; Hu, S.; Gao, W.; Du, Y.; Jia, X.; Liu, S.; Zhou, M.; Chen, J. *ACS Sustainable Chem. Eng.* **2022,** *10,* 10294–10302. doi:10.1021/acssuschemeng.2c02597
282. Murakami, M.; Ishida, N. *Chem. Lett.* **2017,** *46,* 1692–1700. doi:10.1246/cl.170834
283. Murakami, M.; Ishida, N. *Chem. Rev.* **2021,** *121,* 264–299. doi:10.1021/acs.chemrev.0c00569
284. McDonald, T. R.; Mills, L. R.; West, M. S.; Rousseaux, S. A. L. *Chem. Rev.* **2021,** *121,* 3–79. doi:10.1021/acs.chemrev.0c00346
285. Wu, X.; Zhu, C. *Chem. Rec.* **2018,** *18,* 587–598. doi:10.1002/tcr.201700090
286. Hareram, M. D.; El Gehani, A. A. M. A.; Harnedy, J.; Seastram, A. C.; Jones, A. C.; Burns, M.; Wirth, T.; Browne, D. L.; Morrill, L. C. *Org. Lett.* **2022,** *24,* 3890–3895. doi:10.1021/acs.orglett.2c01552
287. Zhang, W.-C.; Li, C.-J. *J. Org. Chem.* **2000,** *65,* 5831–5833. doi:10.1021/jo000129r
288. Wang, S.; Guo, L.-N.; Wang, H.; Duan, X.-H. *Org. Lett.* **2015,** *17,* 4798–4801. doi:10.1021/acs.orglett.5b02353
289. Ren, R.; Zhao, H.; Huan, L.; Zhu, C. *Angew. Chem., Int. Ed.* **2015,** *54,* 12692–12696. doi:10.1002/anie.201506578
290. Huan, L.; Zhu, C. *Org. Chem. Front.* **2016,** *3,* 1467–1471. doi:10.1039/c6qo00443a
291. Zhao, H.; Fan, X.; Yu, J.; Zhu, C. *J. Am. Chem. Soc.* **2015,** *137,* 3490–3493. doi:10.1021/jacs.5b00939
292. Yamamoto, K.; Toguchi, H.; Kuriyama, M.; Watanabe, S.; Iwasaki, F.; Onomura, O. *J. Org. Chem.* **2021,** *86,* 16177–16186. doi:10.1021/acs.joc.1c01264
293. Pablo, Ó.; Guijarro, D.; Yus, M. *J. Org. Chem.* **2013,** *78,* 9181–9189. doi:10.1021/jo4014386
294. Zawodny, W.; Montgomery, S. L.; Marshall, J. R.; Finnigan, J. D.; Turner, N. J.; Clayden, J. *J. Am. Chem. Soc.* **2018,** *140,* 17872–17877. doi:10.1021/jacs.8b11891
295. Huang, F.; Zhang, S. *Org. Lett.* **2019,** *21,* 7430–7434. doi:10.1021/acs.orglett.9b02740
296. Li, K.; Kardelis, V.; Adronov, A. *J. Polym. Sci., Part A: Polym. Chem.* **2018,** *56,* 2053–2058. doi:10.1002/pola.29093
297. Abberley, J. P.; Killah, R.; Walker, R.; Storey, J. M. D.; Imrie, C. T.; Salamończyk, M.; Zhu, C.; Gorecka, E.; Pociecha, D. *Nat. Commun.* **2018,** *9,* 228. doi:10.1038/s41467-017-02626-6
298. Arakawa, Y.; Komatsu, K.; Inui, S.; Tsuji, H. *J. Mol. Struct.* **2020,** *1199,* 126913. doi:10.1016/j.molstruc.2019.126913
299. Perrone, R.; Berardi, F.; Colabufo, N. A.; Lacivita, E.; Leopoldo, M.; Tortorella, V. *J. Med. Chem.* **2003,** *46,* 646–649. doi:10.1021/jm020994z
300. Sonda, S.; Kawahara, T.; Katayama, K.; Sato, N.; Asano, K. *Bioorg. Med. Chem.* **2005,** *13,* 3295–3308. doi:10.1016/j.bmc.2005.02.016
301. Kubohara, Y.; Kikuchi, H.; Nakamura, K.; Matsuo, Y.; Oshima, Y. *Biochem. Biophys. Res. Commun.* **2010,** *396,* 364–369. doi:10.1016/j.bbrc.2010.04.098
302. Kim, H.; Kim, H.; Lambert, T. H.; Lin, S. *J. Am. Chem. Soc.* **2020,** *142,* 2087–2092. doi:10.1021/jacs.9b10678
303. Rehm, D.; Weller, A. *Isr. J. Chem.* **1970,** *8,* 259–271. doi:10.1002/ijch.197000029
304. Eriksen, J.; Lund, H.; Nyvad, A. I.; Yamato, T.; Mitchell, R. H.; Dingle, T. W.; Williams, R. V.; Mahedevan, R. *Acta Chem. Scand., Ser. B* **1983,** *37,* 459–466. doi:10.3891/acta.chem.scand.37b-0459
305. Breslin, D. T.; Fox, M. A. *J. Am. Chem. Soc.* **1993,** *115,* 11716–11721. doi:10.1021/ja00078a009
306. Gumy, J.-C.; Vauthey, E. *J. Phys. Chem. A* **1997,** *101,* 8575–8580. doi:10.1021/jp972066v
307. Schmalzbauer, M.; Ghosh, I.; König, B. *Faraday Discuss.* **2019,** *215,* 364–378. doi:10.1039/c8fd00176f
308. Cowper, N. G. W.; Chernowsky, C. P.; Williams, O. P.; Wickens, Z. K. *J. Am. Chem. Soc.* **2020,** *142,* 2093–2099. doi:10.1021/jacs.9b12328
309. Sun, G.; Ren, S.; Zhu, X.; Huang, M.; Wan, Y. *Org. Lett.* **2016,** *18,* 544–547. doi:10.1021/acs.orglett.5b03581
310. Gosztola, D.; Niemczyk, M. P.; Svec, W.; Lukas, A. S.; Wasielewski, M. R. *J. Phys. Chem. A* **2000,** *104,* 6545–6551. doi:10.1021/jp000706f
311. Plumb, J. B.; Obrycki, R.; Griffin, C. E. *J. Org. Chem.* **1966,** *31,* 2455–2458. doi:10.1021/jo01346a006
312. Bhattacharya, A. K.; Thyagarajan, G. *Chem. Rev.* **1981,** *81,* 415–430. doi:10.1021/cr00044a004
313. Pause, L.; Robert, M.; Savéant, J.-M. *J. Am. Chem. Soc.* **1999,** *121,* 7158–7159. doi:10.1021/ja991365q
314. Chernowsky, C. P.; Chmiel, A. F.; Wickens, Z. K. *Angew. Chem., Int. Ed.* **2021,** *60,* 21418–21425. doi:10.1002/anie.202107169
315. Shang, T.-Y.; Lu, L.-H.; Cao, Z.; Liu, Y.; He, W.-M.; Yu, B. *Chem. Commun.* **2019,** *55,* 5408–5419. doi:10.1039/c9cc01047e
316. Singh, P. P.; Srivastava, V. *Org. Biomol. Chem.* **2021,** *19,* 313–321. doi:10.1039/d0ob01884h
317. Caby, S.; Bouchet, L. M.; Argüello, J. E.; Rossi, R. A.; Bardagi, J. I. *ChemCatChem* **2021,** *13,* 3001–3009. doi:10.1002/cctc.202100359
318. Fujitsuka, M.; Kim, S. S.; Lu, C.; Tojo, S.; Majima, T. *J. Phys. Chem. B* **2015,** *119,* 7275–7282. doi:10.1021/jp510850z
319. Tian, X.; Karl, T. A.; Reiter, S.; Yakubov, S.; de Vivie-Riedle, R.; König, B.; Barham, J. P. *Angew. Chem., Int. Ed.* **2021,** *60,* 20817–20825. doi:10.1002/anie.202105895
320. Lopez, R. M.; Hays, D. S.; Fu, G. C. *J. Am. Chem. Soc.* **1997,** *119,* 6949–6950. doi:10.1021/ja971400y
321. Lam, K.; Markó, I. E. *Org. Lett.* **2011,** *13,* 406–409. doi:10.1021/ol102714s
322. Donabauer, K.; Maity, M.; Berger, A. L.; Huff, G. S.; Crespi, S.; König, B. *Chem. Sci.* **2019,** *10,* 5162–5166. doi:10.1039/c9sc01356c
323. Meng, Q.-Y.; Schirmer, T. E.; Berger, A. L.; Donabauer, K.; König, B. *J. Am. Chem. Soc.* **2019,** *141,* 11393–11397. doi:10.1021/jacs.9b05360
324. Rieth, A. J.; Gonzalez, M. I.; Kudisch, B.; Nava, M.; Nocera, D. G. *J. Am. Chem. Soc.* **2021,** *143,* 14352–14359. doi:10.1021/jacs.1c06844
325. Sakai, H. A.; Liu, W.; Le, C.; MacMillan, D. W. C. *J. Am. Chem. Soc.* **2020,** *142,* 11691–11697. doi:10.1021/jacs.0c04812
326. Ratani, T. S.; Bachman, S.; Fu, G. C.; Peters, J. C. *J. Am. Chem. Soc.* **2015,** *137,* 13902–13907. doi:10.1021/jacs.5b08452
327. Demarteau, J.; Debuigne, A.; Detrembleur, C. *Chem. Rev.* **2019,** *119,* 6906–6955. doi:10.1021/acs.chemrev.8b00715
328. Mondal, S.; Dumur, F.; Gigmes, D.; Sibi, M. P.; Bertrand, M. P.; Nechab, M. *Chem. Rev.* **2022,** *122,* 5842–5976. doi:10.1021/acs.chemrev.1c00582
329. Choi, J.; Fu, G. C. *Science* **2017,** *356,* eaaf7230. doi:10.1126/science.aaf7230
330. Wang, Z.; Bachman, S.; Dudnik, A. S.; Fu, G. C. *Angew. Chem., Int. Ed.* **2018,** *57,* 14529–14532. doi:10.1002/anie.201806015

331. Poremba, K. E.; Kadunce, N. T.; Suzuki, N.; Cherney, A. H.; Reisman, S. E. *J. Am. Chem. Soc.* **2017,** *139,* 5684–5687. doi:10.1021/jacs.7b01705
332. Ju, L.; Lin, Q.; LiBretto, N. J.; Wagner, C. L.; Hu, C. T.; Miller, J. T.; Diao, T. *J. Am. Chem. Soc.* **2021,** *143,* 14458–14463. doi:10.1021/jacs.1c07139
333. Wu, X.; Hao, W.; Ye, K.-Y.; Jiang, B.; Pombar, G.; Song, Z.; Lin, S. *J. Am. Chem. Soc.* **2018,** *140,* 14836–14843. doi:10.1021/jacs.8b08605
334. Claros, M.; Ungeheuer, F.; Franco, F.; Martin-Diaconescu, V.; Casitas, A.; Lloret-Fillol, J. *Angew. Chem., Int. Ed.* **2019,** *58,* 4869–4874. doi:10.1002/anie.201812702
335. Harkins, S. B.; Peters, J. C. *J. Am. Chem. Soc.* **2005,** *127,* 2030–2031. doi:10.1021/ja043092r
336. Zott, M. D.; Canestraight, V. M.; Peters, J. C. *ACS Catal.* **2022,** *12,* 10781–10786. doi:10.1021/acscatal.2c03215
337. Wang, K.; Liu, X.; Yang, S.; Tian, Y.; Zhou, M.; Zhou, J.; Jia, X.; Li, B.; Liu, S.; Chen, J. *Org. Lett.* **2022,** *24,* 3471–3476. doi:10.1021/acs.orglett.2c01022
338. Rössler, S. L.; Jelier, B. J.; Magnier, E.; Dagousset, G.; Carreira, E. M.; Togni, A. *Angew. Chem., Int. Ed.* **2020,** *59,* 9264–9280. doi:10.1002/anie.201911660
339. He, F.-S.; Ye, S.; Wu, J. *ACS Catal.* **2019,** *9,* 8943–8960. doi:10.1021/acscatal.9b03084
340. Bhunia, A.; Studer, A. *Chem* **2021,** *7,* 2060–2100. doi:10.1016/j.chempr.2021.03.023
341. Yi, J.; Badir, S. O.; Kammer, L. M.; Ribagorda, M.; Molander, G. A. *Org. Lett.* **2019,** *21,* 3346–3351. doi:10.1021/acs.orglett.9b01097
342. Ociepa, M.; Turkowska, J.; Gryko, D. *ACS Catal.* **2018,** *8,* 11362–11367. doi:10.1021/acscatal.8b03437
343. Liu, Y.; Xue, L.; Shi, B.; Bu, F.; Wang, D.; Lu, L.; Shi, R.; Lei, A. *Chem. Commun.* **2019,** *55,* 14922–14925. doi:10.1039/c9cc08528a
344. Mandigma, M. J. P.; Kaur, J.; Barham, J. P. *ChemCatChem* **2023,** *15,* e202201542. doi:10.1002/cctc.202201542
345. Sempere, Y.; Morgenstern, M.; Bach, T.; Plaza, M. *Photochem. Photobiol. Sci.* **2022,** *21,* 719–737. doi:10.1007/s43630-021-00146-3

License and Terms

BEILSTEIN JOURNAL OF ORGANIC CHEMISTRY

Enabling artificial photosynthesis systems with molecular recycling: A review of photo- and electrochemical methods for regenerating organic sacrificial electron donors

Grace A. Lowe

Review

Open Access

Address:
van 't Hoff Institute for Molecular Sciences (HIMS), Universiteit van Amsterdam (UvA), Science Park 904, Amsterdam, 1098 XH, The Netherlands

Email:
Grace A. Lowe - g.a.lowe@uva.nl

Keywords:
artificial photosynthesis; photocatalysis; redox couple; sacrificial electron donor; solar fuels

Beilstein J. Org. Chem. **2023,** *19,* 1198–1215.
https://doi.org/10.3762/bjoc.19.88

Received: 15 May 2023
Accepted: 17 July 2023
Published: 08 August 2023

This article is part of the thematic issue "Artificial photosynthesis".

Guest Editor: A. Pannwitz

Abstract

This review surveys advances in the literature that impact organic sacrificial electron donor recycling in artificial photosynthesis. Systems for photocatalytic carbon dioxide reduction are optimized using sacrificial electron donors. One strategy for coupling carbon dioxide reduction and water oxidation to achieve artificial photosynthesis is to use a redox mediator, or recyclable electron donor. This review highlights photo- and electrochemical methods for recycling amines and NADH analogues that can be used as electron donors in artificial photosynthesis. Important properties of sacrificial donors and recycling strategies are also discussed. Compounds from other fields, such as redox flow batteries and decoupled water splitting research, are introduced as alternative recyclable sacrificial electron donors and their oxidation potentials are compared to the redox potentials of some model photosensitizers. The aim of this review is to act as a reference for researchers developing photocatalytic systems with sacrificial electron donors, and for researchers interested in designing new redox mediator and recyclable electron donor species.

Introduction

Artificial photosynthesis research has resulted in the discovery and creation of incredible chemical systems and materials. The ultimate goal is to harness energy from the sun and use it to transfer electrons and protons from water onto carbon dioxide and create molecules to replace fossil fuels [1,2]. However, when developing the components of artificial photosynthesis systems species other than water are consumed to provide these electrons and protons [3,4]. Ideally these sacrificial donors would be replaced with redox mediators, regenerated using water, or form stable, commercially valuable oxidation products. However, common sacrificial electron donors, such as triethylamine, breakdown after oxidation which prevents regeneration [3,5]. Furthermore, there have also been studies where systems have been developed with sacrificial donors that interact and actually change the reactivity of the system [5,6]. Replacing these sacrificial donors becomes more challenging in

these scenarios. There is currently a steadily growing body of research investigating recycling of sacrificial electron donors. Meanwhile, advances in other fields have resulted in a vast array of alternative redox mediators and recyclable electron donors to explore.

Sacrificial donors have been used in artificial photosynthesis research to model different key photosynthesis processes. In plants, photosynthesis is a complex process where light-harvesting reactions are carried out in two photosystems to split water and recycle NADH and ADP. NADPH and ATP are then consumed in the Calvin cycle to reduce and fixate carbon dioxide [7]. Quite sensibly, many research groups investigating artificial photosynthesis develop components and systems for water splitting and carbon dioxide reduction separately before they or others seek to combine them. This modular approach is hugely beneficial because it can allow coupling of different reaction systems [2,8]. This strategy also works well for developing photoelectrochemical systems where the oxidation and reduction can be confined at separate electrodes.

When developing reactions for carbon dioxide reduction in a modular fashion isolated from water splitting, sacrificial electron donors are used as an electron source to act as a placeholder for NADPH and the water-splitting reaction. To recouple water splitting and carbon dioxide reduction the sacrificial donors need to be replaced by redox mediators. A redox mediator is a compound or material that shuttles electrons from one species to another through a series of chemically reversible reduction and oxidation reactions. In contrast, a sacrificial electron donor is a species that is oxidized to reduce another species and is consumed rather than regenerated. If a redox mediator is not re-reduced, then it is functioning as a sacrificial electron donor. However, not all sacrificial donors used to develop carbon dioxide reduction systems can be used as redox mediators because during oxidation they form products that cannot be regenerated. As a result, a different redox mediator compound or material is needed to couple the carbon dioxide reduction system to water splitting. That said, to successfully reduce a molecule there must always be a sacrificial electron donor or stoichiometric reductant. In photosynthesis the sacrificial donor is water, and the byproduct is oxygen.

Sacrificial electron donors are usually small organic molecules which are used in large quantities and need to be cheap. This often means they are less optimized than expensive catalysts and dyes. However, systems that employ redox mediators can use lower concentrations of more expensive species. For example, inorganic Z-schemes have used cobalt complexes and polyoxometalates to shuttle electrons between water oxidation and carbon dioxide reduction photocatalysts [2,4]. However, the photocatalysts of these systems are usually first developed separately with sacrificial electron donors. Other methods for bringing together the 2 halves of artificial photosynthesis include photoelectrochemical cells and artificial leaves, single molecule/particle photocatalysts, photovoltaic-powered electrochemical cells, and biophotoelectrochemical cells [8,9]. Some of these systems, like natural photosynthesis, are decoupled; the water oxidation and carbon dioxide reduction occur at different catalytic centers (locations) and in some cases at different times [8]. Decoupling is generally facilitated by the accumulation of charge or reacted species that can be stored. In artificial photosynthesis decoupling is also possible by storing reduced redox mediators, or regenerated electron donor species if they cannot simply be re-reduced. Not all approaches to carbon dioxide reduction in artificial photosynthesis require small organic sacrificial donors or mediators. This review focuses on regeneration and recycling of small organic molecules that can be used as sacrificial donors in photochemical carbon dioxide reduction.

A large scale decoupled, or macro, model of photosynthesis is electrochemical carbon dioxide reduction powered by renewable energy sources. Electrochemical carbon dioxide reduction has been commercialized. Specifically, the company Twelve are making large advances in the electrolysis of carbon dioxide to carbon monoxide. Their contracts started with materials and have now expanded to fuels [10]. However, industrial electrochemistry either requires a dedicated power source, or plugging into a national electricity grid. In countries like the UK, the competition to install new batteries and renewable energy sources appears to have created an increase in demand and waiting times for installing grid connections [11,12]. This is potentially a large barrier to fast adoption and scaling of purely electrochemical methods. However, in the short term this means that there is an opportunity, or unmet need, for simple photochemical systems that generate storable fuel/feedstocks without a grid connection or similar infrastructure. Consequently, this potential gap in the solar fuel/feedstock market makes it more important to replace unrecyclable sacrificial donors in molecular systems. Recently researchers have been looking at replacing traditional sacrificial donors with food and plastic waste [13]. This exciting new field of photoreforming does not involve regeneration of donors or the use of redox mediators, so it will not be covered in this review.

Most molecular components for photoreduction catalysis are not being developed or optimized with sacrificial electron donors that can be recycled. This means that the conditions must be reoptimized if redox mediators or other recyclable donors need to be used to couple the reduction to water oxidation or other reactions. Furthermore, the performance of the mo-

lecular photosensitizer and catalyst combinations developed are often very dependent on the properties of the sacrificial donors. This review has two aims: 1. Highlight work being done to recycle sacrificial donors used in photoreduction catalysis for artificial photosynthesis. Specifically, organic electron or hydride donors usually applied in molecular photocatalysis. 2. Survey the literature from different fields and present a sample of potentially recyclable electron donors for artificial photosynthesis, alongside the properties important for comparing the suitability of different donors. Such a resource should hopefully help to increase adoption of recyclable donors when developing photoreduction systems for artificial photosynthesis, as well as highlight gaps where new donor compounds are required.

Review

What makes a good sacrificial electron donor?

Before exploring sacrificial electron donor recycling, it is important to understand what chemical properties and behavior make efficient sacrificial electron donors. Sacrificial electron donors reduce either photoexcited or photooxidized photosensitizers in systems for carbon dioxide reduction (see Figure 1). Reductive quenching of the photosensitizer occurs when the sacrificial donor reduces the photoexcited photosensitizer (reductive quenching pathway). Regeneration of photooxidized photosensitizers occurs when the excited dye is first oxidatively quenched by a substrate or catalyst and then reduced by the sacrificial donor (oxidative quenching pathway). In the presence of protons, proton donors, or oxidized donor species with a low pK_a, a proton-coupled electron transfer (PCET) can take place [14,15]. PCET reactions are important in artificial photosynthesis research not only because they occur in biological photosynthesis but also because the PCET can circumvent unstable one electron-reduced intermediates. This makes PCET mechanisms well-suited for complex multielectron reactions required to transfer electrons and protons from water onto carbon dioxide [16]. Excited-state PCET, which is of particular interest for interactions between hydrogen atom or hydride-donating sacrificial donors, has recently been reviewed in detail by Dempsey and co-workers [17].

To select an effective sacrificial electron donor, at least four properties need to be considered: solubility in the chosen solvent, absorption spectrum, oxidation potential, and the revers-

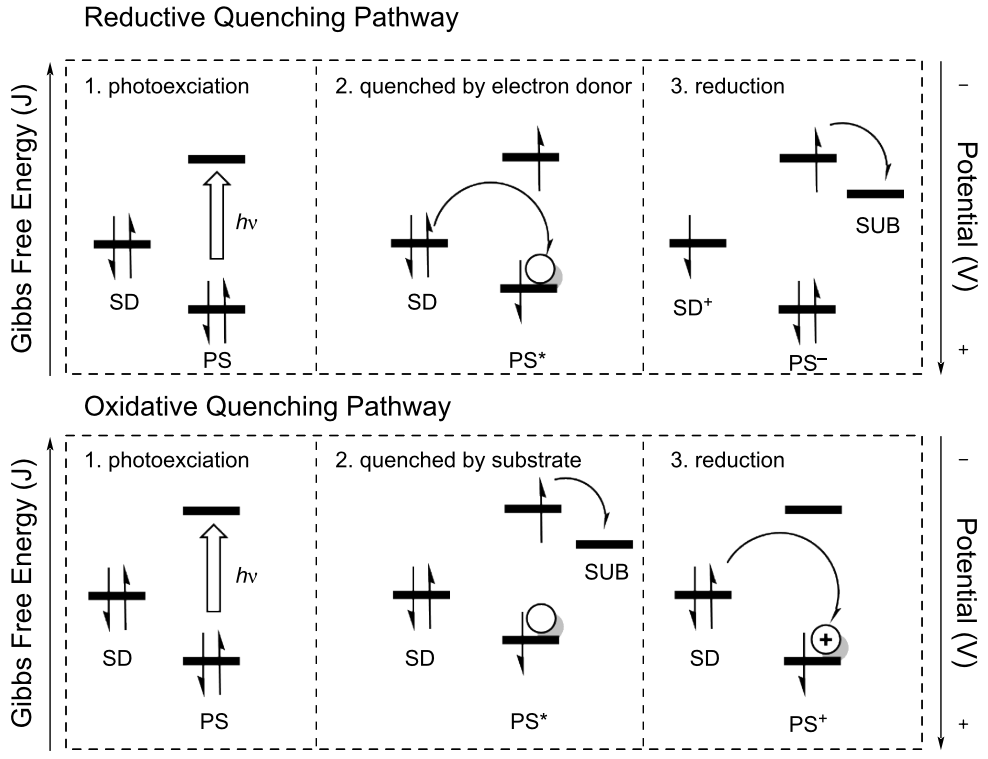

Figure 1: Diagram comparing the two reaction pathways for sacrificial electron donors (SD) in photocatalyzed reductions: reductive quenching and oxidative quenching. Energy levels of the photosensitizer (PS), sacrificial electron donor (SD), and substrate/catalyst (SUB) have been sketched relative to each other on an energy axis. Electron transfer between energy levels is indicated by half-arrows, and photoexcitation is indicated by arrows labelled *h*ν. The numbers indicate the order of electron transfer and orbital population is indicated by short arrows and circles. This figure was created to illustrate ideas communicated in references [3] and [18].

ibility of the sacrificial donor oxidation. As the sacrificial donor is a reactant in the photoreduction reaction of carbon dioxide, it needs to be highly soluble in the solvent used. It also needs to have a low absorption in the visible region to prevent side reactions and allow the photosensitizer to absorb as much light as possible. The oxidation potential of the sacrificial electron donor must be less positive than the reduction potential of the excited or oxidized photosensitizer for quenching or regeneration to occur. As shown in Figure 1, the scale of electrochemical potential measured in volts is an inverted scale of free energy. Therefore, it is thermodynamically favorable for electrons to be transferred from higher energy sacrificial donor orbitals with less positive oxidation potentials to lower energy orbitals on photooxidized or photoexcited photosensitizers with more positive potentials.

Cyclic voltammetry can be used to measure ground-state redox potentials by varying the potential at a working electrode with respect to a reference electrode and measuring the current response [19]. In photochemical carbon dioxide reduction research, this technique is used to measure the reduction potential of the oxidized photosensitizer and the oxidation potential of the electron donor. However, the reduction potential of the photoexcited photosensitizer is usually estimated using the Rehm–Weller equation and the ground-state redox potentials of the photosensitizer [18,20], or simulated [21,22]. There are actually methods for directly measuring the excited-state redox potentials of a photosensitizer, such as photomodulated voltammetry but they often require a more elaborate experimental setup [23]. It is important to note that unless special electrodes (ultra microelectrodes) or cells are used, voltammetric measurements of redox potentials require an ionically conductive salt to be added to the solution [19].

Oxidation and reduction potentials can vary with factors such as pH [14,15] and solvent polarity [24,25]. Hence, it is important when considering new reagents and catalysts to only compare potentials measured in conditions as close to the photocatalytic conditions as possible. For instance, quinones have 2 one-electron reductions in aprotic media and one two-electron reduction at a shifted potential in aqueous media [26]. As a demonstrative example concerning quenching, Schulz and co-workers only detected the 2-electron-reduced product of the Cu(I) 4*H*-imidazolate complex when it was irradiated in aprotic media in the presence of the sacrificial donor *p*-(dimethylamino)toluene (DMT) [27]. However, voltammetry in aprotic media indicated that a stable one-electron-reduced product should have been formed. Adding an inert ammonium salt to the voltammetry experiment mimicked the associative behavior of oxidized DMT and recreated the 2-electron reduction that occurred during photocatalysis. Cyclic voltammetry carried out in standard conditions for mimicking an acetonitrile system had not been close enough to the catalytic conditions to get the required redox potentials.

The difference between the oxidation potential of a sacrificial donor and the reduction potential of the excited or oxidized photosensitizer is the driving force for the electron transfer and photosensitizer regeneration. This driving force determines the rate of electron transfer from the electron donor to the photosensitizer which regulates the amount of photosensitizer available to harvest light energy and controls the turnover rate (often measured as turnover number), and productivity of the entire photocatalytic system. In order for the photoreduction system to work, either the reductive quenching or the oxidative quenching of the photosensitizer must be faster than the decay of the photosensitizer's excited state. Hence, Stern–Volmer plots derived from quenching measurements and photosensitizer excited-state lifetimes measured by transient spectroscopy are crucial to understanding and optimizing the system as a whole [18].

Recently, Kientz et al. demonstrated that the dark regeneration of oxidatively quenched photosensitizers can also limit the whole system in photochemical carbon dioxide reduction [28]. In the study, the driving force for reduction of an oxidized sensitizer was varied by using a series of photosensitizers with tunable oxidation potentials. They found that the turnover of the carbon dioxide reduction system was limited by the rate of the photooxidized sensitizer re-reduction.

In their review of sacrificial electron donors for solar fuels, Pellegrin and Odobel noted that an effective sacrificial donor must be irreversibly oxidized into inert molecules [3]. This prevents side reactions and allows the accumulation of the oxidized species and almost complete consumption of the sacrificial donor. However, thermodynamically irreversible does not mean that the sacrificial donor must break down into unrecyclable fragments like triethylamine (TEA). An irreversible electron transfer is slow and mitigates geminate recombination and, in principle, if there is no proceeding chemical step, the product can be re-reduced if an appropriate reducing agent or potential is applied. A reversible electron transfer followed by a fast chemical step, such as dimerization of oxidized dithiolates to sulfides, or a separate deprotonation event can also result in similar behavior. Gimeno et al. highlighted this when they designed novel benzimidazole (BIH) donors for the photoreduction with $[Cu(dipp)_2]^{2+}$ photocatalysts [29,30]. They contrasted their work to a previous study by Cunningham and McMillin who used a similar photocatalyst to systematically study ferrocene derivatives as sacrificial donors [31]. The ferrocene derivatives reductively quenched the photosensitizer but could not

accumulate as effectively as the BIH derivatives used by Gimeno et al. [29,31]. In contrast, Z-schemes that employ redox mediators can use compounds such as cobalt bipyridine complexes which undergo fast reversible electron transfer reactions [2,4,8]. Z-schemes require a steady state concentration of both oxidized and reduced redox mediator species to allow an efficient shuttling of electrons between photocatalysts. Unlike photocatalysis with unrecycled sacrificial donors, the reaction does not depend on the total consumption of the donor. Z-schemes are generally achieved by transfer of electrons to semiconductor particles with photocharged interfaces that can accumulate charge and provide a potential gradient to prevent significant recombination. These features make reversible redox couples suitable donors for Z-schemes when they are not necessarily the most efficient sacrificial donors for other photocatalysis schemes.

Recycling sacrificial reagents literature highlights

In 2011, Carpenter and co-workers published a study in which they used a cyclic tertiary amine sacrificial donor that they had designed to be regenerated [32]. This was significant because instead of replacing amine sacrificial donors with redox mediators, this paper proposed an alternate strategy of an ex-situ regeneration of organic donors. The authors designed and synthesized a tertiary amine that could be oxidized and rehydrogenated. They used their amine to successfully replace triethylamine in a photocatalytic carbon dioxide reduction reaction from the literature and proved that the recyclable byproduct was formed. In another experiment, the team chemically oxidized the sacrificial donor and regenerated it by hydrogenation.

Carpenter and co-workers briefly discussed phase separation to enable sacrificial donor recycling by improving the recovery of the oxidized donor [32]. This idea was central to the works published by Girault, Scanlon and co-workers on photocatalytic water splitting [33-35]. They used the redox mediator decamethylferrocene (DcMFc) in biphasic systems and semi-immobilized their photosensitizers and catalysts at interfaces between two immiscible electrolyte solutions (ITIES). This facilitated the in-situ redox mediator recycling and separation. The authors actually employed this strategy using 3 different reactor configurations (Figure 2). The first and simplest ex-situ photorecycling method involved adding and extracting 2 aqueous phases containing the catalysts and reactant to discharge and charge the donor-containing organic phase (Figure 2A) [34]. The first solution contained an organic lithium salt and a hydrogen-evolution catalyst which could generate hydrogen via a light-driven or dark process. The second solution contained an organic chloride salt and a water oxidation photocatalyst which re-reduced DcMFc and evolved oxygen. The same reaction scheme was used but in a modified H-cell (Figure 2B) [35]. Both catalysts were confined at the ITIES in two separate chambers and the redox mediator diffused between the two cells via the organic phase. The protons for hydrogen evolution migrated and diffused via the aqueous layer. The photoelectrochemical recycling was also studied in a system with one ITIES where the photocatalyst was immobilized and water oxidation was carried out at an electrode in the aqueous layer (Figure 2C). This electrode was connected to a counter electrode in the non-aqueous half-cell where DcMFc was re-reduced [35]. The potential difference in this reactor was generated by the photocatalyst excitation at the ITIES and not at the electrode, making it a photogalvanic cell. A subtle but important feature of these systems is that the partition of the electrolyte salt between the two solutions imposed an electrochemical bias that decreased the rate of chemical recombination between the two phases. Rastgar and Wittstock studied this phenomenon and the mechanistic details of photo- and electrocatalysis at ITIES with modified scanning electrochemical microscopy [36,37]. In nature, chemical gradients and phase separation are maintained by compartmentalization in liposomes, micelles, and vesicles rather than at interfaces such as ITIES. Artificial photosynthesis systems are being designed to mimic this behavior and recently the field of artificial photosynthesis using liposomes was thoroughly reviewed with special attention paid to donors and redox mediators [38]. Species such as methyl viologen were employed as redox mediators in some of the systems reviewed, however, the regeneration still required consumption of species other than water, such as EDTA.

Carpenter and co-workers also proposed, but did not test, recycling their amine with electrochemistry and light [32]. They cited a work by Itoh et al. who modified a proton exchange membrane electrolyzer with a Rh–Pt catalyst to generate hydrogen from water to hydrogenate benzene to cyclohexane in one reactor [39]. Itoh and co-workers were studying electrochemical hydrogenation for LOHCs rather than the regeneration of sacrificial donors. A lot of small organic compounds have been considered for electrochemical hydrogenation for LOHCs but many do not have the required oxidation potentials to be sacrificial donors [40]. More recently, other groups have published the electrochemical hydrogenation of carbonyl compounds using more earth-abundant electrocatalysts. For instance, Siewert and co-worker used a manganese complex as an electrocatalyst for the chemoselective carbonyl hydrogenation [41]. Behrouzi et al. reported the electrochemical hydrogenation of carbonyl and amido compounds using nickel electrodes and water as the proton and electron source [42]. Furthermore, the carbonyl and amido compounds used in these electrochemical hydrogenation

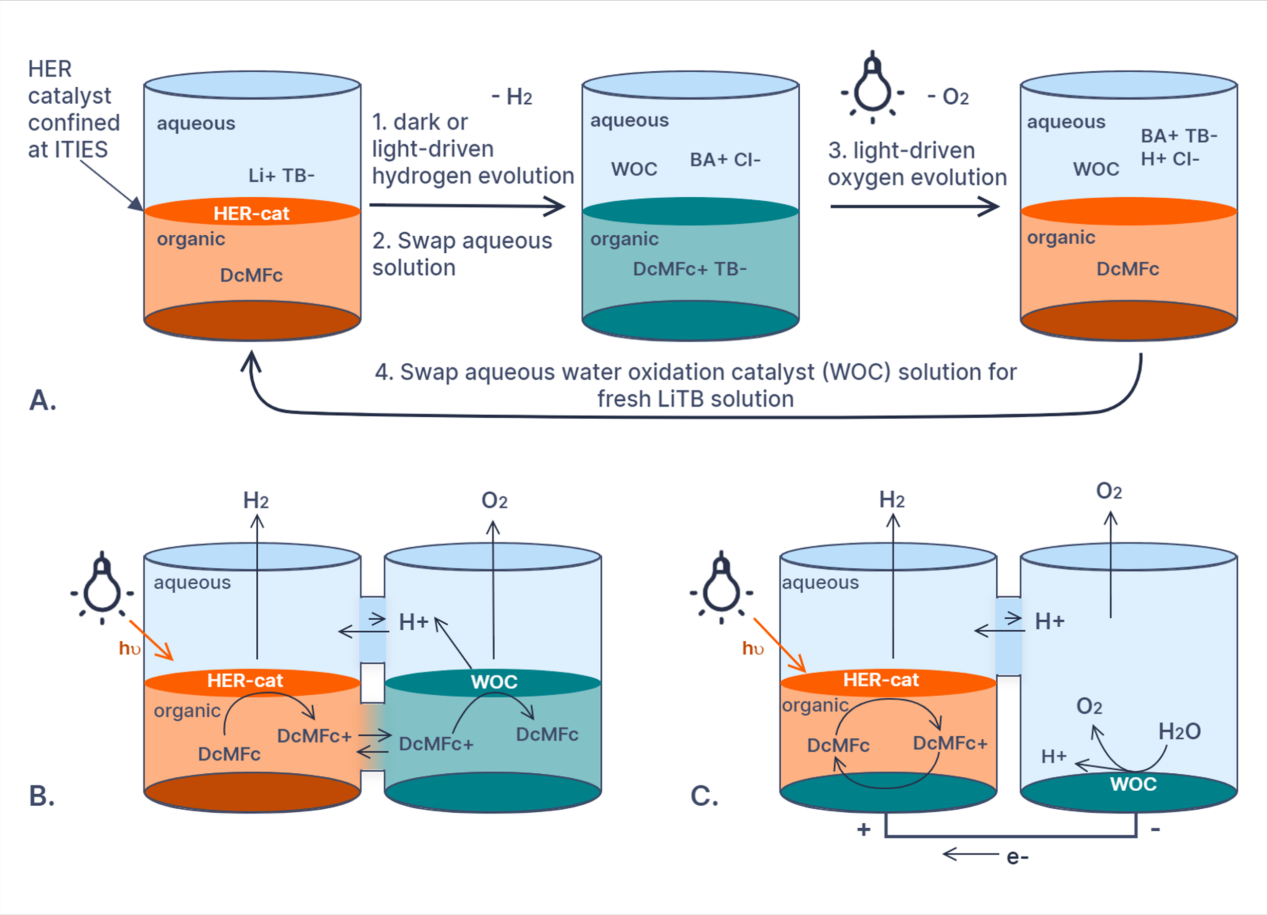

Figure 2: Diagram showing water-splitting systems developed by Girault, Scanlon, and co-workers that employ interfaces between two immiscible electrolyte solutions (ITIES) to enable recycling of the decamethylferrocene (DcMFc) sacrificial donor [35]. A. Photocharging and recycling of DcMFc by swapping aqueous solutions between mixtures containing a water-oxidation catalyst (WOC) and a hydrogen-evolution reaction catalyst (HER-cat). B. Photorecycling of DcMFc using ITIES to separate charge and catalysts for water splitting. This scheme can be described as a decoupled Z-scheme. C. Photogalvanic cell where the potential is established by photocharging of the ITIES. DcMFc is electrochemically recycled in-situ and water oxidation happens at the counter electrode. Note, that water is omitted for clarity in A, B, and C. The conductive salts are omitted for clarity in B and C. The lipophilic tetrakis(pentafluorophenyl)borate (TB^-) and bis(triphenylphosphoranylidene)ammonium (BA^+) salts were crucial to allow charge transfer at the ITIES.

studies are more structurally similar to organic sacrificial donors than cyclohexane. Although these papers were not demonstrating the recycling of sacrificial donors, they both demonstrate that electrochemical hydrogenation could be an extension of artificial photosynthesis for the production of solar fuels and feedstocks [41,42]. There is also a large body of work using simple alcohols as a proton and electron source in electrochemical hydrogenations [43]. This could also evolve into an extension of artificial photosynthesis if the alcohols used as donors are generated by artificial or natural photosynthesis (i.e., photosynthetic bacteria).

NADH and NADH-analogues are the subject of most studies for recycling sacrificial donors. NADH has been electrochemically recycled but a careful control of pH is required to prevent dimerization reactions [44,45]. For example, Glusac and co-workers recycled BIH and acridine analogues using platinum electrodes in acetonitrile with proton donors [45]. They carefully calculated the pK_aH of their proton donors and NADH analogues to control the PCET and to prevent side reactions. In another interesting example, NADH was recycled at a copper electrode in aqueous buffers and NADH was found to be more stable in a tris buffer rather than phosphate [44]. Instead of using the regenerated NADH in a photocatalytic system, this team actually used an enzyme to consume the regenerated NADH and check its viability.

Robert and co-workers recycled the NADH analogue 1,4-BNAH using different photosensitizers and cobalt catalysts in an acetonitrile/water mixture [46]. They used combinations of deuterated solvents and ^{1}H NMR spectroscopy to confirm that water was the main source of the protons for the regeneration. Furthermore, they successfully replaced ruthenium photosensitizers with organic dyes so that the system used predominantly

earth-abundant materials. The recycling of NADH analogues has been carried out using precious metal complexes, such as $[CpRh(bpy)(H_2O)]^{2+}$ [47]. This rhodium complex was adhered to a photoelectrode in a photoelectrochemical cell which also contained a second photoelectrode functionalized with a set of enzymes [47]. The enzymes reduce carbon dioxide to methanol and consumed NADH which was then recycled at the photoelectrode functionalized with the rhodium complex. The overall electron donor in this work was water which makes it an excellent example of in-situ recycling. Kuk et al. also noted that $[CpRh(bpy)(H_2O)]^{2+}$ could slowly produce formate, a key biocatalytic intermediate, in the absence of the enzymes but they validated their system by proving that overall the formate production and conversion to methanol by the biocatalytic enzyme cascade far outcompeted any side-reactions.

Ishitani and co-workers introduced BIH analogues based on the *N*,*N*'-dimethyl-2-phenylbenzimidazole scaffold as more efficient alternatives to NADH-derived electron donors for carbon dioxide reduction photocatalysis [48]. Consequently, BIH analogues are becoming increasingly popular sacrificial electron donors in artificial photosynthesis [3,29,48]. Glusac and co-workers published studies on the photochemical recycling of BIH analogues [49]. They used an organic photocatalyst to reduce the oxidized benzimidazole 1,3-dimethyl-2-(2,4,6-trimethoxyphenyl)-2*H*-benzimidazole (BIM) twice in the presence of various acids [49]. This system is completely metal-free and uses one photocatalyst rather than separate sensitizer and catalyst species. However, the electron source for the reductions was a thiolate sacrificial donor and not water. Thiolates are used as redox mediators in other systems such as dye-sensitized solar cells [50,51].

As discussed, if a sacrificial donor is recycled in-situ it becomes a redox mediator. In artificial photosynthesis redox mediators are most commonly employed in Z-schemes. A Z-scheme describes the combination of two photocatalytic systems, one for photooxidation and one for photoreduction, with their energy levels arranged so that they operate together to transfer electrons from one substrate to another (Figure 3). Artificial Z-schemes were used for photochemical water splitting before carbon dioxide reduction and are mainly being investigated using particulate semiconductor photocatalyst composites, such as decorated quantum dots [4]. Most of the particulate Z-schemes use inorganic rather than organic redox mediators [2]. Interestingly, soluble redox mediators can be replaced by conducting substrates in inorganic Z-schemes to create 'redox

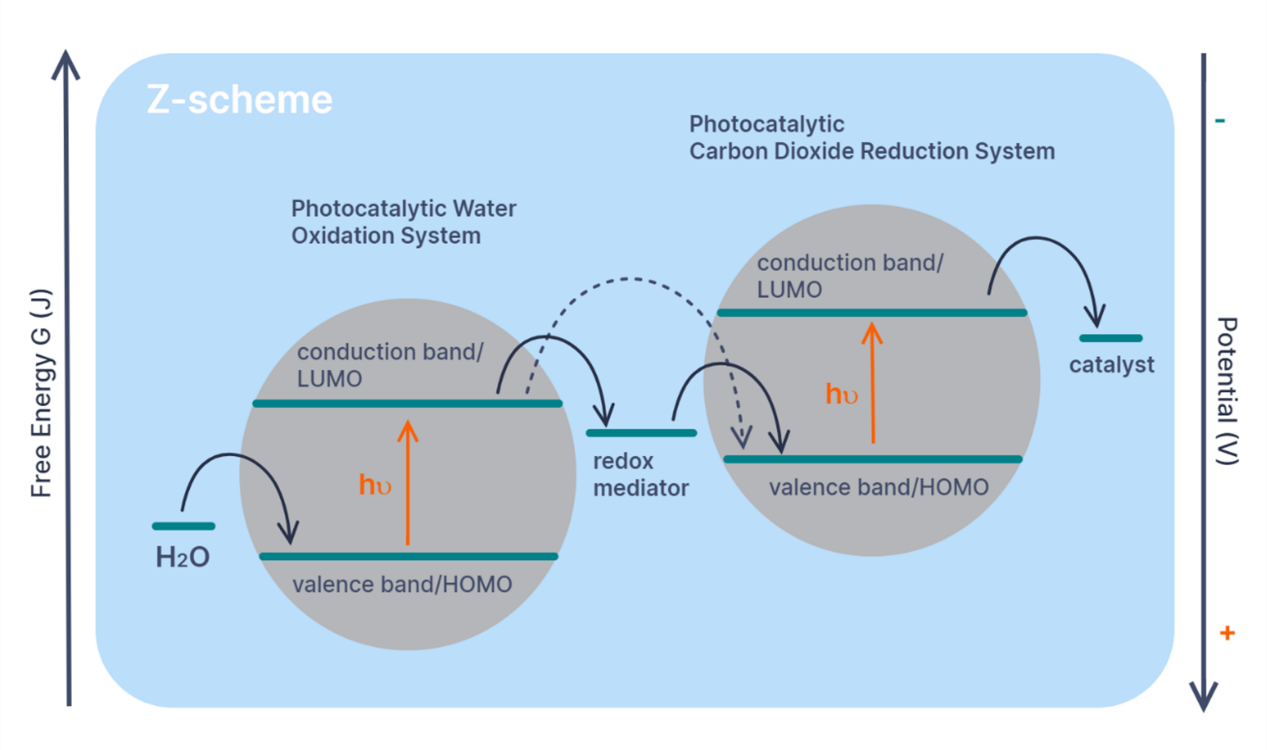

Figure 3: Diagram illustrating the transfer of electrons in a photocatalytic particulate suspensions Z-scheme for carbon dioxide reduction. The dotted arrow indicates the transfer of electrons between the two photocatalytic systems in the absence of a redox mediator, for example, when two systems are anchored together close enough to permit successful electron transfer. The redox mediator can also be replaced by immobilizing the photocatalytic systems on conductive materials or electrodes in an electrochemical cell.

mediator-free' schemes [2,4]. For example, Domen, Reisner and co-workers have realized a Z-scheme using a photoelectrochemical cell to produce formate with water as the electron source [52]. Their photocatalyst sheets are electrically connected and thus do not require redox mediators. Domen and co-workers have even connected carbon dioxide and water splitting on a single light-absorbing material Al-$SrTiO_3$ [53]. However, as demonstrated by Domen and co-workers optimizing the conditions for these redox-mediator-free schemes is very different to optimizing particulate suspension Z-schemes [54].

The photocatalytic assemblies for Z-schemes are usually developed independently with different donors. Recently Ma et al. have developed a carbon dioxide reduction photosystem composed of a cobalt–quaterpyridine catalyst anchored to carbon nitride semiconductor particles [55]. Rather than an inorganic sacrificial donor, they developed this system using a benzimidazole sacrificial donor. As we have discussed, examples of recycling benzimidazoles already exist which makes them excellent candidates for donor recycling.

In contrast to those developed for water splitting, one of the first visible light-driven Z-scheme for carbon dioxide reduction consumed the sacrificial donor methanol to form formic acid and formaldehyde [56]. This system is interesting for a number of reasons. Rather than intermediate redox mediators shuttling charge between two photocatalytic assemblies, Ishitani, Domen, and co-workers covalently connected the catalytic systems and photosensitizers to enable direct electron transfer between them. In contrast to the system of Domen where the photoexcitation only occurs at the Al-$SrTiO_3$ particle [53], the system developed by Ishitani included a second ruthenium chromophore linked the TaON particle to a ruthenium carbonyl catalyst [56]. This allowed the electron to be promoted by 2 photon absorption events, making it a Z-scheme. It can be argued that the linking ruthenium chromophore was acting as a redox mediator. Rather than using water as the sacrificial donor in this work, they used methanol which can be produced by photocatalytic or electrochemical carbon dioxide reduction. The oxidation product, formaldehyde, can be re-reduced. However, separation of formaldehyde and the carbon dioxide reduction product formic acid would be difficult. Therefore, a logical route for sustainably sourcing methanol would be using this system in combination with another that photo- or electrochemically reduces carbon dioxide to methanol.

Recycling strategies

There are currently two favored methods emerging for sacrificial donor regeneration: photochemical recycling and electrochemical regeneration. The rehydrogenation of model compounds by thermochemical methods has also been demonstrated by Carpenter and co-workers [32]. The two clear strategies for recycling sacrificial donors are in-situ and ex-situ recycling. With the exception of existing Z-schemes and the ITIES water-splitting work, most sacrificial donor recycling methods are being developed separately from photocatalytic systems even if they are intended to be used for in-situ recycling. Although in-situ recycling is closer to actual photosynthesis, ex-situ recycling of sacrificial donors should be considered as another avenue to realize net artificial photosynthesis.

In-situ recycling of sacrificial donors and redox mediators would require less donor/mediator because the species would constantly be regenerated and not consumed. If the donor or mediator is stable under the reaction conditions, the cost and complexity of the donor can be higher than that of a sacrificial donor. However, it is likely that high steady-state concentrations of a donor will be needed and using the costs targets set for redox flow battery electrolytes is probably a sensible starting point. In an ideal system, the only inputs needed would be carbon dioxide, water, and light. This implies photochemical recycling in-situ. However, electrochemical in-situ recycling could be achieved in 2 ways: 1. The driving force for recycling an oxidized donor at an electrode could be supplied by a photosensitizer. 2. The driving force for donor re-reduction could be an applied voltage from renewable energy sources.

Following the example of 'decoupled water splitting' and redox flow batteries (RFBs) by recycling the electron donor ex-situ offers several potential advantages [8,57,58]. For example, decoupling carbon dioxide reduction and water oxidation in two separate reactors would allow the development of simpler chemical systems with less components and less factors to optimize per reactor. This would require less re-optimization of existing chemistry. Recyclable donors could be stored in tanks like RFB electrolytes, which decouples the 2 reactions and means rates do not have to be perfectly balanced [8]. Furthermore, photogenerated reactants could be stored in excess to keep any 'dark' processes running overnight. Schulz and co-workers reported a Cu(I) 4*H*-imidazolate photosensitizer that was reductively quenched in the presence of DMT to generate a stable reduced species [27]. The reduced species was so stable that it could be stored in the dark for hours and then be used to reduce methyl viologen. If DMT can be replaced with a more sustainable electron source, this could be part of a decoupled cycle either regenerating an oxidized sacrificial donor or using the reduced Cu(I) 4*H*-imidazolate itself as a donor. However, regenerated donors would need to be stored in large amounts to fuel a carbon dioxide reduction process at an industrially rele-

vant rate. This means that they would have to be inexpensive, easy to synthesize, and made from earth abundant materials. They would also have to be stored in oxygen-free conditions to prevent re-oxidation.

A major advantage of ex-situ or decoupled sacrificial electron donor recycling is that, like decoupled water splitting, the gaseous products can be evolved separately preventing explosive mixtures. However, if the sacrificial donor needs to be separated from other homogenous catalysts or supporting electrolytes, this could be a challenge. Phase-separation systems such as the ITIES methods developed by Girault and Scanlon for water splitting could be a crucial starting point for developing scalable systems [35]. There is also a branch of artificial photosynthesis research investigating the compartmentalization of different reactions using liposomes and membranes [38]. Another alternative could be to use redox-active polymers as recyclable donors which would allow microporous membrane separation. Redox-active polymers are a very active area of research for aqueous and non-aqueous RFBs [59,60]. This is because often the most expensive component of an RFB is the ion-exchange membrane used to prevent the mixing of charged species and recombination. Microporous membranes are much less expensive, and the particulate size of redox-active polymers could be tuned to prevent unwanted crossover. Photosensitizers and catalysts have been successfully immobilized in polymeric matrices, which is also another approach to phase separation [61,62].

Exploring candidates for recyclable electron donors

From our consideration of what makes an effective sacrificial electron donor we can highlight the chemical properties required by an effective recyclable electron donor or redox mediator. For a system that requires oxidative or reductive quenching, the oxidation potential of the donor must be less positive than the reduction potential of the oxidized photosensitizer or excited photosensitizer, respectively. The donor must be highly soluble, absorb light in a region that does not overlap with the absorption of the photosensitizer, and form a stable oxidation product that can be re-reduced in the presence of water. Redox mediators for in-situ recycling benefit from fast reversible electron transfer. However, if they are interacting with a molecular photosensitizer care needs to be taken to choose a species that maximizes cage escape yield and minimizes geminate recombination. Recyclable donors that must accumulate need to undergo electrochemically irreversible oxidation or an EC mechanism where the oxidized donor undergoes a chemical step that prevents recombination but forms a stable, recyclable byproduct. The dimerization of thiolates to disulfides is a good example because unlike dimers of NADH analogues that form carbon–carbon bonds the S–S bond is easily broken. The chemical step can also be a phase change as demonstrated in the work by Girault and co-workers [35]. Systems designed for PCET, whether excited-state PCET or PCET of the ground state species, will benefit from donors that carry a hydride or hydrogen atom equivalent rather than just electrons, as well as by carefully matching the oxidation potential of the donor to the redox potentials of the system. However, one must also carefully calculate the pK_a values of the system and choose a donor to match [17,45,49].

Measuring or calculating the redox potentials of photosensitizers is important for designing photocatalytic systems. Potential electron donors can be screened by comparing their oxidation potential to the redox potentials of the photosensitizer. Because redox potentials are solvent and pH-dependent, it is important to compare potentials recorded in conditions as close to the final catalysis conditions as possible. Once candidate donors have been identified using their oxidation potential, their quenching behavior and the effect on the photocatalytic performance can be tested.

To help identify potential recyclable replacements for sacrificial donors such as triethylamine, the oxidation potentials of different families of electron donors have been plotted for both aqueous (Figure 4) and non-aqueous media (Figure 5). The oxidation and excited-state reduction potentials of ruthenium trisbipyridine ($Ru(bpy)_3$) have been added to each figure. $Ru(bpy)_3$ is a well-studied photosensitizer and the basis for many analogues used in artificial photosynthesis. This makes it a good compound to use as a guide for how low the oxidation potential of electron donor candidates needs to be. The oxidation potential of $Ru(bpy)_3$ indicates the LUMO energy of the photooxidized sensitizer, and it is the relevant reduction potential for the regeneration of the photooxidized photosensitizer. The excited-state reduction potential of $Ru(bpy)_3$ is the reduction potential relevant to reductive quenching. The potential axes on the graph have been inverted to aid the reader to visualize the electron transferring from higher energy electron donors to the lower energy levels of the photooxidized or photoexcited $Ru(bpy)_3$. The data used to create the figures is available in the tables in Supporting Information File 1.

The examples of candidates for recyclable donors in aqueous systems shown in Figure 4 have been chosen from literature on redox flow batteries and decoupled hydrogen evolution, as well as photocatalysis. The oxidation and reduction potentials have been collected from various references and were converted to the potential scale vs SCE. Unless otherwise stated, the potentials were recorded in neutral conditions, or the pH was not specified.

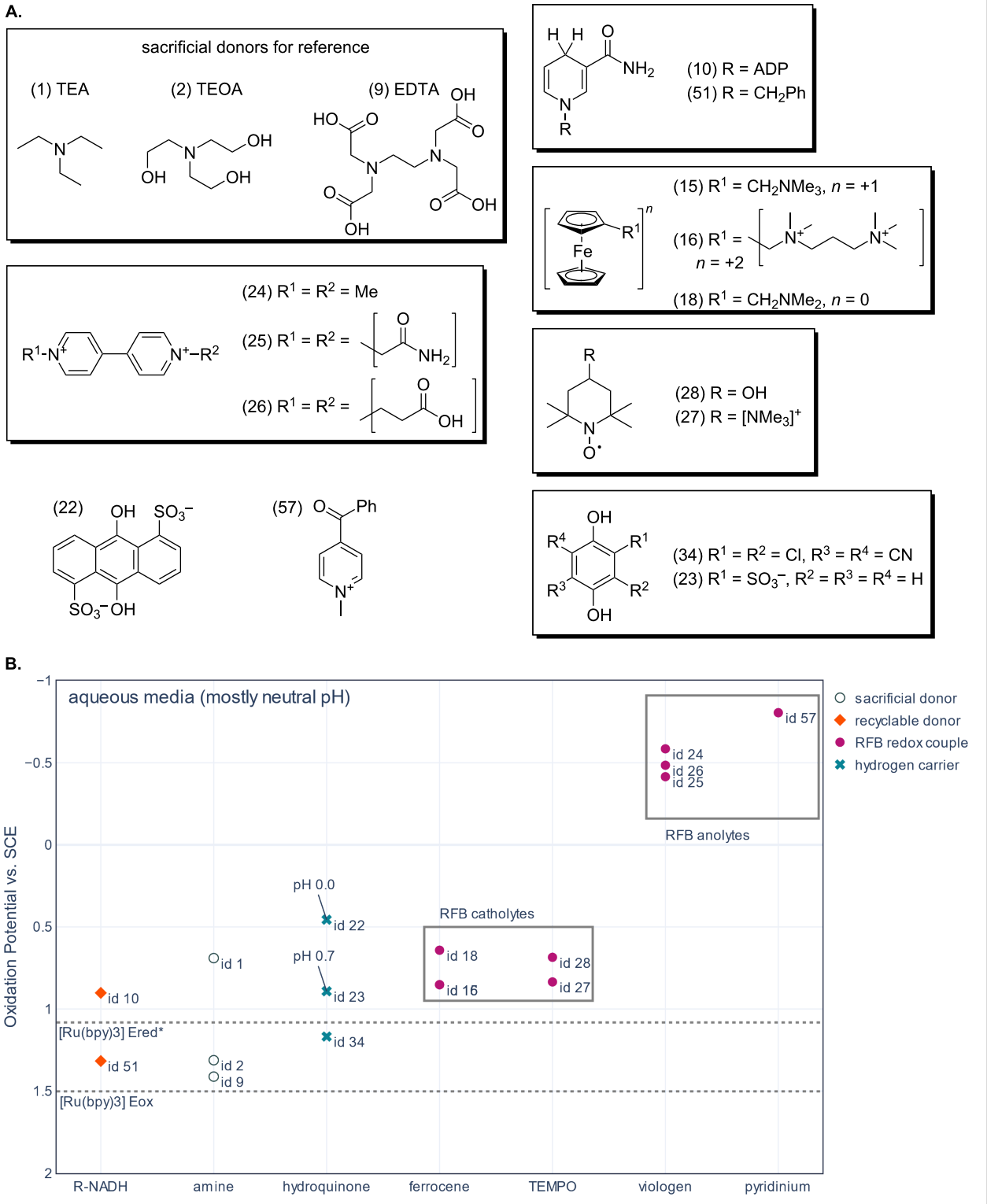

Figure 4: A. Structures of the molecules represented in part B. The numbers in brackets correspond to the compound id in Supporting Information File 1 and the data point labels in part B. B. Plot of oxidation potential vs SCE in aqueous media for compounds sorted by redox-active moiety. Note that the potentials are shown for the one electron-reduced viologen species, not the doubly reduced species. Dotted lines have been added to indicate the excited-state reduction potential (E_{red}*) and oxidation potential (E_{ox}) of ruthenium trisbipyridine chloride in aqueous media. Unless the data point is labelled, the potentials were recorded at neutral or unspecified pH. The references for the potentials can be found in the text and in Supporting Information File 1. The data point labels correspond to the compound id in Supporting Information File 1.

The three amine examples, EDTA (1.41 V vs SCE), triethanolamine (1.31 V vs SCE), and triethylamine (0.69 V vs SCE), are all common sacrificial donors in photocatalysis. Although they cannot be regenerated, these examples indicate the operational potential range expected for photosensitizer quenching. Triethylamine has the lowest oxidation potential and is the most reducing of the 3 species (0.69 V vs SCE) which means that it can both reductively quench $Ru(bpy)_3$ and regenerate photooxidized $Ru(bpy)_3$ if the lifetime and electron-transfer rates are appropriate. EDTA has the highest reported oxidation potential and is the least reducing member of the amines shown (1.41 V vs SCE). Hence, it should only regenerate photooxidized $Ru(bpy)_3$ in aqueous conditions. Unfortunately, Carpenter and co-workers did not measure the oxidation potential of their recyclable amine species for comparison [32].

The ferrocene, TEMPO, and viologen derivatives shown in Figure 4 are used in aqueous organic redox flow batteries [59,63]. The batteries store charge in concentrated aqueous solutions of small organic redox mediators that can be oxidized and re-reduced (or reduced and reoxidized) for 100s or 1000s of cycles. These redox mediators need to be highly soluble, stable, and their charged products need to be stable for days if not months. This makes them excellent candidates for redox mediators, or recyclable electron donors in aqueous artificial photosynthesis.

TEMPO and ferrocene derivatives are used to store positive charge in RFB catholytes [59,63]. Both parent compounds undergo reversible one-electron oxidation and re-reduction but had to be modified to improve their solubility. TEMPTMA and both ferrocene derivatives have one or more ammonium groups added to the core TEMPO or ferrocene charge-carrying moiety. This both increases the solubility of the species and the oxidation potential in aqueous media. TEMPOL uses an alcohol group to the same effect. Redox couples for RFB catholytes are optimized for increasing the oxidation which decreases their reduction capabilities. However, the TEMPO and ferrocene derivatives have oxidation potentials similar to triethylamine, which would be an ideal range to target. Although the oxidation potentials of the ferrocene and TEMPO derivatives are in an ideal range for electron donors, these compounds and their oxidation products are positively charged. This will stabilize the charge-transfer complex formed during quenching and combined with fast electron transfer will likely increase the rate of recombination and decrease their effectiveness as donors.

The oxidation potentials of the viologens (Figure 4) are shown for the one-electron-reduced viologen species ([methyl viologen]$^{\bullet-}$ −0.59 V vs SCE, [ethylcarboxy viologen]$^{\bullet-}$ −0.49 V vs SCE, [ethylamide viologen]$^{\bullet-}$ −0.42 V vs SCE) [59]. Viologens usually act as electron acceptors in aqueous RFB anolytes. In general, RFB anolytes are optimized to have very low reduction potentials. Once reduced, anolyte redox mediators become excellent reducing agents and viologens can be reduced twice in two separate one-electron transfer events. The viologen family of compounds has been the target of structural modifications to tune the redox potentials and enhance the solubility for RFBs [59]. Meanwhile, methyl viologen has been used as a sacrificial electron acceptor in photochemistry [27]. Therefore, viologen species could be used as redox mediators for linking water oxidation to carbon dioxide reduction by accepting electrons during water oxidation and donating them during carbon dioxide reduction to be reoxidized. Because viologens are positively charged and are reduced to neutral compounds, it is likely that the resulting charge-transfer complex will have a higher cage escape yield than a complex where the oxidized donor has a positive charge. However, in some rare cases the excessive driving force provided by reduced viologens (up to 1.28 V > triethylamine) might be too large a difference in energy and lead to Marcus inversion [64]. A more practical issue is the reoxidation of viologen in the presence of oxygen.

Redox flow battery anolyte research focuses on increasing solubility and stability while decreasing the reduction potential, weight, and cost of the anolyte species. To this end, Sanford and co-workers have worked on developing pyridinium analogues to out-perform the bipyridinium viologens [65,66]. The pyridinium analogue represented in Figure 4 can be reduced to a stable radical and reoxidized in aqueous media [65]. Depending on the pH, the reduction potential to form the 2 electron-reduced species is close to that of the stable radical. In non-aqueous media analogues of this species form stable 2 electron-reduction products. In aqueous media the 2 electron-reduced product can undergo side reactions. Interestingly at low pH the 2-electron product behaves like a redox catalyst for hydrogen evolution and can increase the pH from 4 to 11. Although this behavior is not desirable for RFBs it might be interesting for artificial photosynthesis. It is also noteworthy that the reduced pyridinium compounds resemble Hantzsch esters which are organic reductants commonly used in organic synthesis.

Quinones and hydroquinones have also been used in RFBs. Notably, 1,4-hydroquinone and 1,4-benzoquinone were used to create membrane-less RFBs with ITIES and charge-separation maintained in a flowing system [67,68]. Two of the examples shown in Figure 4 AQDS (0.46 V vs SCE at pH 0) and hydroquinone sulfate (0.89 V vs SCE at pH 0.7) have been used as hydrogen carriers in decoupled water splitting, rather than in RFBs [57]. Hydrogen carriers in decoupled water-splitting studies are re-reduced using protons from water in acidic condi-

tions, and are used to transport hydrogen equivalents across membranes and between reactors. Some examples have been used as recyclable reductants [58]. These particular quinones have low enough oxidation potentials for reductive quenching of $Ru(bpy)_3$ and reduction of photooxidized $Ru(bpy)_3$. Furthermore, quinones have well-studied PCET chemistry [26]. 2,3-Dichloro-5,6-cyano-1,4,hydroquinone, the hydrogenated form of 2,3-dichloro-5,6-cyano-1,4-benzoquinone (DDQ), has the highest oxidation potential of the 3 quinone examples (1.17 V vs SCE). This means it does not have the energy to reductively quench $Ru(bpy)_3$ [26]. Hydroquinones are a large family of compounds with a wide range of redox potentials and only a small sample has been shown here.

The NADH analogue BNAH which has been successfully regenerated using water is also shown in Figure 4. In aqueous media the oxidation potential of BNAH stays constant between pH 7 and 13 (if stable buffer is used) [69]. However, the oxidation potential increases and the reducing ability of BNAH and other NADH analogues decreases with pH after pH 7. NADH analogues are excellent candidates for electron donors in systems that require PCET because PCET prevents dimerizable radical formation. However, a too low pH value could be detrimental. The redox potentials recorded for BNAH were also reported to be very sensitive to the electrode material.

Many carbon dioxide reduction systems are being developed in non-aqueous solvents. Amines, disulfide-forming thiolates, and NADH derivatives, such as benzimidazoles and acridines, are used as sacrificial donors. Other families of compounds used in other applications such as non-aqueous RFBs, dye-sensitized solar cells, and LOHCs will also be discussed. The oxidation potentials of these compounds in non-aqueous media vs Fc/Fc^+ are shown in Figure 5. The excited-state reduction potential of $Ir(ppy)_3$ in DMF (V vs Fc/Fc^+) has been added to the plot for comparison [70], as well as the redox potentials for $Ru(bpy)_3$ in acetonitrile [20]. $Ir(ppy)_3$ is a photosensitizer used for carbon dioxide reduction because it is one of the most photoreducing dyes available [71]. The redox potentials presented were recorded in a variety of non-aqueous solvents which means this graph is only a rough comparison. It is highly recommended that the oxidation potential of any compound of interest are re-recorded before using them to screen conditions for photocatalysis.

Although most benzimidazole examples have been marked as sacrificial donors in Figure 5, BIM (−0.07 V vs Fc/Fc^+) and other analogues have been recycled by Glusac and co-workers [49]. It is highly likely that the same recycling methods could be extended to the rest of the benzimidazole family. Benzimidazoles are being adopted in organic photoreductions [30], and have been shown to increase the efficiency of carbon dioxide reduction systems using ruthenium-based photocatalytic systems [48,72]. This can be explained by the low oxidation potentials (0.31 to −0.47 V vs Fc/Fc^+) amongst other factors. Bases are often added to enhance the quenching rate by deprotonation of benzimidazoles which means they are commonly used with TEA or TEOA [29,30]. Benzimidazoles are also one of the redox mediators that can be recycled photo- and electrochemically [45,49]. As illustrated in Figure 5, structural modification of the benzimidazole core alters the redox behavior and allows tuning of the oxidation potential. The benzimidazoles shown all have enough reducing power to reductively quench $Ru(bpy)_3$ and possibly $Ir(ppy)_3$. The tunability of benzimidazoles is particularly helpful when developing photocatalysis systems with new photosensitizers and their capability to undergo PCET in certain environments could be an advantage for some systems. Acridine compounds are also analogues of NADH and have electrochemical behavior amenable to recycling. The example shown has a redox potential that is more positive than most benzimidazoles but still suitable for the reductive quenching of $Ru(bpy)_3$ (0.28 V vs Fc/Fc^+) [45]. In aprotic media both benzimidazoles and acridines donate 2 electrons and a proton in separate redox events. However, only the oxidation potential to remove the first electron is shown for these species because it is this initial oxidation that generates the other electron-donating intermediates.

A variety of compounds have been grouped together with the amines label in Figure 5. 4-(*N*,*N*-Dimethylamino)toluene (DMT), has been used as a sacrificial electron donor in artificial photosynthesis [3]. The radical species that forms after oxidation can dimerize by forming a carbon–carbon bond which cannot be broken by re-reduction [3,73]. Voltammetric studies to identify the byproducts of DMT oxidation noted that the corresponding dimethyl amine – *p*-benzaldehyde oxidized at 0.79 V vs Fc/Fc^+ and underwent a slow re-reduction [73]. Similar compounds, ketone derivatives rather than aldehyde, were developed with more negative potentials as anolytes for aqueous and non-aqueous RFBs by Sanford and co-workers [65,66]. The redox potential of the aldehyde is too positive for reductive quenching but low enough to regenerate photooxidized $Ru(bpy)_3$. The aldehyde has been added to the figure because it is an interesting compound to consider when designing recyclable sacrificial donors, even though an example could not be found where it was used in artificial photosynthesis or RFB research.

The carbazole 9-ethyldodecahydro-1*H*-carbazole (DEC-H12) has an oxidation potential of 0.57 vs Fc/Fc^+ and can carry 6 hydrogen equivalents [74] (DEC-H12 has been classified as an amine in Figure 5). The oxidation potential of DEC-H12 is

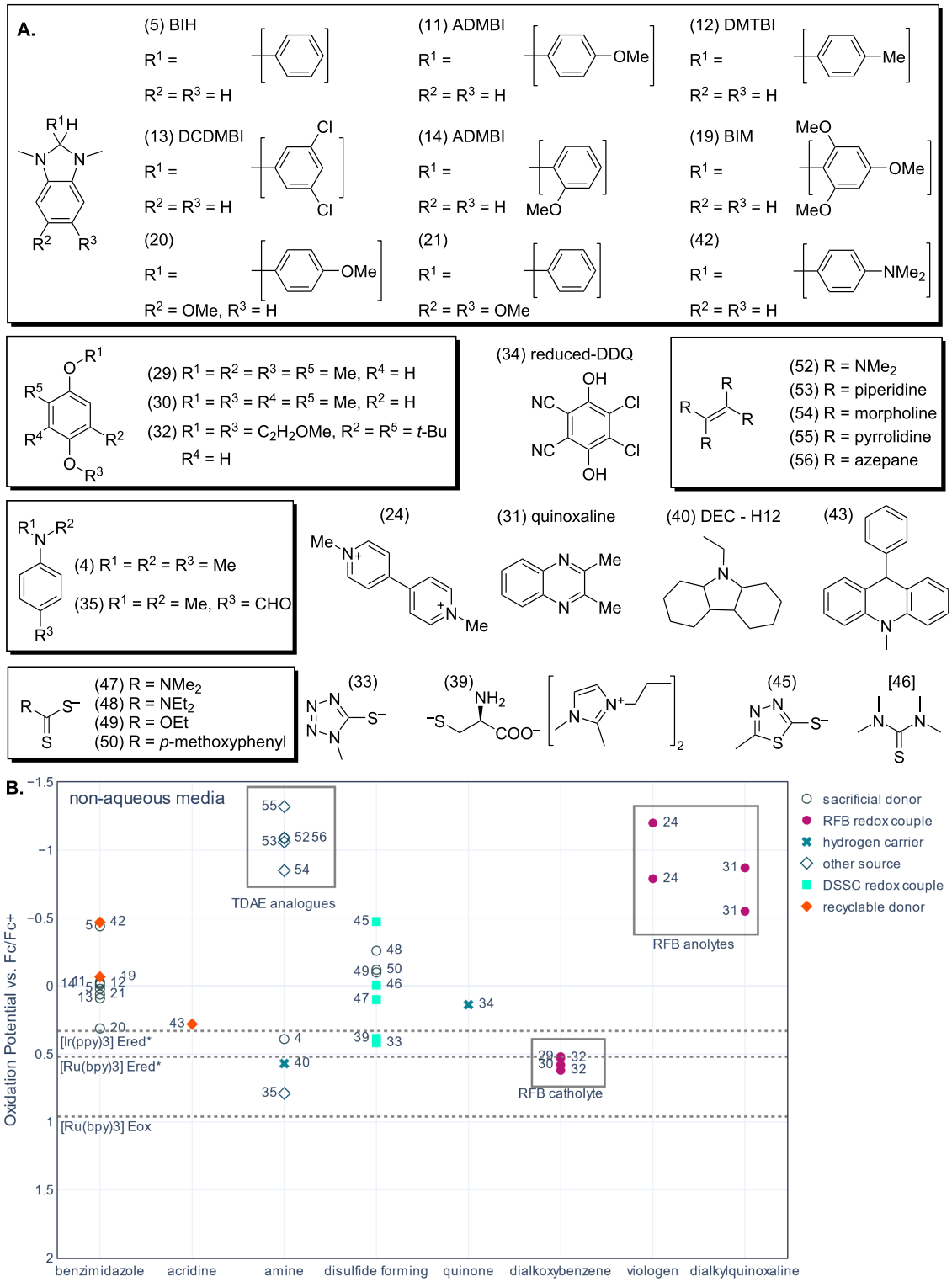

Figure 5: A. Structures of the molecules represented in part B. The numbers in brackets correspond to the compound id in Supporting Information File 1 and the data point labels in part B. B. Plot of oxidation potential vs Fc/Fc^+ in non-aqueous media for compounds sorted by redox-active moiety. Note, that the potentials are shown for the dialkylquinoxaline example are the oxidation of the 1 and 2 electron-reduced species. Dotted lines have been added to indicate the excited-state reduction potential (E_{red}^*) and oxidation potential (E_{ox}) of ruthenium trisbipy in acetonitrile aqueous media, as well as E_{red}^* of $Ir(ppy)_3$ in DMF. The references for the potentials can be found in the text and in Supporting Information File 1, Table S2. The data point labels correspond to the compound id in Supporting Information File 1.

lower than the oxidation potential of Ru(II)(bpy)$_3$, which makes it a candidate for regenerating photooxidized Ru(bpy)$_3$ in acetonitrile (depending on lifetimes etc.). However, the oxidation potential of DEC-H12 is not negative enough to allow reductive quenching. DEC-H12 has been studied in detail as a LOHC, which are small organic molecules that can be catalytically dehydrogenated and rehydrogenated [75]. Many other amines and organic molecules have been investigated as hydrogen carriers [40]. They mostly resemble traditional amine sacrificial electron donors but form more stable carbazole heterocyclic oxidation products [75]. LOHC compounds could potentially provide both protons and electrons for artificial photosynthesis. The thermodynamics of electrochemically hydrogenating several LOHCs using a modified water-splitting device have been investigated [40]. However, other electrochemical hydrogenation methods might be more appropriate [41,42].

There is already work on electrochemical dehydrogenation of LOHCs [76,77]. In one example, DDQ was used to remove hydrogen from secondary amines by oxidizing them, followed by reoxidation of the hydrogenated DDQ at the electrode to establish a redox catalysis cycle [76]. In non-aqueous media DDQ has a low oxidation potential (0.14 V vs Fc/Fc$^+$ in acetonitrile) so that DDQ could potentially reductively quench Ir(ppy)$_3$ and Ru(bpy)$_3$ and regenerate the photooxidized species in acetonitrile [26]. However, in water the oxidation potential of DDQ (1.17 V vs SCE or 0.86 V vs Fc/Fc$^+$) is too positive to thermodynamically allow quenching of Ru(bpy)$_3$ [26]. This change in position and relationship between the various redox potentials is an illustrative example of the dramatic thermodynamic changes possible when moving from a non-aqueous system to an aqueous one. DDQ is also a particularly interesting example because it could potentially be used as an intermediate redox mediator to accumulate protons and electrons, or hydride equivalents from other donors. Similar schemes have been achieved using dithiols. However, the dithiols are usually attached to a photo- or electrocatalyst, and take advantage of potential inversion [78,79]. In the electrocatalytic study of DDQ one of the amines tested was successfully dehydrogenated in the presence of DDQ, yet in the absence of DDQ the amines generally formed polymeric byproducts under the same electrolysis conditions [76].

Another interesting family of amines are the tetraaminoethylene analogues (grey box in Figure 5). Tetra(dimethylamino)ethene (TDAE) is a strong one-electron reductant with a ground-state oxidation potential of −1.09 V vs Fc/Fc$^+$ [80]. There are few organic electron donors with oxidation potentials this negative, except reduced RFB catholytes. However, TDAE has been used as a photocatalyst absorbing at 440 nm for dehalogenation which is within the visible region usually used by photosensitizers. It is also a very toxic, corrosive, and air-sensitive compound [80]. Hence, TDAE is not a good candidate for a recyclable donor. However, Charboneau et al. synthesized and reported a set of more stable analogues for use as reductants in catalysis for synthesis [81]. Tetrakis(*N*-pyrrolidinyl)ethylene (TPyE, −1.32 V vs Fc/Fc$^+$) requires handling in a glovebox. However, 1,1,2,2-tetrapiperidinoethene (TPiE, −1.06 V vs Fc/Fc$^+$) a piperidine analogue, TME (−0.85 V vs Fc/Fc$^+$) a morphine analogue, and 1-[1,2,2-tris(azepan-1-yl)ethenyl]azepane (TAzE, −1.09 V vs Fc/Fc$^+$) an aziridine analogue are all stable enough to handle at the lab bench. The visible absorption properties of these compounds were not reported but the more stable analogues may allow researchers to develop more reducing photosensitizers.

In contrast to aqueous organic RFBs, non-aqueous RFBs use small organic molecules that are highly soluble in non-aqueous media. Similar to their aqueous counterparts, redox mediators for organic RFBs are optimized to form stable charged intermediates by single-electron transfer reactions that can be charged and discharged over many cycles. Non-aqueous catholytes are also optimized to have more positive oxidation potentials and anolytes to have more extreme reduction potentials.

Sanford and co-workers used an innovative evolution strategy to engineer lightweight pyridinium anolytes to replace viologens in non-aqueous RFBs [66]. These species resemble oxidized Hantzsch esters but are stabilized in the *para* position. A similar pruning strategy was adopted by Huang et al. to create dialkoxybenzene anolytes for organic RFBs based on DBBB (2,5-di-*tert*-butyl-1,4-bis(2-methoxyethoxy)benzene) an alkylated quinone structure [82]. Hydroquinones and aqueous RFB anolytes have low enough potentials to be candidates for quenching Ru(bpy)$_3$ in aqueous media. Dialkoxybenzene anolytes were developed from lithium ion battery chemistry and for non-aqueous RFBs as stable one-electron redox couples in lithium carbonate electrolytes [82,83]. The oxidation potentials recorded for a sample of these species range from 0.52 to 0.62 V vs Fc/Fc$^+$. One compound, DBBB, has a 0.09 V shift in the oxidation potential recorded for two different carbonate solvents (0.53 V in EC/EMC and 0.62 V in PEC vs Fc/Fc$^+$). These potentials are close to the excited-state reduction potential measured for Ru(bpy)$_3$ in acetonitrile, however, the solvent dependence of the redox potentials means that it is not clear if the dialkoxybenzenes have enough reducing power for quenching ruthenium photosensitizers.

Dialkylquinoxalines were studied alongside DBBB as an alternative to viologens as doubly reducible anolytes for non-aqueous RFBs [83]. The two redox events shown in Figure 5

are two one-electron reduction potentials for the same dialkylquinoxaline species (−0.87 and −0.55 V vs Fc/Fc^+). This example was the more electrochemically stable example in the study. Singly reduced viologens in water are at least 1.5 V more negative than the excited-state reduction potential of $Ru(bpy)_3$, while in non-aqueous media dialkylquinoxalines appear closer to the excited-state reduction potential of $Ru(bpy)_3$. However, like viologens, they are electron acceptors synthesized in their oxidized form and need to be reduced to be used as electron donors. This makes them excellent candidates for electrochemical or photochemical charging, perhaps even in two-phase systems to couple the charging to water oxidation. However, such species can also be reoxidized in the presence of oxygen which must be considered when designing an in-situ recycling system. For initial photocatalyst screening it is worth noting that reductants such as tetraaminoethene derivates or Hantzsch esters could be used to mimic the redox potentials of anolytes like quinoxalines. However, it would be better to generate the reduced viologens and quinoxalines to use for screening.

Thiolates such as ethylxanthate (−0.1 V vs Fc/Fc^+), 4-methoxyphenylthioate (−0.12 V vs Fc/Fc^+) and diethylthiocarbamic acid (−0.26 V vs Fc/Fc^+) have been used as sacrificial electron donors in artificial photosynthesis and their very low oxidation potentials making them excellent reducing reagents [30]. Related thiazoles have been used in dye-sensitized solar cells as redox mediators because they oxidize to form a disulfide bridge that can be re-reduced [50,84]. These compounds seem like ideal candidates for recyclable electron donors because they exhibit an EC mechanism which results in an electrochemically recyclable dimer [50,51,84,85]. For instance, methylthiocarbamate (0.1 V vs Fc/Fc^+), a redox mediator investigated for dye-sensitized solar cells, is a derivative of the sacrificial donor diethylthiocarbamic acid with only a slightly less driving force for the reductive quenching than the sacrificial donor [86]. Another redox mediator developed for dye-sensitized solar cells, 2-mercapto-5-methyl-1,3,4-thiadiazole has a much lower oxidation potential (−0.48 V vs Fc/Fc^+) [87]. The work for dye-sensitized solar cells is particularly interesting because the thiols were developed as non-visible absorbing redox couples to replace colored I^-/I_3^- redox couple in dye-sensitized solar cell research [84]. They also span a wide potential range and mixing the thiolates to make mixed disulfides alters the oxidation potential of the mixture which offers an interesting optimization opportunity [85]. Cysteine has been used as a sacrificial donor and explored in non-aqueous dye-sensitized solar cells with an imidazolium cation (0.39 V vs Fc/Fc^+) [51]. The resulting compound is similar in structure to an ionic liquid. In contrast, in artificial photosynthesis cysteine is often used in aqueous systems. Aromatic dithiols have been studied for accumulating charge by taking advantage of potential inversion, however, they often consume other thiols or thiolates to accumulate the charge [78,79]. For some of the thiolates herein the oxidation potential is reported rather than the standard potential because the peak-to-peak separation can be very large [85].

Finally, this is not an exhaustive list of candidates for recyclable donors. The field of RFBs, for instance, is constantly expanding the library of small organic redox mediators [88]. However, hopefully this discussion may act as a starting point for those interested in exploring the area.

Conclusion

This review highlighted several species from different research fields with a range of appropriate oxidation potentials that can be recycled, either electrochemically or photochemically. This information will hopefully enable artificial photosynthesis researchers to continue to move away from unrecyclable sacrificial donors when developing their catalytic systems and utilize existing species that can be recycled, such as benzimidazole. However, oxidation potentials are only one property of recyclable electron donors that need to be optimized. More small organic recyclable electron donors need to be designed with economic and sustainable syntheses. They need to be highly soluble and possess modifiable, modular structures that can be used to simply tune the redox potentials, quenching rates, and pK_aH to match different dyes and quenching pathways. Finally, although recyclable donors such as benzimidazoles are being used in developing new carbon dioxide reduction catalysts, more proof-of-concept studies are required to demonstrate combining photocatalysis with sacrificial donor recycling.

Commonly used Abbreviations and Symbols

Table 1: Explanations of abbreviations.

Abbreviation	Explanation
BIM	1,3-dimethyl-2-(2,4,6-trimethoxyphenyl)-2*H*-benzimidazole
DEC-H12	9-ethyldodecahydro-1*H*-carbazole
DcMFc	decamethylferrocene
ITIES	interface between two immiscible electrolyte solutions
LOHC	liquid organic hydrogen carrier
PCET	proton-coupled electron transfer
RFB	redox flow battery
$Ru(bpy)_3$	ruthenium trisbipyridine cation in varying oxidation states

Supporting Information

Link to a github code repository containing redox potential data collected from various references and the code used to create the plots of oxidation potential https://github.com/glowe691/redox_donors_notebooks/tree/submitted_belstein_JOC_for_peer_review .

Supporting Information File 1

A spreadsheet containing the tables with the oxidation potential data for the electron donors and redox active compounds discussed in this review. The table contains DOI numbers for the references where the potentials were reported.
[https://www.beilstein-journals.org/bjoc/content/supplementary/1860-5397-19-88-S1.xlsx]

Acknowledgements

I would like to thank Dieter Sorsche and Graham Newton for their valuable scientific discussion, and the editors of this issue for the opportunity to write this review. I would also like to thank my colleagues past and present for their continued support, encouragement, and inspiration. Finally, this review was greatly improved by two anonymous reviewers. Thank you for your constructive and well-deserved criticism. I learnt a lot from it, and I am deeply grateful for it.

ORCID® iDs

Grace A. Lowe - https://orcid.org/0000-0002-5616-5440

References

1. Takeda, H.; Cometto, C.; Ishitani, O.; Robert, M. *ACS Catal.* **2017,** *7,* 70–88. doi:10.1021/acscatal.6b02181
2. Wang, Y.; Suzuki, H.; Xie, J.; Tomita, O.; Martin, D. J.; Higashi, M.; Kong, D.; Abe, R.; Tang, J. *Chem. Rev.* **2018,** *118,* 5201–5241. doi:10.1021/acs.chemrev.7b00286
3. Pellegrin, Y.; Odobel, F. *C. R. Chim.* **2017,** *20,* 283–295. doi:10.1016/j.crci.2015.11.026
4. Yoshino, S.; Takayama, T.; Yamaguchi, Y.; Iwase, A.; Kudo, A. *Acc. Chem. Res.* **2022,** *55,* 966–977. doi:10.1021/acs.accounts.1c00676
5. Schneider, J.; Bahnemann, D. W. *J. Phys. Chem. Lett.* **2013,** *4,* 3479–3483. doi:10.1021/jz4018199
6. Sampaio, R. N.; Grills, D. C.; Polyansky, D. E.; Szalda, D. J.; Fujita, E. *J. Am. Chem. Soc.* **2020,** *142,* 2413–2428. doi:10.1021/jacs.9b11897
7. Balzani, V.; Ceroni, P.; Juris, A. Natural and Artificial Photosynthesis. *Photochemistry and Photophysics Concepts, Research, Applications;* Wiley-VCH Verlag GmbH & Co: Germany, 2014; pp 281–304.
8. Zhang, L.; Wang, Y. *Angew. Chem., Int. Ed.* **2023,** *62,* e202219076. doi:10.1002/anie.202219076
9. Weliwatte, N. S.; Grattieri, M.; Minteer, S. D. *Photochem. Photobiol. Sci.* **2021,** *20,* 1333–1356. doi:10.1007/s43630-021-00099-7
10. Lyngaas, C. Alaska Airlines, Microsoft and Twelve partner to advance new form of sustainable aviation fuel; In *Alaska Airlines News & Stories;* Alaska Airlines, Ink.: USA, 2022.
11. McGlone, C. How Grid Connection Delays Are Threatening Net-Zero Goals. *E&T Engineering & Technology*, **2023,** *18*(2).
12. The Department for Business, Energy & Industrial Strategy. *Facilitating the Deployment of Large-Scale and Long-Duration Electricity Strorage: Government Response*; HM Government: London, 2022.
13. Bhattacharjee, S.; Rahaman, M.; Andrei, V.; Miller, M.; Rodríguez-Jiménez, S.; Lam, E.; Pornrungroj, C.; Reisner, E. *Nat. Synth.* **2023,** *2,* 182–192. doi:10.1038/s44160-022-00196-0
14. Costentin, C.; Robert, M.; Savéant, J.-M.; Tard, C. *Acc. Chem. Res.* **2014,** *47,* 271–280. doi:10.1021/ar4001444
15. McCarthy, B. D.; Dempsey, J. L. *Inorg. Chem.* **2017,** *56,* 1225–1231. doi:10.1021/acs.inorgchem.6b02325
16. Pannwitz, A.; Wenger, O. S. *Dalton Trans.* **2019,** *48,* 5861–5868. doi:10.1039/c8dt04373f
17. Lennox, J. C.; Kurtz, D. A.; Huang, T.; Dempsey, J. L. *ACS Energy Lett.* **2017,** *2,* 1246–1256. doi:10.1021/acsenergylett.7b00063
18. Arias-Rotondo, D. M.; McCusker, J. K. *Chem. Soc. Rev.* **2016,** *45,* 5803–5820. doi:10.1039/c6cs00526h
19. Elgrishi, N.; Rountree, K. J.; McCarthy, B. D.; Rountree, E. S.; Eisenhart, T. T.; Dempsey, J. L. *J. Chem. Educ.* **2018,** *95,* 197–206. doi:10.1021/acs.jchemed.7b00361
20. Jones, W. E., Jr.; Fox, M. A. *J. Phys. Chem.* **1994,** *98,* 5095–5099. doi:10.1021/j100070a025
21. Müller, C.; Schwab, A.; Randell, N. M.; Kupfer, S.; Dietzek-Ivanšić, B.; Chavarot-Kerlidou, M. *Chem. – Eur. J.* **2022,** *28,* e202103882. doi:10.1002/chem.202103882
22. Hua, S.-A.; Cattaneo, M.; Oelschlegel, M.; Heindl, M.; Schmid, L.; Dechert, S.; Wenger, O. S.; Siewert, I.; González, L.; Meyer, F. *Inorg. Chem.* **2020,** *59,* 4972–4984. doi:10.1021/acs.inorgchem.0c00220
23. Fukatsu, A.; Kondo, M.; Masaoka, S. *Coord. Chem. Rev.* **2018,** *374,* 416–429. doi:10.1016/j.ccr.2018.06.016
24. Svith, H.; Jensen, H.; Almstedt, J.; Andersson, P.; Lundbäck, T.; Daasbjerg, K.; Jonsson, M. *J. Phys. Chem. A* **2004,** *108,* 4805–4811. doi:10.1021/jp031268q
25. Bond, A. M.; McLennan, E. A.; Stojanovic, R. S.; Thomas, F. G. *Anal. Chem. (Washington, DC, U. S.)* **1987,** *59,* 2853–2860. doi:10.1021/ac00151a007
26. Huynh, M. T.; Anson, C. W.; Cavell, A. C.; Stahl, S. S.; Hammes-Schiffer, S. *J. Am. Chem. Soc.* **2016,** *138,* 15903–15910. doi:10.1021/jacs.6b05797
27. Schulz, M.; Hagmeyer, N.; Wehmeyer, F.; Lowe, G.; Rosenkranz, M.; Seidler, B.; Popov, A.; Streb, C.; Vos, J. G.; Dietzek, B. *J. Am. Chem. Soc.* **2020,** *142,* 15722–15728. doi:10.1021/jacs.0c03779
28. Kientz, M.; Lowe, G.; McCarthy, B. G.; Miyake, G. M.; Bonin, J.; Robert, M. *ChemPhotoChem* **2022,** *6,* e202200009. doi:10.1002/cptc.202200009
29. Gimeno, L.; Queffelec, C.; Blart, E.; Pellegrin, Y. *ACS Omega* **2022,** *7,* 13112–13119. doi:10.1021/acsomega.2c00531
30. Gimeno, L.; Queffélec, C.; Mall Haidaraly, K.; Blart, E.; Pellegrin, Y. *Catal. Sci. Technol.* **2021,** *11,* 6041–6047. doi:10.1039/d1cy01209f
31. Cunningham, K. L.; McMillin, D. R. *Inorg. Chem.* **1998,** *37,* 4114–4119. doi:10.1021/ic980213d
32. Richardson, R. D.; Holland, E. J.; Carpenter, B. K. *Nat. Chem.* **2011,** *3,* 301–303. doi:10.1038/nchem.1000

33. Rivier, L.; Peljo, P.; Vannay, L. A. C.; Gschwend, G. C.; Méndez, M. A.; Corminboeuf, C.; Scanlon, M. D.; Girault, H. H. *Angew. Chem., Int. Ed.* **2017,** *56,* 2324–2327. doi:10.1002/anie.201610240
34. Rivier, L.; Peljo, P.; Maye, S.; Méndez, M. A.; Vrubel, H.; Vannay, L. A. C.; Corminboeuf, C.; Scanlon, M. D.; Girault, H. H. *Chem. – Eur. J.* **2019,** *25,* 12769–12779. doi:10.1002/chem.201902353
35. Ge, P.; Hojeij, M.; Scanlon, M. D.; Girault, H. H. *ChemPhysChem* **2020,** *21,* 2630–2633. doi:10.1002/cphc.202000844
36. Rastgar, S.; Wittstock, G. *J. Phys. Chem. C* **2017,** *121,* 25941–25948. doi:10.1021/acs.jpcc.7b09550
37. Rastgar, S.; Teixeira Santos, K.; Angelucci, C. A.; Wittstock, G. *Chem. – Eur. J.* **2020,** *26,* 10882–10890. doi:10.1002/chem.202001967
38. Pannwitz, A.; Klein, D. M.; Rodríguez-Jiménez, S.; Casadevall, C.; Song, H.; Reisner, E.; Hammarström, L.; Bonnet, S. *Chem. Soc. Rev.* **2021,** *50,* 4833–4855. doi:10.1039/d0cs00737d
39. Itoh, N.; Xu, W. C.; Hara, S.; Sakaki, K. *Catal. Today* **2000,** *56,* 307–314. doi:10.1016/s0920-5861(99)00288-6
40. Araujo, C. M.; Simone, D. L.; Konezny, S. J.; Shim, A.; Crabtree, R. H.; Soloveichik, G. L.; Batista, V. S. *Energy Environ. Sci.* **2012,** *5,* 9534. doi:10.1039/c2ee22749e
41. Fokin, I.; Siewert, I. *Chem. – Eur. J.* **2020,** *26,* 14137–14143. doi:10.1002/chem.202002075
42. Behrouzi, L.; Zand, Z.; Fotuhi, M.; Kaboudin, B.; Najafpour, M. M. *Sci. Rep.* **2022,** *12,* 19968. doi:10.1038/s41598-022-23777-7
43. Wolff, N.; Rivada-Wheelaghan, O.; Tocqueville, D. *ChemElectroChem* **2021,** *8,* 4019–4027. doi:10.1002/celc.202100617
44. Aamer, E.; Thöming, J.; Baune, M.; Reimer, N.; Dringen, R.; Romero, M.; Bösing, I. *Sci. Rep.* **2022,** *12,* 16380. doi:10.1038/s41598-022-20508-w
45. Ilic, S.; Alherz, A.; Musgrave, C. B.; Glusac, K. D. *Chem. Commun.* **2019,** *55,* 5583–5586. doi:10.1039/c9cc00928k
46. Kwok, C.-L.; Cheng, S.-C.; Ho, P.-Y.; Yiu, S.-M.; Man, W.-L.; Au, V. K.-M.; Tsang, P.-K.; Leung, C.-F.; Ko, C.-C.; Robert, M. *Chem. Commun.* **2020,** *56,* 7491–7494. doi:10.1039/d0cc02604b
47. Kuk, S. K.; Singh, R. K.; Nam, D. H.; Singh, R.; Lee, J.-K.; Park, C. B. *Angew. Chem., Int. Ed.* **2017,** *56,* 3827–3832. doi:10.1002/anie.201611379
48. Tamaki, Y.; Koike, K.; Morimoto, T.; Ishitani, O. *J. Catal.* **2013,** *304,* 22–28. doi:10.1016/j.jcat.2013.04.002
49. Weerasooriya, R. B.; Drummer, M. C.; Phelan, B. T.; Gesiorski, J. L.; Sprague-Klein, E. A.; Chen, L. X.; Glusac, K. D. *J. Phys. Chem. C* **2022,** *126,* 17816–17825. doi:10.1021/acs.jpcc.2c03541
50. Wang, M.; Chamberland, N.; Breau, L.; Moser, J.-E.; Humphry-Baker, R.; Marsan, B.; Zakeeruddin, S. M.; Grätzel, M. *Nat. Chem.* **2010,** *2,* 385–389. doi:10.1038/nchem.610
51. Cheng, M.; Yang, X.; Li, S.; Wang, X.; Sun, L. *Energy Environ. Sci.* **2012,** *5,* 6290–6293. doi:10.1039/c1ee02540f
52. Wang, Q.; Warnan, J.; Rodríguez-Jiménez, S.; Leung, J. J.; Kalathil, S.; Andrei, V.; Domen, K.; Reisner, E. *Nat. Energy* **2020,** *5,* 703–710. doi:10.1038/s41560-020-0678-6
53. Wang, S.; Teramura, K.; Hisatomi, T.; Domen, K.; Asakura, H.; Hosokawa, S.; Tanaka, T. *ACS Sustainable Chem. Eng.* **2021,** *9,* 9327–9335. doi:10.1021/acssuschemeng.1c02126
54. Song, Z.; Hisatomi, T.; Chen, S.; Wang, Q.; Ma, G.; Li, S.; Zhu, X.; Sun, S.; Domen, K. *ChemSusChem* **2019,** *12,* 1906–1910. doi:10.1002/cssc.201802306
55. Ma, B.; Chen, G.; Fave, C.; Chen, L.; Kuriki, R.; Maeda, K.; Ishitani, O.; Lau, T.-C.; Bonin, J.; Robert, M. *J. Am. Chem. Soc.* **2020,** *142,* 6188–6195. doi:10.1021/jacs.9b13930
56. Sekizawa, K.; Maeda, K.; Domen, K.; Koike, K.; Ishitani, O. *J. Am. Chem. Soc.* **2013,** *135,* 4596–4599. doi:10.1021/ja311541a
57. McHugh, P. J.; Stergiou, A. D.; Symes, M. D. *Adv. Energy Mater.* **2020,** *10,* 2002453. doi:10.1002/aenm.202002453
58. Paul, A.; Symes, M. D. *Curr. Opin. Green Sustainable Chem.* **2021,** *29,* 100453. doi:10.1016/j.cogsc.2021.100453
59. Janoschka, T.; Martin, N.; Hager, M. D.; Schubert, U. S. *Angew. Chem., Int. Ed.* **2016,** *55,* 14427–14430. doi:10.1002/anie.201606472
60. Hendriks, K. H.; Robinson, S. G.; Braten, M. N.; Sevov, C. S.; Helms, B. A.; Sigman, M. S.; Minteer, S. D.; Sanford, M. S. *ACS Cent. Sci.* **2018,** *4,* 189–196. doi:10.1021/acscentsci.7b00544
61. Costabel, D.; Nabiyan, A.; Chettri, A.; Jacobi, F.; Heiland, M.; Guthmuller, J.; Kupfer, S.; Wächtler, M.; Dietzek-Ivanšić, B.; Streb, C.; Schacher, F. H.; Peneva, K. *ACS Appl. Mater. Interfaces* **2023,** *15,* 20833–20842. doi:10.1021/acsami.2c18529
62. Wahyuono, R. A.; Seidler, B.; Bold, S.; Dellith, A.; Dellith, J.; Ahner, J.; Wintergerst, P.; Lowe, G.; Hager, M. D.; Wächtler, M.; Streb, C.; Schubert, U. S.; Rau, S.; Dietzek, B. *Sci. Rep.* **2021,** *11,* 2787. doi:10.1038/s41598-021-82395-x
63. Hu, B.; DeBruler, C.; Rhodes, Z.; Liu, T. L. *J. Am. Chem. Soc.* **2017,** *139,* 1207–1214. doi:10.1021/jacs.6b10984
64. Dempsey, J. L. *Science* **2019,** *364,* 436–437. doi:10.1126/science.aaw9900
65. Sevov, C. S.; Hendriks, K. H.; Sanford, M. S. *J. Phys. Chem. C* **2017,** *121,* 24376–24380. doi:10.1021/acs.jpcc.7b06247
66. Sevov, C. S.; Brooner, R. E. M.; Chénard, E.; Assary, R. S.; Moore, J. S.; Rodríguez-López, J.; Sanford, M. S. *J. Am. Chem. Soc.* **2015,** *137,* 14465–14472. doi:10.1021/jacs.5b09572
67. Molina-Osorio, A. F.; Gamero-Quijano, A.; Peljo, P.; Scanlon, M. D. *Curr. Opin. Electrochem.* **2020,** *21,* 100–108. doi:10.1016/j.coelec.2020.01.013
68. Navalpotro, P.; Palma, J.; Anderson, M.; Marcilla, R. *Angew. Chem., Int. Ed.* **2017,** *56,* 12460–12465. doi:10.1002/anie.201704318
69. Leduc, P.; Thévenot, D. *Bioelectrochem. Bioenerg.* **1974,** *1,* 96–107. doi:10.1016/0302-4598(74)85011-7
70. Chen, L.; Doeven, E. H.; Wilson, D. J. D.; Kerr, E.; Hayne, D. J.; Hogan, C. F.; Yang, W.; Pham, T. T.; Francis, P. S. *ChemElectroChem* **2017,** *4,* 1797–1808. doi:10.1002/celc.201700222
71. Rao, H.; Schmidt, L. C.; Bonin, J.; Robert, M. *Nature* **2017,** *548,* 74–77. doi:10.1038/nature23016
72. Tamaki, Y.; Koike, K.; Ishitani, O. *Chem. Sci.* **2015,** *6,* 7213–7221. doi:10.1039/c5sc02018b
73. Melicharek, M.; Nelson, R. F. *J. Electroanal. Chem. Interfacial Electrochem.* **1970,** *26,* 201–209. doi:10.1016/s0022-0728(70)80304-7
74. Buttler, F. Electrochemical Hydrogen Storage in Organic Molecules. Ph.D. Thesis, Universität Duisburg-Essen, Germany, 2017.
75. Crabtree, R. H. *ACS Sustainable Chem. Eng.* **2017,** *5,* 4491–4498. doi:10.1021/acssuschemeng.7b00983
76. Luca, O. R.; Wang, T.; Konezny, S. J.; Batista, V. S.; Crabtree, R. H. *New J. Chem.* **2011,** *35,* 998. doi:10.1039/c0nj01011a
77. Shiraz, H. G.; Vagin, M.; Ruoko, T.-P.; Gueskine, V.; Karoń, K.; Łapkowski, M.; Abrahamsson, T.; Ederth, T.; Berggren, M.; Crispin, X. *J. Energy Chem.* **2022,** *73,* 292–300. doi:10.1016/j.jechem.2022.06.015
78. Hua, S.-A.; Paul, L. A.; Oelschlegel, M.; Dechert, S.; Meyer, F.; Siewert, I. *J. Am. Chem. Soc.* **2021,** *143,* 6238–6247. doi:10.1021/jacs.1c01763

79. Nomrowski, J.; Wenger, O. S. *J. Am. Chem. Soc.* **2018,** *140,* 5343–5346. doi:10.1021/jacs.8b02443
80. Glaser, F.; Larsen, C. B.; Kerzig, C.; Wenger, O. S. *Photochem. Photobiol. Sci.* **2020,** *19,* 1035–1041. doi:10.1039/d0pp00127a
81. Charboneau, D. J.; Huang, H.; Barth, E. L.; Germe, C. C.; Hazari, N.; Mercado, B. Q.; Uehling, M. R.; Zultanski, S. L. *J. Am. Chem. Soc.* **2021,** *143,* 21024–21036. doi:10.1021/jacs.1c10932
82. Huang, J.; Pan, B.; Duan, W.; Wei, X.; Assary, R. S.; Su, L.; Brushett, F. R.; Cheng, L.; Liao, C.; Ferrandon, M. S.; Wang, W.; Zhang, Z.; Burrell, A. K.; Curtiss, L. A.; Shkrob, I. A.; Moore, J. S.; Zhang, L. *Sci. Rep.* **2016,** *6,* 32102. doi:10.1038/srep32102
83. Brushett, F. R.; Vaughey, J. T.; Jansen, A. N. *Adv. Energy Mater.* **2012,** *2,* 1390–1396. doi:10.1002/aenm.201200322
84. Burschka, J.; Brault, V.; Ahmad, S.; Breau, L.; Nazeeruddin, M. K.; Marsan, B.; Zakeeruddin, S. M.; Grätzel, M. *Energy Environ. Sci.* **2012,** *5,* 6089. doi:10.1039/c2ee03005e
85. Cho, W.; Song, D.; Lee, Y.-G.; Chae, H.; Kim, Y. R.; Pyun, Y. B.; Nagarajan, S.; Sudhagar, P.; Kang, Y. S. *J. Mater. Chem. A* **2013,** *1,* 233–236. doi:10.1039/c2ta00719c
86. Li, D.; Li, H.; Luo, Y.; Li, K.; Meng, Q.; Armand, M.; Chen, L. *Adv. Funct. Mater.* **2010,** *20,* 3358–3365. doi:10.1002/adfm.201000150
87. Tian, H.; Jiang, X.; Yu, Z.; Kloo, L.; Hagfeldt, A.; Sun, L. *Angew. Chem., Int. Ed.* **2010,** *49,* 7328–7331. doi:10.1002/anie.201003740
88. Armstrong, C. G.; Toghill, K. E. *Electrochem. Commun.* **2018,** *91,* 19–24. doi:10.1016/j.elecom.2018.04.017

License and Terms

BEILSTEIN JOURNAL OF ORGANIC CHEMISTRY

Selectivity control towards CO versus H_2 for photo-driven CO_2 reduction with a novel Co(II) catalyst

Lisa-Lou Gracia[1], Philip Henkel[1], Olaf Fuhr[2,3] and Claudia Bizzarri[*1]

Full Research Paper

Open Access

Address:
[1]Institute of Organic Chemistry (IOC), Karlsruhe Institute of Technology (KIT), Kaiserstrasse 12, 76131 Karlsruhe, Germany, [2]Institute of Nanotechnology (INT), Karlsruhe Institute of Technology (KIT), Kaiserstrasse 12, 76131 Karlsruhe, Germany and [3]Karlsruhe Nano Micro Facility (KNMFi), Karlsruhe Institute of Technology (KIT), Kaiserstrasse 12, 76131 Karlsruhe, Germany

Email:
Claudia Bizzarri[*] - bizzarri@kit.edu

* Corresponding author

Keywords:
carbon monoxide selectivity; cobalt(II) complex; copper(I) complex; earth-abundant; hexafluoropropanol; photocatalytic CO_2 reduction

Beilstein J. Org. Chem. **2023,** *19,* 1766–1775.
https://doi.org/10.3762/bjoc.19.129

Received: 17 August 2023
Accepted: 09 November 2023
Published: 17 November 2023

This article is part of the thematic issue "Artificial photosynthesis".

Guest Editor: A. Pannwitz

Abstract

Developing efficient catalysts for reducing carbon dioxide, a highly stable combustion waste product, is a relevant task to lower the atmospheric concentration of this greenhouse gas by upcycling. Selectivity towards CO_2-reduction products is highly desirable, although it can be challenging to achieve since the metal-hydrides formation is sometimes favored and leads to H_2 evolution. In this work, we designed a cobalt-based catalyst, and we present herein its physicochemical properties. Moreover, we tailored a fully earth-abundant photocatalytic system to achieve specifically CO_2 reduction, optimizing efficiency and selectivity. By changing the conditions, we enhanced the turnover number (TON) of CO production from only 0.5 to more than 60 and the selectivity from 6% to 97% after four hours of irradiation at 420 nm. Further efficiency enhancement was achieved by adding 1,1,1,3,3,3-hexafluoropropan-2-ol, producing CO with a TON up to 230, although at the expense of selectivity (54%).

Introduction

Solar energy conversion into chemical energy addresses the issues of energy shortage with the exploitation of renewable sources [1]. Photoinduced CO_2 reduction is included in the vast research field of artificial photosynthesis. Taking Nature as a model, the absorption of photons can drive electron-transfer processes, leading to the production of highly energetic molecules. By aiming at the conversion of CO_2, a greenhouse gas implicated in climate change, the closure of the carbon cycle can be achieved [2]. For this purpose, three main components are needed: a photosensitizer (PS), which acts like a light-antennae harvesting system in natural photosynthesis, a catalyst (Cat.), reacting directly with CO_2 after being reduced, and a sacrificial electron donor (SeD). When the involved (photo)catalysts are homogeneous transition-metal-based com-

plexes, the outcomes are generally two-electron reduction products, such as carbon monoxide (CO), formic acid (HCO_2H), or formate (HCO_2^-). To mitigate the strong energetic requirements of the reaction shown in Equation 1, the reduction of CO_2 occurs in the presence of protons, so that the energy barriers of the reactions shown in Equation 2 and Equation 3 are lowered.

$$CO_2 + 2e^- \longrightarrow CO_2^{-\bullet} \quad E = -1.9\ V \quad (1)$$

$$CO_2 + 2H^+ + 2e^- \longrightarrow CO + H_2O \quad E = -0.53\ V \quad (2)$$

$$CO_2 + 2H^+ + 2e^- \longrightarrow HCO_2H \quad E = -0.61\ V \quad (3)$$

$$2H^+ + 2e^- \longrightarrow H_2 \quad E = -0.42\ V \quad (4)$$

In fact, the formation of the radical anion $CO_2^{-\bullet}$ takes place at −1.9 V versus normal hydrogen electrode (NHE), while the proton-assisted reductions of CO_2 to CO and formic acid happen at −0.53 V and −0.61 V (versus NHE), respectively [3]. However, the molecular hydrogen evolution might compete, as it occurs at a more favorable reduction potential, lowering the selectivity of the catalytic system. While the addition of a proton source is beneficial to lower the overpotential, a metal-hydride (M–H) intermediate could be favored concerning the formation of the CO_2 adduct with the reduced metal center. Thus, besides the development of novel efficient catalysts, different strategies have been pursued to switch the catalyst selectivity towards carbon products [4,5]. Generally, scientists can interplay by developing the major components of a photocatalytic system for CO_2 reduction, such as the photosensitizer (PS), the catalyst, and the sacrificial electron donor (SeD). Nevertheless, the solvent and eventual additives play an important role too [6], as they can influence the (photo)redox properties of the major components, fostering or dropping the efficiency. Thus, a rational design of novel molecular catalysts should consider an additional development of the whole system [7]. Moreover, it would be beneficial for future applications, if major efforts are focused on earth-abundant materials [8-11]. Among the most employed earth-abundant metal-based PS, Cu(I) complexes have the first place, not only in artificial photosynthesis, but also in a large variety of photo(redox)catalyses [12-17]. On the other hand, several complexes based on 3d transition metals, like manganese [18], iron [19-21], cobalt [22,23], and nickel [24,25], have been designed as CO_2 reduction catalysts. This (supra)molecular approach is appealing for gaining a structure–property understanding with the goal of tunable and efficient activity.

Among the 3d transition metals, cobalt is relatively abundant (26.6 ppm) in the Earth crust [26]. Although it should not be considered a cost-effective option at present, as several social and environmental concerns are associated with its extraction, the high stability of the Co(II) ion and the versatility of the ligands used for coordination offer some advantages for tailoring new catalysts to specific reactions and optimize selectivity [22,27]. Cobalt catalysts successfully employed in CO_2 reduction are mainly based on macrocyclic ligands, such as tetraazacyclodecene and its derivatives [3,28,29], porphyrins [30-34], or phthalocyanines [35]. The use of bimetallic complexes has resulted in a favorable mechanism, increasing yields tremendously [36-38].

Targeting efficient completely earth-abundant metal-based systems, we have designed a novel Co(II) catalyst for the reduction of CO_2 (complex **1** in Figure 1). The design aimed at a stable complex obtainable via a straightforward synthesis, with improved solubility, concerning our previous Co(II) complexes [21]. Thus, the new Co(II) complex bears two 1-benzyl-4-(quinolin-2-yl)-1*H*-1,2,3-triazole (BzQuTr) units, that were obtained through a copper-catalyzed alkyne–azide cycloaddition (CuAAC) [39,40], and two thiocyanate ligands. As observed for other cobalt complexes [21], the photoinduced CO_2 reduction gave preferentially molecular hydrogen, when performed in acetonitrile. Moreover, we targeted a photocatalytic system that is fully earth-abundant. For this reason, we selected the known complex [Cu(dmp)DPEPhos](BF_4), well-investigated and used

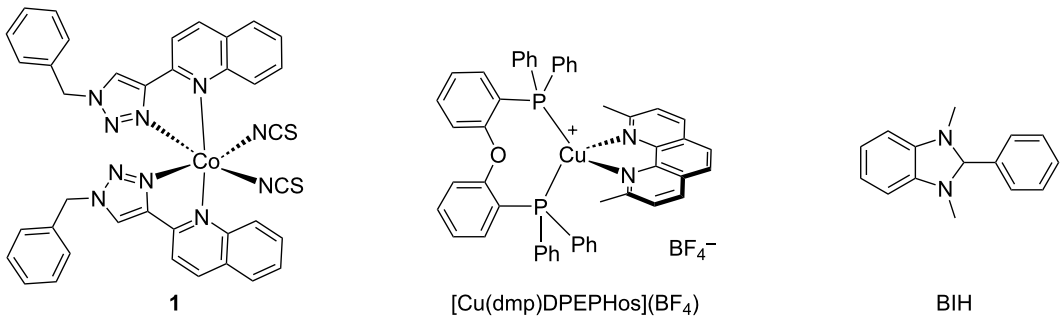

Figure 1: Chemical structures of the molecular components used in this work: Co(II) complex **1** as the novel catalyst, the heteroleptic Cu(I) complex as photosensitizer, and the benzimidazolidine derivative BIH as the sacrificial electron donor.

in several photocatalytic reactions [20,21,41], acting as a cost-effective benchmark photosensitizer. Herein, we present a study for the selectivity control of the novel Co(II) catalyst **1**, aiming at maximizing the catalytic efficiency, and maintaining high selectivity for carbon products.

Results and Discussion

Synthesis and characterization of the new Co(II)-based catalyst

The novel cobalt(II) complex **1** was synthesized in dry methanol (MeOH) by mixing in a 2:1 ratio, the chelating diimine ligand, 1-benzyl-4-(quinolin-2-yl)-1*H*-1,2,3-triazole (BzQuTr) [42] and the cobalt precursor $Co(NCS)_2(py)_4$ [43], where py is pyridine. The reaction was performed under an argon atmosphere at room temperature. The resulting complex **1** was obtained after evaporation of the solvent, as a lilac precipitate in good yield (60%). The structure was investigated by high-resolution mass spectrometry (ESI), where it was shown the fragment corresponding to complex **1** that lost one isothiocyanate, $[M - NCS]^+$, as the primary signal. Elemental analysis matched the calculated values, incorporating an additional MeOH molecule. Recrystallization was afforded by re-dissolving the powder in acetonitrile and layering on top of diethyl ether (Et_2O). Slow diffusion of the antisolvent Et_2O allowed the growth of magenta-colored crystals. Interestingly, two different sets of data could be solved, which is an indication that compound **1** has two polymorphs, **1a** and **1b** (Figure 2). Efforts to selectively achieve one polymorph, through differentiated crystallization processes, were unsuccessful. When analyzing the molecular structure in both crystals, the cobalt core is hexacoordinated, as expected. The two isothiocyanate ions are oriented *cis* to each other and *trans* to the coordinating nitrogen of the 1,2,3-triazole units. The nitrogen atoms of the two quinoline moieties are therefore *trans* to each other. This conformation might be induced by the cobalt precursor $Co(NCS)_2(py)_4$, which has already the NCS monodentate ligands *cis* to each other, as it was not the case for other $Co(NCS)_2(NN)$ complexes, where NN is a chelating diimine compound such as pyridyl-tetrazole [44], or a pyridine-oxazole [45]. The bond lengths are very similar when comparing the polymorphs **1a** and **1b**. Nevertheless, the bond angles vary significantly (see Table S2 in Supporting Information File 1). Polymorph **1a** crystallizes with two molecules of acetonitrile in a triclinic system, while **1b** contains one CH_3CN molecule and has an orthorhombic crystal system. The lattice packing of the two polymorphs with solvent molecules is shown in Supporting Information File 1 (Figures S1 and S2). We were not able to detect, if the two polymorphs show different catalytic activity, as in the following investigations the amorphic powder was used.

Spectroscopic and electrochemical characterization

The Co(II) complex **1** was characterized by UV–vis absorption spectroscopy in *N,N*-dimethylacetamide (DMA), as it was the chosen solvent for photocatalysis. The absorption profile evokes the structured band of the free ligand BzQuTr [42], with two intense π–π* ligand-centered transitions at circa 319 nm and 330 nm (Figure 3). The pink solid dissolves as an intense blue DMA solution. Nevertheless, the d–d transitions associated with

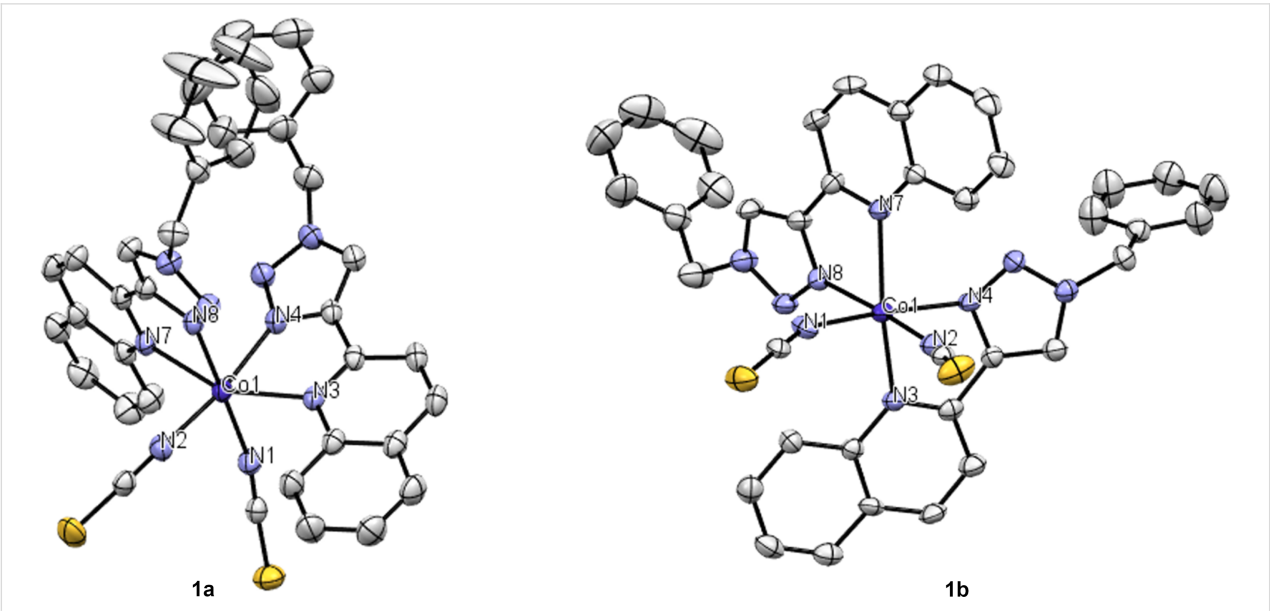

Figure 2: ORTEP drawing of crystal polymorph **1a** (left) and **1b** (right), shown at the 50% probability level. Hydrogen atoms and co-crystallized solvent molecules are omitted for clarity.

this absorption centered at 615 nm possess a low molar extinction coefficient (ε ≈ 220 cm^{-1} M^{-1}, inset in Figure 3). Infrared (IR) spectroscopy was performed via attenuated total reflectance (ATR) and showed the characteristic stretching vibration of the NCS groups at 2069 cm^{-1} (Figure S3 in Supporting Information File 1).

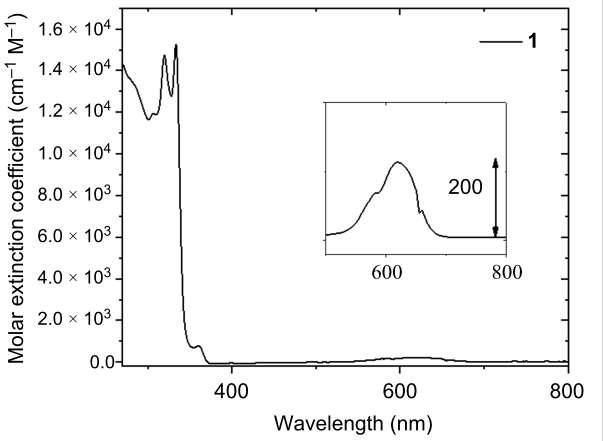

Figure 3: UV–vis absorbance of complex **1** in DMA. Inset: zoom-in of the 500–800 nm range to visualize the low-intensity bands associated with metal-centered d–d transitions.

The redox properties of **1** were investigated using cyclic voltammetry in a DMA solution with 0.1 M tetrabutylammonium hexafluorophosphate ($TBAPF_6$) as the supporting electrolyte (Table 1). The concentration of the analyte was 5 mM. Only the cathodic scan resulted in a rich profile of redox processes (Figure 4a, black lines). In particular, two irreversible reductions occur at the cathodic potentials −1.53 V and −1.9 V versus ferrocene. These electrochemical processes may correspond to the first and second reduction of the metal core Co(II)/Co(I) and Co(I)/Co(0), respectively. A more intense current arises with the third redox process occurring at −2.52 V, which could be assigned to the reduction localized on the ligand (compare with the cyclic voltammogram in Supporting Information File 1, Figure S8).

Table 1: Optical and electrochemical properties of complex **1** in DMA.

λ_{abs}, nm	ε, M^{-1} cm^{-1}	E_{red},[a] V	E_{red},[b] V
319	14720	−1.53	−1.56
333	15257	−1.90	−2.02
615	220	−2.52	

[a]In 0.1 M $TBAPF_6$ solution of DMA, versus Fc/Fc^+ potential; [b]in DMA/TEA 7:1, 0.1 M $TBAPF_6$ versus $Me_{10}Fc/Me_{10}Fc^+$.

We investigated the electrochemical properties also under a CO_2 atmosphere (Figure 4, red curves). In DMA, the electrochemical behavior changed only moderately, suggesting that the reduced complex **1** does not react promptly with carbon dioxide under these conditions. On the other hand, when a 5:1 mixture of DMA/triethanolamine (TEOA) was used as the solvent, a significant catalytic current was observed at the onset potential of −1.4 V. Although a direct comparison between Co(II) and Fe(II) ions cannot be made, it is reasonable to suggest that after the first reduction a ^-NCS ligand detaches and an adduct with CO_2 is formed, as it was calculated for a similar thiocyanate-

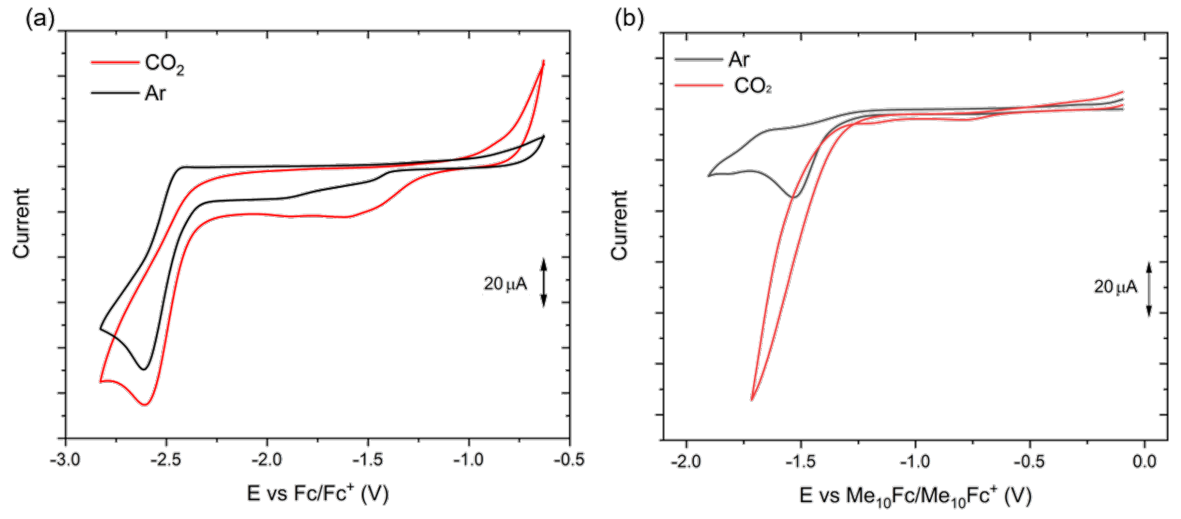

Figure 4: Cyclic voltammetry of complex **1** in 0.1 M $TBAPF_6$ solution of (a) DMA and (b) DMA/TEOA 5:1 (v/v). Black curves are registered under Ar and red curves are recorded under CO_2 atmosphere. A glassy-carbon disk was used as the working electrode and the internal references used are (a) ferrocene and (b) decamethylferrocene. Scan rate was 100 mV s^{-1}.

based Fe(II) complex [46]. These results suggested that cobalt complex **1** can be used in CO_2 reduction reactions (CO_2RR).

Photo-driven CO_2 reduction

Next, we explored catalyst **1** in the CO_2 reduction via photoirradiation. A well-known Cu(I) complex was selected as a photosensitizer since we were interested in the development of earth-abundant systems. In particular, we chose the heteroleptic complex [Cu(dmp)DPEPhos](BF_4), where dmp is 2,9-dimethyl-1,10-phenanthroline and DPEPhos is bis[(2-diphenylphosphino)phenyl] ether, which had been already successfully employed in other artificial photosynthesis [20,21,41]. In addition, the benzimidazolidine derivative, BIH (1,3-dimethyl-2-phenylbenzo[*d*]imidazolidine) (shown in Figure 1) suited well as a sacrificial electron donor, because of its high reducing power [47]. The photocatalytic experiments were performed under 420 nm light irradiation unless otherwise specified. Gaseous products were determined by a gas chromatograph equipped with two barrier discharge ionization detectors (GC–BID). Typically, the concentrations used for the first screening were: 1 mM for PS, 0.1 mM for catalyst **1**, and 20 mM for BIH, and the bases used were either triethanolamine (TEOA) or triethylamine (TEA), see Table 2. Although in the literature some cobalt-based catalysts performed well in acetonitrile [48], our system functioned poorly in CH_3CN/TEOA 5:1 (v/v), producing only 0.2 µmol of CO and 2.5 µmol of H_2. Thus, we changed the mixture of solvents, using *N,N*-dimethylacetamide (DMA) as the major component. Although this solvent has very similar properties as the mostly used *N,N*-dimethylformamide (DMF), it is highly stable and does not produce formate upon hydrolysis [49]. In the solvent system DMA/TEOA 3:1 (v/v), we could observe that carbon monoxide was formed, however, the system produced preferentially molecular hydrogen (Table 2, entry 2).

The role of TEOA was studied thoroughly. In many cases, it is a suitable electron donor [47], however, for PS such as Cu(dmp)DPEPhos a higher reducing power is needed. Besides that, TEOA works not only as a Brønsted base (helping in the deprotonation of the radical cation $BIH^{\bullet+}$ formed after the reductive quenching of the PS), but also can actively assist the catalysis, by capturing CO_2 [50-52]. On the other hand, having three hydroxy groups, TEOA is also considered a proton donor and the formation of metal hydrides is possible. In some cases, this metal hydride favors the production of formate [51]. However, it may induce the concomitant formation of H_2. This might have been the case of the photo-driven catalysis by complex **1** in DMA/TEOA (Table 2, entries 2–4), where upon decreasing the concentration of TEOA down to 12.5%, the selectivity towards CO increased up to 40%. Nevertheless, H_2 was still the major product. Thus, we decided to use triethylamine instead of TEOA, since a base is necessary for the reduction of CO_2, as also demonstrated by control experiments (Supporting Information File 1, Table S4), where in the absence of a base, only little amounts of CO were formed. With TEA, the photocatalytic system generates carbon monoxide with a turnover number (TON) of circa 10. A better selectivity (up to 97%) was achieved when 12.5% of TEA were used (Table 2, entry 6) while increasing the concentration of the electron donor BIH did not result in any increase in the performance (Table 2, entries 7 and 8).

Furthermore, different concentrations of catalyst **1** were evaluated (Table 3). By lowering the concentration of the catalyst, we increased the number of PS molecules per catalyst, resulting in a more efficient electron transfer and consequently an enhancement of the TON. In some cases, the production of H_2 was too low to be detected by our instrumentation, so we can affirm that the selectivity is higher than 97%, measured in previous cases. A maximum efficiency could be reached with 5 µM of **1**, which produced CO with a TON ≈ 61 after 4 h (Table 3, entry 5). Longer irradiation times (15 h) were evaluated for the concentration of 10 µM and 5 µM of complex **1**, showing that the ca-

Table 2: Selectivity study of photocatalytic CO_2 reduction with complex **1** as the catalyst.[a]

Entry	Solvent	[BIH], mM	CO, µmol	H_2, µmol	TON_{CO}	$Sel._{CO}$
1	CH_3CN/TEOA 5:1	20	0.2	2.5	0.5	6.5%
2	DMA/TEOA 3:1	20	0.9	8.5	2.2	10%
3	DMA/TEOA 5:1	20	2.8	11.1	7.0	20%
4	DMA/TEOA 7:1	20	1.1	1.6	2.7	40%
5	DMA/TEA 5:1	20	4.2	0.9	10.4	83%
6	DMA/TEA 7:1	20	3.8	0.1	9.6	97%
7	DMA/TEA 7:1	60	3.9	0.5	9.7	88%
8	DMA/TEA 7:1	80	3.8	0.1	9.6	97%

[a]In a 20 mL flask, 4 mL of solution with the following concentrations, PS (1 mM), complex **1** (0.1 mM) was irradiated at 420 nm for 4 h. Every entry is an average value of at least two tests.

talysis continued beyond 4 hours and reached a TON higher than 80 and 50, for [**1**] of 5 and 10 μM, respectively (Table 3, entries 6 and 7).

Table 3: Photocatalytic CO_2 reduction tests with different concentrations of **1**[a].

Entry	[**1**], mM	Cat., μmol	CO, μmol	TON_{CO}
1	0.1	0.5	4.2	8.4
2	0.05	0.25	4.0	16.0
3	0.025	0.125	2.8	22.5
4	0.01	0.05	1.4	27.8
5	0.005	0.025	1.5	60.9
6[b]	0.005	0.025	2.15	86.0
7[b]	0.01	0.05	2.75	53.0

[a]In a 20 mL flask, 5 mL of a solution with the following concentrations, PS (0.5 mM), BIH (20 mM) and complex **1** at the given concentrations was irradiated for 4 h. Every entry is an average value of at least two tests. [b]Irradiation time was 15 h.

The reaction kinetics was evaluated in photocatalytic systems containing 0.025 mM of **1**, since the amount of produced CO should be sufficient to be detected by GC-BID, even after a very short time from starting the reaction. As shown in Figure 5, in the first four hours, the formation of CO presents a power functional profile, without any induction period. Moreover, the turnover frequency (TOF) is maximum at 0.5 h, with a value of 19 h^{-1}. The catalysis continues; however, the TOF is decreased considerably.

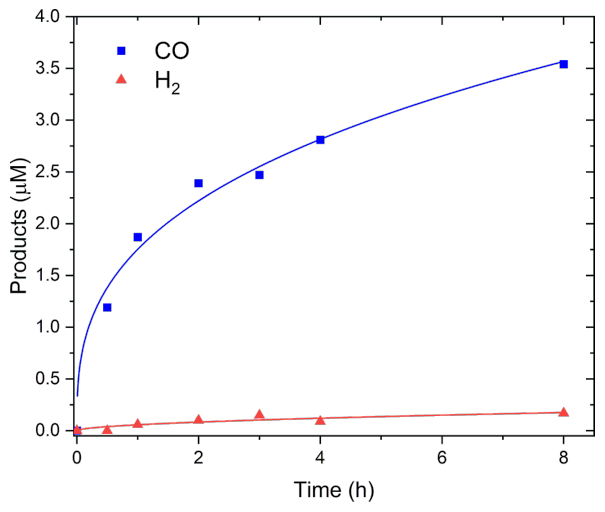

Figure 5: Time evolution of CO (blue squares) and H_2 (red triangles) with the power functional fitting (blue and red curve, respectively). Data were collected for photocatalytic tests in 5 mL DMA/TEA 7:1, [PS] = 0.5 mM; [**1**] = 0.025 mM; [BIH] = 10 mM.

Redox potentials were measured in the same solvent mixture as the photocatalytic tests (DMA/TEA 7:1), to study the thermodynamics of the reaction. The plots are shown in Supporting Information File 1 (Figures S5–S7) and the values are reported versus $Me_{10}Fc$, as the internal standard (Table S3). The first reduction of the cobalt-based catalyst is −1.56 V, thus the electron donation from PS^- (−1.67 V) is plausible, albeit the difference is not high. Estimation of the redox potentials of the excited state of PS (E_{ox}* and E_{red}*) was done assuming that the energy difference (E_{00}) between the energies of the excited and ground states, both at their zero levels, is the same as the emission maximum. Being the emission of [Cu(dmp)DPEPhos](BF_4) in DMA/TEA 7:1 567 nm, the value of E_{00} is 2.19 eV. It follows that E_{ox}* is −1.22 V and E_{red}* is 0.52 V (see Table S3 in Supporting Information File 1). Thermodynamically, an oxidative quenching of PS* by the catalyst **1** is not feasible (ΔG > 0.3 V), while a reductive quenching by BIH could be possible since the oxidation potential of BIH is 0.27 V (ΔG < −0.25 V).

We performed Stern–Volmer analyses to verify our hypothesis. As expected, the lifetime of the PS* (τ_0 = 14 ns in aerated DMA/TEA 7:1), is reduced upon the addition of the sacrificial electron donor (Figure S13 in Supporting Information File 1). The quenching constant, calculated from the linear fit according to the Stern–Volmer equation, is 3.7×10^9 s^{-1} M^{-1}. Thus, the reductive quenching of the photoexcited PS* by BIH is thermodynamically and kinetically feasible. The changes in the UV–vis absorption of a typical photocatalytic solution under irradiation were monitored over a period of four hours (Figure S12 in Supporting Information File 1) and the spectra show the development of a new broad band at 590 nm, reaching its maximum intensity after 2.5 h. This could be due to the accumulation of the reduced PS^- species.

We propose the following mechanism (Scheme 1). The PS absorbs a photon (420 nm) and in its excited state is quenched by BIH, which is deprotonated by the base (TEA) and forms a radical (BI•). Since this radical is highly reducing, it can happen that this species can also serve as a reductant [47]. The reduced species PS^- can be oxidized back to PS by a molecule of **1**, which could detach a $^-$NCS anion and offer a vacant site to coordinate a proton (then following an H_2 evolution path) or a molecule of CO_2 [46]. The adduct with CO_2 is further reduced (by PS^- or BI•) and after the addition of two protons, CO and H_2O are produced.

The cycle could be closed by the coordination of thiocyanate to the cationic Co(II) species, which is left after the generation of the products, or maybe the reduction of the above-mentioned species occurs with another PS cycle. This proposed mecha-

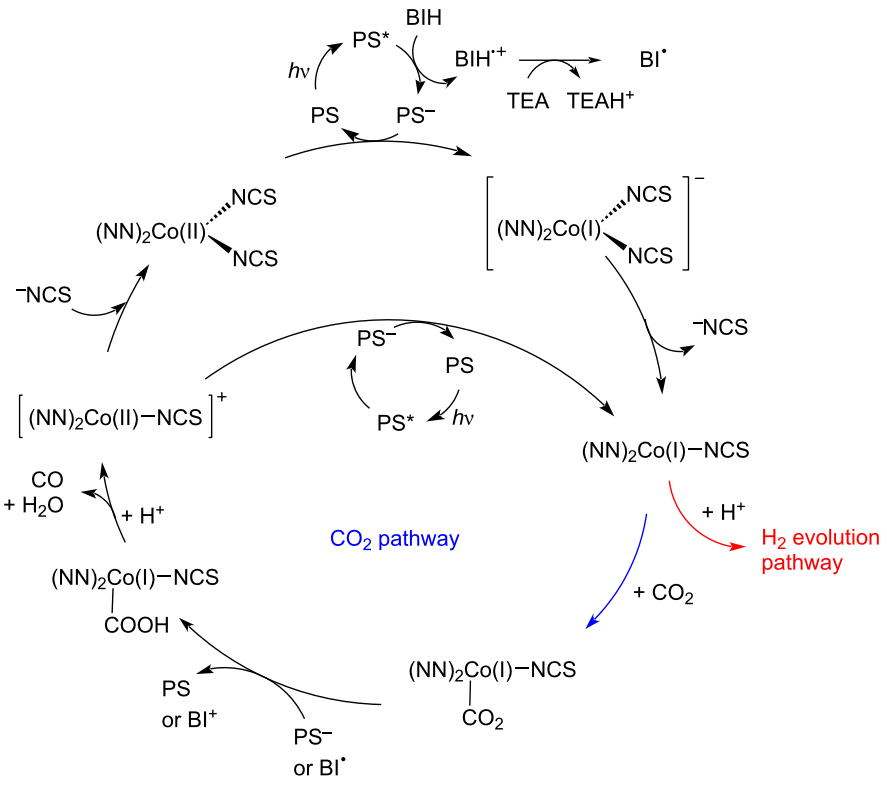

Scheme 1: Proposed mechanism for the photoinduced reduction of carbon dioxide with the system presented in this work.

nism is only tentative and should be confirmed by further analyses and theoretical calculations.

In any case, the addition of proton sources should be beneficial for the CO_2 pathway, and in the system, we studied so far, the only plausible proton source is the bezimidazolidine derivative. Thus, aiming at enhancing the catalytic activity, we performed some additional photocatalytic tests, upon the addition of different concentrations of 1,1,1,3,3,3-hexafluoropropan-2-ol (HFIP). This alcohol has interesting physical and chemical properties, and, being well miscible with many organic solvents and with water, it has been used in a large variety of (electro)chemical reactions [53]. The hydroxy group of this alcohol has a pK_a of 9.3 [54,55], so we can expect that it is a suitable proton donor for this kind of reaction. We performed the photocatalytic CO_2 reduction by dissolving in 5 mL 1%, 2%, and 5% of HFIP (see Table 4). The concentrations of the main components were: [**1**] = 5 μM, [PS] = 0.5 mM, and [BIH] = 10 mM. After four hours of irradiation at 420 nm, the production of CO increased remarkably, reaching a TON higher than 230 when 5% HFIP were used (Table 4, entry 3). Unfortunately, also the generation of H_2 increased with the concentration of HFIP, lowering the selectivity to 55%. Nevertheless, these results are promising, and further optimization studies are necessary to achieve high efficiencies and selectivity at the same time.

Conclusion

We presented a novel Co(II)-based catalyst and its employment in photo-driven CO_2 reduction. The cobalt core was hexacoordinated by two chelating quinolyl-triazole ligands and two

Table 4: Photocatalytic CO_2 reduction tests with different concentrations of HFIP.[a]

Entry	HFIP, %	CO, μmol	H_2, μmol	TON_{CO}	TON_{H2}	$Sel._{CO}$
1	1	4.6	3.1	184	126	59%
2	2	4.9	2.1	198	83	70%
3	5	6.0	4.7	231	189	55%

[a]In a 20 mL flask, 5 mL of a solution with the following concentrations, PS (0.5 mM), BIH (20 mM), complex **1** (0.005 mM) and the indicated amounts of HFIP was irradiated for 4 h.

$^{-}$NCS groups. The electrochemical properties suggested that this complex could reduce carbon dioxide. The photocatalytic system chosen for this target was fully earth-abundant, as the complex [Cu(dmp)DPEPhos](BF$_4$) was used as the photosensitizer. Preliminary tests in the solvent mixture of DMA/TEOA showed that the novel catalyst reduces CO_2 to CO. However, the evolution of molecular hydrogen was prevailing. Thus, we modified the conditions to switch the selectivity towards the two electron-reduction product of CO_2, carbon monoxide. We successfully achieved a selectivity of 97% with the use of TEA (12.5%) instead of TEOA. The following optimization studies allowed us to tune the efficiency for CO production with a maximum TON of 86, after 15 h of irradiation. Finally, further tests were performed with the addition of an additional proton source (HFIP). Although the selectivity was lowered, the CO evolution was enhanced remarkably, reaching a TON up to 230, after 4 h of irradiation.

Experimental

Synthesis of catalyst **1**, (BzQuTr)$_2$Co(NCS)$_2$

In a two-necked round-bottomed flask, under argon, the chelating ligand BzQuTr (100 mg, 0.35 mmol, 2.0 equiv) dissolved in 10 mL of dry MeOH was added dropwise to Co(NCS)$_2$(py)$_4$ (86 mg, 0.175 mmol, 1.00 equiv), dissolved in 5 mL of MeOH. The mixture was stirred for two hours at room temperature. The solvent was removed under reduced pressure and the crude product was washed with cold MeOH and Et_2O, obtaining a lilac precipitate (82 mg, 0.11 mmol, 60%). Paramagnetic properties were estimated by the Evans method [56] in acetonitrile and resulted in three unpaired electrons. ATR–IR (cm^{-1}) ν: 3109, 3027, 2065, 1606, 1574, 1507, 1496, 1469, 1453, 1438, 1431, 1375, 1358, 1350, 1332, 1313, 1251, 1210, 1162, 1145, 1130, 1101, 1061, 1027, 1011, 952, 832, 817, 803, 783, 764, 732, 717, 694, 679, 654, 636, 599, 572, 531, 516, 482, 459, 399, 384; ESIMS *m*/*z* (%): 689.14 [M − NCS] (100%); 690.15 [M + H − NCS] (43%); Anal. calcd for $C_{38}H_{28}CoN_{10}S_2{\cdot}CH_3OH$: C, 60.07; N, 17.96; H, 4.11; S, 8.22; found: C, 60.05; N, 17.84; H, 3.66; S, 8.18.

Photocatalytic CO_2 reduction

Typically, the tests were performed in glass vials (20 mL) equipped with a screw-cap septum. The solutions were prepared under air and CO_2 (or argon) was bubbled inside for at least 10 minutes. TEA or TEOA was distilled twice before use. Experiments were performed in a photoreactor from Luzchem (model: LZC-ICH2) equipped with two lamps at 420 nm (fluorescent lamps of 8 W each) and four mini-stirrers. On each stirrer, two samples were irradiated at the same time, for a total of eight simultaneous reactions. A drawing of the photoreactor is shown in the Supporting Information File 1 (Figure S9) and the emission spectrum of the lamp is reported in Figure S10. Typically, the solutions contained the photosensitizer (1 mM or 0.5 mM), catalyst **1** (different concentrations were studied), and BIH (usually 10 mM or 20 mM), unless otherwise noted. The temperature of the reactor was controlled with an in-built ventilator, T = (25 ± 5) °C. The moles of products (CO and H_2) were measured by quantitative analyses of the headspace of the reactions with a gas chromatograph from Shimadzu (GC-2030) equipped with two barrier discharge ionization detectors (BID). Every test was repeated at least twice. The photon flux was evaluated with actinometry, according to a previously published procedure [42], and it was 0.025 μE s^{-1}. Therefore, an apparent photoluminescent quantum yield could be estimated to be up to 2.4%, after 4 h, according to Equation 5:

$$\Phi = \frac{\text{CO moles}}{\text{incident photons} \times (1 - 10^{A})} \times 100 \quad (5)$$

Where A is the initial absorption value of the photocatalytic system at the irradiation wavelength.

TON and TOF were calculated according to Equation 6, Equation 7, and Equation 8:

$$\text{TON}_{CO} = \frac{n_{CO}}{n_{catalyst}} \quad (6)$$

$$\text{TON}_{H2} = \frac{n_{H2}}{n_{catalyst}} \quad (7)$$

$$\text{TOF} = \frac{\text{TON}}{t_{reaction}} \quad (8)$$

Where n is the number of moles of the products and of the catalyst; t is the time of the reaction.

Supporting Information

Additional information regarding the instrumentation, structural analyses, and X-ray structures is provided. Crystal structures were deposited in the Cambridge Crystallographic Data Centre (CCDC) with the numbers 2285968 (**1a**) and 2285968 (**1b**).

Supporting Information File 1

General information, further synthetic and experimental procedures, and additional results.
[https://www.beilstein-journals.org/bjoc/content/supplementary/1860-5397-19-129-S1.pdf]

Acknowledgements

Prof. Stefan Bräse and Dr. Nicole Jung (KIT) are acknowledged for providing lab space and access to the GC-BID instrument.

Funding

German Research Foundation (DFG) transregional collaborative research center SFB/TRR 88 (project B9) and by the German Scholar Organization through the Klaus Tschira Boost Fund (project KT26).

ORCID® iDs

Lisa-Lou Gracia - https://orcid.org/0000-0003-3002-4700
Philip Henkel - https://orcid.org/0009-0004-4510-8346
Olaf Fuhr - https://orcid.org/0000-0003-3516-2440
Claudia Bizzarri - https://orcid.org/0000-0002-4077-2553

References

1. Osman, A. I.; Chen, L.; Yang, M.; Msigwa, G.; Farghali, M.; Fawzy, S.; Rooney, D. W.; Yap, P.-S. *Environ. Chem. Lett.* **2023,** *21,* 741–764. doi:10.1007/s10311-022-01532-8
2. Alissandratos, A.; Easton, C. J. *Beilstein J. Org. Chem.* **2015,** *11,* 2370–2387. doi:10.3762/bjoc.11.259
3. Fujita, E. *Coord. Chem. Rev.* **1999,** *185–186,* 373–384. doi:10.1016/s0010-8545(99)00023-5
4. Saha, P.; Amanullah, S.; Dey, A. *Acc. Chem. Res.* **2022,** *55,* 134–144. doi:10.1021/acs.accounts.1c00678
5. Navarro-Jaén, S.; Virginie, M.; Bonin, J.; Robert, M.; Wojcieszak, R.; Khodakov, A. Y. *Nat. Rev. Chem.* **2021,** *5,* 564–579. doi:10.1038/s41570-021-00289-y
6. Li, X.; Yu, J.; Jaroniec, M.; Chen, X. *Chem. Rev.* **2019,** *119,* 3962–4179. doi:10.1021/acs.chemrev.8b00400
7. Morris, A. J.; Meyer, G. J.; Fujita, E. *Acc. Chem. Res.* **2009,** *42,* 1983–1994. doi:10.1021/ar9001679
8. Takeda, H.; Cometto, C.; Ishitani, O.; Robert, M. *ACS Catal.* **2017,** *7,* 70–88. doi:10.1021/acscatal.6b02181
9. Wenger, O. S. *J. Am. Chem. Soc.* **2018,** *140,* 13522–13533. doi:10.1021/jacs.8b08822
10. Bizzarri, C. *Eur. J. Org. Chem.* **2022,** e202200185. doi:10.1002/ejoc.202200185
11. Chen, H.; Chen, L.; Chen, G.; Robert, M.; Lau, T.-C. *ChemPhysChem* **2021,** *22,* 1835–1843. doi:10.1002/cphc.202100330
12. Zhong, M.; Pannecoucke, X.; Jubault, P.; Poisson, T. *Beilstein J. Org. Chem.* **2020,** *16,* 451–481. doi:10.3762/bjoc.16.42
13. Hernandez-Perez, A. C.; Collins, S. K. *Acc. Chem. Res.* **2016,** *49,* 1557–1565. doi:10.1021/acs.accounts.6b00250
14. Engl, S.; Reiser, O. *Eur. J. Org. Chem.* **2020,** 1523–1533. doi:10.1002/ejoc.201900839
15. Beaudelot, J.; Oger, S.; Peruško, S.; Phan, T.-A.; Teunens, T.; Moucheron, C.; Evano, G. *Chem. Rev.* **2022,** *122,* 16365–16609. doi:10.1021/acs.chemrev.2c00033
16. Forero Cortés, P. A.; Marx, M.; Trose, M.; Beller, M. *Chem Catal.* **2021,** *1,* 298–338. doi:10.1016/j.checat.2021.05.005
17. Bruschi, C.; Gui, X.; Salaeh-arae, N.; Barchi, T.; Fuhr, O.; Lebedkin, S.; Klopper, W.; Bizzarri, C. *Eur. J. Inorg. Chem.* **2021,** 4074–4084. doi:10.1002/ejic.202100653
18. Bassan, E.; Inoue, R.; Fabry, D.; Calogero, F.; Potenti, S.; Gualandi, A.; Cozzi, P. G.; Kamogawa, K.; Ceroni, P.; Tamaki, Y.; Ishitani, O. *Sustainable Energy Fuels* **2023,** *7,* 3454–3463. doi:10.1039/d3se00546a
19. Rosas-Hernández, A.; Alsabeh, P. G.; Barsch, E.; Junge, H.; Ludwig, R.; Beller, M. *Chem. Commun.* **2016,** *52,* 8393–8396. doi:10.1039/c6cc01671e
20. Takeda, H.; Ohashi, K.; Sekine, A.; Ishitani, O. *J. Am. Chem. Soc.* **2016,** *138,* 4354–4357. doi:10.1021/jacs.6b01970
21. Gracia, L.-L.; Barani, E.; Braun, J.; Carter, A. B.; Fuhr, O.; Powell, A. K.; Fink, K.; Bizzarri, C. *ChemCatChem* **2022,** *14,* e202201163. doi:10.1002/cctc.202201163
22. Wang, F. *ChemSusChem* **2017,** *10,* 4393–4402. doi:10.1002/cssc.201701385
23. Shimoda, T.; Morishima, T.; Kodama, K.; Hirose, T.; Polyansky, D. E.; Manbeck, G. F.; Muckerman, J. T.; Fujita, E. *Inorg. Chem.* **2018,** *57,* 5486–5498. doi:10.1021/acs.inorgchem.8b00433
24. Kojima, T. *ChemPhotoChem* **2021,** *5,* 512–520. doi:10.1002/cptc.202000263
25. Burks, D. B.; Davis, S.; Lamb, R. W.; Liu, X.; Rodrigues, R. R.; Liyanage, N. P.; Sun, Y.; Webster, C. E.; Delcamp, J. H.; Papish, E. T. *Chem. Commun.* **2018,** *54,* 3819–3822. doi:10.1039/c7cc09507d
26. Royal Society of Chemistry's Periodic table of the elements, Cobalt. https://www.rsc.org/periodic-table/element/27/cobalt.
27. Usman, M.; Humayun, M.; Garba, M. D.; Ullah, L.; Zeb, Z.; Helal, A.; Suliman, M. H.; Alfaifi, B. Y.; Iqbal, N.; Abdinejad, M.; Tahir, A. A.; Ullah, H. *Nanomaterials* **2021,** *11,* 2029. doi:10.3390/nano11082029
28. Obermeier, M.; Beckmann, F.; Schaer, R. S.; Wenger, O. S.; Schwalbe, M. *Front. Chem. (Lausanne, Switz.)* **2021,** *9,* 751716. doi:10.3389/fchem.2021.751716
29. Wang, J.-W.; Li, Z.; Luo, Z.-M.; Huang, Y.; Ma, F.; Kupfer, S.; Ouyang, G. *Proc. Natl. Acad. Sci. U. S. A.* **2023,** *120,* e2221219120. doi:10.1073/pnas.2221219120
30. Wang, J.-W.; Zhang, X.; Velasco, L.; Karnahl, M.; Li, Z.; Luo, Z.-M.; Huang, Y.; Yu, J.; Hu, W.; Zhang, X.; Yamauchi, K.; Sakai, K.; Moonshiram, D.; Ouyang, G. *JACS Au* **2023,** *3,* 1984–1997. doi:10.1021/jacsau.3c00218
31. Call, A.; Cibian, M.; Yamauchi, K.; Sakai, K. *Sustainable Energy Fuels* **2022,** *6,* 2160–2164. doi:10.1039/d2se00291d
32. Domingo-Tafalla, B.; Chatterjee, T.; Palomares, E. *J. Porphyrins Phthalocyanines* **2023,** *27,* 23–46. doi:10.1142/s1088424623300033
33. Call, A.; Cibian, M.; Yamamoto, K.; Nakazono, T.; Yamauchi, K.; Sakai, K. *ACS Catal.* **2019,** *9,* 4867–4874. doi:10.1021/acscatal.8b04975
34. Zhang, X.; Yamauchi, K.; Sakai, K. *ACS Catal.* **2021,** *11,* 10436–10449. doi:10.1021/acscatal.1c02475
35. Wang, M.; Torbensen, K.; Salvatore, D.; Ren, S.; Joulié, D.; Dumoulin, F.; Mendoza, D.; Lassalle-Kaiser, B.; Işci, U.; Berlinguette, C. P.; Robert, M. *Nat. Commun.* **2019,** *10,* 3602. doi:10.1038/s41467-019-11542-w
36. Ouyang, T.; Wang, H.-J.; Huang, H.-H.; Wang, J.-W.; Guo, S.; Liu, W.-J.; Zhong, D.-C.; Lu, T.-B. *Angew. Chem., Int. Ed.* **2018,** *57,* 16480–16485. doi:10.1002/anie.201811010
37. Zhang, L.; Li, S.; Liu, H.; Cheng, Y.-S.; Wei, X.-W.; Chai, X.; Yuan, G. *Inorg. Chem.* **2020,** *59,* 17464–17472. doi:10.1021/acs.inorgchem.0c02733

38. Guo, Z.; Chen, G.; Cometto, C.; Ma, B.; Zhao, H.; Groizard, T.; Chen, L.; Fan, H.; Man, W.-L.; Yiu, S.-M.; Lau, K.-C.; Lau, T.-C.; Robert, M. *Nat. Catal.* **2019,** *2,* 801–808. doi:10.1038/s41929-019-0331-6
39. Elliott, P. I. P. Organometallic complexes with 1,2,3-triazole-derived ligands. In *Organometallic Chemistry;* Fairlamb, I. J. S.; Lynam, J. M., Eds.; The Royal Society of Chemistry: Cambridge, UK, 2014; Vol. 39, pp 1–25.
40. Rostovtsev, V. V.; Green, L. G.; Fokin, V. V.; Sharpless, K. B. *Angew. Chem., Int. Ed.* **2002,** *41,* 2596–2599. doi:10.1002/1521-3773(20020715)41:14<2596::aid-anie2596>3.0.co;2-4
41. Takeda, H.; Monma, Y.; Sugiyama, H.; Uekusa, H.; Ishitani, O. *Front. Chem. (Lausanne, Switz.)* **2019,** *7,* 418. doi:10.3389/fchem.2019.00418
42. Gracia, L.-L.; Luci, L.; Bruschi, C.; Sambri, L.; Weis, P.; Fuhr, O.; Bizzarri, C. *Chem. – Eur. J.* **2020,** *26,* 9929–9937. doi:10.1002/chem.202001279
43. Zsakó, J.; Várhelyi, C.; Csegedi, B.; Kékedy, E. *Thermochim. Acta* **1985,** *83,* 181–191. doi:10.1016/0040-6031(85)87002-7
44. Sheridan, U.; McGinley, J.; Gallagher, J. F.; Fleming, A.; Kelleher, F. *Polyhedron* **2013,** *59,* 8–16. doi:10.1016/j.poly.2013.04.025
45. Rhoufal, F.; Laachir, A.; Guesmi, S.; Jouffret, L.; Sergent, N.; Obbade, S.; Akkurt, M.; Bentiss, F. *ChemistrySelect* **2019,** *4,* 7773–7783. doi:10.1002/slct.201901219
46. Isegawa, M. *Organometallics* **2022,** *41,* 3568–3580. doi:10.1021/acs.organomet.2c00416
47. Pellegrin, Y.; Odobel, F. *C. R. Chim.* **2017,** *20,* 283–295. doi:10.1016/j.crci.2015.11.026
48. Su, C.; Chen, Z.; Feng, Q.; Wei, F.; Mo, A.; Huang, H.-H.; Hu, H.; Zou, H.; Liang, F.; Liu, D. *Dalton Trans.* **2023,** *52,* 4548–4553. doi:10.1039/d3dt00054k
49. Kuramochi, Y.; Kamiya, M.; Ishida, H. *Inorg. Chem.* **2014,** *53,* 3326–3332. doi:10.1021/ic500050q
50. Morimoto, T.; Nakajima, T.; Sawa, S.; Nakanishi, R.; Imori, D.; Ishitani, O. *J. Am. Chem. Soc.* **2013,** *135,* 16825–16828. doi:10.1021/ja409271s
51. Sampaio, R. N.; Grills, D. C.; Polyansky, D. E.; Szalda, D. J.; Fujita, E. *J. Am. Chem. Soc.* **2020,** *142,* 2413–2428. doi:10.1021/jacs.9b11897
52. Tsipis, A. C.; Sarantou, A. A. *Dalton Trans.* **2021,** *50,* 14797–14809. doi:10.1039/d1dt02188e
53. Colomer, I.; Chamberlain, A. E. R.; Haughey, M. B.; Donohoe, T. J. *Nat. Rev. Chem.* **2017,** *1,* 0088. doi:10.1038/s41570-017-0088
54. Pozhydaiev, V.; Power, M.; Gandon, V.; Moran, J.; Lebœuf, D. *Chem. Commun.* **2020,** *56,* 11548–11564. doi:10.1039/d0cc05194b
55. Parman, E.; Toom, L.; Selberg, S.; Leito, I. *J. Phys. Org. Chem.* **2019,** *32,* e3940. doi:10.1002/poc.3940
56. Schubert, E. M. *J. Chem. Educ.* **1992,** *69,* 62. doi:10.1021/ed069p62.1

License and Terms

BEILSTEIN JOURNAL OF ORGANIC CHEMISTRY

Optimizing reaction conditions for the light-driven hydrogen evolution in a loop photoreactor

Pengcheng Li[1], Daniel Kowalczyk[1], Johannes Liessem[2], Mohamed M. Elnagar[2], Dariusz Mitoraj[2], Radim Beranek[2] and Dirk Ziegenbalg[*1]

Full Research Paper

Open Access

Address:
[1]Institute of Chemical Engineering, Ulm University, Albert-Einstein-Allee 11, 89081 Ulm, Germany and [2]Institute of Electrochemistry, Ulm University, Albert-Einstein-Allee 47, 89081 Ulm, Germany

Email:
Dirk Ziegenbalg[*] - dirk.ziegenbalg@uni-ulm.de

* Corresponding author

Keywords:
loop photoreactor; parametric study; photocatalytic hydrogen evolution; polymeric carbon nitride; solar energy storage

Beilstein J. Org. Chem. **2024,** *20,* 74–91.
https://doi.org/10.3762/bjoc.20.9

Received: 15 August 2023
Accepted: 27 December 2023
Published: 16 January 2024

This article is part of the thematic issue "Artificial photosynthesis".

Guest Editor: A. Pannwitz

Abstract

Photocatalytic hydrogen production from water is a promising way to fulfill energy demands and attain carbon emission reduction goals effectively. In this study, a loop photoreactor with a total volume of around 500 mL is presented for the photocatalytic hydrogen evolution using a Pt-loaded polymeric carbon nitride photocatalyst under 365 nm irradiation in the presence of sacrificial reducing agents. The fluid flow pattern of the developed photoreactor was characterized experimentally and the photon flux incident to the loop photoreactor was measured by chemical actinometry. The system displayed exceptional stability, with operation sustained over 70 hours. A design of experiment (DOE) analysis was used to systematically investigate the influence of key parameters – photon flux, photocatalyst loading, stirring speed, and inert gas flow rate – on the hydrogen generation rate. Linear relationships were found between hydrogen evolution rate and photon flux as well as inert gas flow rate. Photocatalyst loading and stirring speed also showed linear correlations, but could not be correctly described by DOE analysis. Instead, linear single parameter correlations could be applied. Notably, the loop photoreactor demonstrated an external photon efficiency up to 17 times higher than reported in literature studies, while scaling the reactor size by a factor of 10.

Introduction

The world is in the midst of the first truly global energy crisis with unprecedented breadth and complexity [1]. Meanwhile, the rise of the world's population and economic growth demands more energy. Of all energy sources, fossil fuels have been dominating over 80% of the global energy market for decades [1-3]. However, the combustion of fossil fuels contributes greatly to environmental degradation, global warming, and air pollution, which further damages public health [4-6]. Given the nature of how fossil fuels are formed, which takes millions of years to come to be [7], they are considered limited resources and nonrenewable compared to the current consumption rate [8]. Therefore, a pressing need exists to transition towards renewable

energy sources to ensure sustainable energy development and environmental preservation. Solar energy stands out as the most compelling renewable energy source, holding the potential to fully satisfy the energy requirements of humanity [9]. The reliance on geographic locations and seasonal changes, however, makes it difficult to maintain a constant supply of solar energy year-round [10]. To harness solar energy in a proper way, solar energy can be converted to hydrogen fuels. Hydrogen as an energy carrier has zero carbon emission and a high energy density [11,12]. While significant efforts are directed towards developing effective photocatalysts for solar water splitting [13-16], a crucial emphasis must also be placed on upscaling reactors and catalytic systems to facilitate the transition to cleaner energy sources.

There are mainly three categories of solar to hydrogen generation methods based on semiconductors, namely photovoltaic-powered electrolysis (PV-E), photoelectrochemical (PEC) processes, and photocatalysis. Upon upscaling, both PV-E and PEC reactors exhibit pH gradients at electrodes and elevated solution electrical resistivity. These challenges arise from the substantial separation between reduction and oxidation sites, alongside mass transport restrictions in the liquid phase due to extended ion transport distances. These effects cause significant potential losses, eventually reducing the efficiency of the reactors. The addition of large amounts of supporting electrolyte and vigorous circulation of the electrolyte solution also complicates the scale-up process [17,18]. On the contrary, expanding photocatalytic systems, particularly those employing powdered photocatalysts, to a larger scale is notably more straightforward [17,18]. However, complications arise when attempting to scale up reactors solely based on geometric similarity, as alterations in mixing and hydrodynamic attributes occur during the process of scale-up [19,20]. Therefore, a suitable reactor, which ensures excellent fluid dynamics and transport properties during scale-up, is needed for photocatalytic hydrogen generation.

Loop reactors utilize partial inner circulation of the chosen reaction medium around an internal concentrically fitted draft tube, and are widely used in industry, such as microbiology fermentation and Fischer–Tropsch synthesis [21,22]. This type of reactors provides very high mass transfer rates, well-defined fluid flow patterns, and a simple design [23,24]. The construction and operation of loop reactors are simple. Furthermore, investment and operational costs are typically low. For these reasons, the suitability of a loop reactor was studied in this work for the photocatalytic hydrogen generation process as a potentially scalable photoreactor concept.

Suitable light sources are one of the requirements for photocatalytic studies, as they directly influence the performance of photocatalytic reactions. While the ultimate goal is to utilize sunlight directly for photocatalytic hydrogen generation, the limited intensity of sunlight poses challenges [25]. Beside this, identifying photocatalysts capable of efficient performance across broad sunlight wavelength ranges proves to be a complex endeavor [26-28]. Therefore, artificial light sources are typically applied for lab testing of photocatalytic reactions. Compared to conventional light sources, light-emitting diodes (LEDs) have plenty of advantages including long life span (up to 100 000 h), robustness, compact size, and high energy efficiency, which make LEDs very attractive as a light source for photocatalytic hydrogen generation studies [29].

In this work, a loop photoreactor for scaling up the photocatalytic hydrogen generation is designed and equipped with 365 nm LEDs. Fluid dynamics in the loop photoreactor are characterized using a color tracer mixing experiment and image analysis. Photonic characterization is performed with the ferrioxalate actinometer. Finally, the photocatalytic hydrogen evolution with Pt-loaded polymeric carbon nitride (Pt-PCN) powder using methanol as sacrificial agent (Scheme 1) is studied as a benchmark in the designed loop photoreactor. Four parameters, namely photon flux, photocatalyst loading, stirring speed, and inert gas flow rate, are investigated for their effect on the activity of the hydrogen evolution. The efficiency of the loop photoreactor is also compared with results from literature obtained in a Schlenk tube system [30].

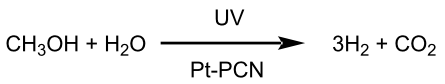

Scheme 1: Photocatalytic hydrogen evolution with Pt-loaded polymeric carbon nitride.

Results and Discussion

Photocatalyst characterization

The surface morphology of the Pt-PCN photocatalyst has been analyzed by scanning electron microscopy (SEM) at different magnifications, as shown in Figure 1a–d. The images reveal a layered structure exhibiting a rough surface with agglomerated, irregular, and dense particles. Figure 2a–e shows the elemental mapping analysis of Pt-PCN conducted using SEM-EDX. A homogeneous distribution of Pt (Figure 2d) was found across the surfaces of the Pt-PCN, confirming their uniformity. To ensure that the homogeneous distribution of Pt on the surface of PCN is not random, multiple particles were analyzed using SEM-EDX (see Supporting Information File 1, Figure S1), which shows the uniform distribution of Pt on the surfaces of PCN over all particles. Moreover, the EDX elemental composition analysis indicates that the Pt content is 0.6 atom %.

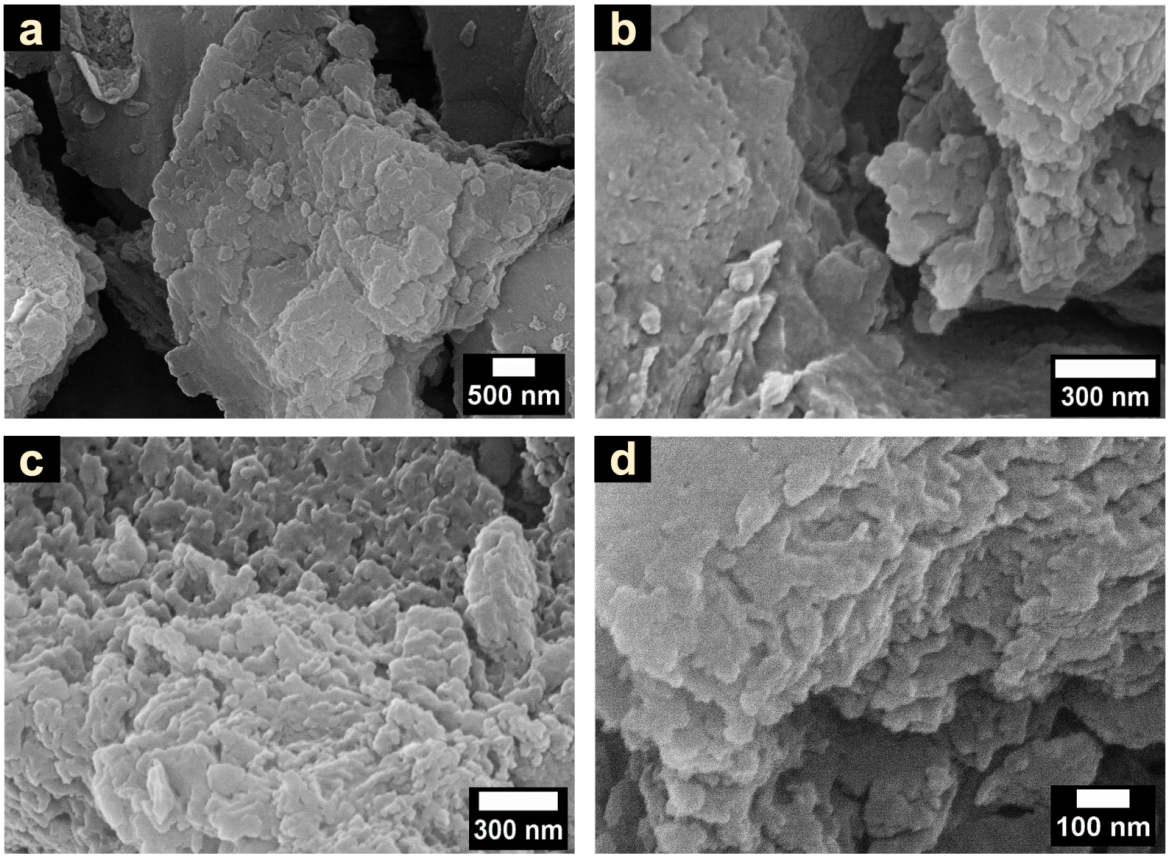

Figure 1: SEM images of the Pt-PCN photocatalyst at different magnifications.

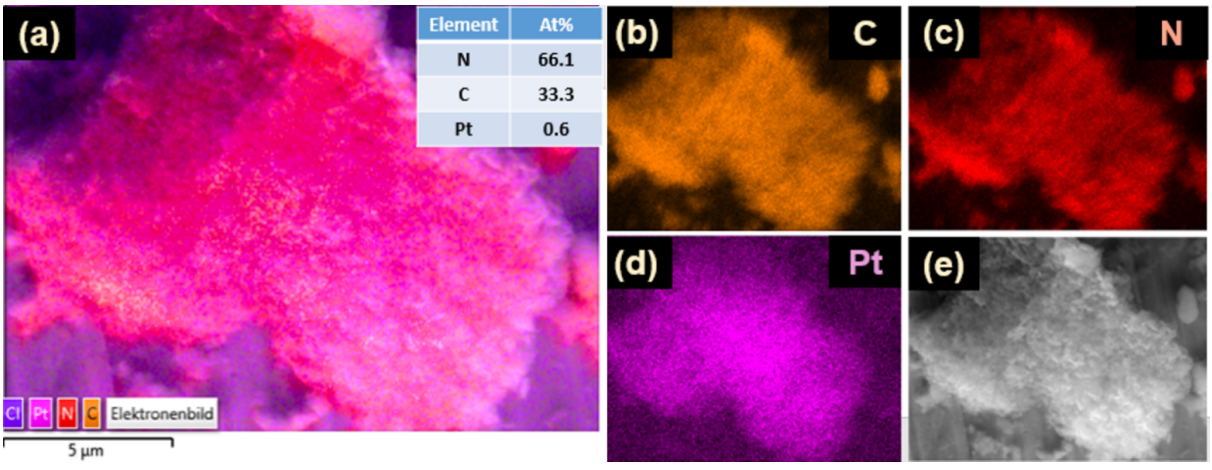

Figure 2: SEM-EDX elemental mapping images of C, N, and Pt on a particle.

Reactor characterization

Fluid flow pattern

Figure 3 shows four representative frames of a mixing experiment at times of 1.2, 2.2, 4.2, and 7.8 s using a stirring speed of 560 rpm. The regions of interests (ROIs) shown on frame of 1.2 s are denoted as left side (blue ROI), draft tube (green ROI), and right side (yellow ROI). The color of water changed first in the draft tube and then outside the draft tube until the mixing was complete. Thus, the liquid was first sucked into the draft tube and flowed through the draft tube downwards until it

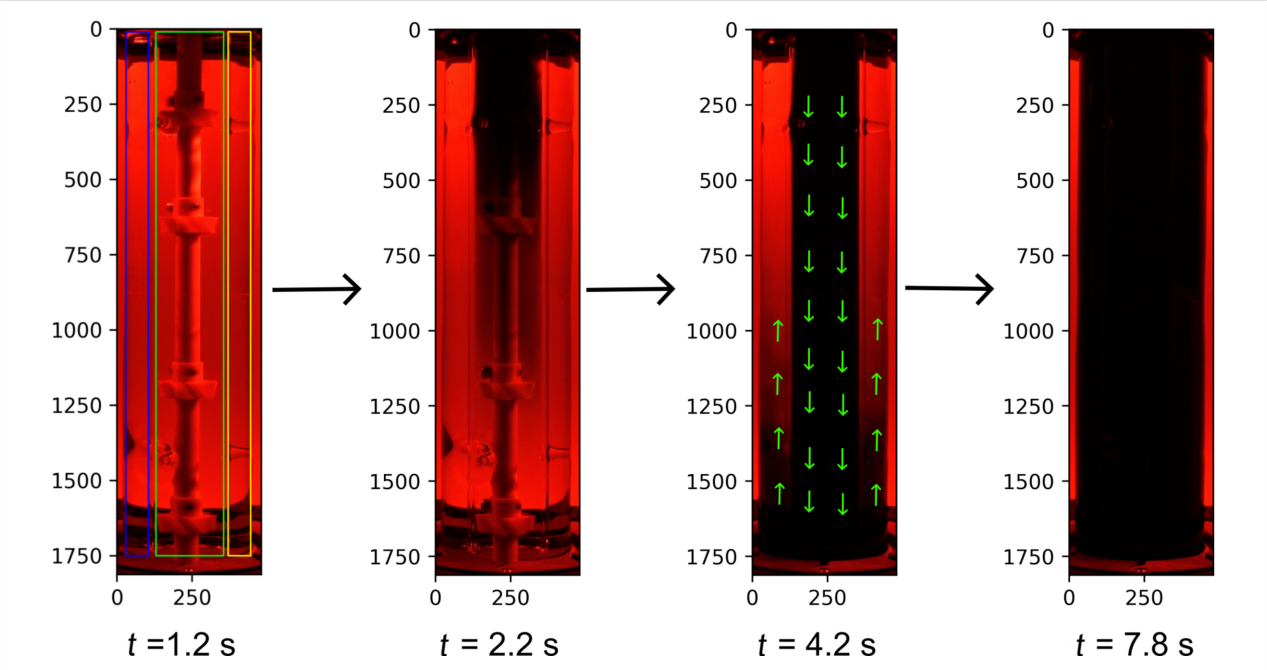

Figure 3: Exemplary results of the mixing experiments using methylene blue to visualize and quantify fluid flow pattern in the loop photoreactor at stirring speed of 560 rpm.

reached the bottom of the reactor, where it was redirected to flow upward outside the draft tube back to the top of the reactor. The arrows on the frame of 4.2 s show the fluid flow direction. This confirms the desired operation of the reactor design concept of a guided inner circulation around the draft tube.

Figure 4 shows the red channel values of ROIs for the mixing experiments with different stirring speeds (430, 560, 740, and 860 rpm). The mixing time in the draft tube only slightly depends on the stirring speed. However, the mixing time outside of the draft tube shows a clear dependence on the stirring speed. As expected, both sides of the reactor show an almost identical mixing behavior. Data for a stirring speed of 430 rpm shows pronounced fluctuation. This is because not the whole methylene blue solution is immediately sucked into the draft tube. Instead, parts of the tracer solution are swirling above the draft tube, eventually being sucked slowly into the draft tube and causing the observed fluctuations (see Supporting Information File 2, loop_430rpm).

Figure 5 shows the determined mixing times for the different regions. The mixing time in the draft tube ranged from 2.72 s to 1.92 s and the mixing time outside of the draft tube from 4.48 s to 2.52 s for 430 rpm and 860 rpm, respectively. The low dependency of the mixing time in the draft tube on the stirring speed might be related to the small size of the propellers used in the draft tube, which might interfere with the draft tube, finally

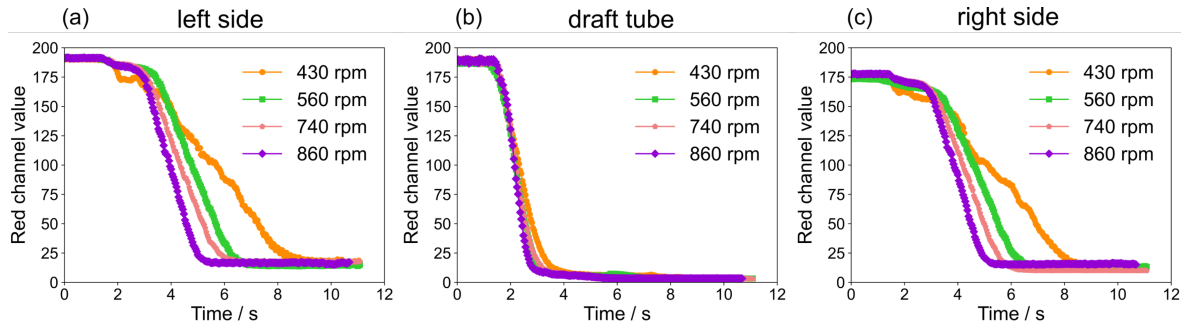

Figure 4: Red channel values of ROIs with different stirring speeds: (a) left space between reactor and draft tube, (b) in draft tube, (c) right space between reactor and draft tube.

reducing their effectiveness at higher stirring speeds. However, the propeller used below the draft tube is larger and will not suffer from interference with the draft tube, enhancing the convection outside the draft tube.

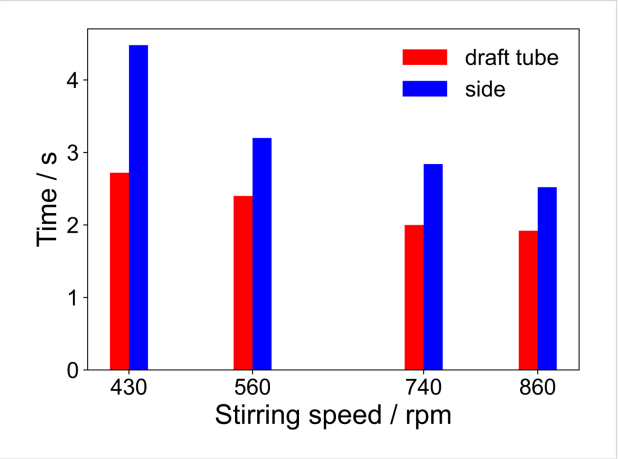

Figure 5: Quantified mixing time using different stirring speeds.

Photonic characterization

The loop photoreactor using 6 LEDs was photonically characterized by chemical actinometry. Figure 6 shows the actinometer conversions and calculated photon fluxes at different irradiation times. The reasonable linear fits of the conversion (see Figure 6a) prove the applicability of the chosen experimental protocol for the loop photoreactor [31]. Consequently, time-independent photon fluxes were calculated for the different operational conditions (see Figure 6b). Only for very short times in combination with high electrical currents of LEDs (e.g., 500 mA) a change of the photon flux is observed. For short times this is caused by very low conversions and the associated experimental uncertainties and for the latter conditions by the application limits of the ferrioxalate actinometer [32].

The average photon flux incident on the reaction solution depends linearly on the LEDs electrical current (see Figure 7). The good linear regression shows that the chemical actinometry gave quite reliable photon flux values in the loop photoreactor. This relation was used to extrapolate the photon fluxes for experiments with more than 6 LEDs or with higher electrical current.

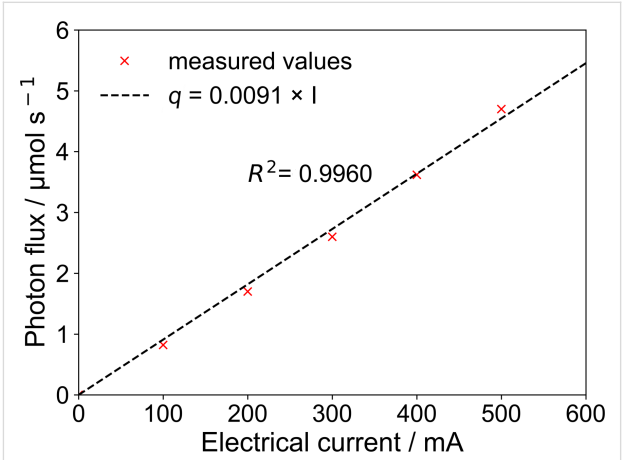

Figure 7: Photon flux in the loop reactor with respect to the LED electrical current.

Light absorption

According to the Beer–Lambert law, the absorption of light in a solution can be described by Equation 1 [33].

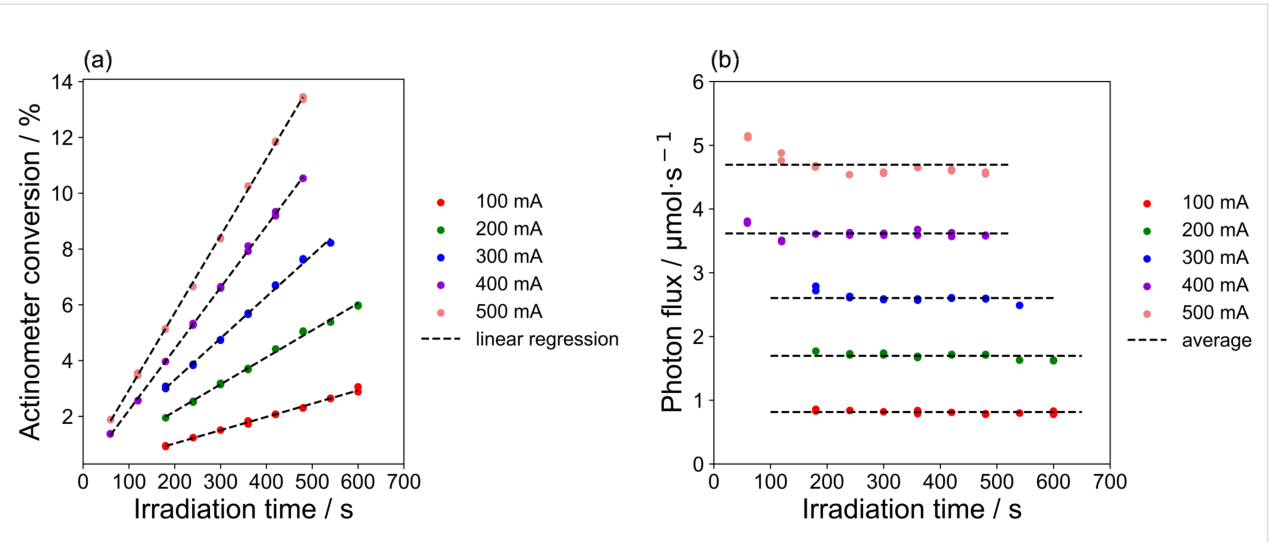

Figure 6: Chemical actinometry results: (a) actinometer conversion at different irradiation time, (b) photon flux at different irradiation time.

$$A = \log_{10}\frac{I_0}{I_d} = \varepsilon \times c \times d \quad (1)$$

where A is the absorbance, I_0 is the intensity of light entering the solution perpendicularly to one face, I_d is the intensity of light exiting the solution, ε is the extinction coefficient, c is the concentration of a light-absorbing solute, and d is the optical path length. Figure 8 shows the measured absorbance as function of the photocatalyst loadings in the methanol/water solution using different optical path lengths. The absorbance depends linearly on the photocatalyst concentration for low concentrations, which agrees with the Beer–Lambert law [33,34]. An extinction coefficient of 3.5 L g^{-1} cm^{-1} was determined by fitting the experimental data. The deviation of the absorbance from the linear relation is attributed to increased scattering at high loadings and/or long optical paths, where consequently the requirements for the application of the Beer–Lambert law are not fulfilled anymore. Considering the inner diameter of the loop reactor of 5 cm, a catalyst loading of 0.11 g L^{-1} is sufficient to absorb more than 95% of the photons.

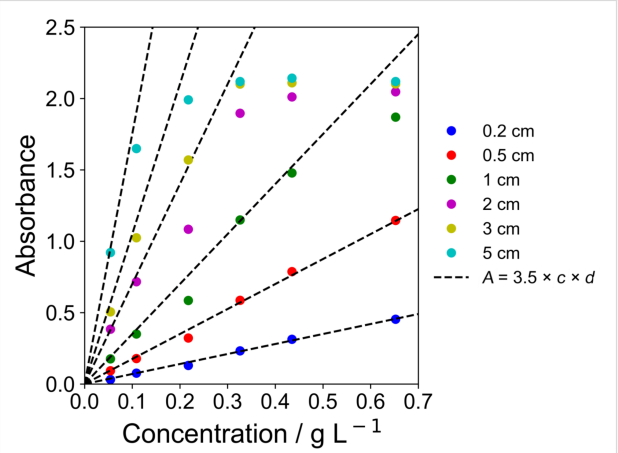

Figure 8: Absorbance as function of photocatalyst loading for different optical path lengths.

Photocatalytic hydrogen evolution

Long-term operation

Photocatalytic hydrogen evolution was performed using water and methanol under UV LED irradiation with a Pt-PCN photocatalyst (R1). The volume ratio of water and methanol used in this work is 9:1 with a total volume of 460 mL. The used setup was equipped with a micro-GC for online measurements of the hydrogen evolution, which enabled sampling every 3 minutes and thus provides insights on the kinetics of hydrogen evolution. Compared to conventional manual sampling with gas-tight syringes, online measurements also improve reproducibility by minimizing potential errors such as contamination by air or sampling mistakes.

The long-term stability of the photocatalyst was initially tested in the loop photoreactor with a photocatalyst loading of 0.22 g L^{-1}, a stirring speed of 560 rpm, a photon flux of 4.70 µmol s^{-1}, and an inert gas flow rate of 75 mL min^{-1}. Figure 9 shows the hydrogen generation rate as function of irradiation time. The hydrogen generation rate first increases to a maximum value and decreases subsequently. After around 10 hours of irradiation, a steady level of hydrogen evolution is reached. Even though some fluctuations in the range of ±8% can be observed, the hydrogen evolution rate remained at this level for 70 hours of irradiation. These results prove the long-term stability of the systems, which is a prerequisite for any future application.

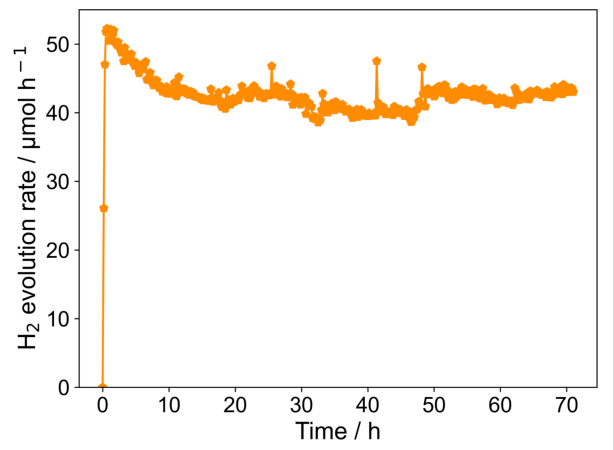

Figure 9: Long-term operation of the loop photoreactor.

Design of experiment analysis

During design of experiment (DOE) analysis, the default linear and quadratic model were found to describe the experimental data reasonably well (see Table 1). While R^2 is higher for the quadratic model, it must be checked whether the model is over-parameterized with terms that are not statistically significant. To do this, the R^2_{adj} and R^2_{pred} were analyzed. The R^2_{adj} plateaus when insignificant terms are added to the model, and R^2_{pred} will decrease when there are too many insignificant terms. The low R^2_{pred} value of 0.6213 confirms that the default quadratic model is over-parameterized. For a reasonable model, the difference of R^2_{adj} and R^2_{pred} should be within approximately 0.2 [35]. As it is evident from Table 1, this is the case for the linear (0.0831) but not for the quadratic mode one (0.3033). Therefore, compared to the default quadratic model, the linear model is more appropriate for predicting maximum hydrogen generation rate within the value range of the studied parameters.

The significance of the chosen parameters was evaluated by analysis of variance (ANOVA). The “Prob>F” probability value gives the estimation of whether the parameter has a significant

Table 1: Performance metric values for the suggested models from DOE analysis.

Performance metric	Model		
	Linear	Quadratic	Modified
R^2	0.8619	0.9686	0.9526
R^2_{adj}	0.8343	0.9246	0.9289
R^2_{pred}	0.7512	0.6213	0.8426
$R^2_{adj} - R^2_{pred}$	0.0831	0.3033	0.0863

effect on the response, and generally a parameter with a probability value less than 0.05 is considered as significant. A probability value larger than 0.10 renders the parameter generally as insignificant [35]. It is evident from Table 2 that light intensity and inert gas flow can be regarded as significant, while the photocatalyst amount and the stirring speed are insignificant.

Table 2: "Prob>F" values of the studied parameters from DOE ANOVA analysis.

Parameter	Prob>F	
	Linear model	Modified quadratic model
q	<0.0001	<0.0001
c	0.1671	0.8276
v	0.9278	0.1305
$\dot{V}$	0.0028	<0.0001
$q \times \dot{V}$	–	0.0068
$c \times v$	–	0.0279
c^2	–	0.0164
v^2	–	0.0054

In addition to this analysis, it is necessary to check if there are any interactions between the studied parameters. After the insignificant parameter interaction terms were removed from the quadratic model, the interaction of photocatalyst loading and stirring speed has a "Prob>F" value of 0.0279, which means this interaction term also significantly affects the maximum hydrogen generation rate. The interaction effect was summarized in the modified quadratic model, which has a difference between R^2_{adj} and R^2_{pred} of 0.0863. Moreover, an ANOVA showed that the p-value of the linear and modified quadratic model is lower than 0.0001, which confirms that the model is adequate with a significance level of more than 99%. Therefore, the linear and modified quadratic models are suitable for describing the relation between photocatalytic hydrogen generation and the four studied parameters.

The linear and modified model from DOE analysis are described with Equation 2 and Equation 3:

$$PR = -13.92 + 6.49\ q + 15.70\ c + 1.07\times10^{-3}\ v + 0.42\dot{V} \quad (2)$$

$$PR = -150.23 + 3.31\ q + 255.36\ c + 0.38\ v - 7.77\times10^{-3}\ \dot{V} + 0.1\ q\times\dot{V} - 0.22\ c\times v - 149.86\ c^2 - 2.42\times10^{-4}\ v^2 \quad (3)$$

where PR represents the predicted maximum photocatalytic hydrogen generation rate (μmol h^{-1}), q is the photon flux (μmol s^{-1}), c is the photocatalyst loading (g L^{-1}), v is the stirring speed (rpm), and $\dot{V}$ is the inert gas flow rate (mL min^{-1}). The response surfaces for the modified model are shown in Figure 10. Linear correlations dominate the response to the photon flux and inert gas flow rate, while the power law correlations dominate the photocatalyst loading and the stirring speed.

Figure 11 shows that a reasonable parity between the predicted hydrogen generation rate and the actual experimental hydrogen generation rate could be achieved. No significant difference between the prediction accuracy of the two models is observable. The only difference between the two models is that the modified model considers the interaction of parameters. Therefore, to validate the model from DOE analysis, experiments that vary only the individual parameters were performed to see which model is more appropriate.

Analysis of individual reaction parameters

General considerations: To test the validity of the model derived with the DOE approach, the capabilities of the model prediction were tested against conventional single parameter studies. For that, additional experiments were conducted and analyzed, when possible, together with the data points from the DOE study. Given the significance of the photon flux and the inert gas flow rate, these parameters were studied first. To mimic the conventional experimental approach, the photocatalyst loading and the stirrer speed were investigated as well.

Photon flux: The effect of the photon flux on the temporal evolution of the hydrogen generation rate was investigated individually for a constant set of operating parameters (c = 0.22 g L^{-1}, v = 560 rpm, $\dot{V}$ = 75 mL min^{-1}). The photon flux related to the LEDs' electrical current is calculated based on the actinometry results presented in section "Photonic characterization" (see Figure 7). The characteristics of the temporal evolution of the hydrogen generation rate were found to depend on the photon flux (Figure 12a). For all conditions, the observed hydrogen evolution rate increased initially. At a low

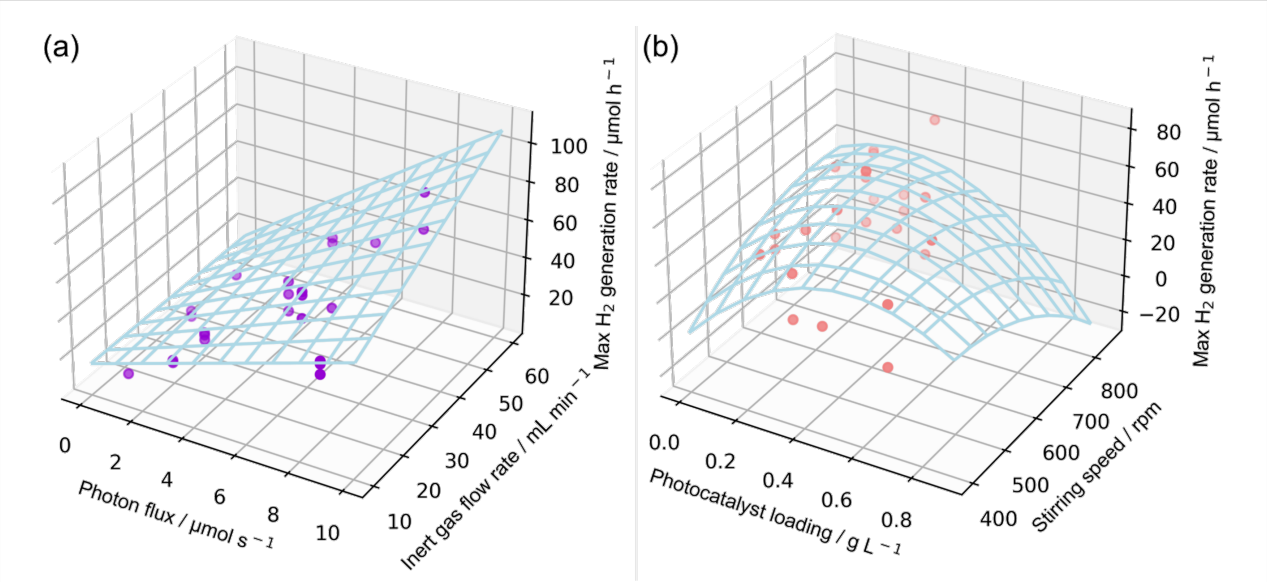

Figure 10: Visualization of the response surfaces of the modified DOE model for the four parameters: (a) photon flux and inert gas flow rate, (b) photocatalyst loading and stirring speed.

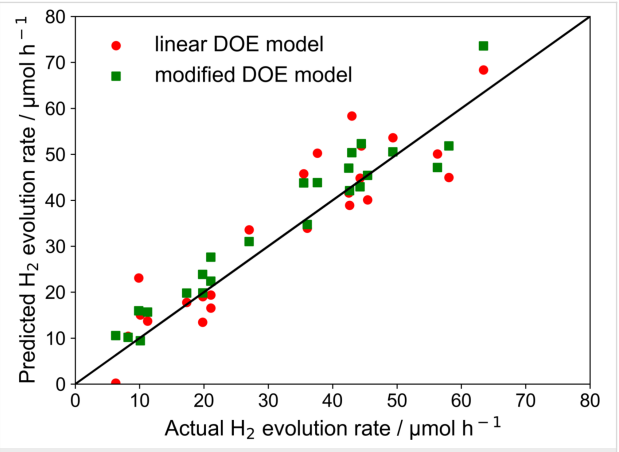

Figure 11: Parity plot of the measured photocatalytic hydrogen generation rate versus the values predicted by the models from DOE analysis.

photon flux, a steady state evolution rate was reached quickly and remained stable during the reaction. However, at higher photon fluxes, the hydrogen generation rate decreased slowly with the irradiation time (up to 18% after 15 hours for a photon flux of 4.70 µmol s^{-1}).

An increase of the maximum hydrogen generation rate with an increase of the incident photon flux was found. The maximum hydrogen generation rate was 3.5 times higher for a 5 times higher photon flux of 4.70 µmol s^{-1} than at a photon flux of 0.82 µmol s^{-1} [36]. Furthermore, it was observed that an increasing photon flux reduced the time needed for reaching the maximum hydrogen generation rate. Nomikos et al. reasoned a similar observation with a decreased time needed for complete reforming of methanol and reaction intermediates at higher intensities [37].

For further studies, the reactor setup was equipped with four heat sinks around the reactor, each equipped with 6 LEDs. This was the constructive maximum of LEDs that could be installed and allowed for providing a maximum photon flux of 32.77 µmol s^{-1} to the reactor. Systematic studies on varying photon fluxes showed an almost linear increase of the hydrogen evolution rate with lower photon fluxes (see Figure 12b).

Generally, three regimes can be differentiated for the correlation of the reaction rate with the photon flux [37-42]. At low photon fluxes (regime 1), the hydrogen generation rate is typically limited by the available photon flux and can be approximated first order with respect to light intensity. For higher photon fluxes, kinetic limitations appear (second regime) since the larger amount of charge carriers present in the photocatalysts causes accelerated recombination in parts of the reactor. When extremely high photon fluxes are used, the reaction would be kinetically limited at every point in the reactor (regime 3). Increasing the photon flux would not increase the reaction rate anymore. Bloh proposed a model linking the photon flux and reaction rate [42], which was used in this work to fit the experiment results (see Equation 4).

$$\langle r \rangle = \frac{k^* \times \theta}{\alpha} \times \ln\left(\frac{\phi \times q_p \times \alpha \times c_0}{k^* \times \theta \times c_0 \times k_r} + 1\right) \quad (4)$$

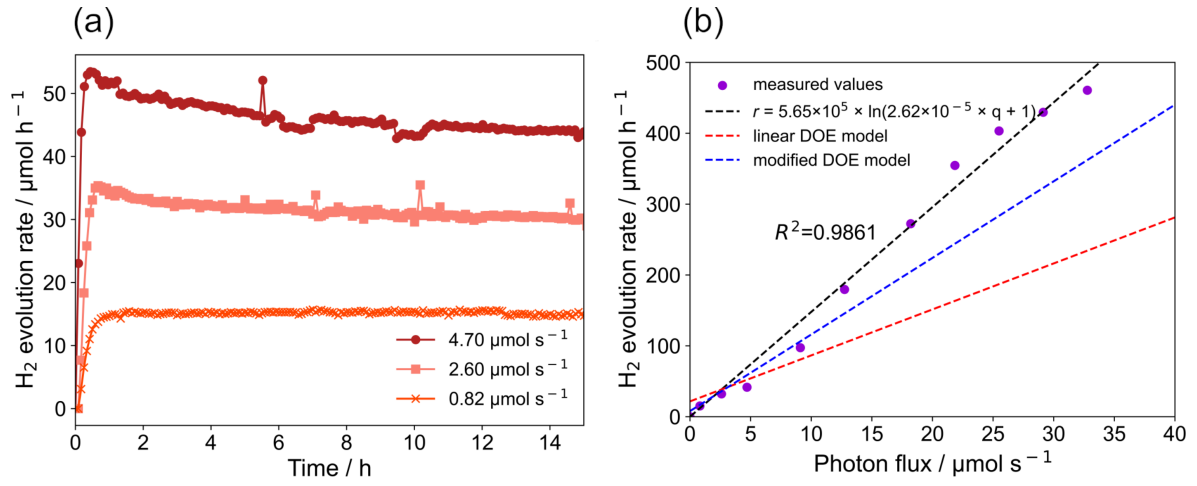

Figure 12: Effect of photon flux on hydrogen generation rate: (a) hydrogen generation rate as function of the irradiation time under different light intensities, (b) hydrogen generation rate as function of the photon flux.

where $\langle r \rangle$ is the average (observed) reaction rate, k^* is the kinetic rate constant, θ is the surface coverage of the photocatalyst, α is the optical density, ϕ is the quantum yield, q_p is the volumetric photon flux density, c_0 is the photocatalyst concentration, and k_r is the recombination rate.

The linear correlation between reaction rate and photon flux visible in Figure 12b indicates that the system is still in regime 1 and the hydrogen generation rate is limited by the available photon flux, even for the highest photon flux used in this study. The predictions from the DOE analysis hold for low photon fluxes but the inaccuracy increases with the photon flux. The deviations to the experimental data are larger for the linear as for the modified DOE model. For instance, the linear model predicts an about 50% lower hydrogen evolution rate for a photon flux of about 35 µmol s^{-1}.

Inert gas flow rate: The effect of inert gas flow rate on hydrogen generation rate is shown in Figure 13a (q = 4.70 µmol s^{-1}, c = 0.22 g L^{-1}, v = 560 rpm). The maximum hydrogen generation rate increased by 74% when the inert gas flow rate was increased from 25 to 75 mL min^{-1}. This effect is attributed to an enhanced mass transfer of hydrogen from the photocatalyst to the gas phase. The relevant mass transport steps for hydrogen include the diffusion from the photocatalyst surface to the liquid bulk, transfer from the liquid bulk to liquid–gas interface, and transfer from liquid–gas interface to gas phase [43]. Since the inert gas was purged into the reactor continuously, the gener-

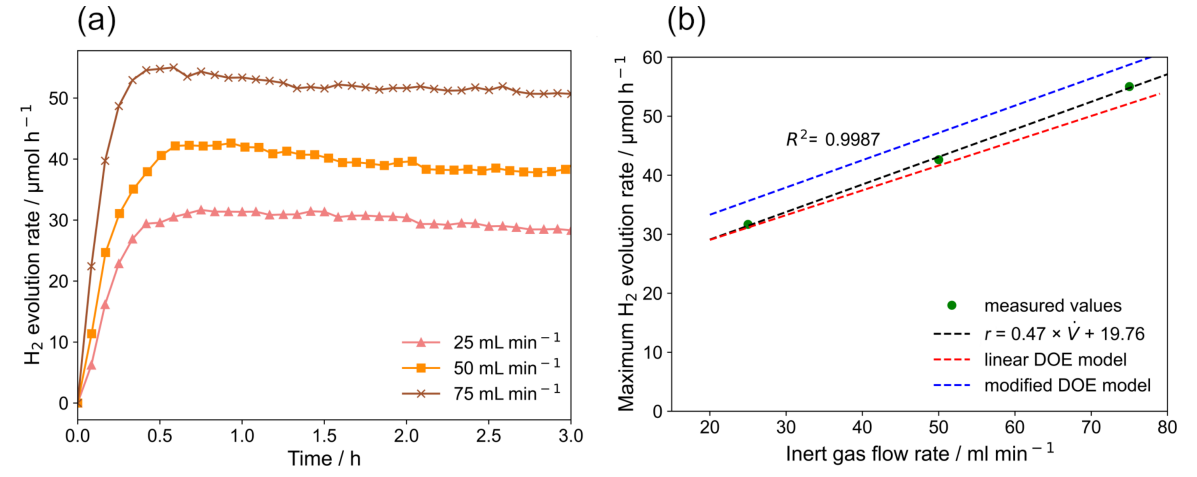

Figure 13: Effect of inert gas flow rate on hydrogen generation rate: (a) hydrogen generation rate as a function of the irradiation time, (b) maximum hydrogen generation rate as a function of the inert gas flow rate in the solution.

ated hydrogen could also directly be transferred from the photocatalyst surface to the gas phase if a gas bubble got in contact with the catalyst surface. Furthermore, it is evident from Figure 13a that higher inert gas flow rates decrease the irradiation time needed to reach the maximum hydrogen generation rate. At a flow rate of 25 mL min^{-1} it took around 45 min to reach to maximum hydrogen generation rate, while at a flow rate of 75 mL min^{-1} only around 30 min was sufficient. Besides, the decrease of the activity with reaction time is less pronounced compared to the studies on the influence of the photon flux. Both observations are also attributed to the enhancement of mass transfer induced by a higher inert gas flow rate.

The maximum hydrogen generation rate is linearly correlated to the inert gas flow rate (see Figure 13b). This is in accordance with the mass transfer studies published by Escudero et al. [43], who also showed that the hydrogen generation rate is linearly related to the gas flow rate. Moreover, the linear relationship is also supported by the DOE analysis. Both DOE models predict the experiment results quite well. The linear model yields a slightly better prediction. A linear regression of only the data points shown here shows an expected good agreement with the experimental data.

Photocatalyst loading: The temporal hydrogen evolution activity for different photocatalyst loadings is shown in Figure 14a (q = 4.70 µmol s^{-1}, v = 560 rpm, $\dot{V}$ = 75 mL min^{-1}). Again, the hydrogen generation rate increased to a maximum and then slowly decreased until a steady state rate was reached, likely due to the same reasons as discussed above. An increase of the photocatalyst loading enhanced the hydrogen generation rate, which might be a result of improved overall light harvesting at higher loadings and indicates that the mass transport issues (i.e., transport of the reactants to and of the products away from the surface catalytic sites) is still not rate-limiting in this regime [38].

Figure 14b shows the predicted maximum hydrogen generation rate for varying photocatalyst loadings. It is obvious that the modified model deviates less from the experimental results. Despite this, it also becomes clear that the quadratic model used for the modified model is not suited for extrapolations since a decrease of the hydrogen evolution activity is predicted which is not found experimentally. In fact, a linear model, that is fitted solely to this small data set and ignores the effect of the other reaction parameters, yields a better prediction (see Figure 14b). This would also be in line with observations reported by Nomikos et al. for a 0.5 wt % Pt/TiO_2 photocatalyst suspended in water and methanol solution at low loadings (from 0 to 0.33 g L^{-1}) [37]. These authors found a saturation point at higher photocatalyst loadings after which hydrogen generation activity did not increase any further.

Stirring speed: Figure 15a shows the hydrogen evolution activity for different stirring speeds (q = 4.70 µmol s^{-1}, c = 0.22 g L^{-1}, $\dot{V}$ = 50 mL min^{-1}). Increasing the stirring speed results in an increase in the maximum hydrogen generation rate. The maximum hydrogen generation rate was 1.5 times higher at 740 rpm than at 430 rpm. This gives evidence that increased convection improves the mass transfer of generated hydrogen from the liquid phase to the gas phase or even directly from the catalyst to the gas phase. This is in line with the measured mixing time. Furthermore, the experiments show that a certain threshold is required to achieve higher activity. Only for stirring speeds above 430 rpm, an improvement is observed. This is

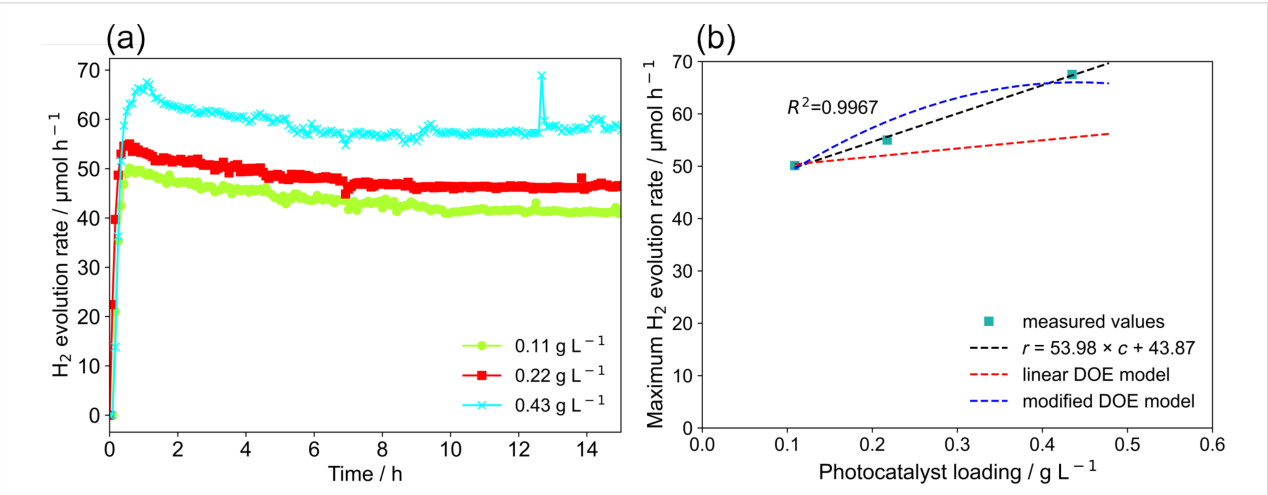

Figure 14: Effect of photocatalyst loading on the hydrogen generation rate: (a) hydrogen generation rate as function of irradiation time, (b) maximum hydrogen generation rate as function of photocatalyst concentration.

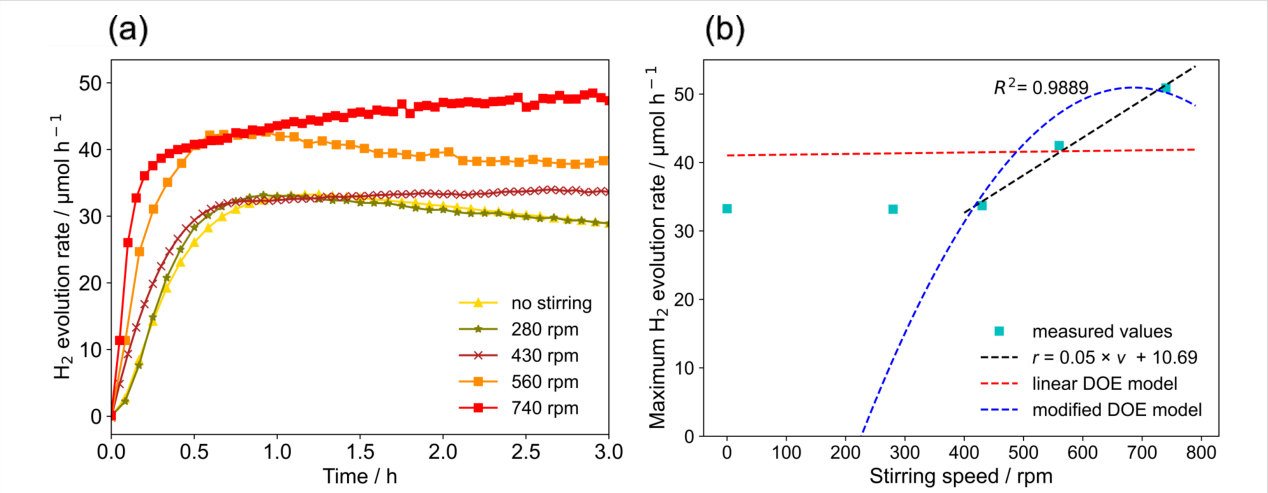

Figure 15: Effect of stirring speed on hydrogen generation rate: (a) hydrogen generation rate as function of irradiation time, (b) maximum hydrogen generation rate as function of stirring speed.

most likely due to limited convection at lower stirring speeds and the hydrodynamic issues discussed above.

Figure 15b shows the prediction of the maximum hydrogen generation rate for different stirring speeds. The modified DOE model shows a better agreement with the experimental results for conditions above 280 rpm than the linear model, but again the physicochemical plausibility of the quadratic model is questionable. It is evident from the shown data that a linear fit describes the experimental data well when the correlations with other parameters and the data points for "no stirring" and a stirring speed of 280 rpm are excluded. The required threshold for achieving sufficient convection is likely the reason why a linear description cannot be applied for the data set.

Discussion: Analysis of the single parameter studies in comparison to the DOE analysis shows that the studied parameter set possesses complex correlations that cannot be described in the required quality with the simple mathematical models available for the DOE analysis. With power law models the description of the experimental data can be improved in terms of statistics, but physical and chemical plausibility cannot be ensured with this approach. Thus, only interpolations in a predefined parameter space are possible. In conclusion, application of simple statistical models to reduce the experimental efforts is not suited for the studied photocatalytic processes. The non-linear interplay of various parameters limits the value of the derived DOE models.

Independent from this statistical analysis, it is possible to compare the performance of the loop photoreactor and the suspended photocatalysts to results presented in the literature. The apparent quantum efficiency (AQE) is a suited performance metric for such a comparison and defined as [41]:

$$\Phi_{\text{app}} = \frac{n \times r}{q} \tag{5}$$

where n is the number of electrons involved in the photocatalytic reaction (2 in this case), r is the hydrogen generation rate, and q is the total photon flux entering the reaction volume.

Figure 16 depicts the AQE at 365 nm calculated for all experimental data points. The determined AQE ranges from 0.25 to 1.05%, which is a factor of 4 to 17 higher as reported in the literature for the photocatalytic hydrogen evolution using Pt loaded polymeric carbon nitride in a 21 mL Schlenk tube (AQE = 0.06%) [30]. The maximum hydrogen generation rate observed was 460.66 µmol h^{-1} at a photon flux of 32.77 µmol s^{-1}, a catalyst loading of 0.22 g L^{-1}, a stirring speed of 560 rpm and an inert gas flow rate of 50 mL min^{-1}. Under these conditions, an AQE of 0.75% was determined. The highest AQE of 1.05% was found for the lowest photon flux of 0.82 µmol s^{-1} (c = 0.22 g L^{-1}, v = 560 rpm, $\dot{V}$ = 75 mL min^{-1}). With respect to a high overall performance of the system, it is notable that even for high photon fluxes of more than 12 µmol s^{-1} AQE larger than 0.75% are observed. This indicates that the performance is not decreasing due to an increased rate of recombination, which is in line with the analysis of the photon flux dependency. Overall, the loop photoreactor not only allows for an order of magnitude increase in reaction scale, but also significantly increases the efficiency of light utilization.

Conclusion

The presented investigations show that loop photoreactors are suited to scale up the light-driven hydrogen evolution with Pt-loaded polymeric carbon nitride photocatalysts. With the presented design, a scale-up by more than one order of magni-

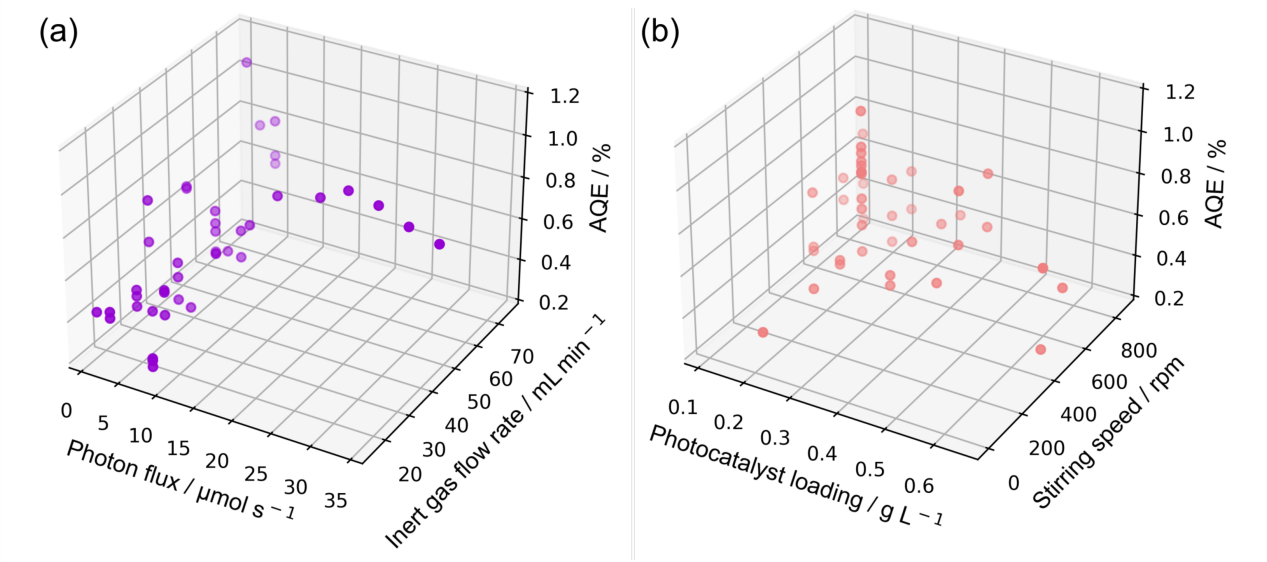

Figure 16: 3D plot of AQE for different studied parameters: (a) AQE for different photon fluxes and inert gas flow rates, (b) AQE for differrent photocatalyst loadings and stirring speeds.

tude could be realized compared to literature-reported systems. Systematic evaluation of operational parameters revealed a significant influence of the photon flux as well as the inert gas flow rate. The latter finding indicates that sufficiently fast mass transport is of major importance for the performance of the studied reaction. The used loop reactor provides excellent mass transport properties, which eventually enabled an increase of the apparent quantum yield by a factor of 10. This result is even more relevant than the demonstration of the scale-up as efficient use of photons provided to the reaction solution is the basis for a future large-scale application of solar-driven hydrogen evolution.

The findings emphasize that an interdisciplinary investigation of light-driven reactions is of utmost importance for implementing photocatalytic hydrogen generation on a large scale. The strong interaction of the radiation field with mass transport of the involved species, i.e., light absorber, catalyst, reactants, and hydrogen as product, has a tremendous effect on the overall performance. Engineering aspects may have direct implications for the design of photocatalytic materials to cope, e.g., with mass transport issues on a larger scale. Consequently, reaction engineering studies should not only be conducted after a catalytic system was developed but should be an integral part of research on light-driven systems already during development of photocatalytic active materials.

Experimental

Reactor design

The design parameters for the loop photoreactor are based on the optimal design parameters suggested by Blenke et al. [44]. The draft tube diameter is adjusted to achieve maximal mass transfer in the reactor [45-48]. The design parameters used in this work are defined by Equations 6–9:

$$D_D = 0.44 \times D_R \quad (6)$$

$$L_D = 4.4 \times D_R \quad (7)$$

$$L_T = 0.4 \times D_R \quad (8)$$

$$L_B = 0.4 \times D_R \quad (9)$$

where D_R is the inner diameter of the reactor, D_D is the inner diameter of the draft tube, L_D is the draft tube length, L_T is the distance of the draft tube to the reactor top, L_B is the distance of the reactor bottom to the draft tube. The reactor is manufactured from 2 mm thick borosilicate glass with a total height of 40 cm. Borosilicate glass was chosen as the reactor body material based on the following reasons: (1) the transmission of borosilicate glass at UV range is already over 90%, (2) borosilicate glass is easier to work with for manufacturing the reactor with the proposed design, and (3) borosilicate glass is the cheaper material. With 2 mm thickness, about 10% of the incident light is absorbed by the reactor wall. The inner diameter of the reactor D_R is set as 5 cm, yielding a total reactor volume of around 500 mL.

The designed loop photoreactor consists of three separate parts, the reactor head with a gas inlet and a gas outlet (GL18 thread), the reactor body with draft tube, and the reactor bottom (see Figure 17a). The three parts are assembled using two clamps

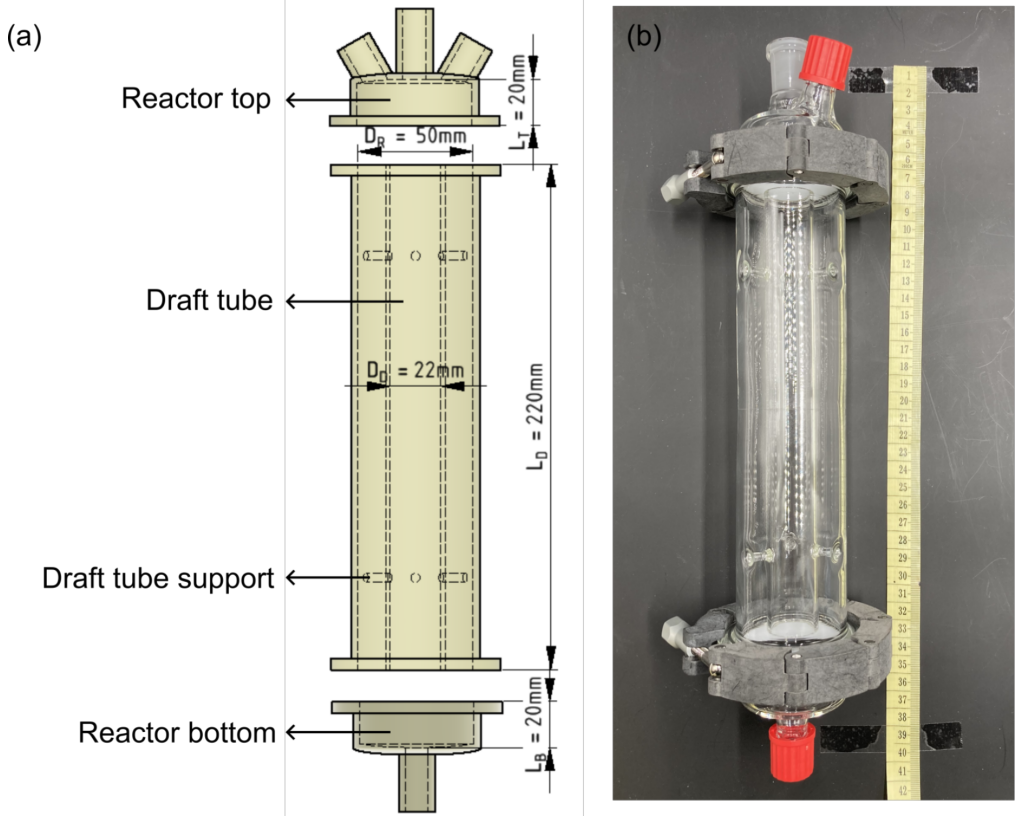

Figure 17: Reactor design: (a) CAD drawing of the loop reactor, (b) picture of the manufactured loop reactor.

(plastic black, DN 50) and O-rings. The reactor top has a 29/32 ground joint for an overhead stirrer.

3D-printed support structures were used to ensure a reproducible installation for the reactor setup (see Figure 18a). The propellers used to induce the required convection in the draft tube were also 3D-printed. One large propeller was mounted at the bottom of the shaft tube and four small propellers were mounted on the shaft above the big propeller (see Figure 18b). The mounted position of the propeller on the shaft is shown in Supporting Information File 1, Figure S2a. To ensure that the propellers were fixed at the same position on the shaft tube, holes with M3 thread were drilled in the shaft. All 3D-printed parts were printed with a 3D printer (Pro2 Plus, Raise3D) using a polylactic acid (PLA) filament. The 3D printer setting is shown in Supporting Information File 1, Table S1.

As light source 365 nm UV LEDs (Luminus SST-10-UV, Luminus Devices, Inc.) were used. The technical specification of the UV LED is shown in Supporting Information File 1, Table S2. If not mentioned specifically, a total number of 6 LEDs was used, which were mounted on 2 plate-fin heat sinks (each heat sink was equipped with 3 LEDs). The position of the LEDs on the heat sink is shown in Supporting Information File 1, Figure S2b. The design of reactor support and propellers are shown in Supporting Information File 1, Figures S3 and S4.

Reactor characterization

The fluid flow pattern in the loop photoreactor was experimentally studied with a tracer experiment. The reactor was initially filled with 460 mL deionized water. The stirrer motor was then turned on with an appropriate rotational speed. When a steady hydrodynamic state was reached in the reactor, 5 mL of a 0.8 g L^{-1} methylene blue solution was injected at the top surface of water at the top of the reactor. To ensure reproducibility and comparability, the methylene blue solution was always rapidly injected at the same spot using a syringe with a large opening. The tracer injection time was kept constant throughout the experiment at 1.2 s. The coloring of the solution was monitored with a video camera (Sony ZV-1). The video was shot under red light, which matched the absorption properties of the dye, to obtain optimal optical visualization. Digital images extracted from videos (see Supporting Information File 2) were processed with the Python OpenCV package to quantify the mixing time (see Supporting Information File 3, Python code)

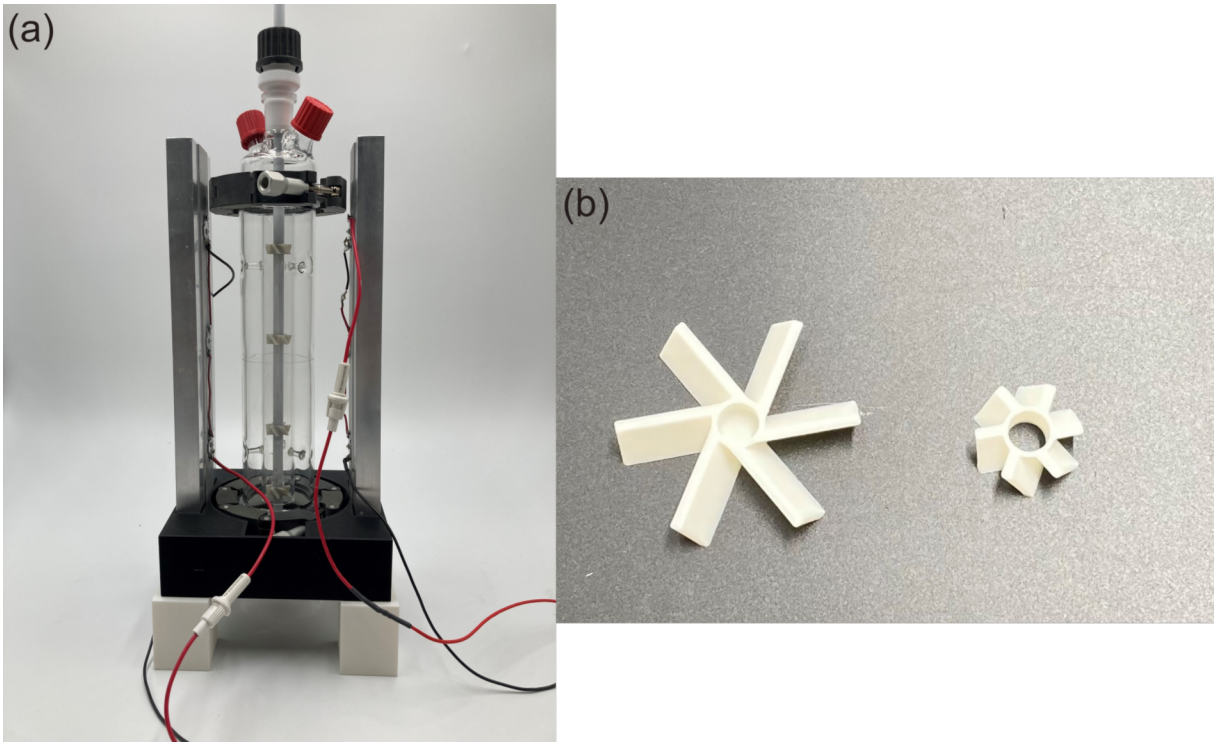

Figure 18: Assembled reactor and 3D printed parts: (a) the whole reactor setup, (b) 3D printed propellers.

by following the color evolution in the videos from red towards black under the red-light environment [49]. ROI used as the working zone were defined on the images when these were processed to quantify the mixing time. The three rectangles shown in Figure 3 on frame at 1.2 s showed the regions used for image processing. To quantify the mixing time, the RGB color model was used, representing each color as a mixture of pure red, green, and blue light of varying levels ranging from 0 to 255 [50]. Because the videos were shot under red light, only the red channel values were used for mixing time quantification. For each frame of the video, the average red channel value of all the pixels in the marked ROIs were calculated. The mixing time calculation is explained in Supporting Information File 1 and the Python code for the corresponding calculation is shown in Supporting Information File 3.

The loop photoreactor was photonically characterized by chemical actinometry using a ferrioxalate actinometer [31,51]. For each measurement, 495 mL 0.04 M $K_3Fe(C_2O_4)_3$ solution was irradiated with 365 nm LEDs (6 in total, mounted on 2 heat sinks). Then different electrical currents of LEDs are used to get the corresponding photon flux in the reactor. Depending on the electrical current used for the experiment, the irradiation time was in a range of 1–10 min (conversion between 1 and 13%). From the conversion, the incident photon flux was calculated.

Photocatalyst synthesis and characterization

For the synthesis of the photocatalyst, melamine (99%, Sigma-Aldrich), $H_2PtCl_6{\cdot}6H_2O$ (with a minimum Pt content of 37.50%, Sigma-Aldrich), and methanol (99.9%, VWR) were utilized. The heptazine-based polymeric carbon nitride (PCN) was synthesized by thermally condensing 30 g of melamine at 550 °C for 4 h with a heating rate of 10 °C min^{-1}. The resulting yellow solid was then finely grounded using an agate mortar. For the photochemical deposition of the Pt co-catalyst, 6 g of the produced PCN were first dispersed in 340 mL of water and subjected to sonication for 90 min. Subsequently, a mixture containing 40 mL of methanol and 20 mL of an $H_2PtCl_6{\cdot}6H_2O$ solution (0.03 mM) was added to the dispersion. The resulting suspension was stirred under N_2 atmosphere for 45 min followed by irradiation over 2 h with six 365 nm LEDs (with a total photon flux of 4.7 µmol s^{-1}) mounted on 2 heat sinks (see Supporting Information File 1, Figure S2b), while maintaining a continuous flow of N_2 in the headspace through a septum. The resulting suspension exhibited a yellow/greenish color and was subsequently washed with deionized water 3–5 times, followed by drying at 70 °C overnight and grinding. The synthesized photocatalyst is referred to as Pt-PCN.

The surface morphology, chemical composition, and elemental distribution of the Pt-PCN were analyzed using a ZEISS LEO 1550 VP scanning electron microscope (SEM) equipped with

energy dispersive spectroscopy (EDS) from Ametek, USA. The SEM was operated at an acceleration voltage of 15 kV. To prepare the sample for SEM imaging, a few milligrams of the Pt-PCN material were dispersed in 1.0 mL of ethanol using sonication for 5 min. Subsequently, a thin film of the sample was obtained by drop-casting a few microliters of the suspended sample onto a conductive Cu foil substrate and allowed to dry at room temperature. To improve the conductivity and achieve higher resolution SEM imaging, a 20 nm thick layer of Au was sputtered onto the sample surface. For EDS mapping, the samples were not sputtered with Au to avoid interference during the determination of Pt.

UV–vis electronic absorption measurement

Light attenuation in the reaction solution was measured for different optical paths (0.2, 0.5, 1, 2, 3, and 5 cm) with the same concentration of photocatalyst in water and methanol solution as used for photocatalytic hydrogen evolution. Cuvettes were used to model the reactor system. The cuvette was first put in a self-designed cuvette holder covered with cuvette holder cover (see CAD drawing of 1 cm light path cuvette holder and cuvette holder cover design as an example in Supporting Information File 1, Figures S5 and S6) with collimators (COL-UV/VIS, Avantes). All the 3D models for cuvette holder and cuvette holder cover used for different light paths are provided in Supporting Information File 4. Two Avantes fiber cables (FC-UV-600-2-BX and FC-UVIR600-2-ME) were used for the absorbance measurement. The light source used was an Avantes light source (AVALIGHT-DHC s/n: LS-2001019) and an Avantes spectrometer (AvaSpec-Mini2048CL) was used to measure the absorbance with AvaSoft software. An example of the whole absorption measurement setup using 1cm light-path cuvette and the cuvette holder setup is shown in Supporting Information File 1, Figure S7.

Photocatalytic hydrogen evolution

The flow diagram of the setup used for photocatalytic hydrogen evolution is shown in Figure 19. The photocatalyst particles were first put into 414 mL water and dispersed by ultrasonication. The suspension was then filled into the loop photoreactor together with 46 mL methanol, adding up to a total of 460 mL solution in the reactor (methanol/water = 1:9, v/v). The reactor was then sealed and the overhead stirrer motor (HS-D, Witeg Labortechnik GmbH) was turned on for stirring with the magnetic stirrer (Magnetic Stirrer Head (P-MRK), BOLA). Argon gas served both as carrier gas for the used micro GC (DynamiQ-S, Qmicro B.V.) and as inert gas to remove the oxygen in the reactor. Before the light source was turned on, argon gas was purged into the solution to remove dissolved oxygen. During the reaction, a constant argon flow was set with a mass flow controller (MFC, F-201CV-2K0-RGD-33-V, Bronkhorst High-Tech B.V.). The light source was then turned on and the photocatalytic reaction was allowed to proceed. The outlet of the reactor was connected to the GC as online analytics, probing the gas composition in 3 min intervals. The product gas stream was allowed to vent into an exhaust gas line. To align the results using photocatalysts from different batches, an adjustment factor of 2.212 was calculated. The

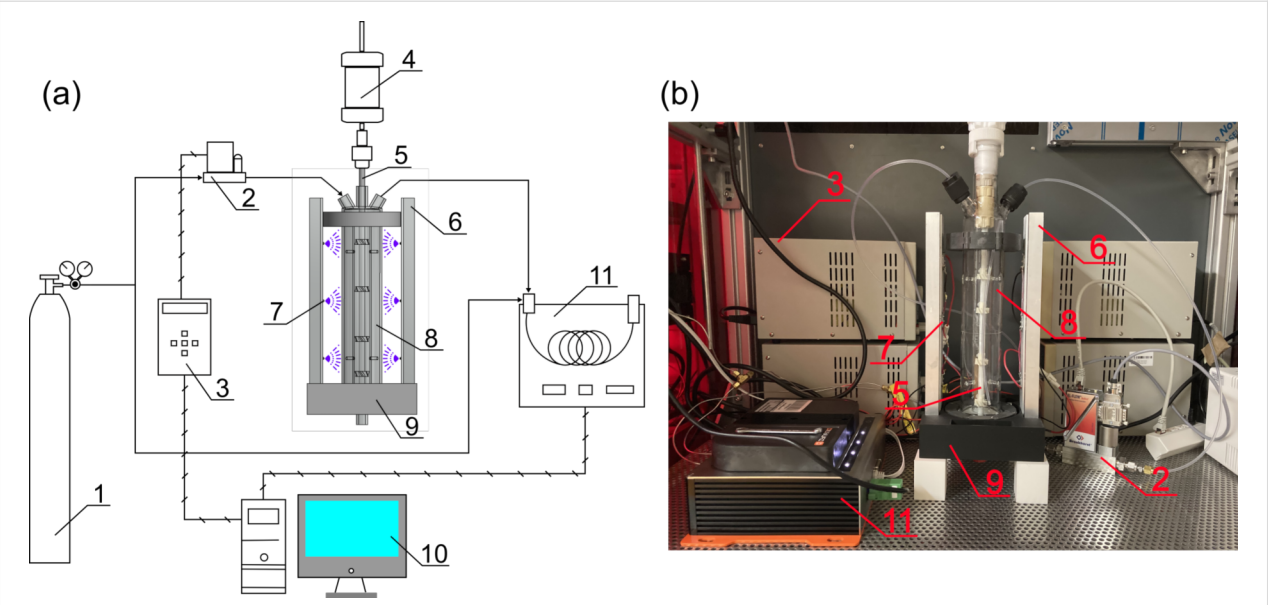

Figure 19: Photocatalytic reaction setup: (a) reaction setup flow diagram, (b) reaction setup in lab. 1 argon gas cylinder, 2 mass flow controller (MFC), 3 MFC controller, 4 overhead stirrer motor, 5 shaft tube with propellers, 6 heat sink for LEDs, 7 LED, 8 loop photoreactor, 9 3D-printed support structures, 10 computer, and 11 micro GC.

calculations are shown in Supporting Information File 1, Figure S8.

Design of experiments

A DOE analysis was used to evaluate the effect of four operating parameters, i.e., photon flux q, photocatalyst load c, stirring speed v, and inert gas flow rate $\dot{V}$ on maximum photocatalytic hydrogen generation rate. These selected parameters were considered as the independent variables and the maximum hydrogen generation rate (μmol h^{-1}) was selected as the dependent variable (response). Design-Expert® software (10.0.5.0 Stat-Ease, Inc.) was used to perform the DOE analysis. To avoid random experimental values from a range of chosen values of the parameters when using the software, the values for the independent variables were chosen manually based on the technical properties of the reaction setup, which are listed in Table 3. The studied DOE set of experiments with different combination of parameters is shown in Supporting Information File 1, Table S3. A total of 25 parameter combinations for the four independent variables was used for parameter analysis. Collected results were evaluated based on the coefficient of determination (R^2), adjusted coefficient of determination (R^2_{adj}) and predicted coefficient of determination (R^2_{pred}). These coefficients were calculated based on Equations 10–12.

$$R^2 = 1 - \sum_{i=1}^{n} \frac{(y_{i,pred} - y_{i,\exp})^2}{(\overline{y}_{i,pred} - y_{i,\exp})^2} \quad (10)$$

$$R^2_{adj} = 1 - \left[\left(1 - R^2\right) \frac{n-1}{n-K-1} \right] \quad (11)$$

$$R^2_{pred} = 1 - \frac{\sum_{i=1}^{n} (e_{-i})^2}{\sum_{i=1}^{n} (\overline{y}_{\exp} - y_{i,\exp})^2} \quad (12)$$

where n represents the number of data points, K is the number of input variables, $y_{i,pred}$ is the predicted response, $y_{i,exp}$ is the experimental data, $\overline{y}_{exp}$ is the arithmetic mean of the experimental data, and e_{-i} is a deletion residual computed by fitting a model without the ith run then predicting the ith observation with the resulting model used in the Design-Expert® software statistical analysis.

Supporting Information

Supporting Information File 1

Details of technical drawings, technical specifications, adjustment factor calculation, and DOE table.
[https://www.beilstein-journals.org/bjoc/content/supplementary/1860-5397-20-9-S1.pdf]

Supporting Information File 2

Videos from fluid flow characterization.
[https://www.beilstein-journals.org/bjoc/content/supplementary/1860-5397-20-9-S2.zip]

Supporting Information File 3

Python code for video processing to get mixing time.
[https://www.beilstein-journals.org/bjoc/content/supplementary/1860-5397-20-9-S3.zip]

Supporting Information File 4

.stl files for 3D-printed parts and CAD drawings.
[https://www.beilstein-journals.org/bjoc/content/supplementary/1860-5397-20-9-S4.zip]

Funding

This research was funded by the Deutsche Forschungsgemeinschaft DFG as part of the collaborative research center TRR234 "CataLight" (364549901), project B6 and C6.

ORCID® iDs

Mohamed M. Elnagar - https://orcid.org/0000-0003-4315-3878
Dirk Ziegenbalg - https://orcid.org/0000-0001-6104-4953

Data Availability Statement

The data that supports the findings of this study is available from the corresponding author upon reasonable request.

Table 3: Parameter label and values used for design of experiments analysis.

Parameter	Label	Levels				
photon flux [μmol s^{-1}]	q	0.82	2.60	4.70	6.37	8.19
photocatalyst loading [g L^{-1}]	c	0.11	0.22	0.33	0.43	0.65
stirring speed [rpm]	v	430	560	740	860	
inert gas flow rate [mL min^{-1}]	$\dot{V}$	15	25	35	50	

Preprint

A non-peer-reviewed version of this article has been previously published as a preprint: doi:10.26434/chemrxiv-2023-ngkhc-v3

References

1. IEA. *World Energy Outlook 2022*. https://www.iea.org/reports/world-energy-outlook-2022.
2. *BP Statistical Review of World Energy 2022 (71st Edition)*. 2022; https://www.bp.com/content/dam/bp/business-sites/en/global/corporate/pdfs/energy-economics/statistical-review/bp-stats-review-2022-full-report.pdf.
3. Shafiee, S.; Topal, E. *Energy Policy* **2009,** *37,* 181–189. doi:10.1016/j.enpol.2008.08.016
4. Ediger, V. Ş. *Energy Procedia* **2019,** *156,* 2–6. doi:10.1016/j.egypro.2018.11.073
5. Perera, F.; Nadeau, K. *N. Engl. J. Med.* **2022,** *386,* 2303–2314. doi:10.1056/nejmra2117706
6. Lelieveld, J.; Klingmüller, K.; Pozzer, A.; Burnett, R. T.; Haines, A.; Ramanathan, V. *Proc. Natl. Acad. Sci. U. S. A.* **2019,** *116,* 7192–7197. doi:10.1073/pnas.1819989116
7. Dogan, B.; Erol, D. The Future of Fossil and Alternative Fuels Used in Automotive Industry. In *2019 3rd International Symposium on Multidisciplinary Studies and Innovative Technologies (ISMSIT),* Ankara, Turkey, Oct 11–13, 2019; pp 1–8. doi:10.1109/ismsit.2019.8932925
8. Kalair, A.; Abas, N.; Saleem, M. S.; Kalair, A. R.; Khan, N. *Energy Storage* **2021,** *3,* e135. doi:10.1002/est2.135
9. Hayat, M. B.; Ali, D.; Monyake, K. C.; Alagha, L.; Ahmed, N. *Int. J. Energy Res.* **2019,** *43,* 1049–1067. doi:10.1002/er.4252
10. Jafari, T.; Moharreri, E.; Amin, A. S.; Miao, R.; Song, W.; Suib, S. L. *Molecules* **2016,** *21,* 900. doi:10.3390/molecules21070900
11. Nadeem, M. A.; Khan, M. A.; Ziani, A. A.; Idriss, H. *Catalysts* **2021,** *11,* 60. doi:10.3390/catal11010060
12. Gadgil, T.; Ibrayev, N.; Nuraje, N. Photocatalytic Water Oxidation. In *Heterogeneous Photocatalysis;* Colmenares, J. C.; Xu, Y.-J., Eds.; Green Chemistry and Sustainable Technology; Springer: Berlin, Heidelberg, 2016; pp 33–61. doi:10.1007/978-3-662-48719-8_2
13. Pfeffer, M. G.; Müller, C.; Kastl, E. T. E.; Mengele, A. K.; Bagemihl, B.; Fauth, S. S.; Habermehl, J.; Petermann, L.; Wächtler, M.; Schulz, M.; Chartrand, D.; Laverdière, F.; Seeber, P.; Kupfer, S.; Gräfe, S.; Hanan, G. S.; Vos, J. G.; Dietzek-Ivanšić, B.; Rau, S. *Nat. Chem.* **2022,** *14,* 500–506. doi:10.1038/s41557-021-00860-6
14. Li, X.; Yu, J.; Low, J.; Fang, Y.; Xiao, J.; Chen, X. *J. Mater. Chem. A* **2015,** *3,* 2485–2534. doi:10.1039/c4ta04461d
15. Hu, Y.; Huang, H.; Feng, J.; Wang, W.; Guan, H.; Li, Z.; Zou, Z. *Sol. RRL* **2021,** *5,* 2100100. doi:10.1002/solr.202100100
16. Huang, Y.; Liu, J.; Deng, Y.; Qian, Y.; Jia, X.; Ma, M.; Yang, C.; Liu, K.; Wang, Z.; Qu, S.; Wang, Z. *J. Semicond.* **2020,** *41,* 011701. doi:10.1088/1674-4926/41/1/011701
17. Goto, Y.; Hisatomi, T.; Wang, Q.; Higashi, T.; Ishikiriyama, K.; Maeda, T.; Sakata, Y.; Okunaka, S.; Tokudome, H.; Katayama, M.; Akiyama, S.; Nishiyama, H.; Inoue, Y.; Takewaki, T.; Setoyama, T.; Minegishi, T.; Takata, T.; Yamada, T.; Domen, K. *Joule* **2018,** *2,* 509–520. doi:10.1016/j.joule.2017.12.009
18. Takata, T.; Domen, K. *ACS Energy Lett.* **2019,** *4,* 542–549. doi:10.1021/acsenergylett.8b02209
19. Shaikh, A.; Al-Dahhan, M. *Ind. Eng. Chem. Res.* **2013,** *52,* 8091–8108. doi:10.1021/ie302080m
20. Harrison, S. T. L.; Kotsiopoulos, A.; Stevenson, R.; Cilliers, J. J. *Chem. Eng. Res. Des.* **2020,** *153,* 865–874. doi:10.1016/j.cherd.2019.10.049
21. Warmeling, H.; Behr, A.; Vorholt, A. J. *Chem. Eng. Sci.* **2016,** *149,* 229–248. doi:10.1016/j.ces.2016.04.032
22. Tao, J.; Huang, J.; Geng, S.; Gao, F.; He, T.; Huang, Q. *Chem. Eng. J.* **2020,** *386,* 122769. doi:10.1016/j.cej.2019.122769
23. Chaudhari, R. V.; Shah, Y. T.; Foster, N. R. *Catal. Rev.: Sci. Eng.* **1986,** *28,* 431–518. doi:10.1080/01614948608067543
24. Blenke, H. Loop Reactors. In *Advances in Biochemical Engineering;* Ghose, T. K.; Blakebrough, N.; Fiechter, A., Eds.; Springer: Berlin, Heidelberg, 1979; Vol. 13, pp 121–214. doi:10.1007/3540094687_8
25. Taştan, Ü.; Ziegenbalg, D. *Chem. – Eur. J.* **2016,** *22,* 18824–18832. doi:10.1002/chem.201602709
26. Hisatomi, T.; Domen, K. *Faraday Discuss.* **2017,** *198,* 11–35. doi:10.1039/c6fd00221h
27. Barba-Nieto, I.; Caudillo-Flores, U.; Fernández-García, M.; Kubacka, A. *Molecules* **2020,** *25,* 4008. doi:10.3390/molecules25174008
28. Marković, S.; Stanković, A.; Dostanić, J.; Veselinović, L.; Mančić, L.; Škapin, S. D.; Dražič, G.; Janković-Častvan, I.; Uskoković, D. *RSC Adv.* **2017,** *7,* 42725–42737. doi:10.1039/c7ra06895f
29. Sender, M.; Ziegenbalg, D. *Chem. Ing. Tech.* **2017,** *89,* 1159–1173. doi:10.1002/cite.201600191
30. Rajagopal, A.; Akbarzadeh, E.; Li, C.; Mitoraj, D.; Krivtsov, I.; Adler, C.; Diemant, T.; Biskupek, J.; Kaiser, U.; Im, C.; Heiland, M.; Jacob, T.; Streb, C.; Dietzek, B.; Beranek, R. *Sustainable Energy Fuels* **2020,** *4,* 6085–6095. doi:10.1039/d0se01366h
31. Wriedt, B.; Ziegenbalg, D. *J. Flow Chem.* **2020,** *10,* 295–306. doi:10.1007/s41981-019-00072-7
32. Wriedt, B.; Ziegenbalg, D. *ChemPhotoChem* **2021,** *5,* 947–956. doi:10.1002/cptc.202100122
33. Lanfermann, P.; Weidmann, C.; Dege, J.; Celik, S.; Tasch, A.; Maaß, M. C.; Waitz, T. *World J. Chem. Educ.* **2021,** *9,* 185–189. doi:10.12691/wjce-9-4-11
34. Arancibia-Bulnes, C. A.; Jiménez, A. E.; Estrada, C. A. *Adv. Chem. Eng.* **2009,** *36,* 185–227. doi:10.1016/s0065-2377(09)00406-2
35. *The Handbook for Experimenters*. Stat-Ease Inc.: Minneapolis, MN, USA, 2019; https://cdnm.statease.com/pubs/handbk_for_exp_sv.pdf.
36. Kandiel, T. A.; Dillert, R.; Robben, L.; Bahnemann, D. W. *Catal. Today* **2011,** *161,* 196–201. doi:10.1016/j.cattod.2010.08.012
37. Nomikos, G. N.; Panagiotopoulou, P.; Kondarides, D. I.; Verykios, X. E. *Appl. Catal., B* **2014,** *146,* 249–257. doi:10.1016/j.apcatb.2013.03.018
38. Baniasadi, E.; Dincer, I.; Naterer, G. F. *Int. J. Hydrogen Energy* **2013,** *38,* 9158–9168. doi:10.1016/j.ijhydene.2013.05.017
39. Hisatomi, T.; Maeda, K.; Takanabe, K.; Kubota, J.; Domen, K. *J. Phys. Chem. C* **2009,** *113,* 21458–21466. doi:10.1021/jp9079662
40. Tabata, S.; Ohnishi, H.; Yagasaki, E.; Ippommatsu, M.; Domen, K. *Catal. Lett.* **1994,** *28,* 417–422. doi:10.1007/bf00806072
41. Hisatomi, T.; Takanabe, K.; Domen, K. *Catal. Lett.* **2015,** *145,* 95–108. doi:10.1007/s10562-014-1397-z
42. Bloh, J. Z. *Front. Chem. (Lausanne, Switz.)* **2019,** *7,* 128. doi:10.3389/fchem.2019.00128
43. Escudero, J. C.; Simarro, R.; Cervera-March, S.; Giménez, J. *Chem. Eng. Sci.* **1989,** *44,* 583–593. doi:10.1016/0009-2509(89)85035-3
44. Blenke, H.; Bohner, K.; Pfeiffer, W. *Chem. Ing. Tech.* **1971,** *43,* 10–17. doi:10.1002/cite.330430103
45. Velan, M.; Ramanujam, T. K. *Chem. Eng. Sci.* **1992,** *47,* 2871–2876. doi:10.1016/0009-2509(92)87144-f

46. Velan, M.; Ramanujam, T. K. *Bioprocess Eng.* **1992,** *7,* 193–197. doi:10.1007/bf00369545
47. Prasad, K. Y.; Ramanujam, T. K. *Bioprocess Eng.* **1995,** *12,* 209–214. doi:10.1007/bf01767469
48. Weber, S. Jet Aerated Loop Reactors as Alternative to Stirred Tank Reactors. Ph.D. Thesis, Martin-Luther-Universität Halle-Wittenberg, Halle, Germany, 2019. doi:10.25673/14027
49. Bradski, G. *Dr Dobb's J. Software Tools* **2000,** *25,* 120–125.
50. Cabaret, F.; Bonnot, S.; Fradette, L.; Tanguy, P. A. *Ind. Eng. Chem. Res.* **2007,** *46,* 5032–5042. doi:10.1021/ie0613265
51. Wriedt, B.; Kowalczyk, D.; Ziegenbalg, D. *ChemPhotoChem* **2018,** *2,* 913–921. doi:10.1002/cptc.201800106

License and Terms